DOE/ER-0045/16

Alloy Development for Irradiation Performance

Semiannual Progress Report
For Period Ending March 31, **1986**

U.S. Department of Energy
Office of Fusion Energy

DOE/ER-0045/16

Alloy Development for Irradiation Performance

Semiannual Progress Report
For Period Ending March 31, **1986**

U.S. Department of Energy
Office of Fusion Energy

Printed in the United States of America Available from
National Technical Information Service
U S Department of Commerce
5285 Port Royal Road, Springfield. Virginia 22161
NTIS price codes — Printed Copy A10 Microfiche A01

This report was prepared as an account of work sponsored by an agency of the United States Government Neither the United States Government nor any agency thereof. nor any of their employees. makes any warranty, express or implied. or assumes any legal liability or responsibility for the accuracy, completeness, or usefulness of any information, apparatus. product, or process disclosed. or represents that its use would not infringe privately owned rights Reference herein to any specific commercial product, process. or service by trade name, trademark. manufacturer. or otherwise, does not necessarily constitute or imply its endorsement. recommendation, or favoring by the United States Government or any agency thereof The views and opinions of authors expressed herein do not necessarily state or reflect those of the United States Government or any agency thereof

DOE/ER-0045/16
Distribution
Category
UC-20, 20c

ALLOY DEVELOPMENT FOR IRRADIATION PERFORMANCE
SEMIANNUAL PROGRESS REPORT FOR PERIOD ENDING MARCH 31, 1986

ARGONNE NATIONAL LABORATORY

AUBURN UNIVERSITY

GA TECHNOLOGIES, INC.

McDONNELL DOUGLAS ASTRONAUTICS COMPANY

MASSACHUSETTS INSTITUTE OF TECHNOLOGY

NAVAL RESEARCH LABORATORY

OAK RIDGE NATIONAL LABORATORY

WESTINGHOUSE HANFORD COMPANY

Date Published: September 1986

Prepared by
OAK RIDGE NATIONAL LABORATORY
Oak Ridge, Tennessee 37831
operated by
MARTIN MARIETTA ENERGY SYSTEMS, INC.
for the
U. S. DEPARTMENT OF ENERGY
under contract DE-AC05-840R21400

Reports previously issued in this series are as follows:

DOE/ET-0058/1	Period Ending March 31, 1978
DOE/ET-0058/2	Period Ending June 30, 1978
DOE/ET-0058/3	Period Ending September 30, 1978
DOE/ET-0058/4	Period Ending December 31, 1978
DOE/ET-0058/5	Period Ending March 31, 1979
DOE/ET-0058/6	Period Ending June 30, 1979
DOE/ET-0058/7	Period Ending September 30, 1979
DOE/ER-0045/1	Period Ending December 31, 1979
DOE/ER-0045/2	Period Ending March 31, 1980
DOE/ER-0045/3	Period Ending June 30, 1980
DOE/ER-0045/4	Period Ending September 30, 1980
DOE/ER-0045/5	Period Ending December 31, 1980
DOE/ER-0045/6	Period Ending March 31, 1981
DOE/ER-0045/7	Period Ending September 30, 1981
DOE/ER-0045/8	Period Ending March 31, 1982
DOE/ER-0045/9	Period Ending September 30, 1982
DOE/ER-0045/10	Period Ending March 31, 1983
DOE/ER-0045/11	Period Ending September 30, 1983
DOE/ER-0045/12	Period Ending March 31, 1984
DOE/ER-0045/13	Period Ending September 30, 1984
DOE/ER-0045/14	Period Ending March 31, 1985
DOE/ER-0045/15	Period Ending September 30, 1985

FOREWORD

This report is the twenty-third in a series of Technical Progress Reports ***On Alloy Development for Irradiation Performance*** (AOIP), which is one element of the Fusion Reactor Materials Program, conducted in support of the Magnetic Fusion Energy Program of the U.S. Department of Energy. Other elements of the Materials Program are

- ***Damage Analysis and Fundamental Studies (DAFS)***
- ***Plasma-Materials Interaction (PMI)***
- ***Special-Purpose Materials (SPM)***
- ***High Heat Flux Components***

The first seven reports in this series are numbered DOE/ET-0058/1 through 7. This report is the sixteenth in a new numbering sequence that begins with DOE/ER-0045/1.

The ADIP program element is a national effort composed of contributions from a number of National Laboratories and other government laboratories, universities, and industrial laboratories. It was organized by the Materials and Radiation Effects Branch, Office of Fusion Energy, DOE, and a Task Group on ***Alloy Development for Irradiation Performance,*** which now operates under the auspices of the Reactor Technologies Branch. The purpose of this series of reports is to provide a working technical record of that effort for the use of the program participants, for the fusion energy program in general, and for the Department of Energy.

This report is organized along topical lines with Chapters 3 through 8 devoted to the various alloy classes that are currently under investigation. Thus the work of a given laboratory may appear at several different places in the report. The materials compatibility and environmental effects work on all alloy classes is collected together in Chapter 9. The Table of Contents is annotated for the convenience of the reader.

This report has been compiled and edited under the guidance of the Chairman of the Task Group on ***Alloy Development for Irradiation Performance.*** A. F. Rowcliffe, Oak Ridge National Laboratory, and his efforts and those of the supporting staff of ORNL and the many persons who made technical contributions are gratefully acknowledged. T. C. Reuther, Reactor Technologies Branch, is the Department of Energy Counterpart to the Task Group Chairman and has responsibility for the ADIP Program within DOE.

G. M. Haas, Chief
Reactor Technologies Branch
Office of Fusion Energy

FOREWORD iii

1. ANALYSIS AND EVALUATION STUDIES 1

1.1 Materials Handbook for Fusion Energy Systems (McDonnell Douglas Astronautics Company - St. Louis Division) 2

Work is progressing smoothly on the handbook and the backlog of data sheets, which numbers approximately 200, is steadily decreasing. In addition a number of new contributions on magnet case materials and high heat flux materials (copper alloys) have been received and are out for review prior to release. Work in progress includes V-15Cr-5Ti, ceramic insulators, and a special appendix to the handbook on Damage Correlations which is being prepared by the DFAS working group.

2. TEST MATRICES, EXPERIMENT DESCRIPTIONS, AND MICROSTRUCTURAL DEVELOPMENT 3

2.1 Status of U.S./Japan Colloborative Testing in HFIR AND ORR (Japan Atomic Energy Research Institute). 4

Examination is almost completed on capsules JP1 and JP3. Irradiation was completed for capsules JP6, JP7, and JP2 and specimen testing is underway. Irradiation of samples JP4, JP5, and JP8 continues. Results to date on U.S. and Japanese PCA alloys have shown low swelling when irradiated to about 30 dpa and about 2000 ppm He.

2.2 Operation of the U.S./Japan ORR Spectral Tailoring Experiments (Oak Ridge National Laboratory) 8

The ORR MFE-6J and -7J experiments continued irradiation during this reporting period ending on March 31, 1986. The total accumulated time is 200.2 Full Power Days (FPD) at 30 MW.

2.3 Design of the HFIR (JP Type) Instrumented Target Temperature Test (TTT) Capsule (Oak Ridge National Laboratory) 9

The JP-TTT experiment is scheduled to he inserted as soon as the HFIR Instrumented Target facility is completed. The conceptual design is complete. The mechanical design of the JP-TTT capsule is in progress, and some components are on order.

2.4 Neutronics Analysis in Support of the U.S.-Japan Spectral Tailoring Capsules (Oak Ridge National Laboratory) 12

Scale factors obtained previously are being used to scale the neutron fluences obtained from three-dimensional neutronics calculations. As of March 31, 1986, this procedure yields 17.81 at. ppm He (not including 2.0 at. ppm He from E-10) and 3.57 dps for type 316 stainless steel in ORR-WE-63 and 31.23 at. ppm He and 3.71 dpa in ORR-MFE-7J. The calculated and measured fluxes in the HFIR RB MFE Hafnium Dosimetry Experiment have been compared. This comparison allowed the calculation of Rf and Cd shield thicknesses required for spectral tailoring when the MFE-6J and -7J experiments are moved to HFIR RE positions.

2.5 Neutron Dosimetry and Damage Calculations (Argonne National Laboratory) 17

A one-cycle (22 day) test of the Hf liner was conducted in the RB position of HFIR at 100 MW. The Hf reduces the termal flux about an order of magnitude. Estimated damage and gas production rates are included.

Results are reported for the JP1, JP3 U.S./Japanese experiments in HFIR. Both experiments had an identical exposure history with a fast fluence (>0.1 MeV) of about 3.9×10^{22} n/cm^2 producing about 32 dpa and 2147 appm helium in 316 stainless steels.

Results are reported for several short experiments in the Omega West Reactor (LANL) designed for comparison with similar 14 MeV irradiations at RTNS 11 (LLNL). The measured fluences ranged from $5\text{-}54\times10^{18}$ n/cm/^{2}.

A new computer code, SPECOMP, has been developed to calculate displacement damage for alloys, insulators, and breeder materials. Examples are given for $LiAlO_2$ where we find 20-40% more damage in the compound than would he expected from a linear combination of the elemental calculations in SPECTER. Other compounds are now being studied.

The status of all dosimetry experiments is summarized in Table 2.5.1.

3. AUSTENIIC STAINLESS STEELS 25

3.1 Microstrucutral Oevelopment in the PCAs Irradiated to 34 dpa in HFIR at 300 and 400°C (Oak Ridge National Laboratory) 27

Microstructural observation on both U.S. and Japan PCAs indicated that all specimens developed a high concentration of fine bubbles and MC precipitates, as well as Frank faulted loops. Mutual stability of the MC particles and associated fine bubbles contributed to the extension of the transient regime of swelling to higher fluence. The irradiation response of JPCA and U.S.-PCA were similar in this HFIR irradiation condition, despite of the minor compositional difference (P,B) between the two materials. These data suggest useful fusion application of solution-annealed (SA)-PCA as well as cold-worked (CW)-PCA in the 300 to 400°C temperature range.

3.2 The Tensile Properties of Solution-Annealed (SA) JPCA Irradiated in HFIR (Oak Ridge National Laboratory) 34

The tensile properties of HFIR irradiated SA-JPCA were determined from 300 to 500°C. Comparison with microstructural observations shows that the major source of hardening at 300 and 400°C is a high concentration of cavities; MC-precipitate which formed during HFIR irradiation will be the additional source for hardening at 400°C. Total elongation of the JPCA remains above 6% in all test-temperature ranges.

This data shows the useful application of solution-annealed JPCA in the temperature range 300 to 500°C at 16 to 28 dpa damage levels.

3.3 Microchemical Compositions of Precipitates in JPCA Irradiated to 34 dpa in HFIR (Oak Ridge National Laboratory) 38

Control specimens (SA, CW, and aged) contain only MC-type precipitates. The compositions of MC particles have a strong size dependence. Smaller MC particles contain less titanium and more chromium and molybdenum. After HFIR irradiation at 400°C to 34 dpa, the specimens contain small amounts of $M_{23}C_6$ end M_6C precipitates as well as MC precipitates. The size dependence becomes more appreciable compared to that found in control specimens.

3.4 Modification of the Grain Boundary Microstructure of the Austenitic PCA Stainless Steel to Improve Helium Embrittlement Resistance (Oak Ridge National Laboratory) 43

Grain boundary MC precipitation was produced by a modified thermal mechanical pretreatment in 25% cold worked (CW) austenitic prime candidate alloy (PCA) stainless steel prior to HFIR irradiation. Postirradiation tensile results and fracture analysis showed that the modified material (B3) resisted helium embrittlement better than either solution annealed (SA) or 25% CW PCA irradiated at 500 to 600°C to -21 dpa and 1370 at. ppm He. PCA was not embrittled at 300 to 400°C. Grain boundary MC survives in PCA-B3 during HFIR irradiation at 500°C but dissolves at 600°C; it does not form in either SA or 25% CW PCA during similar irradiation. The grain boundary MC appears to play an important role in the embrittlement resistance of PCA-83.

3.5 Microstructures of Type 316 Stainless Steel Irradiated to 30 dpa at 300 and 400°C in HFIR (Oak Ridge National Laboratory) 50

Type 316 stainless steel solution annealed (SA) and 20% cold-worked (20% CW) specimens were irradiated in HFIR at 300 and 400°C to fluences of -33 dpa and 2250 at. ppm He. The swelling by bubbles was 0.3% at 300°C and 0.5% at 400°C, and was similar in SA and 20% CW material, respectively. A few fine and large precipitates with Moire fringes were observed in the trains and along train boundaries, but no γ′ precipitates were observed.

4. HIGHER STRENGTH Fe-Ni-Cr ALLOYS 58

5. REACTIVE AND REFRACTORY ALLOYS 59

5.1 The Tensile Properties and Swelling of Several Vanadium Alloys after Irradiation to 40 dpa in FFTF (Oak Ridge National Laboratory) 60

The V-3Ti-1Si alloy exhibited better resistance to irradiation hardening and helium embrittlement than V-15Cr-5Ti or VANSTAR-7 after irradiation in the Fast Flux Test Facility (FFTF) to 40 dpa at 420, 520, and 600°C. All three alloys were low swelling except VANSTAR-7 which showed high swelling at 520°C. In all cases, the preimplanted helium enhanced swelling. The V-3Ti-1Si alloy clearly outperformed the other two alloys and should be investigated end developed further.

5.2 Microstructural Evolutton and Computed Yield Stress Increase for Ion-Irradiated V-15Cr-5Ti Alloy (Argonne National Laboratory) 65

The effect of 4-MeV $^{58}Ni^{++}$ ion irradiation on the microstructure of the V-15Cr-5Ti alloy was determined for irradiation temperatures ranging from 550°C to 750°C dnd for damage levels of 50 to 260 dpa. The swelling of the alloy that could be attributed to voids was negligible (<0.1%). The principle effect of the irradiation was to induce the formation of disc-shape precipitates in the alloy microstructure. The increase of the yield stress for the alloy resulting from the irradiations was evaluated from the irradiation-produced dislocation density and the number density end size of irradiation-produced precipitates. These evaluations showed that the increase of yield stress for the alloy on irradiation has a maximum value at -50 dpa, and the increase of yield stress decreases for irradiation temperatures above 600°C.

5.3 Environmental and Chemical Effects on the Properties of Vanadium-Base Alloys (Argonne National Laboratory) 71

The susceptibility of V-15Cr-5Ti to stress corrosion cracking in high-purity water at 288% is being evaluated by means of constant extension rate tensile (CERT) tests. No stress corrosion cracking was observed in tests conducted at a strain rate of 1×10^{-6} s^{-1} and dissolved oxygen levels in the range <0.005 to 7.7 wppm.

5.4 Preparation and Fabrication of Vanadium Base Alloys (Argonne National Laboratory) 73

Fabrication of V-15Cr-5Ti alloy has begun to replenish the inventory of vanadium ternary alloy for Path C Scoping Studies. A process flowsheet has been devised to generate alloy material having optimum properties. Process operations are designed to minimize the pickup of interstitial elements O, N, H and C for R&D requirements.

Pure vanadium, chromium and titanium feedstock materials have been prepared for alloy consolidation melting. Premary and secondary plasma arc melting of 350 g ingots has begun. Two flat stock rolling experiments were conducted on as-cast material. Alloy sheet delivery is planned to begin early in the third quarter.

6. INNOVATIVE MATERIAL CONCEPTS 78

6.1 The Effect of Strain Rate and Long-Term Aging on the Properties of Iron-Base LRO Alloys (Auburn University) 79

Tensile tests covering strain rates from 10^{-6} to 10^{0}/s were performed on the ordered alloys at room temperature. The results indicate that there is little or no effect of strain rate on the tensile strength and ductility. The long-term thermal exposure at 600°C does not cause any significant change in tensile properties. The deformation and fracture characteristics along with controlling mechanisms change as a function of strain rate and aging time.

7. FERRITIC STEELS 90

7.1 Helium Effects on Void Formation in 9Cr-1MoVNb and 12 Cr-1MoVW Irradiated in HFIR (Oak Ridge National Laboratory) 91

Up to 2 wt % Ni was added to 9Cr-1MoVNb and 12Cr-1MoVW ferritic steels to increase helium production by transmutation during HFIR irradiation. The various steels were irradiated to -39 dpa. Voids were found in all the undoped and nickel-doped steels irradiated at 400°C. Voids developed in most of the steels at 500°C, but not in any of them at 300 or 600°C. Bubble formation, however, was increased at all temperatures in the nickel-doped steels. Maximum void formation was found at 400°C, but swelling remained less than 0.5% even with up to 440 appm X. Irradiation at 300 to 500°C caused dissolution of as-tempered $M_{23}C_6$ precipitates and coarsening of the lath/subgrain structure in the 9-Cr steels, whereas the microstructure generally remained stable in the 12-Cr steels. Irradiation in this temperature range also caused compositional changes in the as-tempered MC phase in all the steels, and produced combinations of fine M_6C, G, and M_2X precipitates in various steels. The subgrain boundaries appear to be strong sinks that enhance resistance to void formation. Nigher helium production during irradiation appears to shorten the incubation period for void formation. The effects of helium on steady state void swelling behavior, however, remain unknown.

7.2 On the Saturation of the OBTT Shift of Irradiated 12Cr-1MoVW with Increasing Fluence (Oak Ridge National Laboratory) 102

Identical subsize Charpy specimen of 12Cr-1MoVW steel were irradiated at 300°C to a fluence of 0.86 × 10^{24} n/m² (E > 0.1 MeV) and at 300 to 400°C to a fluence of -1 × 10^{24} n/m² (E > 0.1 MeV). Impact testing indicated the DBTT was increased by irradiation at 300° by 36 and 164°C, respectively, for the low and high fluences. Irradiation at 400°C led to an increase in the DBTT of 217°C. Aging alone has an insignificant effect on the impact properties. The major portion of the irradiation emhrittlement at 300°C occurs for fluences beyond 1 × 10^{24} n/m².

7.3 The Development of Ferritic Steels for Fast Induced-Radioactivity Decay (Oak Ridge National Laboratory) 109

Tensile studies were continued on eight heats of normelized-end-tempered chromium-tungsten steel that contained variations in the composition of chromium, tungsten, vanadium, and tantalum. The results were compared to results for analogous chromium-molybdenum steels.

7.4 Fatigue Behavior of Irradiated Helium-Containing Ferritic Steels for Fusion Reactor Applications (Oak Ridge National Laboratory) 114

The martensitic alloys 12Cr-1MoVW and 9Cr-1MoVNb have been irradiated in the High Flux Isotope Reactor (HFIR) and subsequently tested in fatigue. In order to achieve helium levels characteristic of fusion reactors, the 12Cr-1MoVW was doped with I and 2% Ni, resulting in helium levels of 210 and 410 at. ppm at damage levels of 25 dpa. The 9Cr-1MoVNb was irradiated to a damage level of 3 dpa and contained <5 at. ppm He. Irradiations were carried out at 55°C and testing at 22°C. No significant changes were found in 9Cr-1MoVNb upon irradiation at this damage level, hut possible effects of helium were found in 12Cr-1MoVW. Alloys with 210 and 410 at. ppm He showed cyclic strengthening of 29 and 34% over unirradiated, helium-free nickel-doped materials, respectively. This cyclic hardening, which may be caused by helium, resulted in a degradation of the cyclic life. However, the fatigue life remained comparable to or better than that of unirradiated 20%-cold-worked 316 stainless steel

7.5 Effects of Irradiation on Ferritic Alloys and Implications for Fusion Reactor Applications (Westinghouse Hanford Company) 123

The ADIP irradiation effects data base on ferritic (martensitic) alloys is reviewed in order to provide reactor design teams with an understanding of how such alloys will behave for fusion reactor first wall applications. Irradiation affects dimensional stability, strength and toughness. Dimensional stability is altered by precipitation and void swelling. Swelling as high as 25% may occur in some ferritic alloys at 500 dpa.

Irradiation alters strength both during irradiation and following irradiation. Irradiation at low temperatures leads to hardening whereas at higher temperetures and high exposures, precipitate coarsening can result in softening. Toughness can also he adversely affected by irradiation. Failure can occur in ferritics in a brittle manner and irradiation induced hardening causes hrittle failure at higher temperatures. Even at high test temperatures, toughness is reduced due to reduced failure initiation stresses.

Ferritic alloys should provide an attractive material for structural applications in a fusion reactor hut the temperature regime over which they are used must be limited.

7.6 Effects of Irradiation on Low Activation Ferritic Alloys to **45** dpa (Westinghouse Hanford Company) 131

Nine low activation ferritic alloys covering the range 2 to 12Cr with alloying additions of tungsten and/or vanadium have been irradiated to intermediate fluences of 30 to 45 dpa and tensile tested or examined by transmission electron microscopy in order to determine the effect of increasing neutron dose on properties and microstructure. Changes in properties and microstructure are for the most part completed within 10 dpa hut swelling and dislocation evolution continue with increasing dose at 420°C and subgrain coarsening occurs at 600°C.

7.7 **Charpy Impact Behavior of Manganese Stabilized Martensitic Steels (Westinghouse Hanford Company)** 140

Tests were conducted to evaluate the irradiation-induced shift in ductile-to-brittle transition behavior of two manganese stabilized martensitic steels. Miniature Charpy specimens were fabricated from two heats of steel similar in composition to HT-9 but with 0.1% C end Mn contents ranging from 3.3 to 6.6%. The 3.3% Mn steel showed a transition temperature similar to that of HT-9 in both the unirradiated condition and in specimens irradiated to 11.3 dpa. The steel containing 6.6% Mn exhibited a higher transition temperature after irradiation than the steel containing 3.3% Mn. The upper shelf energy (USE) after irradiation for the manganese stabilized alloys was much higher than for HT-9.

7.8 **Fracture Toughness of Ferritic Alloys Irradiated in FFTF (Westinghouse Hanford Company)** . . . 145

Ferritic compact tension specimens loaded in the Material Open Test Assembly (MOTA) for irradiation during FFTF Cycle 4 were tested at temperatures ranging from room temperature to 428°C. The electric potential single specimen method was used to measure the fracture toughness of the specimen. Results showed that the fracture toughness of both HT-9 and 9Cr-1Mo decreases with increasing test temperature and that the toughness of HT-9 was about 30% higher than that of 9Cr-1Mo. In addition, increasing irradiation temperature resulted in an increase in tearing modulus for both alloys.

7.9 **Microstructural Examination of 12%Cr Martensitic Stainless Steel After Irradiation at Elevated Temperatures in FFTF (Westinghouse Hanford Company)** 150

A remelted 12%Cr martensitic stainless steel (HT-9) has been examined before and after irradiation in the Materials Open Test Assembly (MOTA) of the Fast Flux Test Facility (FFTF), using a scanning transmission electron microscope. The irradiation temperatures were 365°C, 420°C, 520°C, and 600°C with the fluences as high as 7.3×10^{22} n/cm² (E>0.1 Mev) or 34 dpa. The extracted precipitates from each specimen were identified using X-ray microanalysis and selected area diffraction. The precipitates in the unirradiated condition were primarily $M_{23}C_6$ carbides which formed at martensite lath and prior austenite grain boundaries. During irradiation at elevated temperatures small amounts of other phases formed which were tentatively identified as the chromium rich α', the nickel-silicon rich G-phase and the intermetallic Chi phase. Irradiation-induced voids were observed only in specimens irradiated at 420°C to a dose of 34 dpa; no voids were found for specimens irradiated at 365°C (~11 dpa), 520°C (~34 dpa), and 600°C (~34 dpa). These results are not in agreement with previous experiments in that voids have not been reported in this alloy at relatively high fluence level (~67 dpa) following irradiation in other fast-spectrum reactor (EBR-II) but this is the first observation following FFTF irradiations. The present results indicate that cavities can form in HT-9 at modest fluence levels even without significant generations of helium bubbles. Hence, the cavity formation in this class of ferritic alloys is not simply due to helium generation but rather a more complex mechanism.

8. **COPPER AND ITS ALLOYS** 162

8.1 **Hydrogen Embrittlement in GLIDCOP Al-20 Copper Alloy (Oak Ridge National Laboratory)** 163

The MFE heat of the AI-20 dispersion-strengthened copper alloy becomes embrittled when annealed in vacuum at temperatures greater than 400°C. A chemical analysis of this heat has found that the alloy contains a significant amount of hydrogen. The hydrogen was apparently introduced by the manufacturer during an attempt to deoxidize the alloy. The MFE heat of AI-20 is therefore subject to swelling and hydrogen embrittlement effects at elevated temperatures even when tested in a hydrogen-free environment.

9. **MATERIALS COMPATIBILITY AND HYDROGEN PERMEATION STUDIES** 168

9.1 **Corrosion of Fe–Cr–Mn and Fe–Cr–Mo Alloys in Thermally Convective Lithium (Oak Ridge National Laboratory)** 169

Experiments with Fe-Cr-Mo and austenitic Fe-Cr-Mn alloys exposed to nonisothermal lithium environments revealed the importance of chromium reactions in the corrosion processes. Such reactions were found to significantly affect the temperature dependence of the corrosion of the 12Cr-1MoVW steel by thermally convective lithium. For the Fe-Cr-(12-20 wt %)Mn alloys, preferential depletion and mass transport of manganese were also important corrosion reactions.

9.2 Thermal Convection Loop Corrosion Studies of Ferrous Alloys Exposed to Molten Pb-17 at. % Li (Oak Ridge National Laboratory) 181

Longer-term (>6000 h) data for type 316 stainless steel and 12Cr-1MoVW steel exposed to thermally convective Pb-17 at. % Li yielded more extensive information about dissolution rates and environmentally-induced surface modification of these alloys. The austenitic steel suffered greater corrosion and irregular penetration and dissolution by the lead-lithium, whereas the 12Cr-1MoVW steel tended to corrode uniformly at a lower rate. A model for the nonuniform penetration of type 316 stainless steel by Pb-17 at. % Li was suggested.

9.3 Corrosion of Austenitic and Ferritic Steels in Flowing Lithium Environment (Argonne National Laboratory) 186

Corrosion data are presented for ferritic HT-9 and Fe-9Cr-1Mo steels and austenitic Type 316 stainless steel in a flowing lithium environment at temperatures between 372 and 538°C. Metallic elements detected on the corrosion specimens indicate the presence of corrosion products on the alloy surfaces. These products are ternary nitrides of lithium and major alloy constituents.

9.4 Environmental Effects on Properties of Structural Alloys in Flowing Pb-17Li (Argonne National Laboratory) 190

Corrosion data have been obtained on ferritic HT-9 and Fe-9Cr-1Mo steel and austenitic Type 316 stainless steel in a flowing Pb-I7 at. % Li environment at temperatures between 371 and 482°C. The corrosion behavior is evaluated by measurements of weight loss and depth of internal corrosion as a function of time and temperature.

10. STATUS OF IRRADIATION EXPERIMENTS AND MATERIALS INVENTORY 195

10.1 Fusion Program Research Materials Inventory (Oak Ridge National Laboratory) 196

10.2 Irradiation Experiment Status and Schedule (Oak Ridge National Laboratory) 199

1. ANALYSIS AND EVALUATION STUOIES

1.1 MATERIALS HANDBOOK FOR FUSION ENERGY SYSTEMS - J. W. Davis (McDonnell Douglas Astronautics Company - St. Louis Division)

1.1.1 ADIP Task

Task Number I.A.l, Define material property requirements and make structural life predictions.

1.1.2 Objective

To provide a consistent and authoritative source of material property data for use by the fusion community in concept evaluation, design, and performance/verification studies of the various fusion energy systems. A second objective is the early identification of areas in the materials data base where insufficient information or voids exist.

1.1.3 Summary

Work is progressing smoothly on the handbook and the backlog of data sheets, which numbers approximately 200 is steadily decreasing. In addition a number of new contributions on magnet case materials and high heat flux materials (copper alloys) have been received and are out for review prior to release. Work in progress includes V-15 Cr-5Ti, ceramic insulators, and a special appendix to the handbook on Damage Correlations which is being prepared by the DFAS working group. In addition a Volume 2, Supporting Documentation volume is being prepared for release in the near future. This volume will include the rationale, references, and assumptions used in developing specific data pages.

1.1.4 Progress and Status

The eleventh publication package for the materials handbook has been distributed to qualified handbook holders. This publication package contains a complete rewrite of the fiberglass epoxy insulator (G-10) section as well as the introduction of a new section on fiberglass polyimide. These materials are for use in superconducting magnetics and the cryogenic materials properties reflect this application. In developing these data sheets it became clear that the original outline for the handbook needed to be revamped to more closely reflect the organization of the handbook and the data pages that are in work or planned for inclusion in the future. As a result, a new handbook outline and corresponding tab dividers were developed and distributed in the eleventh publication package.

In addition to data sheets on magnet insulators, new data sheets on the irradiation induced swelling of the ferritic alloy HT-9 were also distributed. This data sheet is the first of a series of radiation effects data pages on the ferritic steels and austenitic steels based on fission reactor correlations which have been extrapolated to operating environments outside of the data set. The next group will be the irradiation induced stress free swelling of 20% cold worked type 316 stainless steel. In preparation are correlations for the irradiation creep of HT-9 and 20% cold worked 316.

With the inclusion of this irradiation information into the handbook, it is becoming apparent that additional information is needed particularly with regard to damage correlations. To assist handbook users in this area a special appendix to the handbook entitled "Damage Correlation" has been created and the DAFS task group was requested to prepare the contribution for this section. In addition to this effort, work is in progress to prepare data sheets on the Vanadium alloy, V-15Cr-5Ti and on copper alloys. Contributions have been received from Nancy Simon of NBS on magnet case steels and on copper alloys from Bill Wiffen of ORNL. These data pages have been submitted to the advisory group for review prior to incorporation into the handbook.

To complement the handbook a second volume is in preparation. This volume is entitled "Supporting Documentation" and will include the rationale, assumptions, and data base used to develop the data pages included in Volume 1, "Design Data." Volume 2 should be released to the handbook holders later this year.

2. TEST MATRICES, EXPERIMENT DESCRIPTIONS, AND MICROSTRUCTURAL DEVELOPMENT

2.1 STATUS OF U.S./JAPAN COLLOBORATIVE TESTING IN HFIR AND ORR — J. L. Scott (Oak Ridge National Laboratory) and M. P. Tanaka (Japan Atomic Energy Research Institute.)

2.1.1 ADIP Task

ADIP task I.A.2, Define Test Matrices and Test Program

2.1.2 Objectives

The objectives of this program are to determine the response of U.S. and Japanese austenitic stainless steels to the combined effects of displacement damage and helium generation at temperatures in the range of 65 to 600°C. Since a basic understanding is sought in addition to an engineering data base, many advanced alloys and model alloys are included in the program.

2.1.3 Summary

Examination is almost completed on capsules JP1 and JP3. Irradiation was completed for capsules JP6, JP7, and JP2 and specimen testing is underway. Irradiation of capsules JP4, JP5, and JP8 continues. Results to date on U.S. and Japanese PCA alloys have shown low swelling when irradiated to about 30 dpa and about 2000 ppm He.

2.1.4 Progress and Status

The program of U.S./Japan collaborative testing in HFIR and ORR consists of eight Phase 1 HFIR target capsules irradiated to peak damage levels of about 30 and 50 dpa and two ORR spectrally tailored capsules to be irradiated to 30 dpa with incremental removal and testing at 5, 10, and 20 dpa. The test matrix and initial results have been described previously.[1-5] The present irradiation status of the Phase 1 HFIR capsules is shown in Table 2.1.1. The two ORR spectrally tailored capsules are operating within the design temperature range and have achieved 200 full power days at 30 MW. During the current reporting period, HFIR capsules JP6, JP7, and JP2 completed irradiation. Final damage levels are given in Tables 2.1.2–2.1.4.

2.1.4.1 Length and Density Changes in Irradiated HFIR Tensile Specimens

Length and immersion density measurements were made of the tensile specimens in capsule JP3 after irradiation. The length change measurement is not considered to be of high precision and has an accuracy of about 0.5%. Results are given in Table 2.1.5. Length changes were within experimental error.

Density measurements were made on the tensile specimens using Avogadro's principle. A precision analytical balance modified for radiation resistance was used with a flourocarbon, FC43*, as the working fluid. A circulating bath with temperature control is used to maintain a constant temperature in the working fluid. Because of the difficulties of working in the hot cells, somewhat lower accuracy is expected than would be the case on unirradiated specimens. To improve accuracy a control specimen from the same lot is measured after a batch of three irradited specimens are measured. Volume changes are calculated from the differences in measured densities between an irradiated specimen and the control specimen. Accuracy is believed to be about ± 0.27.

The measured volume changes are compared with those calculated from length changes assuming isotropic behavior. There is relatively good agreement between the two sets of data even though the immersion density data are considerably more accurate.

Table 2.1.1. Status of U.S.-Japan High Flux Isotope Reactor (HFIR) capsules[a]

Capsule	Reactor exposure[b] (MWd)	Level, dpa	
		Present[c]	Goal[d]
JP1[e]	33,644	33.03	30
JP2[e]	57,507	56.74	50
JP3[e]	34,019	33.40	30
JP4	55,735	54.81	50
JP5	45,376	44.64	50
JP6[e]	36,677	34.06	30
JP7[e]	34,652	34.03	30
JP8	43.268	42.56	50

[a]Date: March 25, 1986.

[b]Reactor Power: 100 MW.

[c]Peak displacements-per-atom (dpa) level in type 316 stainless steel (13.5 wt % Ni).

[d]Average.

*Irradiation completed.

2.1.4.2 Tensile Properties of Irradiated HFIR Specimens

Tensile tests were run on the submini tensile specimens from capsules JP3 and JP6. Results will be reported when the test matrix is completed.

*Trade mark 3M Company.

Table 2.1.2. Displacements per atom and helium contents in High Flux Isotope Reactor (HFIR) JP6 Capsule[e]

Position	Distance from HFIR centerline (cm)	Specimen			Specimen number	Displacements per atom (dpa)	Helium content (at. ppm)
		Type	Temp (°C)	Alloy			
1	23.20	Tensile	600	PCA	EL24	16.33	1057
2	18.76	TEM[b] disks	500	PCA[c]		22.76	1606
	14/31	Tensile	500	316	AA42	27.15	1646
	9.59	Fatiaue	430	PCA	EC156	31.69	2353
5	4.58	Fatigue	430	PCA	EC161	34.10	2551
6	0.00	TEM disks	600	J316[c]		34.06	2188
7	4.58	Fatigue	430	JPCA	FE12	33.96	2499
8	9.59	Fatigue	430	JPCA	FE13	31.56	2307
9	14.31	Tensile	500	JPCA	TE10	27.71	1995
10	18.76	Tensile	400	JPCA	TE11	22.67	1578
11	23.20	Tensile	300	JPCA	TE12	16.27	1046

[a]MWd: 34,677.

*Transmission electron microscopy.

[c]This holder contained several alloys.

Table 2.1.3. Displacements per atom and helium contents in High Flux Isotope Reactor (HFIR) JP7 Capsule[s]

Position	Distance from HFIR centerline (cm)	Specimen			Specimen number	Displacements per atom (dpa)	Helium content (at. ppm)
		Type	Temp (°C)	Alloy			
1	23.20	Tensile	600	PCA	EC36	16.32	1056
2	18.76	Tensile	500	PCA	EL29	22.74	1604
3	14.31	Tensile	500	PCA	EL31	27.80	2034
4	9.59	Fatigue	550	316	AA54	30.88	1905
5	4.58	Fatigue	550	PCA	EF5	34.07	2554
6	0.00	TEM[b] disks	500	J316[c]		34.03	2186
7	4.58	Tensile	600	JPCA	TE16	33.93	2497
8	9.59	Tensile	600	JPCA	TE17	31.54	2305
9	14.31	Tensile	500	JPCA	TE18	27.69	1993
10	18.76	Tensile	400	JPCA	TE19	22.66	1577
11	23.20	Tensile	300	JPCA	TE20	16.26	1045

[a]MWd: 34,652.

*Transmission electron microscopy

[c]This holder contained several alloys.

Table 2.1.4. Displacements per atom and helium contents in High Flux Isotope Reactor (HFIR) JP2 Capsule[a]

Position	Distance from HFIR centerline (cm)	Specimen			Specimen number	Displacements per atom (dpa)	Helium content (at. ppm)
		Type	Temp (°C)	Alloy			
1	23.20	Tensile	300	PCA	EL36	27.56	2031
2	18.76	Tensile	400	PCA	EL37	38.15	2884
3	14.31	Tensile	500	PCA	EL39	46.43	3533
4	9.59	Fatigue	430	PCA	EC157	52.73	4005
5	4.58	Fatigue	430	316	AA3	55.21	3471
6	0.00	TEM[b] disks	300	J316[c]		56.74	3667
7	4.50	Fatigue	430	JPCA	FE3	56.42	4180
8	9.59	Fatigue	430	JPCA	FE4	52.51	3904
9	14.31	Tensile	500	JPCA	TB4	46.24	3446
10	18.76	Tensile	400	JPCA	TB5	37.99	2817
11	23.20	Tensile	300	JPCA	TB6	27.45	1973

[a]MWd: 57,507.

[b]Transmission electron microscopy.

[c]This holder contained several alloys.

Table 2.1.5. Length and Density Changes of Submini Tensile Specimens in High Flux Isotope Reactor (HFIR), JP3 Capsule

Specimen number	Alloy	Conditions	Irradiation temperature (°C)	Length (mm)			Density Change (%)	
				Initial	Final	Increase (%)	$3\Delta L/L_o$	$\frac{\Delta V}{V_o}$
TB9	JPCA	PS2	300	39.40	39.43	0.08	0.24	0.32
TB8	JPCA	PS2	400	39.40	39.46	0.45	0.45	0.38
TB7	JPCA	PS2	500	39.41	39.45	0.10	0.30	0.79
EL30	PCA	B3	300	39.34	39.45	0.14	0.42	0.30
EL34	PCA	B3	400	39.34	39.52	0.47	1.41	0.53
EC29	PCA	A3	500	39.35	39.43	0.20	0.60	0.36

[a]A3 – SA at 1100°C + 25% CW.

B3 – SA at 1100°C + 8 h at 800°C + 25% CW.

PS2 – SA at 1100°C.

PC2 – PS2 + 15% CW.

2.1.4.3 Fatigue Testing

Fatigue tests have started for specimens from capsules JP1 and JP3. Results will be reported when the test matrix is completed.

2.1.4.4 Microstructual Analysis

Present results from microstructural analysis are presented in sections 3.2 and 3.3 of this report.

2.1.5 Future Results

Testing is nearly completed for capsules JP1 and JP3. Density, tensile and fatigue testing and SEM of fractures remain to be done on specimens from JP6, JP7, and JP2. Postirradiation testing on capsules JP4, JPS, and JP8 will be completed in the next reporting period.

2.1.6 References

1. A. F. Rowcliffe, M. L. Grossbeck, and S. Jitsukawa, "The U.S./Japan Collaborative Testing Program in HFIR and ORR: Irradiation Matrices for HFIR Irradiation," pp. 38-43 in *ADIP* Semiann. *Prog. Rep., Mer. 31, 1984,* DOE/ER-0045/12, U.S. DOE, Office of Fusion Energy.

2. A. F. Rowcliffe, M. L. Grossbeck, M. Tanaka and S. Jitsukawa, "The U.S./Japan Collaborative Testing Program in HFIR and ORR: Specimen Matrices for HFIR Irradiation," pp. 61-62, in *ADIP* Semiannu. *Prog. Rep., Sept.* 30, *1984*, DOE/ER-0045/13, U.S. DOE, Office of Fusion Energy.

3. J. L. Scott and M. P. Tanaka, "Preparation for Postirradiation Examination of U.S./Japan HFIR Capsules," pp. 10-11 in *ADIP* Semiannu. *Prog. Rep., March 31, 1985,* DOE/ER-0045/14, U.S. DOE, Office of Fusion Energy.

4. J. L. Scott, M. L. Grossbeck, and M. P. Tanaka, "Phase I HFIR Capsules - Irradiation and Postirradiation Examination," pp. 18-21 In *ADIP* Semiannu. *Prog. Rep., Sept. 30, 1985,* DOE/ER-0045/15, U.S. DOE, Office of Fusion Energy.

5. J. L. Scott et al., "Description of the U.S./Japan Spectral-Tailoring Experiment in ORR," pp. 22-40 in *ADIP Semiannu. Prog. Rep., Sept. 30, 1985,* DOE/ER-0045/15, U.S. DOE, Office of Fusion Energy.

2.2 OPERATION OF THE U.S./JAPAN ORR SPECTRAL TAILORING EXPERIMENTS – I. I. Siman-Tov (Oak Ridge National Laboratory)

2.2.1 ADIP Task

ADIP Task I.A.2, Define Test Matrices and Test Procedures

2.2.2 Objectives

The experiments in the U.S./Japan collaborative testing program in the ORR contain austenitic stainless steel alloys for possible use as first-wall and blanket structural materials in fusion reactors. These alloys will be irradiated with mixed-spectrum neutrons and with spectral tailoring to achieve the helium-to-displacement-per-atom (He/dpa) ratios predicted for fusion reactor service.

2.2.3 Summary

The ORR MFE-6J and -7J experiments continued irradiation during this reporting period ending on March 31, 1986. The total accumulated time is 200.2 Full Power Days (FPD) at 30 MW.

2.2.4 Prowess and Status

The details of the U.S./Japan collaborative irradiation program have been described previously.[1-4]

ORR-MFE-6J: The experiment continued routine operation with typical temperatures ranging between 173 and 200°C in the 200°C region. The total accumulated irradiation time is 200.2 FPD (at 30 MW).

ORR-MFE-7J: The experiment continued operation with a maximum temperature of 330°C in the top region and an average temperature of 400°C (at thermocouple number TE5) in the bottom region. The total accumulated irradiation time is 200.2 FPD (at 30 MW).

On January 7, 1986, during startup, it was discovered that one of the vent tubes over the NaK region was plugged. As a result, we now check the link to the NaK region once a week by operating the reactor at 24 MW for a few minutes and noting the change in the NaK cover gas pressure.

2.2.5 References

1. J. A. Conlin and J. W. Woods, "Irradiation Experiments for the U.S./Japan Collaborative Testing in HFIR and ORR." p. 37 in *ADIP Semiannu. Prog. Rep., Mar. 31, 1984,* DOE/ER-0045/12, U.S. DOE, Office of Fusion Energy.

2. J. A. Conlin and J. W. Woods, "Irradiation Experiments for the U.S./Japan Collaborative Testing in HFIR and ORR," pp. 66–67 in *ADIP Semiannu. Prog. Rep., Sept. 30, 1984,* DOE/ER-0045/13, U.S. DOE, Office of Fusion Energy.

3. I. I. Siman-Tov, J. A. Conlin, and J. W. Woods, "Irradiation Experiments for the U.S./Japan Collaborative Testing in HFIR and ORR," p. 6 in *ADIP Semiannu. Prog. Rep., Mar. 31, 1985*, DOE/ER-0045/14, U.S DOE, Office of Fusion Energy.

4. I. I. Siman-Tov, "Irradiation Experiments for the U.S./Japan Collaborative Testing in HFIR and ORR," p. 41 in *ADIP Semiannu. Prog. Rep. Sept. 30, 1985,* DOE/ER-0045/15, U.S. DOE, Office of Fusion Energy

2.3 DESIGN OF THE HFIR (JP TYPE) INSTRUMENTED TARGET TEMPERATURE TEST (TTT) CAPSULE – I. ▮ -Siman-Tov (Oak Ridge National Laboratory)

2.3.1 AOIP Task

AOIP Task I.A.2, Define Test Matrices and Test Procedures.

2.3.2 Objectives

The primary objective of this experiment is to determine the temperatures in the JP series capsules[1-4] by placing an instrumented JP mockup experiment in the modified HFIR Instrumented Target facility.

A secondary objective is to determine the nuclear heating rate in stainless steel as a function of the axial core position and the time in a HFIR cycle.

2.3.3 Summary

The JP-TTT experiment is scheduled to be inserted as soon as the HFIR Instrumented Target facility is completed. The conceptual design is complete. The mechanical design of the JP-TTT capsule is in progress, and some components are on order.

2.3.4 Prowess and Status

CONCEPTUAL DESIGN – The following decisions have been made

1. Mock up the temperature distribution in the JP-3 and JP-5 capsules; the higher temperatures in the TEM region should produce a more accurate result.

2. Replace positions 1, 3, and 5 by the nuclear heating test while maintaining the same temperature designed for the replaced specimens. This distribution should yield information on the nuclear heating in stainless steel and its dependence on the axial position relative to the core Horizontal Midplane (HMP). The variation of the temperature with time will also yield information on the time dependence of the nuclear heating.

3. A total of three Thermocouple Array Tubes (TCATs) will be used (see configuration in Fig. 2.3.1). Each TCAT contains 7 Thermocouples. The two top TCATs are 0.046 in. in outside diameter (OD), and the third has a 0.041-in. OD. Since the top region consists mostly of heavier sections of stainless steel, the larger diameter of the TCATs will not upset the basic material configuration of the measured regions. A calculation indicated that the change in the TCAT conductance when compared with the stainless steel it replaces is negligible since the effect of the difference in the heat generation rate in MgO and that of the difference in thermal conductivity cancel each other out.

In the lower region where all positions are occupied by mockup specimens, the percentage of replaced material would be higher, so the TCAT OO will be kept to the absolute minimum for seven junctions (0.041 in.).

MECHANICAL DESIGN –

The mechanical design was completed for review. A design review meeting was held on March 19, 1986, to assure compliance with HFIR Quality Assurrance (QA) and safety specifications as well as to ensure that the design is compatible with the new HFIR Instrumented Target facility that is being completed. The drawings of the JP capsules are being revised accordingly and prepared to be issued. An assembly procedure is also being prepared.

FABRICATION –

Some items are on hand from previous capsules, The mockup specimens, holders, and some of the other components are on order. All components are expected to be delivered by May 16, 1986.

TESTING –

Several tests are planned to ensure smooth assembly and accuracy in the temperature measurements:

1. Check the effect of magneforming only sections of the housing tube on the clearance between the nuclear heating specimens and the housing tube. A clearance of between 1.5 and 3 mils is needed without putting the specimens in special holders.

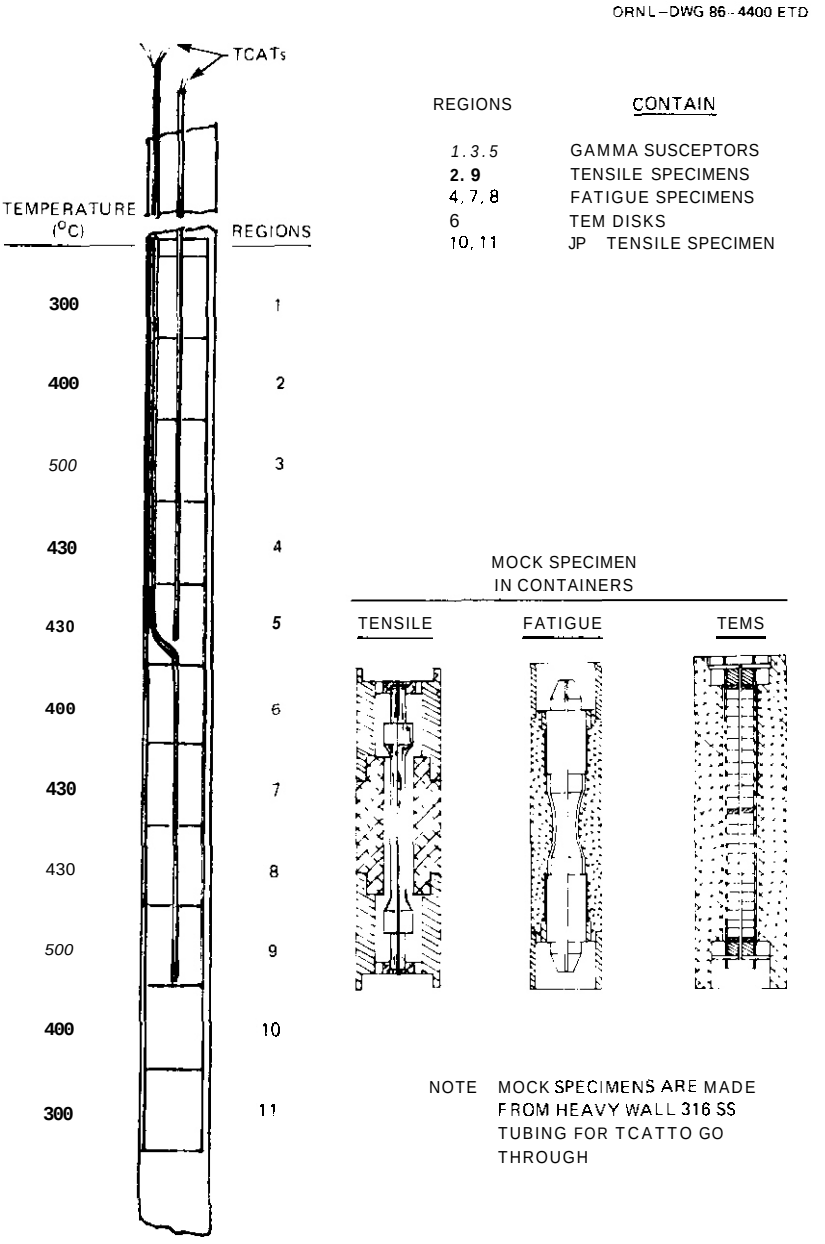

Fig. **2.3.1.** JP-TTT capsule configuration of test regions.

2. Develop a brazing procedure either by induction or furnace brazing to ensure proper primary containment and the integrity of the thermocouples.

3. Practice the specimen loading procedure to ensure proper tolerance fits between. the TCAT's OD, the specimen holes, and the combined loading into the housing tube in order to prevent possible interference and misalignment.

Design, fabrication, and testing should be completed by May 15. Barring any problems during testing, the assembly should be completed by June 16, 1986.

2.3.5 References

1. A. F. Rowcliffe, M. L. Grossbeck, and S. Jitsukawa, "The U.S./Japan Collaborative Testing Program in HFIR and ORR," pp. 38–43 in *ADIP Semiannu. Prog. Rep., March 31, 1984,* DOE/ER-0045/12, U.S. DOE, Office of Fusion Energy.

2. A. F. Rowcliffe et al., "The U.S./Japan Collaborative Testing Program in HFIR and ORR: Specimen Matrices for HFIR Irradiation," pp. 61–62 in *ADIP Semiannu. Prog. Rep., Sept. 30, 1984,* DOE/ER-0045/13, U.S. DOE, Office of Fusion Energy.

3. J. L. Scott and M. P. Tanaka, "Preparation for Postirradiation Examination of U.S./Japan HFIR Capsules," pp. 10–11 in *ADIP Semiannu. Prog. Rep., Mar, 31, 1985,* DOE/ER-0045/14, U.S. DOE, Office of Fusion Energy.

4. J. L. Scott, M. L. Grossbeck, and M. Tanaka, "Phase I HFIR Capsules - Irradiation and Postirradation Examination," pp. 18–21 in *ADIP Semiannu. Prog. Rep., Sspt. 30, 1985,* DOE/ER-0045/15, U.S. DOE, Office of Fusion Energy.

2.4 NEUTRONICS ANALYSIS IN SUPPORT OF THE U.S.-JAPAN SPECTRAL TAILORING CAPSULES – R. A. Lillie (Oak Ridge National Laboratory)

2.4.1 ADIP Task

ADIP Task 1.A.2, Define Test Matrices and Test Procedures.

2.4.2 Objective

The objective of this work is to provide the neutronic design for materials irradiation experiments in both the Oak Ridge Research Reactor (ORR) and High Flux Isotope Reactor (HFIR). Spectral tailoring to control the fast and thermal fluxes is required to provide the desired displacement and helium production rates in alloys containing nickel.

2.4.3 Summary

Scale factors obtained previously' are being used to scale the neutron fluences obtained from three-dimensional neutronics calculations. As of March 31, 1986, this procedure yields 17.81 at. ppm He (not including 2.0 at. ppm He from E-10) and 3.57 dpa for type 316 stainless steel in ORR-MFE-6J and 31.23 at. ppm He and 3.71 dpa in ORR-MFE-7J. The calculated and measured' fluxes in the HFIR RB MFE Hafnium Dosimetry Experiment have been compared. This comparison allowed the calculation of Hf and Cd shield thicknesses required for spectral tailoring when the MFE-6J and -7J experiments are moved to HFIR RB positions.

2.4.4 Progress and Status

The operating and current calculated data based on the fluence scaling factors obtained previously are summarized in Table 2.4.1 for the ORR-MFE-6J and -7J experiments. Both experimental capsules went into the ORR on June 28, 1985, and both capsules have been exposed to 143,793 MWhs as of March 31, 1986. At the present time, the dpa rate based on the scaled total fluences is 6.53 and 6.79 dpa per full power year for the ORR-MFE-6J and -7J experiments, respectively. Because the ORR-MFE-7J experiment is similar to the ORR-MFE-4A and -4B experiments, i.e., it contains more water in its aluminum corepiece, the thermal fluence in the ORR-MFE-7J experiment is approximately 15% greater than the thermal fluence in the ORR-JFE-6J experiment.

The real-time projections of the helium-to-displacement ratios based on current calculated data as of March 31, 1986 are presented in Figs. 2.4.1 and 2.4.2 for the ORR-MFE-6J and -7J experiments, respectively. As with the ORR-MFE-4A and -48 experiments, the projected dates were obtained assuming an ORR duty factor of 0.86. Because of the increased thermal fluence in the ORR-MFE-7J experiment, the solid aluminum core-piece should be inserted on or before Auqust 31, 1986.

Table 2.4.1. Operating and calculated data for the ORR-MFE-6J and -7J experimental capsules as of March 31, 1986

	ORR-MFE-6J	ORR-MFE-7J
Insertion date	6-28-85	6-28-85
Exposure (MWh)	143,793.4	143,793.4
Equivalent full power days[a]	199.7	199.7
Thermal fluence (n/m^2)	3.63 + 25[b]	5.10 + 25
Total fluence (n/m^2)	1.24 + 26	1.42 + 26
He (at. ppm)[c]	17.81	31.23
dpa[c]	**3.57**	**3.71**

[a]Full power for ORR is 30 MW.

[b]3.63 + 25 is read as 3.63×10^{25}.

[c]Helium and dpa values are for type 316 stainless steel.

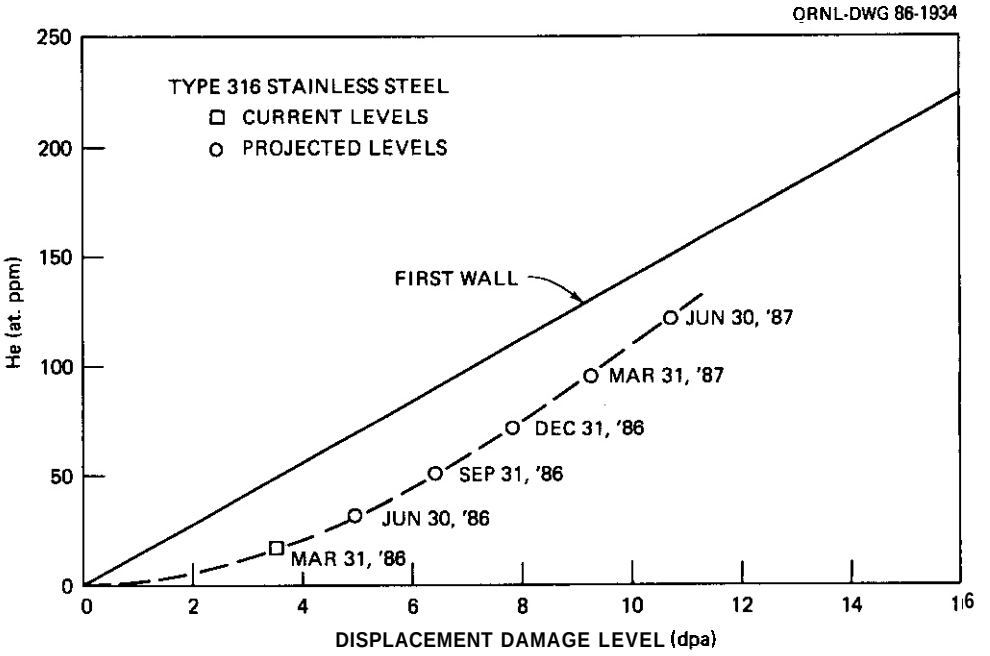

Fig. 2.4.1. Current and projected helium and displacement damage levels in the ORR-MFE-6J experiment.

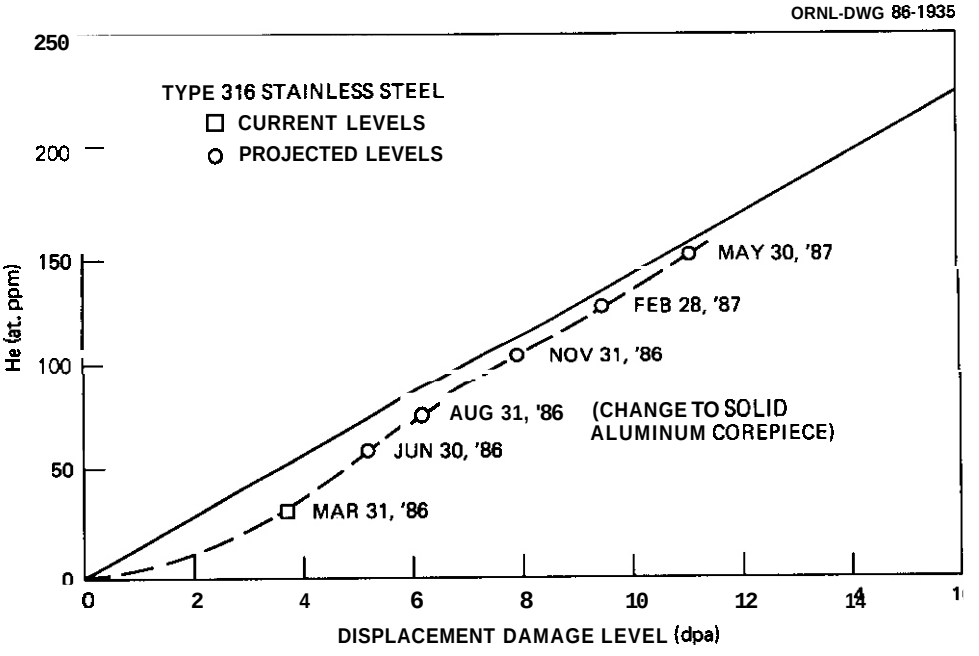

Fig. 2.4.2. Current and projected helium and displacement damage levels in the ORR-MFE-7J experiment.

The ORR-MFE-6J and -7J experiments will be moved from the ORR to the HFIR. Moving these experiments will require the use of substantial thermal neutron shielding to obtain the same He to dpa ratio in type 316 stainless steels as that expected in a fusion device first wall because of the increased thermal flux in the HFIR. Calculations to determine the thickness of hafnium and cadmium which will yield the desired thermal flux reduction have been completed. These calculations were performed assuming that both the ORR-MFE-6J and -7J capsules are removed from the ORR at the 5 dpa level. However, small deviations from this level, e.g., less than 1 dpa, should not appreciably alter the results from these calculations.

The calculations to determine the required shielding thicknesses in the HFIR were carried out using the discrete ordinates radiation transport code ANISN[3] employing a one-dimensional geometric model. However, before performing these calculations, the fluxes in the HFIR RB MFE Hafnium Dosimetry Experiment were calculated and compared with the measured fluxes in this experiment. This comparison was needed to obtain a credible estimate of the neutron source distribution for the one-dimensional calculations. The results of this comparison are presented in Table 2.4.2. In the table, bare represents the dosimetry capsule without Hf, (i.e., with aluminum replacing the Hf). To perform the calculation for this case, a neutron source spectrum at the horizontal midplane of a typical HFIR RB position obtained from the HFIR CASDAR data base' was modified to provide agreement between the calculated and measured fluxes. This modified spectrum was then used as a boundary condition in all succeeding calculations. When the Al was replaced with Hf, the calculation underestimates the amount of flux reduction over the entire energy range. Above 0.1 MeV, the underestimate in flux reduction, i.e., the calculation predicts almost no reduction, is most likely to do inadequate transport cross sections for Hf. Below 0.1 MeV, the underestimates are probably due to the use of a one-dimensional model coupled with the inadequate cross sections above 0.1 MeV.

The calculated relative thermal and total flux reductions obtained as a function of Hf and Cd shield thicknesses when either the ORR-MFE-6J or -7J capsules are placed in a HFIR RB position are given in figs. 2.4.3 and 2.4.4. The underestimates obtained in the above comparison were used to scale the calculated reductions obtained for the three energy ranges listed in Table 2.4.2 in all of the shielding calculations. In Figs. 2.4.3 and 2.4.4, both the flux reductions obtained with no burnup and the flux reductions with burnup averaged over 150 d of full power operation are presented. The time of full power operation, i.e., 150 d, represents approximately seven cycles of HFIR operation. With Hf the difference in relative flux with and without burnup is not very large, whereas with Cd the difference is significant because of the large Cd thermal absorption cross section.

In Table 2.4.3, the Hf and Cd thicknesses required in a HFIR RB position to maintain a He-to-dpa ratio equal to 0.9 of the expected fusion device first ratio are presented. Between 5 and 10 dpa a reduction of 73% in thermal flux is needed resulting in required shielding thicknesses of 3.0 and 1.0 mm for Hf and Cd, respectively. Above 10 dpa, Hf and Cd shielding thicknesses of 4.2 and 1.25 mm are required to obtain the needed thermal flux reduction of 86%. Of the two shielding materials, Cd appears to be the better choice because it only lowers the dpa rate 3% whereas Hf lowers it 12%. A different approach to shielding the experiments would be to use a Cd shield which remains black, i.e., one which yields a thermal flux reduction of greater than 99.9% over 150 d of full power operation. A Cd thickness of 1.5 mm, which is only 0.25 mm larger than the thickness required above 10 dpa, would satisfy this requirement. With this type of shield, the necessary thermal flux reductions could be obtained by drilling holes through the Cd shield. Between 5 and 10 dpa, the holes would need to represent 27% of the shield area. Above 10 dpa the holes would need to represent 14% of the shield area. This type of shield would also have the advantage of maintaining a constant flux reduction over the life of the shield.

Table 2.4.2. Comparison of calculated and measured data for the MFE Hafnium Dosimetry Experiment in a HFIR RB Position

	Bare		With 3.9 mm Hf	
	Calculated	Measured	Calculated	Measured
Flux ($n/m^2/s$)				
<0.5 eV	11.07 + 18[a]	11.07 + 18	1.28 + 18	1.14 + 18
0.5 eV – 0.1 MeV	8.54 + 18	8.53 + 18	5.34 + 18	3.78 + 18
> 0.1 MeV	5.17 + 18	5.17 + 18	5.14 + 18	4.75 + 18
Total	24.78 + 18	24.77 + 18	11.77 + 18	9.67 + 14
dpa/y	12.5	11.3	10.6	8.9
He/y (at. ppm)	854.0	854.0	27.2	26.5

[a] 11.07 + 18 read as 11.07×10^{18}

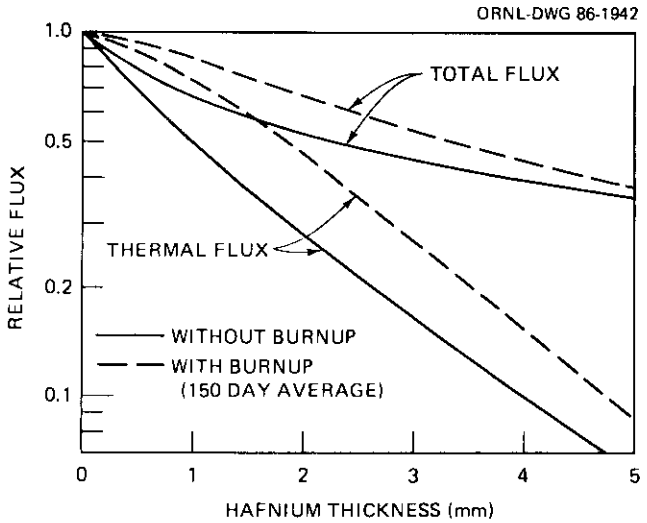

Fig. 2.4.3. Relative flux levels vs hafnium shield thickness for MFE radiation damage capsules in HFIR RB positions.

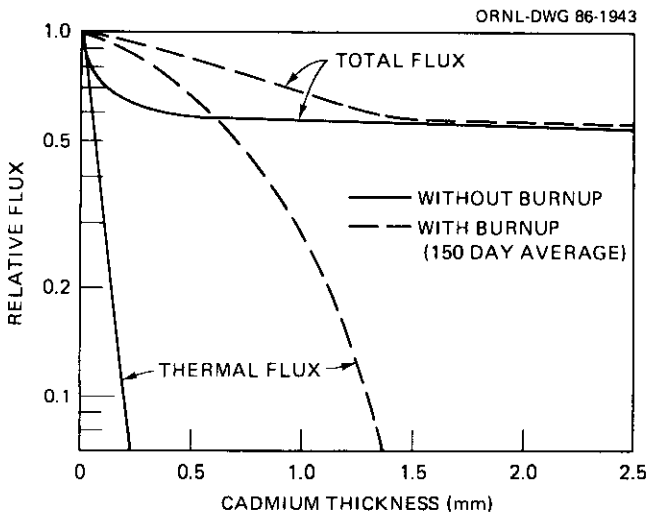

Fig. 2.4.4. Relative flux levels vs cadmium shield thickness for MFE radiation damage capsules in HFIR RB positions.

Table 2.4.3. Hafnium and cadmium shield thicknesses required when the ORR-MFE-6J and -7J capsules are irradiated in HFIR RB positions

dpa Level	5.0–10.0	10.0–30.0
Required thermal flux reduction (%)	73	86
Hafnium thickness (mm)	3.0	4.2
dpa Reduction with hafnium (%)	7	12
Cadmium thickness (mm)	1.0	1.25
dpa Reduction with cadmium (%)	2	3

As a final note, the large discrepancy reported in the last progress report[1] between the He production predicted by the calculated and measured thermal fluxes in the ORR-MFE-6J dosimetry capsule was found to be due to two causes. First, the experimenter used a Ni atom percent of 13% whereas the actual Ni atom percent is 11.35% in the stainless steel specimens. Second, the experimenter calculated a new set of He production cross sections for the equations describing the thermal neutron two-step He production in Ni using the measured neutron spectrum. Using these new cross sections and accounting for the different Ni atom percents reduces the discrepancy in the two-step He production to less than 5%.

2.4.5 Future Work

The three-dimensional neutronics calculations that monitor the radiation environment of the ORR-MFE-6J and -7J experiments will continue with each ORR cycle. The scale factors used to scale the calculated fluences will be updated as new experimental data become available.

2.4.6 References

1. R. A. Lillie, "Neutronics Analysis in Support of the U.S. Japan Spectral Tailoring Capsules," in *ADIP Semiannu. Prog. Rep. Period Ending Sept. 30, 1985,* DOE/ER-0045/15 (February 1986).

2. L. R. Greenwood, "Neutron Dosimetry and Damage Calculations for ORR-6J-Tes, HFIR-RB-Hafnium Test, and the HFIR-RB1 and RB2 Experiments," in *ADIP Semiannu. Prog. Rep. Period Ending Sept. 30, 1985,* DOE/ER-0045/15 (February 1986).

3. W. W. Engle, Jr., "A User's Manual for ANISN, A One-Dimensional Discrete Ordinates Code with Anisotropic Scattering," K-1693 (1967).

4. G. W. Cunningham, private communication, Oak Ridge National Laboratory, (1981).

Table 2.4.3. Hafnium and cadmium shield thicknesses required when the ORR-MFE-6J and -7J capsules are irradiated in HFIR RB positions

dpa Level	5.0–10.0	10.0–30.0
Required thermal flux reduction (%)	73	86
Hafnium thickness (mm)	3.0	4.2
dpa Reduction with hafnium (%)	7	12
Cadmium thickness (mm)	1.0	1.25
dpa Reduction with cadmium (%)	2	3

As a final note, the large discrepancy reported in the last progress report' between the He production predicted by the calculated and measured thermal fluxes in the ORR-MFE-6J dosimetry capsule was found to be due to two causes. First, the experimenter used a Ni atom percent of 13% whereas the actual Ni atom percent is 11.35% in the stainless steel specimens. Second, the experimenter calculated a new set of He production cross sections for the equations describing the thermal neutron two-step He production in Ni using the measured neutron spectrum. Using these new cross sections and accounting for the different Ni atom percents reduces the discrepancy in the two-step He production to less than 5%.

2.4.5 Future Work

The three-dimensional neutronics calculations that monitor the radiation environment of the ORR-MFE-6J and -7J experiments will continue with each ORR cycle. The scale factors used to scale the calculated fluences will be updated as new experimental data become available.

2.4.6 References

1. R. A. Lillie, "Neutronics Analysis in Support of the U.S. Japan Spectral Tailoring Capsules," in *ADIP Semiannu. Prog. Rep. Period Ending Sspt. 30, 1985,* DOE/ER-0045/15 (February 1986).

2. L. R. Greenwood, "Neutron Dosimetry and Damage Calculations for ORR-6J-Tes, HFIR-RE-Hafnium Test, and the HFIR-RB1 and RB2 Experiments," in *ADIP Semiannu. Prog. Rep. Period Ending Sept. 30, 1985,* DOE/ER-0045/15 (February 1986).

3. W. W. Engle, Jr., "A User's Manual for AHISN, A One-Dimensional Discrete Ordinates Code with Anisotropic Scattering," K-1693 (1967).

4. G. W. Cunningham, private communication, Oak Ridge National Laboratory, (1981).

2.5 Neutron Dosimetry and Damage Calculations

L. R. Greenwood (Argonne National Laboratory)

2.5.1 ADIP/DAFS Tasks

ADIP Task I.A.2 - Define test Matrices and Procedures.
DAFS Task II.A.2 - Fission Reactor Dosimetry.

2.5.2 Objective

To characterize neutron irradiation experiments in terms of neutron fluence. spectra, and damage parameters (dpa, gas production).

2.5.3 Summary

A one-cycle (22 day) test of the Hf liner was conducted in the RB position of HFIR at 100 MW. The Hf reduces the thermal flux about an order of magnitude. Estimated yearly damage and gas production rates are included.

Results are reported for the JP1, JP3 U.S./Japanese experiments in HFIR. Both experiments had an identical exposure history with a fast fluence (>0.1 MeV) of about 3.9×10^{21} n/cm^2 producing about 32 dpa and 2147 appm helium in 316 stainless steel.

Results are reported for several short experiments in the Omega West Reactor (LANL) designed for comparison with similar 14 MeV irradiations at RTNS II (LLNL). The measured fluences ranged from $5\text{-}54 \times 10^{18}$ n/cm^2.

A new computer code, SPECOMP, has been developed to calculate displacement damage for alloys, insulators, and breeder materials. Examples are given for $LiAlO_2$ where we find 20-40% more damage in the compound than would be expected from a linear combination of the elemental calculations in SPECTER. Other canpounds are now being studied.

The status of all dosimetry experiments is summarized in Table 2.5.1.

2.5.4.1 Full-Power Hafnium Tests in HFIR-RB Position

Results were reported previously[1] for tests of a hafnium shield to reduce the thermal neutron flux in the RB position of HFIR. These low-power (~11 MW) experiments for one hour allowed us to make spectral measurements employing our full range of dosimetry materials including short-lived products. fissile materials. and thermal shields. The present measurements were performed at Full power (100 MW) for one reactor cycle (22 days) for 2083 MWD from August 10 to September 3, 1985 in order to validate our previous results in the normal range of HFIR operations.

Two dosimetry tubes were irradiated, one in the hafnium sleeve in the RB-1 position and one in aluminum in the RB-3 position. Each tube measured 3.2 mm O.D. X 55.6 cm in length and each was located in the center of the RB assemblies. Smaller dosimetry tubes were also located on the outside of the assemblies in order to measure the radial flux gradients in the RB positions. The main dosimetry tubes contained Fe, Ni. Ti, Cu, Nb, Al, Co, Mn, Zn, Cr, Mo, and V dosimeters and helium gas monitors (Rockwell International). After irradiation all of the samples were gamma counted at Argonne and selected samples were Sent to Rockwell for helium analysis.

The measured activation rates are listed in Table 2.5.2. The midplane values were determined by fitting the data at eight different vertical heights to our equation:

$$f(z) = a\,(1 + bz + cz^2)$$

where a = midplane value, $b = 1.80 \times 10^{-3}$, $c = -1.20 \times 10^{-3}$, and z = height in cm. The radial activities show an interesting pattern. The thermal flux is nearly constant while the fast neutron flux is falling rapidly (44%) from the inner to the outer surface, a distance of about 3 cm. This radial gradient will clearly produce a significant gradient in the damage production radially across material samples.

The midplane activities were used to adjust the neutron flux spectrum determined previously[1] in our spectral measurements. The results of this STAY'SL analysis are listed in Table 2.5.3. Canparison to our previous low-power runs indicates a small spectral shift. The full-power fast flux is about 6% lower than at low power; however, the thermal flux is about 11% higher in the bare case and only 4% higher in the hafnium case. On balance, the total flux is about the same in the 11 MW and 100 MW irradiations and the small spectral differences may be due to the presence of the hafnium.

Table 2.5.1. Status of Dosimetry Experiments

Facility/Experiment		Status/Comments
ORR	- MFE 1	Completed 12/79
	- MFE 2	Completed 06/81
	- MFE 4A1	Completed 12/81
	- MFE 4A2	Completed 11/82
	- MFE 4B	Completed 04/84
	- MFE 4A3, 4B2	Samples received 11/85
	- TBC 07	Completed 07/80
	- TRIO-Test	Completed 07/82
	- TRIO-1	Completed 12/83
	- HF Test	Completed 03/84
	- 56 Test	Completed 07/85
	- J6, 57	Irradiations in Progress
HFIR	- CTR 32	Completed 04/82
	- CTR 31, 34, 35	Completed 04/83
	- T2, RB1	Completed 09/83
	- T1, CTR 39	Completed 01/84
	- CTR 40-45	Completed 09/84
	- CTR 30, 36. 46	Completed 03/85
	- RB2	Completed 06/85
	- CTR 47-56	Irradiations in Progress
	- JP1, JP3	Completed 12/85
	- JP 2-8	Irradiations in Progress
	- Hf Spectral Analysis	Completed 09/85
	- Hf Test	Completed 12/85
Omega West	- Spectral Analysis	Completed 10/80
	- HEDL1	Completed 05/81
	- HEDL2	Completed 01/86
	- HEDL3	Completed 04/86
	- LANL 1	Completed 08/84
BSR	- Spectral Analysis	Planned far 05/86
EBR II	- X287	Completed 09/81
IPNS	- Spectral Analysis	Completed 01/82
	- LANL 1 (Hurley)	Completed 06/82
	- Hurley	Completed 02/83
	- Coltman	Completed 08/83

Table 2.5.2. Activation Rates for Hf Test in HFIR-RB

Midplane values at full power (100 MW)

Reaction	Activation Rate, at/at-s Hf	Bare
$^{58}Fe(n,\gamma)\ ^{59}Fe(x\ 10^{-10}$	1.14	10.71
$^{59}Co(n,\gamma)\ ^{60}Co(x\ 10^{-8})$	0.452	3.25
$^{54}Fe(n,p)\ ^{54}Mn(x\ 10^{-11})$	1.34	1.51
$^{46}Ti(n,p)\ ^{46}Sc(x\ 10^{-12})$	1.88	2.09
$^{63}Cu(n,\gamma)\ ^{60}Co(x\ 10^{-14})$	9.19	10.00
$^{55}Mn(n,2n)\ ^{54}Mn(x\ 10^{-14})$	4.28	4.61

Radial Activity Gradients

Values are listed at three vertical heights on the outer surfaces of the hafnium tube.

Reaction	-15.0 cm		0.2 cm		+15.5 cm	
	Inner	Outer	Inner	Outer	Inner	Outer
$^{58}Fe(n,\gamma)\ ^{59}Fe(x\ 10^{-10})$	6.77	7.16	11.32	10.58	6.28	6.63
$^{59}Co(n,\gamma)\ ^{60}Co(x\ 10^{-8})$	2.32	2.35	3.73	3.56	2.49	2.56
$^{54}Fe(n,p)\ ^{54}Mn(x\ 10^{-11})$	1.23	0.714	1.92	1.02	1.20	0.671
$^{46}Ti(n,p)\ ^{46}Sc(x\ 10^{-12})$	1.84	1.04	2.73	1.53	-	1.10

Table 2.5.3. Neutron Fluxes for HFIR-RB-Hf Test
Midplane values at full power (100 MW)

Energy, MeV	Neutron Flux, x 10^{14} n/cm^2-s Hf	Bare
Total	9.67	24.77
Thermal (<0.5 eV)	1.14	11.07
0.5 eV - 0.1 MeV	3.78	8.53
>0.1 MeV	4.75	5.17

In any case, these adjusted spectra produce a small shift in the damage parameters calculated with SPECTER, as listed in Table 2.5.4. For a 1-year irradiation (365 FPD), we estimate damage rates of 11.3 (bare) to 8.9 (Hf) dpa in 316 SS with a helium production of 854 (bare) to 26.5 (Hf) appm. In other words, the hafnium reduces the yearly helium production by a factor of 32 while the damage rate only falls by 20%. Whether or not this reduction is sufficient for planned materials experiments is now being evaluated at Oak Ridge National Laboratory.

2.5.4.2 Results of the JP1 and JP3 Experiments in HFIR

The JP1 and JP3 experiments are part of a U.S./Japanese collaboration described in previous reports.' Both experiments were irradiated for very nearly the same exposure in the target position of HFIR. JP1 was irradiated for 33.634 MWd between January 4, 1984 and February 1, 1984. while JP3 was irradiated for 34,009 MWd between May 1. 1984 and May 28, 1985.

Dosimetry capsules were placed at six different vertical heights in each experiment. Each capsule measured about 0.05-in. O.D. x 0.25-in. length and contained Fe, Co. Mn, and Ti wires. The uppermost dosimeters could not be retrieved and the Ti wires were not usable due to severe oxidation. The remaining samples were gamma counted and the resultant activation rates are listed in Table 2.5.5. As can be seen, there is virtually no difference between the two experiments. Consequently, the results were averaged for subsequent flux adjustments and damage calculations.

The vertical activity gradients are well-described by our equation determined in the nearby PTP position. as follows:

$$f(z) = a\,(1 + bz + cz^2) \qquad (1)$$

where a = midplane value, b = 5.02 X 10^{-4}, c = -1.00 x 10^{-3}, and z = vertical height (cm). Comparison of these results to those reported previously[3] in the nearby PTP position indicates a slight spectral shift. In the present case, the thermal flux is about 9% higher while the fast flux is about 5% lower than in the PTP positions. This shift is expected since we are about 1-2 cm further into the central target region; however, differences in the capsule designs may also have an influence.

Neutron flux. fluence. and damage rates were calculated using the STAY'SL and SPECTER computer codes and the results are listed in Tables 2.5.6 and 2.5.7. These values represent the conditions at midplane and values at other vertical heights can be determined using Eq. 1 above. Helium production and displacement damage in nickel and stainless steel is listed separately in Table 2.5.8. Thermal damage effects are also listed for copper in Table 2.5.6. In the copper case the helium production is increased by a factor of 7.5 due to the three-stage reaction through ^{65}Zn.

2.5.4.3 Fusion-Fission Correlations in the Omega West Reactor

Dosimetry measurements have been completed for an ongoing series of experiments by Howard Heinisch/ HEDL in the Omega West Reactor at Los Alamos National Laboratory.[4,5] The purpose of these elevated temperature experiments is to compare materials damage in the OWR with that in the 14-MeV flux at the Rotating Target Neutron Source II at Lawrence Livermore National Laboratory. These fission-fusion correlations can then be used to relate damage measured in fission reactors to future fusion reactors.

The three present experiments were conducted from August 16-September 12, 1985 for 671.2 MWH; October 15-18, 1985 for 173.6 MWH; and on October 21-22, 1985 for 64.0 MWH. All three experiments were operated at the full reactor power of 8 MW at an average temperature of 90°C.

Dosimetry packages containing Fe, Ni, Ti, and 0.1%Co-Al wires were inserted in each irradiation capsule. Following the irradiation. these wires were analyzed at ANL by gamma spectroscopy and the measured activation rates are listed in Table 2.5.9.

Table 2.5.4. Estimated Yearly Fluence and Damage Parameters for HFIR-RB Position
Midplane values for 365 FPD at 100 MW

		Hf		Bare	
Fluence >0.1 MeV		1.50×10^{22}		1.63×10^{22} n/cm^2	
Element		DPA	He, appm	DPA	He, appm
Al		17.2	4.21	19.1	4.52
Ti		9.6	3.68	11.2	4.07
V		11.3	0.14	13.0	0.15
Cr		9.6	1.03	10.9	1.13
Mn[a]		10.4	0.87	12.8	0.94
Fe		8.5	1.84	9.6	1.99
Co[a]		9.6	0.57	13.7	0.94
	Fast	9.5	26.5	10.9	29.0
Ni	^{59}Ni	0.3	166.7	11.5	6528.0
	Total	9.8	193.2	22.4	6557.0
	Fast	8.5	1.26	9.7	1.36
cu	^{65}Zn	–	0.02	0.01	7.21
	Total	8.5	1.28	9.71	8.57
Nb		8.8	0.34	9.6	0.38
Mo		6.8	–	7.5	–
316 SS[b]		8.9	26.5	11.3	854.0

[a] Thermal neutron self-shielding **may** reduce damage in Mn, Co.

[b] 316 SS: Fe(0.645), Ni(0.13), Cr(0.18), Mn(0.019), Mo(0.026).

Table 2.5.5. Activation Rates for HFIR-JP1, JP3
Values nromalized *to* 100 MW

	Activation Rate, at/at-s							
	^{58}Fe(n,p) ^{59}Fe ($\times 10^{-9}$)		^{59}Co(n,p) ^{60}Co ($\times 10^{-8}$)		^{54}Fe(n,γ) ^{54}Mn ($\times 10^{-11}$)		^{55}Mn(n,2n) ^{54}Mn ($\times 10^{-12}$)	
Height, cm	JP1	JP3	JP1	JP3	JP1	JP3	JP1	JP3
16.5	1.73	1.72	5.47	5.60	4.97	5.02	1.47	1.51
7.1	2.14	2.15	6.27	7.02	6.52	6.57	1.96	2.00
2.1	2.29	2.28	6.49	7.36	6.44	6.85	2.07	2.01
–12.1	1.96	1.96	5.70	6.36	5.61	5.68	1.70	1.66
–21.0	1.41	1.37	4.57	4.60	3.79	3.74	1.13	1.15

Table 2.5.6. Neutron Flux and Fluences for HFIR-JP1, JP3
Exposure about *340* FPD **at** 100 MW

Energy, MeV	Flux ($\times 10^{15}$ n/cm^2-s)	Fluence ($\times 10^{22}$ n/cm^2)
Total	5.18	15.2
Thermal (<0.5 eV)	2.24	6.57
0.5 eV - 0.1 MeV	1.62	4.76
Fast (>0.1 MeV)	1.32	3.88

Table 2.5.7. Damage Parameters for HFIR-JP1, JP3
Midplane values at 340 FPD (100 MW)

Element		DPA	He, appm
Al		49.6	24.0
Ti		31.6	15.9
V		35.4	0.81
Cr		31.1	5.50
Mn[a]		34.5	4.86
Fe		27.5	9.76
Co[a]		35.4	4.81
	Fast	29.7	128.0
Ni	^{59}Ni	28.8	16331.0
	Total	58.5	16459.0
	Fast	26.9	7.1
cu	^{65}Zn	0.1	45.8
	Total	27.0	52.9
Nb		26.6	1.78
Mo		19.8	-
316 SS		32.1	2147.0

[a] Thermal neutron self-shielding may reduce damage in Mn, Co.

[b] 316 SS: Fe(0.645), Ni(0.13), Cr(0.18), Mn(0.019), Mo(0.026).

Table 2.5.8. Helium and DPA for 316 SS in HFIR JP1, JP3

He includes ^{59}Ni and fast reactions
DPA includes extra kick from thermals (He/567)

Height, cm	He, appm	DPA
0	2147.	32.1
3	2125.	31.8
6	2062.	31.0
9	1954.	29.5
12	1802.	27.5
15	1603.	24.8
18	1357.	21.6
21	1063.	17.7
24	727.	13.3

Table 2.5.9. Activation Rates for Omega West Reactor
Values are normalized to 8 MW:
uncertainty ±2%

Reaction	FPH[a] =	activity (atoms/atom-sec) 83.9	21.6	8.0
$^{59}Co(n,\gamma)^{60}Co$ (10^{-9})		2.26	2.30	2.22
$^{58}Fe(n,\gamma)^{59}Fe$ (10^{-11})		6.73	7.31	7.00
$^{54}Fe(n,p)^{54}Mn$ (10^{-12})		2.80	2.86	2.81
$^{58}Ni(n,p)^{58}Co$ (10^{-12})		3.56	3.73	3.67
$^{46}Ti(n,p)^{46}Sc$ (10^{-13})		3.67	3.95	3.82

[a]Full power hours at 8 MW power level.

The activities in Table 2.5.9 were used to adjust the neutron spectrum measured previously in the Omega West Reactor[4,5] using the STAY'SL computer code. The present results are in good agreement with previous measurements. The thermal flux is about 5% higher and the fast flux about 38 lower than in our previous measurement. The adjusted fluences are listed in Table 2.5.10.

Damage rates for this position have been reported previously[4,5] and damage for the current runs can be easily scaled according to the neutron fluences.

Further measurements are in progress in the OWR and we expect to receive dosimeters shortly.

Table 2.5.10 Neutron Fluences for Omega West Reactor
Estimated Uncertainty ±10%

Energy	FPH[a] =	Neutron Fluence, x 10^{18} n/cm^2 83.9	21.6	8.0
Total		54.2	14.41	5.18
Thermal[b]		22.9	6.06	2.16
0.5 eV-0.1 MeV		14.7	3.92	1.41
>0.1 MeV		16.6	4.43	1.60

[a]Full power hours (8 MW).

[b]Thermal flux below 0.5 eV.

2.5.4.4 Development of the SPECOMP Computer Code

A new computer code SPECOMP is being developed to calculate radiation damage for compound materials. Our SPECTER[6] code routinely calculates damage for 38 pure elements: however, it does not handle compounds and there are no other existing codes which fill this need. Consequently, we have developed SPECOMP.

Fortunately, SPECOMP can make use of the recoil atom energy distributions in SPECTER. Hence, it is not necessary to return to the basic neutron cross sections in ENDF/B-V and recalculate these data. This greatly reduces the size and scope of the code as well as the effort needed to develop the code and the cost to run it.

SPECTER already contains recoil atom energy distributions for each element at 100 neutron energies on a 100-point recoil energy grid. SPECOMP only needs to access these distributions, combine them according to the

alloy or compound of interest, and to integrate over the appropriate secondary damage function for each combination of recoil atom and matrix atom. The secondary displacement model uses the same prescription as SPECTER, relying on the Lindhard partition of the stopping energy and the Robinson model.[7] Hence. the SPECOMP code is relatively small consisting of subroutines which access the SPECTER data files, calculate the appropriate secondary displacements, and integrate over the recoil spectra at each neutron energy.

Although the code is still undergoing testing, sample calculations are shown for a fusion breeder material $LiAlO_2$ in Fig. 2.5.1. As can be seen at low energies, damage is due to the $^6Li(n,\alpha)t$ reaction. At higher energies the displacement damage predicted by SPECOMP is 20–408 higher than would be predicted by taking a simple average of the results from SPECTER. Integral dpa Pates for $LiAlO_2$ are 26–28% higher for a fusion first wall or fast reactor spectra and 7% higher in a mixed–spectrum reactor like HFIR due to the dominance of the ^6Li damage.

Although we have not had time to study SPECOMP predictions in detail, it is clear from early runs that the prediction of Parkin and Coulter[8] holds up, namely. that in cases where the mass differences are small SPECOMP will differ only slightly from a linear sum of the elements in SPECTER. On the other hand, when the masses involved are quite different, then the calculated displacements, from SPECOMP may differ substantially from SPECTER. In the present case we find that calculations for SiO_2 and Al_2O_3 agree within 5% of the linear sum from SPECTER whereas Li_2O, $LiAlO_2$, and TaO disagree by 20-40% over the energy range from 0.1 to 20 MeV.

2.5.5 Conclusion

Analysis is in progress for the MFE4A and 4B experiments in ORR. Further experiments are in progress in HFIR and OWR. We are planning to characterize the new low temperature (4°K) facility in the Bulk Shielding Reactor at ORNL. We plant to construct a library of damage cross sections for compounds and add it to our SPECTER computer code package for routine use.

2.5.6 Reference

1. L. R. Greenwood, Alloy Development for Irradiation Performance, Semiannual Progress Report, DOE/ER-0045/15, pp. 4–15, 1985.

2. J. L. Scott and M. P. Tanaka, Alloy Development for Irradiation Performance, Semiannual Progress Report, DOe/ER-0045/14, pp. 10–19, July 1985.

3. L. R. Greenwood, ibid., pp. 22–26, July 1985.

4. L. R. Greenwood. Damage Analysis and Fundamental Studies Quarterly Progress Report, DOE/ER-0046/4, p. 15 (1981).

5. L. R. Greenwood, Damage Analysis and Fundamental Studies Quarterly Progress Report, DOE/ER-0046/6, p. 11 (1981).

6. L. R. Greenwood and R. K. Smither, SPECTER: Neutron Damage Calculations for Materials Irradiations ANL/FPP-TM-197, 1985.

7. G. R. Odette and D. R. Dorian, Nucl. Technol. 29, 346 (1976).

8. D. M. Parkin and C. A. Coulter, J. Nucl. Mater. 103, 1315-1318 (1981)

2.5.1 Publications

The following papers have been submitted to the International Conference on Fusion Reactor Materials (ICFRM-2) in Chicago, April 13–11, 1986:

1. L. R. Greenwood, New Ideas in Dosimetry and Damage Calculations for Fusion Materials Irradiations.

2. D. W. Kneff, L. R. Greenwood, 8. M. Oliver, and R. P. Skouranski, Helium Production in HFIR–Irradiated Pure Elements.

3. W. A. Coghlan, F. W. Clinard, Jr., N. Itah, and L. R. Greenwood, Swelling of Spinel after Low–Dose Neutron Irradiation.

Two papers have also been submitted to the Symposium on the Effects of Radiation on Materials, Seattle, June 23–25. 1986:

4. L. R. Greenwood, Recent Research in Neutron Dosimetry and Damage Analysis for Materials Irradiations.

5. D. R. Davidson, R. C. Reedy, L. R. Greenwood, W. F. Sommer, and M. S. Wechsler, Additional Measurements of the Radiation Environment at the Los Alamos Spallation Radiation Effects Facility at LAMPF.

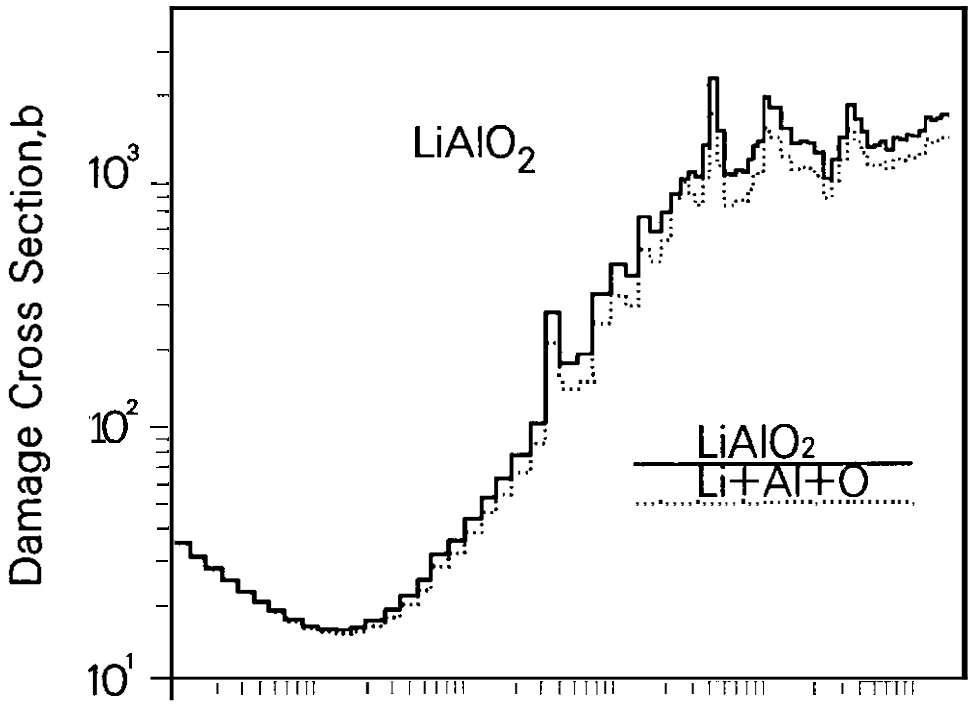

Fig. 2.5.1. Displacement Damage Cross Sections are Compared for $LiAlO_2$ using SPECOMP and a Linear Combination of the SPECTER. Damage is due to the $^6Li(n,\alpha,t)$ Reaction at Low Energies.

3. AUSTENITIC STAINLESS STEELS

3.1 MICROSTRUCUTRAL DEVELOPMENT IN THE PCAs IRRADIATED TO 34 dpa IN HFIR AT 300 and 400°C – M. P. Tanaka and S. Hamada (Japan Atomic Energy Research Institute, assigned to ORNL) and P. J. Maziasz (Oak Ridge National Laboratory)

3.1.1 ADIP Task

ADIP Task I.C.1, Microstructural Stability

3.1.2 Objective

The objective of this work is to determine the microstructural development of JPCA irradiated to 34.0 dpa at 300 and 400°C in the High Flux Isotope Reactor (HFIR), and to compare the results with those obtained on U.S. PCA.

3.1.3 Summary

Microstructural observation on both U.S. and Japan PCAs indicated that all specimens developed a high concentration of fine bubbles and MC precipitates, as well as Frank faulted loops. Mutual stability of the MC particles and associated fine bubbles contributed to the extension of the transient regime of swelling to higher fluence. The irradiation response of JPCA and U.S.-PCA were similar in this HFIR irradiation condition, despite of the minor compositional difference (P,B) between the two materials. These data suggest useful fusion application of solution-annealed (SA)-PCA as well as cold-worked (CW)-PCA in the 300 to 400°C temperature range.

3.1.4 Prowess and Status

This work is a part of the U.S./Japan collaborative program to investigate and compare the irradiation response of structural alloys from both countries in order to evaluate their usefulness for first wall and blanket structural applications in future fusion reactors. This report describes the microstructural development in JPCA and US-PCA during irradiation at 300°C and 400°C to a neutron fluence producing 34.0 dpa and 2501 at. ppm He.

3.1.4.1 Experimental Procedure

The chemical composition of the materials used in this study appears in Table 3.1.1. The major alloying element composition does not vary between the two PCAs. However, there are noticeable differences between the alloys in the content of minor elements like phosphorus and boron. The designation and descriptions of the PCA pretreatments are given in Table 3.1.2. Standard 3-mm-diam disks were punched from the pretreated 0.254-mm-thick sheet materials. The disks were irradiated in target positions of HFIR at 300 and 400°C to produce ~10 and ~34 dpa and helium contents of ~550 and ~2500 at ppm. The disks of QS1, however, were cut from the shoulder of fractured tensile specimens which were irradiated to ~10 dpa at 340 and 400°C in HFIR. Disks for transmission electron microscopy (TEM) were thinned with an automatic dual-jet Tenupol thinning unit in a hot cell and examined via standard methods using JEM 100CX and 2000FX electron microscopes. Microcompositional data were obtained from carbon extraction replicas, using energy dispersive x-ray analysis (EDS) with a TN5500 system attached to the JEM 2000FX electron microscope.

Table 3.1.1. Alloy Compositions (wt %)

Element	Alloys		
	JPCA(1)	JPCA(2)	U.S.-PCA
Fe	Bal	Bal	Bal
Ni	16.22	15.60	16.2
Cr	14.51	14.22	14.0
Ti	0.20	0.24	0.24
C	0.06	0.06	0.05
Mo	2.37	2.28	2.3
Mn	1.79	1.77	1.8
Si	0.53	0.50	0.4
P	0.027	0.027	0.01
S	0.009	0.005	0.003
B	0.0035	0.0031	a
N	0.003	0,0039	0.01

[a]Not analyzed, but assumed to be near 0.001 wt %.

3.1.4.2 Microstructural Development

Quantitative data on dislocation loops, on cavities, and on swelling of the PCAs investigated in this study are listed in Table 3.1.3. All of the specimens contained high concentrations ($>10^{23}$ m^{-3}) of fine cavities (1 to 3 nm in diameter) as well as high concentrations ($>10^{22}$ m^{-3}) of dislocation loops (10 to 15 nm in diameter).

3.1.4.3 Swellina and Cavity Evolution

A prominent feature of these data are the low values of swelling at lower fluences in HFIR for temperatures of 300 and 400°C. Examples of the cavity microstructure in JPCA and U.S.-PCA irradiated in HFIR at 400°C to around 10 dpa are shown in Fig. 3.1.1. The cavities (1.8 nm in diameter) can clearly be observed in both PCAs. The values of helium content show that at 400°C, 60 to 90% of the total transmutation produced helium is contained in those cavities (Table 3.1.3). This suggests that these cavities are most likely helium bubbles.

Although high concentrations of fine cavities are formed at 300 and 400°C for lower fluences of around 10 dpa, they do not appreciably coarsen or convert to voids with increased fluence to 34 dpa in HFIR at either temperature (Table 3.1.3). Figure 3.1.2 shows the cavity microstructures of the JPCA and U.S.-PCA which were irradiated in HFIR to 34 dpa at 400°C. Fine bubbles (~3 nm in diameter) are still observed in high concentrations (~3.2 x 10^{23} m^{-3}) in both SA and CW PCAs. Figure 3.1.3 shows the size distributions of the cavity microstructure.

Table 3.1.2. Thermomechanical Pretreatments

Designation	Alloys	Treatment
QS1	JPCA(1)	SA for 90 min @ 1090°C
PS2	JPCA92)	SA for 60 min @ 1100°C
PS3	JPCA92)	SA + 20% CW
PCA-ED	U.S.-PCA	SA for 15 min @ 1175°C
PCA-ED	U.S.-PCA	SA for 30 min @ 1100°C + 25% CW

Table 3.1.3. Dislocation loop and cavity microstructural data for PCAs irradiated in HFIR

Designation	Alloy	Heat treatment	Irradiation Conditions			Loop Data		Cavity Data				Immersion Density (%)
			temperature (°C)	damage (dpa)	helium Content (at. ppm)	diameter (nm)	concentration (m^{-3})	diameter (nm)	concentration (m^{-3})	Helium Fraction[a]	swelling[b] (%)	
PCA-ED	U.S.-PCA	SA	[illegible]	[illegible]	560	10.5	[illegible]	1.0	[illegible]	[illegible]	0.01	-----
QS1	JPCA(1)	SA	340	10.2	550	10.4	9.0 × 10^{22}	1.2	1.9 × 10^{23}	0.15	0.01	-----
PS2	JPCA(2)	SA	300	33.6	2471	11.5	4.7 × 10^{22}	2.9	1.9 × 10^{23}	0.53	0.23	0.14
PC3	JPCA(2)	20% CW	300	33.6	2471	10.6	9.8 × 10^{22}	2.6	2.3 × 10^{23}	0.48	0.21	0.16
PCA-EC	U.S.-PCA	25% CY	300	33.7	2527	10.8	4.7 × 10^{22}	2.7	2.3 × 10^{23}	0.53	0.24	----
PCA-ED	U.S.-PCA	SA	400	10.5	580	12.0	2.1 × 10^{22}	1.8	2.4 × 10^{23}	0.73	0.07	----
QS1	JPCA(1)	SA	400	10.5	530	12.0	2.0 × 10^{22}	1.8	2.9 × 10^{23}	0.85	0.08	----
PS2	JPCA(2)	SA	400	34.0	2501	12.3	2.4 × 10^{22}	2.6	2.9 × 10^{23}	0.57		
PC3	JPCA(2)	20% CW	400	34.0	2501	14.3	2.6 × 10^{22}	2.9	3.3 × 10^{23}	0.87	0.29	0.29
PCA-EC	U.S.-PCA	25% CW	400	34.1	2558	10.6	3.0 × 10^{23}	2.3	4.5 × 10^{23}	0.66	0.29	0.32

[a]Ratio of helium content contained inside the cavities to that produced in the specimen from transmutation, assuming equilibrium bubbler. which were calculated from a modified Van der Waal's equation.

[b]Swelling calculated from cavity volume fraction.

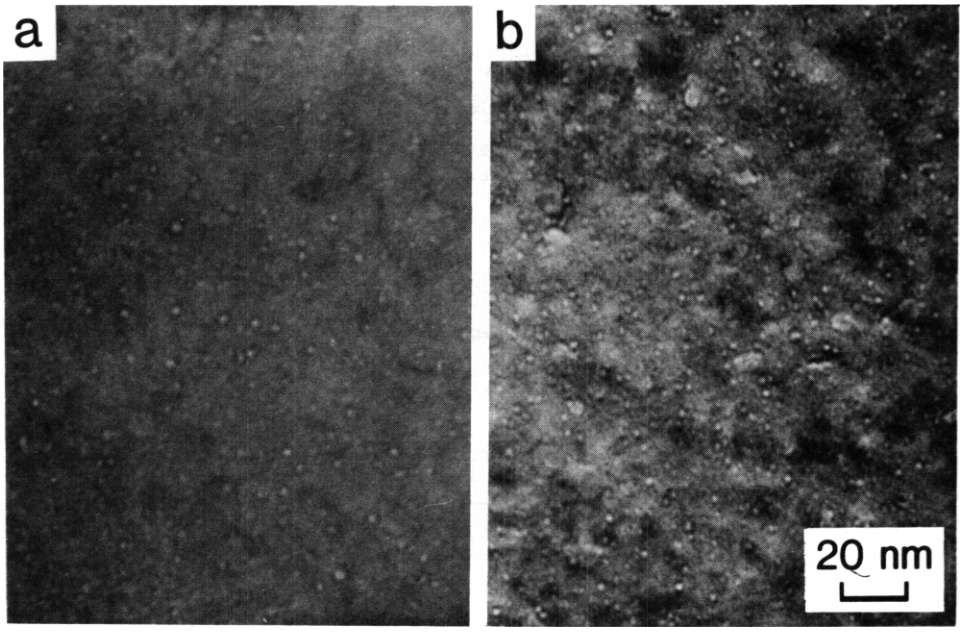

Fig. 3.1.1. Cavity microstructure of Japan and U.S. SA-PCA irradiated in HFIR at 400°C to 10 dpa (*a*) JPCA(1) QS1; (*b*) U.S.-PCA ED.

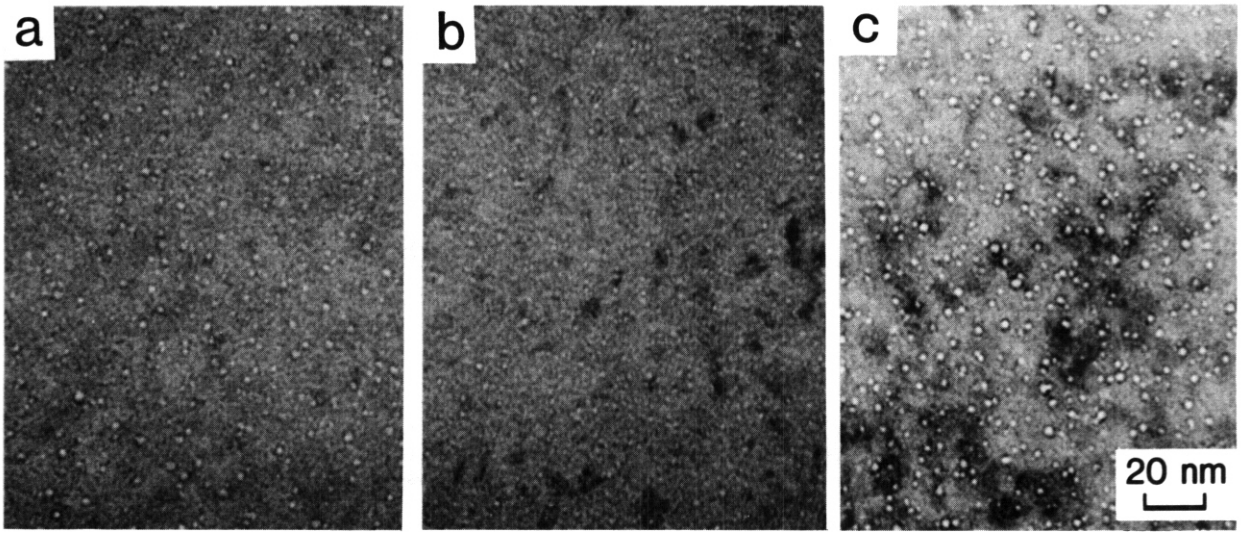

Fig. 3.1.2. Cavity microstructure of Japan and U.S.-PCA irradiated In HFIR at 400°C to 30 dpa (*a*) JPCA(2) SA; (*b*) JPCA(2) 20% CW; (*c*) U.S.-PCA 25% CW.

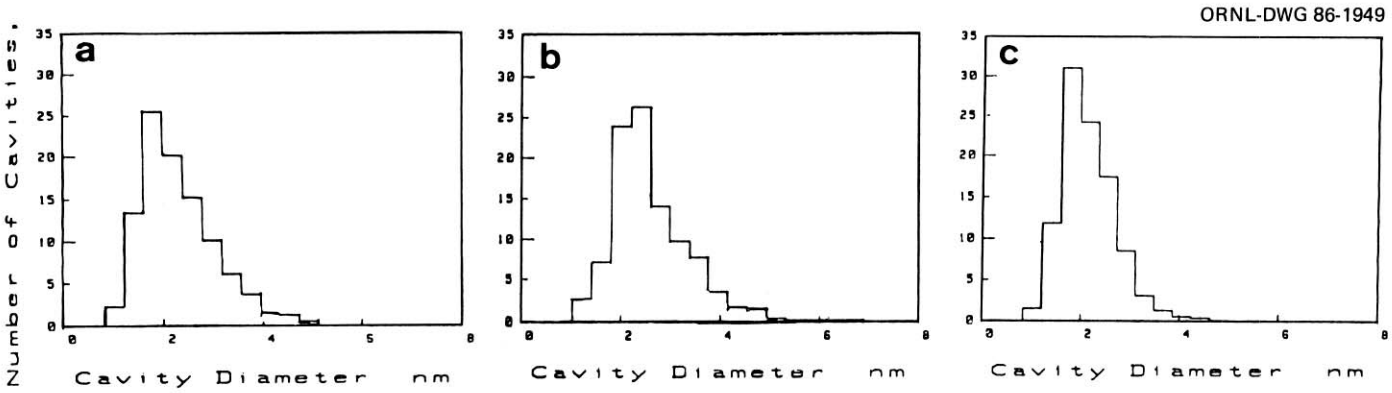

Fig. 3.1.3. Cavity size distribution of Japan and U.S.-PCA irradiated in HFIR at 400°C to 34 dpa. (*a*) JPCA(2) SA; (*b*) JPCA(2) 20% CW; (*c*) U.S.-PCA 25% CW.

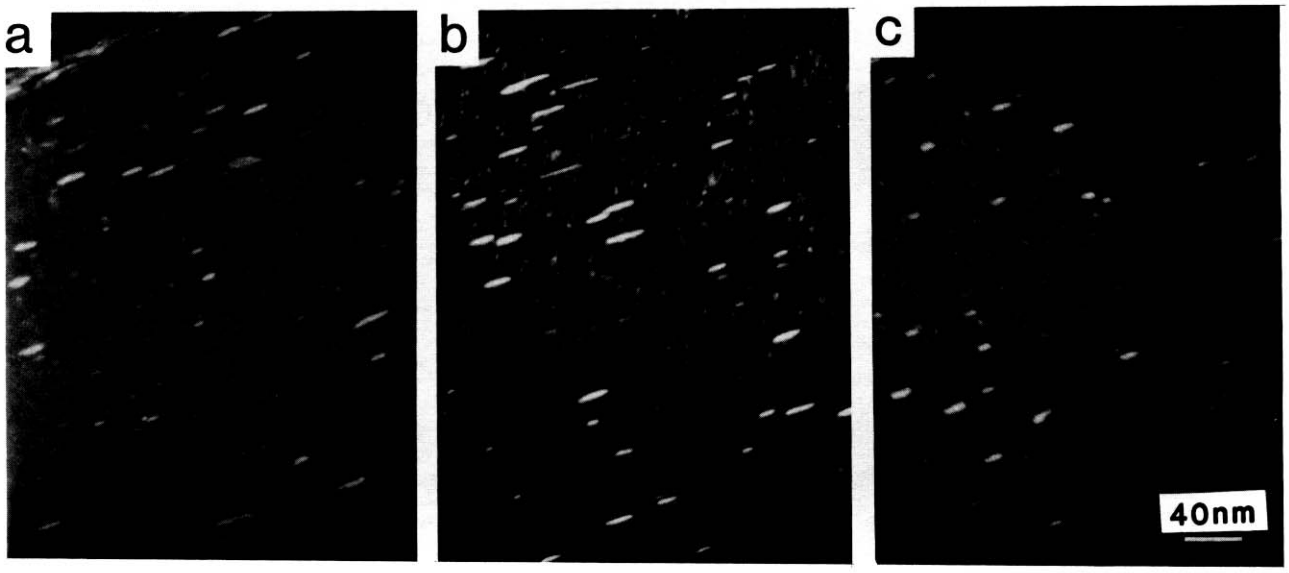

Fig. 3.1.4. Frank loop component of dislocation microstructure of Japan and U.S.-PCA irradiated in HFIR at 400°C to 34 dpa. (*a*) JPCA(2) SA; (*b*) JPCA(2) 20% CW; (*c*) U.S.-PCA 25% CW.

3.1.4.4 Loop Evolution

The dislocation structure of SA and CW PCAs consisted of high concentration of network dislocations and Frank loops. Dislocation parameters are also listed in Table 3.1.3. After 400°C irradiation, Frank loops were slightly larger and their concentrations lower in both SA and CW PCAs compared to irradiation at 300°C. Figure 3.1.4 shows the microstructure of Frank faulted loops, which were imaged separately from the network dislocation using dark field with <111> kinematical satellite streaks around g_{200} type matrix reflections.

3.1.4.5 Precipitation Behavior

The microstructural data for the precipitate observed in both PCAs are summarized in Table 3.1.4. Precipitation was detected by the appearance of Moiré fringes which are measured to be 1.4 nm in both PCAs for the <111> diffracting conditions. The spacing of the Moiré fringe spacing (1.4 nm) is consistent with a precipitate having a lattice parameter of a_0 = 0.43 nm, as generally found for titanium-rich MC phases.

After 10 dpa irradiation at 300°C in HFIR, no radiation-produced precipitates were detected, but after 34 dpa at the same temperature, a high concentration (~2 × 10^{22} m^{-3}) of small precipitates (~3 nm in diameter) were observed. At 400°C irradiation, however, precipitates were observed in all of the specimens at both 10 and 34 dpa. Moiré fringe patterns from precipitates in both JPCA and U.S.-PCA, irradiated in HFIR at 400°C to around 34 dpa, are shown in Figure 3.1.5. Precipitates were slightly larger (~5 nm in diameter) and of lower concentration (~1.4 × 10^{22} m^{-3}) at 400°C compared to 300°C for both PCAs. The inset (2.5 × magnification) of Fig. 3.1.5 shows that several cavities are attached to the fine radiation-produced precipitates.

Table 3.1.4. Precipitate microstructural data for PCAs irradiated in HFIR

Designation	Alloy	Heat treatment	Irradiation Conditions			Precipitation Data	
			Temperature (°C)	damage (dpa)	Helium content (at. ppm)	diameter (nm)	Concentration (m^{-3})
PCA-ED	U.S.-PCA	SA	300	10.5	580		no precipitate
US	JPCA(1)	SA	340	10.2	550		no precipitate
PS2	JPCA(2)	SA	300	33.6	2471	3.1	1.9×10^{22}
PC3	JPCA(2)	20% CW	300	33.6	2471	3.1	2.4×10^{22}
PCA-EC	U.S.-PCA	25% CW	300	33.7	2527	4.9	2.1×10^{22}
PCA-ED	U.S.-PCA	SA	400	10.5	580	3.5	1.9×10^{22}
QS1	JPCA(1)	SA	400	10.0	530	3.5	1.4×10^{22}
PS2	JPCA(2)	SA	400	34.0	2501	4.7	1.4×10^{22}
PC3	JPCA(2)	20% CW	400	34.0	2501	5.6	1.5×10^{22}
PCA-EC	U.S.-PCA	25% CW	400	34.1	2558	6.7	1.7×10^{22}

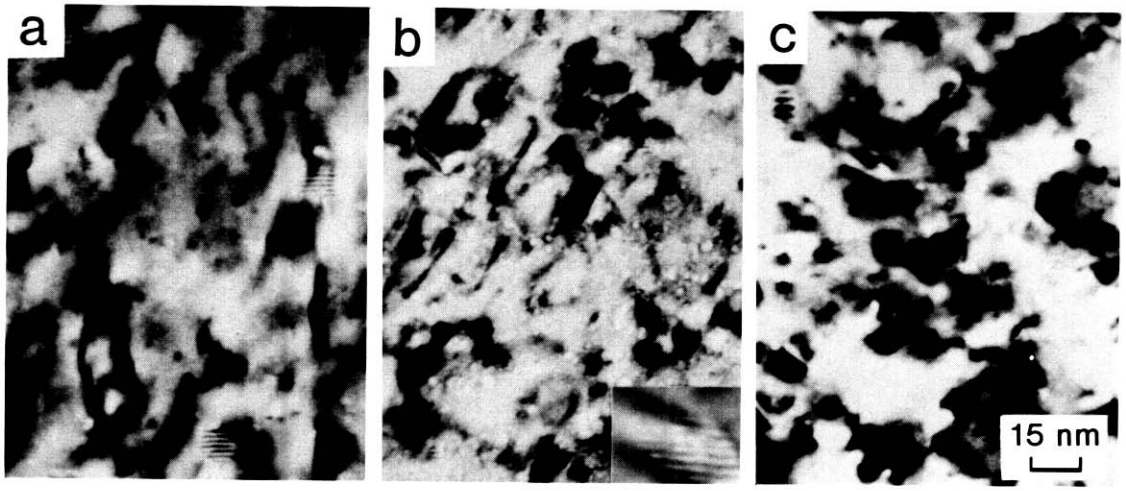

Fig. 3.1.5. Precipitate microstructure of Japan and U.S.-PCA irradiated in HFIR at 400°C to 34 dpa. (*a*) JPCA(2) SA; (*b*) JPCA(2) 20% CW; (*c*) U.S.-PCA 25% CW.

The compositional analysis of the precipitates is still in progress, but preliminary analysis of the precipitates, which were extracted on carbon films, shows the average composition of the precipitate was (in wt %): (40–31)Ti–(16–29)Cr–(23–14)Mo–(6.5–7.9)Fe–(2–9 Ni)–(2.3–1.8 Mn)–(1.0–4.3)Si–(0.5–1.4)P–(0.3–1.3)V–(0.0.02)Al [the first number and the second number in the parantheses correspond to 300 and 400°C irradiation, respectively]. These compositional results indicate a titanium-rich MC phase, but with appreciable enrichment of chromium and molybdenum as well. The contents of Ni, Cr, Mn, Fe, and V are higher and the contents of Ti, P, and Mo are lower than those of thermally produced MC precipitates without irradiation, which was: 50Ti–9.4Cr–34Mo–0.7Fe–0.02Ni–0.3Mn–3.5Si–2.8P–0.09V–0.00Al.

3.1.5 Discussion

The data presented on the microstructural evolution of dislocation structure, cavity, and enhanced thermal precipitation show that the JPCA and U.S.-PCA respond similarly to HFIR irradiation, despite differences in minor element composition (P,B) between the two steels. These data are in good agreement with previous data on U.S.-PCA.[4] The basic difference between this and previous work is the observation of the high concentration of fine helium bubbles (cavities whose growth is gas driven) in both PCAs at damage levels as low as 10 dpa and temperatures of 300 and 400°C. It has now been shown that very fine helium bubbles form even at early stages of HFIR irradiation at both 300 and 400°C. The high concentration of bubbles could become dominant sinks and reduce vacancy supersaturations, because the sink strength of the bubbles in the materials is calculated to be much higher than that of the dislocation structure. Actually,

Table 3.1.4. Precipitate microstructural data for PCAs irradiated in HFIR

Designation	Alloy	Heat treatment	Irradiation Conditions: Temperature (°C)	damage (dpa)	Helium content (at. ppm)	Precioitation Data: diameter (nm)	Concentration (m^{-3})
PCA-ED	U.S.-PCA	SA	300	10.5	580		no precipitate
US	JPCA(1)	SA	340	10.2	550		no precipitate
PS2	JPCA(2)	SA	300	33.6	2471	3.1	1.9×10^{22}
PC3	JPCA(2)	20% CW	300	33.6	2471	3.1	2.4×10^{22}
PCA-EC	U.S.-PCA	25% CW	300	33.7	2527	4.9	2.1×10^{22}
PCA-ED	U.S.-PCA	SA	400	10.5	580	3.5	1.9×10^{22}
QS1	JPCA(1)	SA	400	10.0	530	3.5	1.4×10^{22}
PS2	JPCA(2)	SA	400	34.0	2501	4.7	1.4×10^{22}
PC3	JPCA(2)	20% CW	400	34.0	2501	5.6	1.5×10^{22}
PCA-EC	U.S.-PCA	25% CW	400	34.1	2558	6.7	1.7×10^{22}

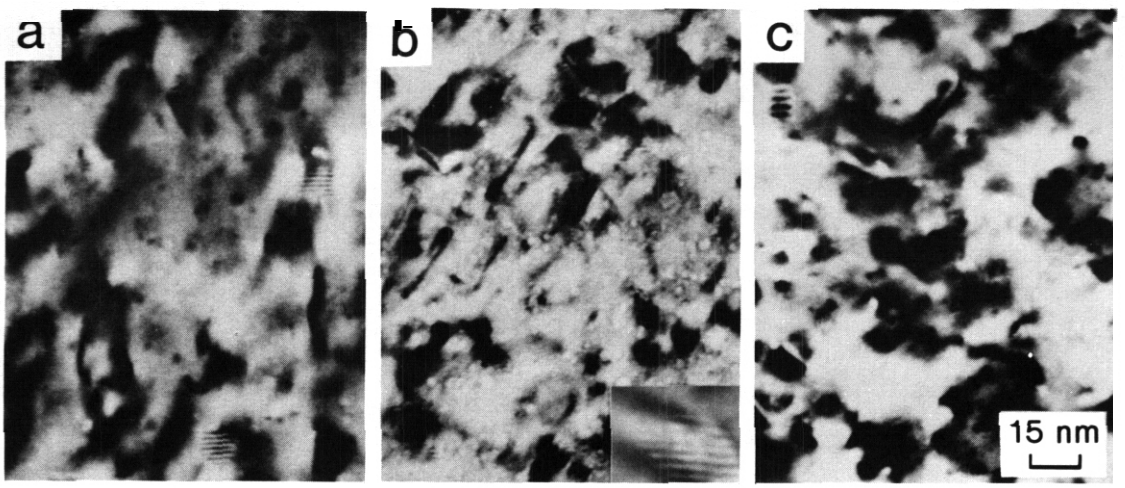

Fig. 3.1.5. Precipitate microstructure of Japan and U.S.-PCA irradiated in HFIR at 400°C to 34 dpa. (a) JPCA(2) SA; (b) JPCA(2) 20% CW; (c) U.S.-PCA 25% CW.

The compositional analysis of the precipitates is still in progress, but preliminary analysis of the precipitates, which were extracted on carbon films, shows the average composition of the precipitate was (in wt X): (40-31)Ti-(16-29)Cr-(23-14)Mo-(6.5-7.9)Fe-(2-9 Ni)-(2.3-1.8 Mn)-(1.0-4.3)Si-(0.5-1.4)P-(0.3-1.3)V-(0.0.02)Al [the first number and the second number in the parantheses correspond to 300 and 400°C irradiation, respectively]. These compositional results indicate a titanium-rich MC phase, but with appreciable enrichment of chromium and molybdenum as well. The contents of Ni, Cr, Mn, Fe, and V are higher and the contents of Ti, P, and Mo are lower than those of thermally produced MC precipitates without irradiation, which was: 50Ti-9.4Cr-34Mo-0.7Fe-0.02Ni-0.3Mn-3.5Si-2.8P-0.09V-0.00Al.

3.1.5 Discussion

The data presented on the microstructural evolution of dislocation structure, cavity, and enhanced thermal precipitation show that the JPCA and U.S.-PCA respond similarly to HFIR irradiation, despite differences in minor element composition (P,B) between the two steels. These data are in good agreement with previous data on U.S.-PCA.[4] The basic difference between this and previous work is the observation of the high concentration of fine helium bubbles (cavities whose growth is gas driven) in both PCAs at damage levels as low as 10 dpa and temperatures of 300 and 400°C. It has now been shown that very fine helium bubbles form even at early stages of HFIR irradiation at both 300 and 400°C. The high concentration of bubbles could become dominant sinks and reduce vacancy supersaturations, because the sink strength of the bubbles in the materials is calculated to be much higher than that of the dislocation structure. Actually,

swelling is low and voids (cavities whose growth is bias driven) did not form, even after 34 dpa HFIR irradiation. These data confirm the theory of Stoller and Odette,[5] which indicates that the increased early bubble nucleatlon, sufficient to make them the dominant sinks in the matrix, would suppress the conversion of bubbles to voids.

The high concentration of helium bubbles also reduces long-range diffusion by partitioning point defects and solute atoms to more sites. This should reduce radiation-induced solute segregation (RISS). The reduction or absence of RISS should then favor the formation of thermal rather than radiation-induced precipitate phases.[6-8] Therefore, the enhanced precipitation of MC is reasonable during the early stages of HFIR irradiation. Thermal diffusion may not be sufficiently enhanced at 300°C to form precipitation at 10 dpa damage levels, but by 34 dpa concentration buildups are sufficient to allow the formation of high concentrations of fine MC. The MC phase particles, which probably nucleated on a fine scale on the dislocation structure (i.e., cold-worked dislocation line and/or dislocation loops) during HFIR irradiation, are also sinks for point defects, in addition to the bubbles. Moreover, the data show that the MC phase remains stable and does not grow or coarsen appreciably for up to 34 dpa irradiation at either 300 or 400°C. As a result, MC particles, and the several fine bubbles associated with each particles, both remain small. The conversion from a subcritical helium bubble to a rapidly growing vold is then also delayed because the precipitate-matrix interface does not exert a strong polnt defect collector effect and because bubbles and precipitates acting together as the domlnant sinks make the critical bubble size very large." These processes extend the transient swelling regime to higher fluence. The lower swelling behavior of HFIR-irradiated SA-PCAs compared to SA 316 could also be explained by similar mechanisms. The enhanced precipitation of thermally stable MC is a key factor for the extension of the transient regime (or time during which bubbles convert to voids). The stability of MC phase at higher fluences at these temperatures, however, remains the subject of future experiments.

Other phases which could contain titanium, such as G-phase or Fe_3P, did not develop at 300 to 400°C. The compositional information on the MC phase produced during HFIR irradiation shows that it contains more chromium as the irradiation temperature and/or damage level becomes higher, relative to the composition of the thermal MC phase. Chromium desegregates via the various RISS processes during irradiation.',' Therefore, this composition evolution of the MC does not appear to be a consequence of RISS. This at least suggests that the MC will be stable or not catastrophically dissolve during irradiation until RISS begins to develop at this temperature.

3.1.6 Summary

Microstructural developments were determined on solution-annealed and cold-worked JPCA and U.S.-PCA irradiated in HFIR at temperatures of aproximately 300, 340, and 400°C. Irradiation produced damage levels of about 10 and 34 dpa and helium concentrations of around 580 and 2500 at. ppm, respectively. The following summarizes the results and conclusions:

(1) The irradiation responses of JPCA and U.S.-PCA were similar in the HFIR, despite minor compositional differences between the two materials.

(2) Both materials showed small amounts of swelling at 300 and 400°C at damage levels of 10 dpa. High concentrations of fine helium bubbles do develop and appear to serve as dominant sinks to reduce vacancy supersaturations during the irradiation. Swelling remained low and voids did not develop at 34 dpa at either irradiation temperature.

(3) High concentration of helium bubbles appear to dilute RISS to allow enhanced formation of the thermal MC phase during HFIR irradiation in both the PCAs.

(4) Mutual stability of the MC particles and associated fine bubbles during HFIR irradiation contributes to the delayed conversion of helium bubbles to voids. This extends the transient regime of swelling to higher fluence.

(5) The stability of the MC phase Is consistent with compositional changes that show no influence of RISS, and is expected to persist with fluence as long as RISS does not develop.

These data suggest useful fusion application of solution-annealed PCA as well as cold-worked PCA at 300 to 400°C. No catastrophic change in the fine MC and bubble microstructures is anticipated at somewhat higher levels of irradiation damage for fusion application. However, further results on bubble suppression of vold formation and dilution of RISS in both PCAs at lower He:dpa ratios are still necessary to prove the long lifetime application of these PCAs in this temperature range. This information will be provided by the ORR spectrally tailored experiments now in progress.

3.1.7 References

1. C. C. Baker et al., ANL/FPP-80-1, Argonnne National Laboratory (September 1980).

2. T. Tone, N. Fujlsawa, and M. Sagihara, *Fusion Technol.* 8(1) part 2A (1985) 214-23.

3. J. L. Soctt and T. Kondo, pp. 99-103 in *ADIP Semiannu. Prog. Rep. Mar. 1984,* DOE/ER-0045/12

4. P. J. Maziasz and D. N. Braski, *J. Nucl. Mater.* 122 and 123 (1984) 311–16.

5. R. E. Stoller and G. R. Odette, *J. Nucl. Mater.* 103 and 104 (1981) 1361–65.

6. G. R. Odette, P. J. Maziasz, and J. A. Spitznagel, *J. Nucl. Mater.* 103 and 104 (1981) 1289-1304,

7. P. J. Maziasz, *J. Nucl. Mater.* 108 and 109 (1982) 359–84.

8. P. J. Maziasz, *J. Nucl. Mater.* 122 and 123 (1984) 472–86.

3.2 THE TENSILE PROPERTIES OF SOLUTION-ANNEALED (SA) JPCA IRRADIATED IN HFIR – M. P. Tanaka and S. Hamada (Japan Atomic Research Institute, assigned to ORNL), and P. J. Maziasz and M. L. Grossbeck (Oak Ridge National Laboratory)

3.2.1 ADIP Task

ADIP Task I.B.13, Tensile Properties of Austenitic Alloys

3.2.2 Objective

The object of this research is to determine the tensile properties of HFIR-irradiated SA-JPCA in the temperature range 300 to 500°C and to compare them with the properties of similarly irradiated SA-U.S.JPCA as a part of the U.S.-Japan collaborative program.'

3.2.3 Summary

The tensile properties of HFIR irradiated SA-JPCA were determined from 300 to 500°C. Comparison with microstructural observations shows that the major source of hardening at 300 and 400°C is a high concentration of cavities; MC-precipitate which formed during HFIR irradiation is an additional source for hardening at 400°C. Total elongation of the JPCA remains above 6% in all test-temperature ranges.

This data shows the useful application of solution-annealed JPCA in the temperature range 300 to 500°C at 16 to 28 dpa damage levels.

3.2.4 Progress and Status

3.2.5 Introduction

Tensile tests in the temperature range 300 to 500°C have been run on the solution-annealed (SA)-JPCA alloys after HFIR irradiation in JP-1 and -3 capsules. Microstructures, reported in another section, are compared with the tensile data.

3.2.6 Experimental Procedure

The composition of JPCA is (wt %): C, 0.06; Si, 0.50; Mn, 1.77; P, 0.027; S, 0.005; Ni, 15.60; Cr, 14.22; Mo, 2.28; Ti, 0.24; B, 0.0031; N, 0.0039; Fe balance. Sheets of 7.5 mm-thick material were annealed at 1100°C in air for 1 h. After a surface layer (1 mm) was ground off each surface, the sheets were reduced to the appropriate thickness by alternate cold rolling and vacuum annealing. After a final solution anneal of 1 h at 1100°C to obtain a grain size of ASTM No. 5.5, submini-tensile specimens were machined from the sheets. Dimensions of the submini-tensile specimen are shown in Fig. 3.2.1. The gage section is 18.3 mm long with a cross section of about 3.23 mm.[2] The specimens were tested in vacuum at the nominal irradiation temperatures in an Instron tensile testing machine fitted with a wire-wound resistance furnace. The crosshead speed was 0.5 mm/min (strain rate = 4.2 × 10^{-4}/s).

The specimens were irradiated in JP-1 and -3 capsules for 16 cycles to about 34,000 MWd. Table 3.2.1 shows the fluence distribution at each specimen.

After the tensile testing, the fracture surfaces were examined by scanning electron microscopy (SEM) to characterize the fracture mode.

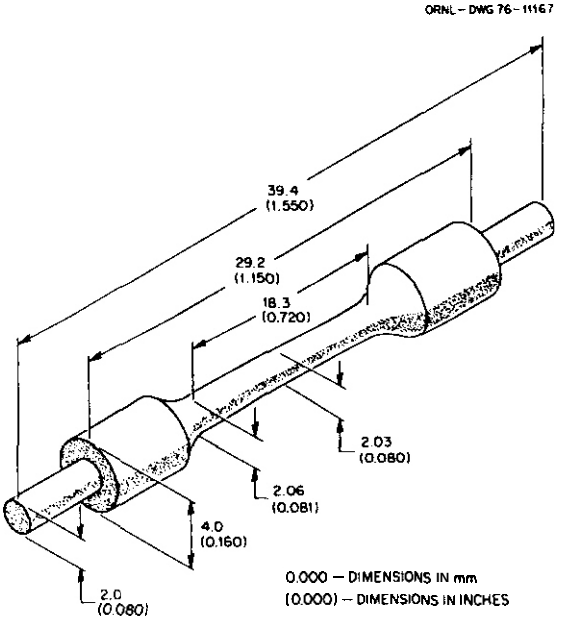

Fig. 3.2.1. HFIR submini-tensile specimen.

3.2.7 Results and Discussions

The results of tensile test are listed in Table 3.2.1, and shown graphically in Fig. 3.2.2. The ultimate and yield strength (0.2% offset) are shown in the upper portion of the figure, while the uniform and total elongation are shown in the lower portion. The tensile properties of the control specimen will be listed in a separate paper.[2] The strength and ductility values of control material are nearly the same as those reported for SA-USPCA.[3]

The irradiation at 300 and 400°C produced considerable hardening, whereas there was less hardening at 500°C. Irradiation also caused considerable loss of ductility in all of the specimens in this temperature range. The total elongation, however, remains above 6% in all specimens at this irradiation level.

Table 3.2.1. Tensile Data for SA-JPCA from JP1 and JP3 HFIR Capsule

Specimen	Material condition	Irradiation temperature (°C)	Damage Conditions		Strengths (MPa)		Elongation (%)	
			Displacement damage (dpa)	Helium level (at. ppm)	Yield	Ultimate	Uniform	Total
TB-9	SA	300	16.0	1019	887	887	0.38	7.9
TB-2	SA	400	21.0	1520	878	888	0.38	6.4
TB-8	SA	400	22.2	1541	898	913	0.43	6.0
TB-1	SA	500	26.9	1925	650	732	4.7	8.2
TB-7	SA	500	27.2	1950	636	721	6.9	8.9

[a]Specimens were tested at the irradiation temperature.

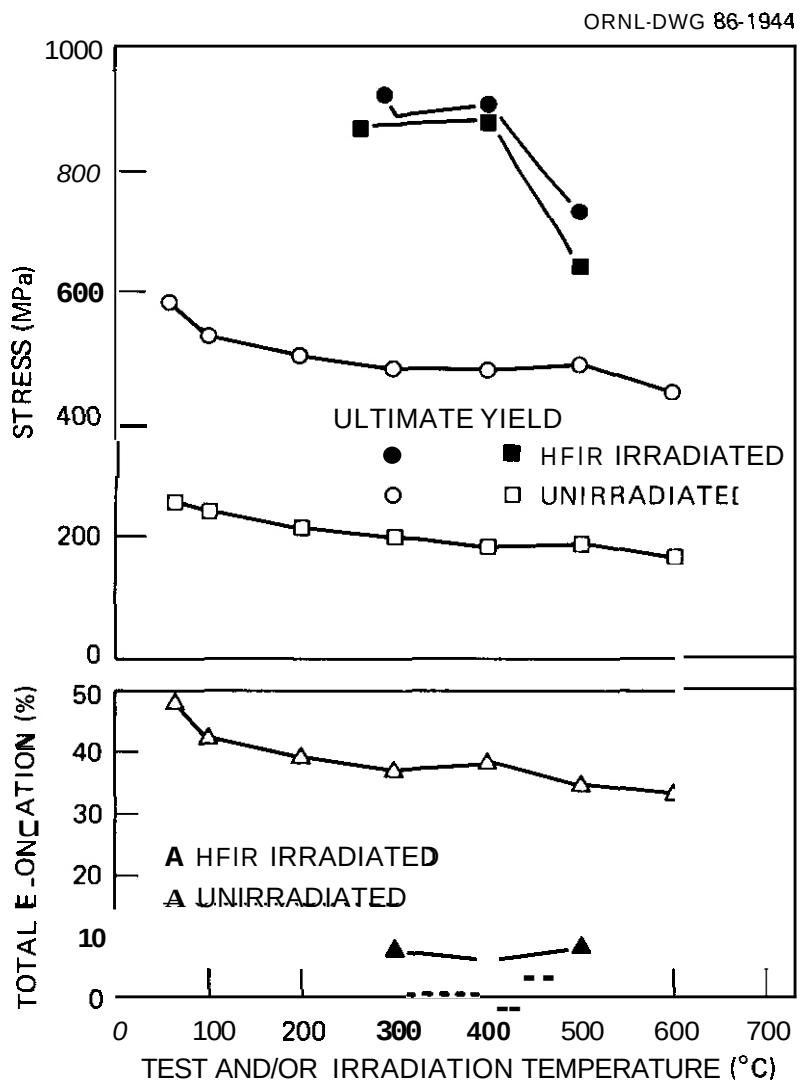

Fig. 3.2.2. Tensile Properties of SA-JPCA as a Function of Temperature.

Figure 3.2.3 shows the results of fractography for the specimens tested at 300, 400, and 500°C. Each micrograph shows that the failure mode is ductile-dimple type at this damage level in this temperature range.

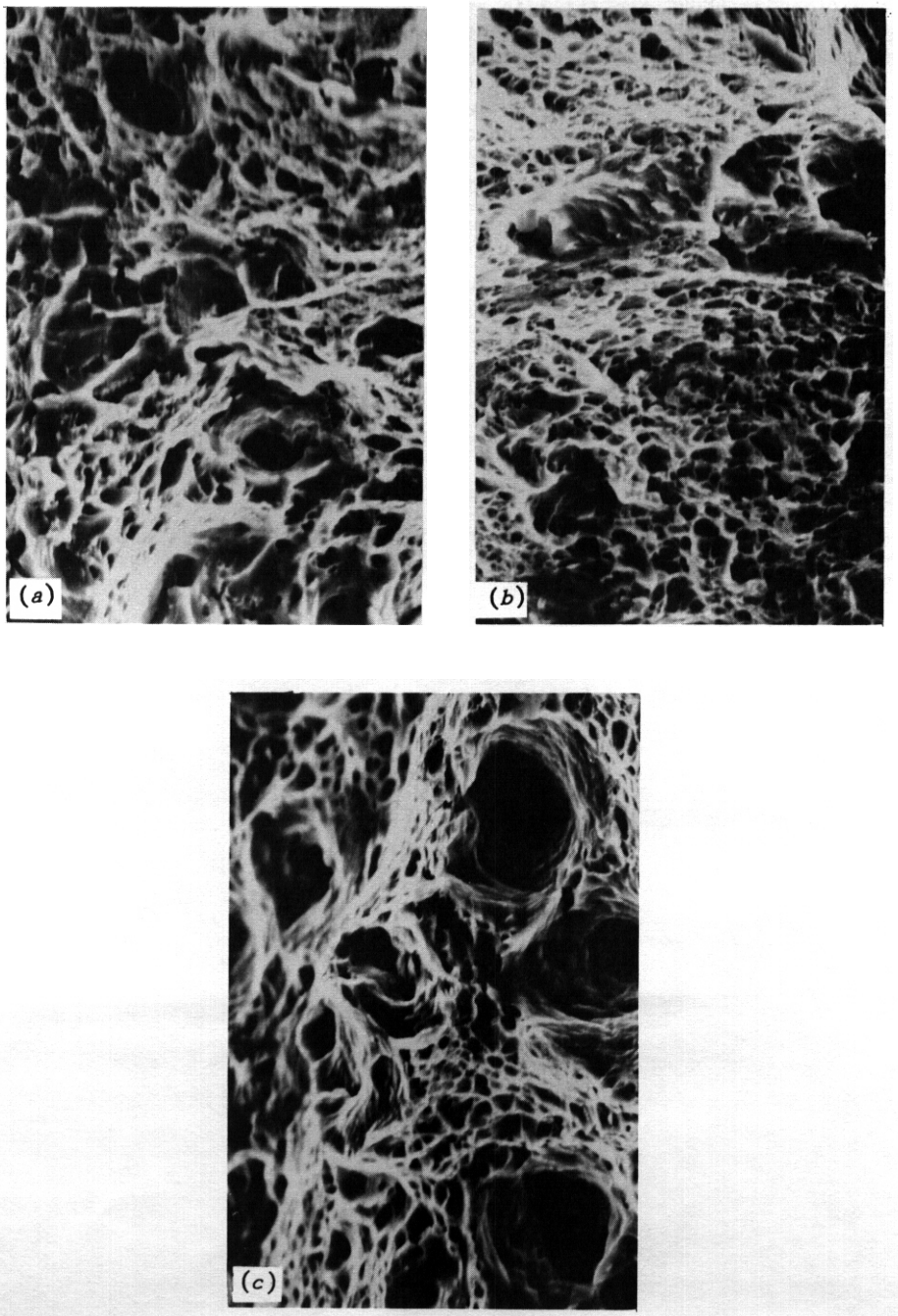

Fig. 3.2.3. SEM-Micrograph of JPCA-SA irradiated at HFIR (*a*) TB9, (300°C, 16 dpa), (*b*) TB8 (400°C, 22.2 dpa), (*c*) TB7 (500°C, 27.2 dpa).

3.2.8 Discussion

High concentrations of fine bubbles and Frank loops both contribute about equally to the yield strength at 300°C. MC precipitates contribute together with bubbles and loops at 400°C. The hardening contribution due to dislocation network, is minimal compared to the other microstructional components at 300 and 400°C. Microstructional observations at 500°C are still in progress, and will be evaluated in the next progress report. Future work will also include re-evaluating the microstructure-properties relationships and their assumptions, which were developed from fast breeder reactor data.[4]

Comparison with HFIR data of SA-USPCA at nearly the same damage level[5] shows that SA-JPCA specimens are more ductile in the 300–500°C temperature range, while strength values are similar for both materials. This irradiation experiment provides a severe test of the capacity of SA-JPCA to accomodate high concentrations of helium. The results suggest that this material can be usefully applied to near term fusion reactors in the temperature range 300 to 500°C at 16 to 28 dpa damage levels.

3.2.9 References

1. J. L. Scott and T. Kondo, "Introduction to U.S./Japan Collaborative Testing Program in HFIR and ORR," pp. 35–36 in *ADIP Semiannu. Prog. Rep., March 31, 1984,* DOE/ER-0045/12, U.S. DOE, Office of Fusion Energy.

2. To be published.

3. D. N. Braski and P. J. Maziasz, "The Tensile Properties of Unirradiated Path A Prime Candidate Alloy," pp. 49–52 in *ADIP Semiannu. Prog. Rep., March 31, 1983,* DOE/ER-0045/10, U.S. DOE, Office of Fusion Energy.

4. G. R. Johnson et al., "Microstructural Interpretation of the Fluence and Temperature Dependence of the Mechanical Properties of Irradiated AISI 316," pp. 393–412 in *Effect of Radiation on Materials: Tenth Conference* ASTM STP 725, ASTM 1981.

5. P. J. Maziasz and D. N. Braski, "Modification of the Grain Boundary Microstructure of the Austenitic PCA Stainless Steel to Improve Helium Embrittlement Resistance," to be published in *J. of Nucl. Mat.*

7.7 MICROCHEMICAL COMPOSITIONS OF PRECIPITATES IN JPCA IRRADIATED TO 34 dpa IN HFIR – M. P. Tanaka, S. Hamada and K. Fukai (Japan Atc te, assigned to ORNL), and P. J. Maziasz (Oak Ridge National Laboratory)

3.3.1 ADIP Task

ADIP Task I.C.1, Microstructural Stability.

3.3.2 Objectives

The objective of this work is to measure the microchemical composition of the precipitates which were observed in JPCA after HFIR irradiation at the temperature range 300 to 400°C as a part of the U.S./Japan collaboration program.[1]

3.3.3 Summary

Control specimens (SA, CW, and aged) contain only MC-type precipitates. The compositions of MC particles have a strong size dependence. Smaller MC particles contain less titanium and more chromium and molybdenum. After HFIR irradiation at 400°C to 34 dpa, the specimens contain small amounts of $M_{23}C_6$ and M_6C precipitates as well as MC precipitates. The size dependence is greater in irradiated specimens than found in control specimens.

3.3.4 Experimental Procedure

Extraction replicas were produced from the materials used for microstructural observation,[2] which are SA, CW, and aged JPCA irradiated at 400°C to about 34 dpa in HFIR. Specimens were prepared for extraction by polishing, lightly etching, and then coating them with a carbon film. Precipitates were extracted from matrix electrolytically using 10% HCl in methanol at a current of 50 mA at room temperature, then the carbon films were washed in ethanol, removed in distilled water, and suspended on beryllium grids. Microchemical compositional data were obtained by using energy dispersive x-ray analysis (EDS) of a TN-5500 system attached to a JEM2000FX electron microscope.

3.3.5 Results

Results of microstructural analysis of these specimens are reported in another section of this progress report.[2] Solution-annealed (SA), cold-worked (CW), and aged specimens, which are designated as PS2, PC3, and PA1, respectively, had only MC-type precipitates. Micrographs of MC precipitates observed in PA1 specimens on carbon-extracted replicas are shown in Fig. 3.3.1. Compositional information of the MC particles observed in these control specimens are listed in Table 3.3.1. These MC compositions show a dependence on particle size. Smaller MC particles contained less titanium and more chromium and molybdenum. The size dependence of the titanium and chromium contents are graphically shown in Figs. 3.3.2 and 3.3.3 in a solid line.

After HFIR irradiation at 400°C to 34 dpa, the specimens contained $M_{23}C_6$ and M_6C precipitates as well as MC precipitates. Micrographs of MC, $M_{23}C_6$ and M_6C precipitates extracted from the irradiated specimens are shown in Figs. 3.3.4 and 3.3.5. The measured compositions of these three types of precipitates are listed in Table 3.3.2. The compositions of $M_{23}C_6$ and M_6C are very similar to those reported previously.[3] MC particles show the same size dependence as those found in the control specimen. The dependence, however, became more appreciable compared to those before irradiation. The dotted line in Figs. 3.3.2 and 3.3.3 shows the size dependence of titanium and chromium, respectively.

The compositional dependence of the MC particle size has been reported in similar alloys that were not irradiated.[4] However, this report clearly shows that the same or more appreciable dependence could be found on the MC particles which formed in the irradiated specimen. One possible explanation of this dependence could be the competing process of nucleation and/or growth between $M_{23}C_6/M_6C$ and MC precipitates during neutron irradiation. Details of this discussion will be presented in the next semiannual report.

J03238

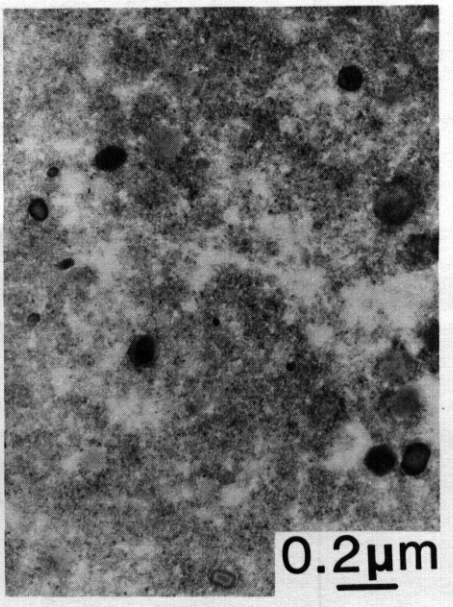

Fig. 3.3.1. MC precipitates observed in unirradiated PA1 specimen.

Table 3.3.1. MC phase composition in JPCA before irradiation

Alloy designation	Average particle size (nm)	Composition, wt %									
		Si	P	Mo	Al	Ti	Cr	Mn	Fe	Ni	V
PS2[a]	205	0.72	0.82	14.21	0.00	82.61	0.02	1.16	0.33	0.02	0.00
	43	2.06	1.01	14.88	0.05	78.74	2.14	0.27	0.57	0.28	0.00
PC3[b]	230	0.48	0.92	14.53	0.01	83.30	0.21	0.10	0.24	0.06	0.21
	109	1.48	1.28	18.29	0.03	77.10	0.69	0.26	0.68	0.17	0.00
PA1[c]	171	0.20	1.12	16.77	0.10	80.74	0.70	0.06	0.25	0.05	0.01
	6.7	3.02	2.83	33.89	0.00	49.96	9.39	0.25	0.54	0.02	0.10

[a]PS2 — solution annealed at 1100°C for 1 h.

[b]PC3 — PS2 + 20% cold work.

[c]PA1 — PC3 + 800°C for 2 h.

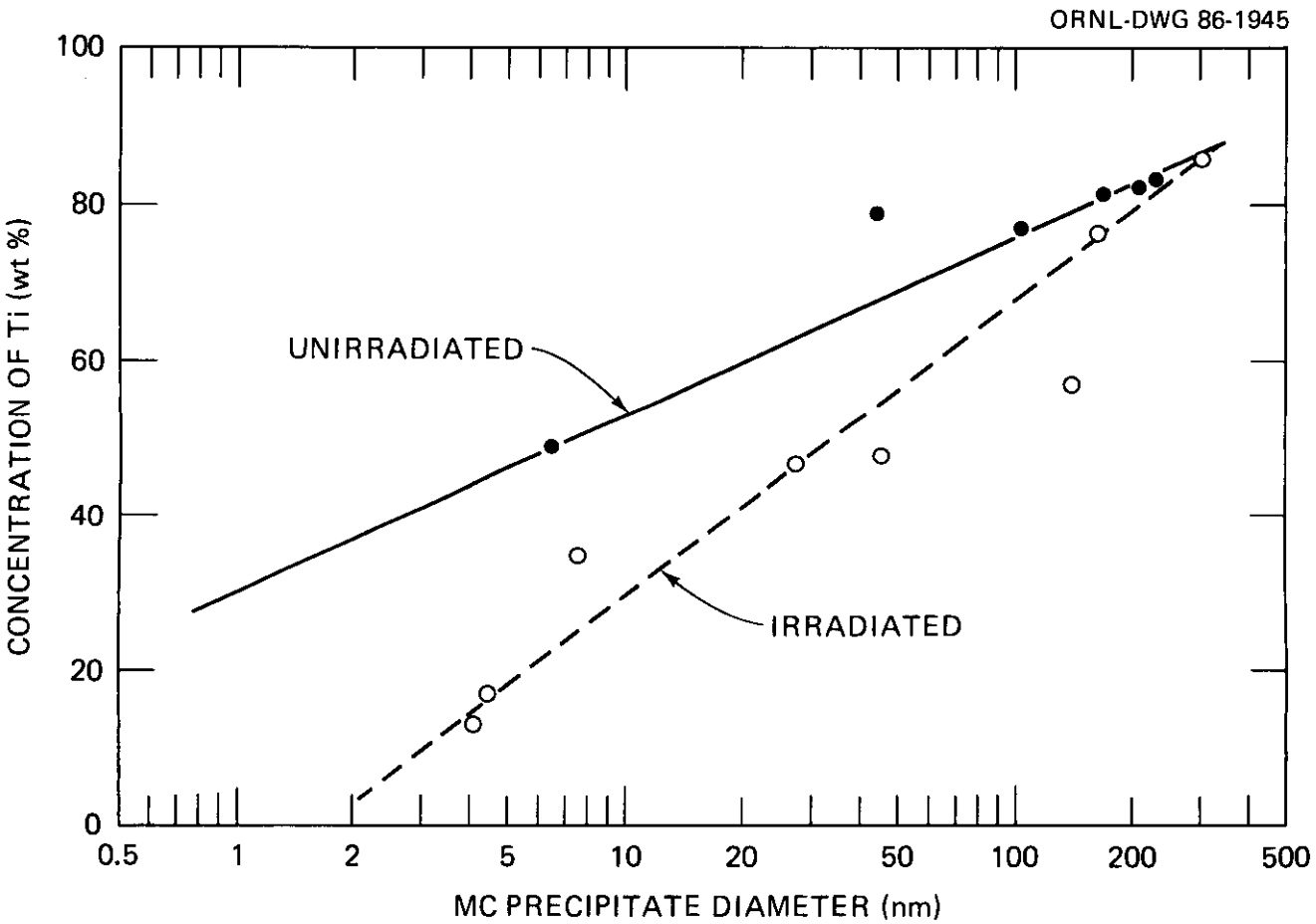

Fig. 3.3.2. Size dependence of titanium content found in unirradiated and irradiated JPCA.

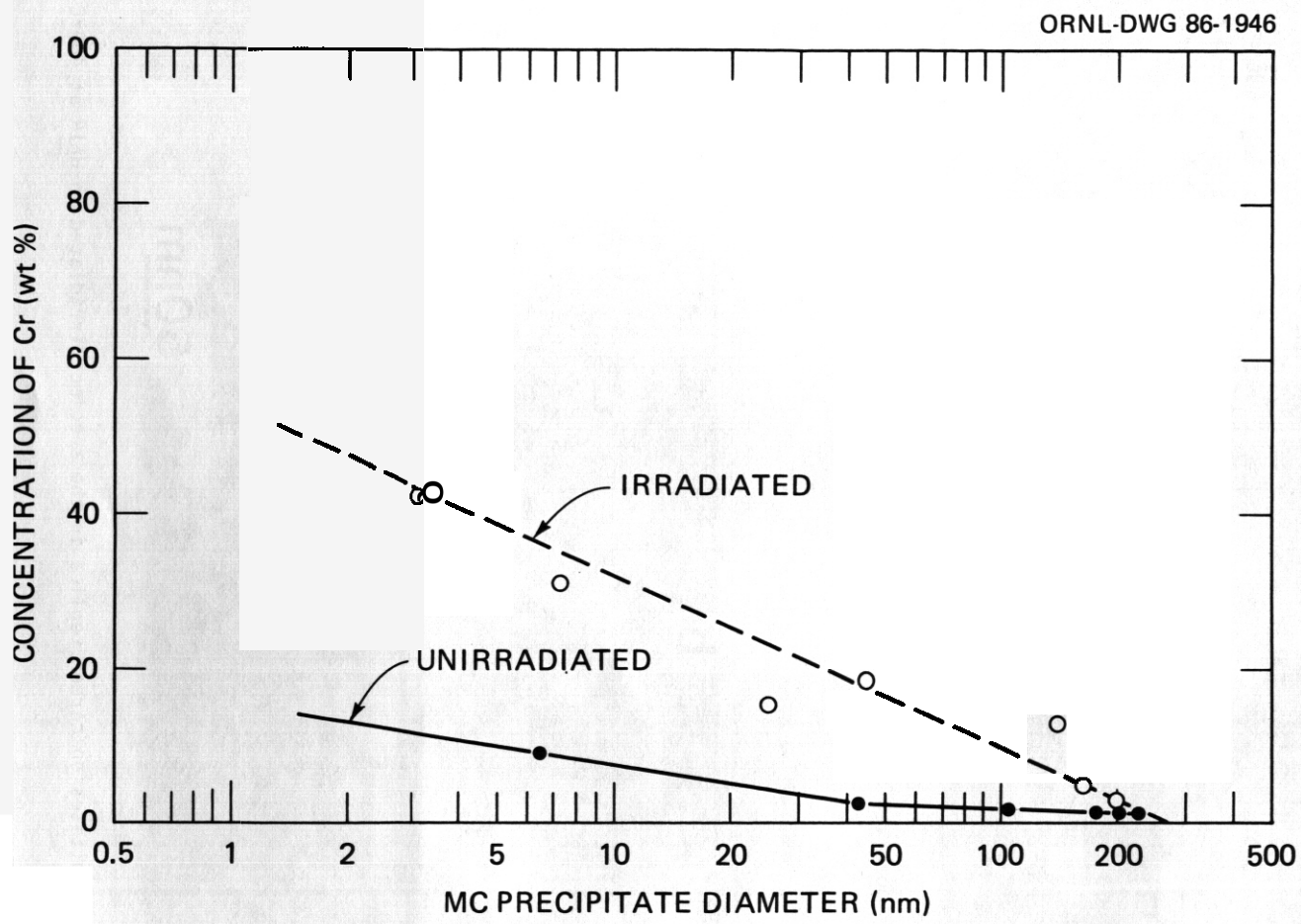

Fig. 3.3.3. Size dependence of chromium content found in unirradiated and irradiated JPCA.

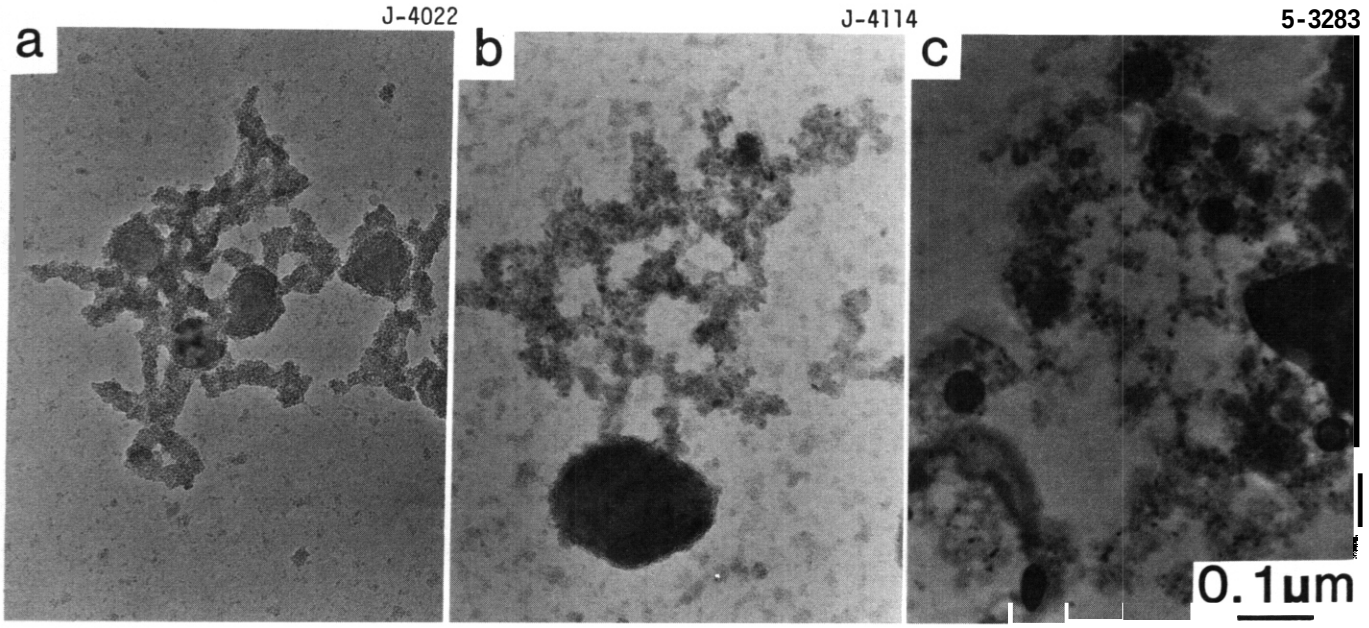

Fig. 3.3.4. MC precipitates observed on carbon extraction replica in the specimen irradiated in HFIR at 400°C to 34 dpa.

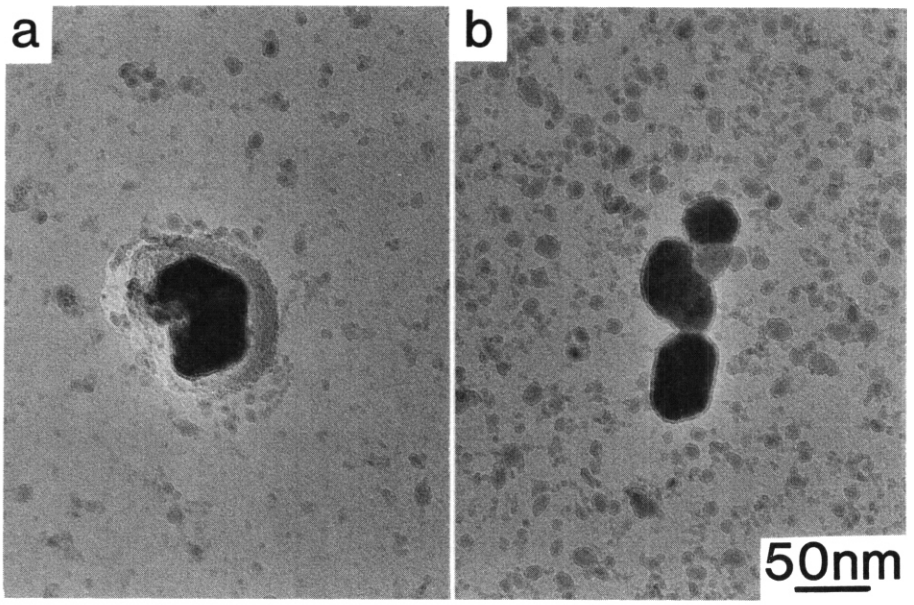

Fig. 3.3.5. $M_{23}C_6$ and M_6C precipitates on carbon replica in the specimen irradiated in HFIR at 400°C to 34 dpa.

Table 3.3.2. Phase composition in JPCA after HFIR Irradiation at 400°C to 34 dpa

Alloy		average (nm)	Composition, wt %									
			Si	P	Mo	Al	Ti	Cr	Mn	Fe	Ni	V
PS2	MC	134	1.12	1.30	14.94	0.00	57.81	12.83	6.62	3.54	1.20	0.63
	MC	3.1	4.01	2.38	15.74	0.08	13.23	40.89	16.22	3.52	1.02	2.91
	$M_{23}C_6$	85	2.96	0.37	2.45	0.00	2.41	50.80	6.88	29.36	4.13	1.24
	MC	3.5	7.44	2.94	17.30	0.00	16.20	43.62	3.94	2.45	2.00	4.05
	M_6C	52	7.67	0.97	1.63	0.11	0.14	37.57	2.28	23.8	25.0	0.88
PA1	MC	200	0.13	0.27	7.90	0.00	88.22	1.23	0.03	1.38	0.45	0.38
	MC	28	7.81	1.27	16.70	0.00	46.21	15.47	2.32	4.87	4.00	1.36
	MC	7.1	1.27	1.10	16.82	0.00	35.27	30.82	1.53	6.87	4.27	1.88
	M_6C	50	7.22	2.02	12.33	0.45	6.87	28.65	1.88	25.54	13.96	1.25
	$M_{23}C_6$	54	0.90	0.78	7.40	0.00	1.60	59.91	2.75	21.96	3.12	1.58

3.3.6 References

1. J. L. Scott and T. Kondo, "Introduction to U.S./Japan Collaborative Testing Program in HFIR and ORR," pp. 35–36 in *ADIP Semiannu. Prog. Rep. March 31, 1984,* DOE/ER-0045/12, U.S. DOE, Office of Fusion Energy.

2. M. P. Tanaka, S. Hamada, and P. J. Maziasz, "Microstructural Development in the PCAs Irradiated to 34 dpa in HFIR at 300 and 400°C," this report.

3. E. H. Lee, P. J. Maziasz, and A. F. Rowcliffe, "Stainless Steels in Thermal and Irradiation Environments," pp. 191–218 in *Proc. of Phase Stability During Irrediation,* Pittsburgh, Pa., (October 1980).

4. P. J. Maziasz and S. Jitsukawa. "Minor Compositional Variations of the Austenitic PCA to Explore MC Formation and Stability Characteristic for Improved' Radiation Resistance," pp. 37–48 in *ADIP Semiannu. Prog. Rep. Mar. 31, 1985,* DOE/ER-0045/14, U.S. DOE, Office of Fusion Energy.

3.4 MODIFICATION OF THE GRAIN BOUNDARY MICROSTRUCTURE OF THE AUSTENITIC PCA STAINLESS STEEL TO IMPROVE HELIUM EMBRITTLEMENT RESISTANCE – P. J. Maziasz and D. N. Braski (Oak Ridge National Laboratory)

3.4.1 AOIP Task

I.B.13 – Tensile Properties of Austenitic Alloys; I.C.l – Microstructural Stability; and I.C.2 Microstructure and Swelling of Austenitic Alloys.

3.4.2 Objectives

The objective is to determine the effect of different initial matrix and grain boundary microstructural conditions on the effect of neutron irradiation and high-helium generation on tensile properties of the PCA over the temperature range 300 to 600°C.

3.4.3 *Summary*

Grain boundary MC precipitation was produced by a modified thermal mechanical pretreatment in 25% cold worked (CW) austenitic prime candidate alloy (PCA) stainless steel prior to HFIR irradiation. Postirradiation tensile results and fracture analysis showed that the modified material (B3) resisted helium embrittlement better than either solution annealed (SA) or 25% CW PCA irradiated at 500 to 600°C to ~21 dpa and 1370 at. ppm He. PCA was not embrittled at 300 to 400°C. Grain boundary MC survives in PCA-B3 during HFIR irradiation at 500°C but dissolves at 600°C; it does not form in either SA or 25% CW PCA during similar irradiation. The grain boundary MC appears to play an important role in the embrittlement resistance of PCA-83.

3.4.4 Prowess and Status

3.4.4.1 Introduction

Recent articles discuss current work and provide perspective on the general problem of helium embrittlement in austenitic stainless steels.[1-3] The problem is expected to be quite severe above 550 to 600°C at the high helium generation rates to be found in a fusion reactor first wall. However, at temperatures in the 400 to 600°C range, high swelling is the most severe radiation problem limiting lifetime. Helium embrittlement imposes lifetime limits only when the steel is already resistant to void swelling.'

The PCA is a 14Cr–16Ni–2.5Mo–0.25Ti–0.4Si–0.05C (all in weight percent) austenitic stainless steel whose composition was developed for void swelling resistance.[5] However. for fusion application with high helium generation rates, neither swelling nor embrittlement resistance are indigenous properties of an alloy. Instead, both properties depend on pre-irradiation microstructural condition. A variety of preirradiation microstructures of PCA have been evaluated after HFIR irradiation.[3,6,7] Swelling resistance was found to be optimum in heavily (20–25%) cold worked material.' Matrix MC, either coarse or fine, introduced via thermal pretreatments dissolves at 500 to 600°C. By contrast, preaging to produce moderately coarse grain boundary MC was the only method to improve embrittlement resistance in HFIR-irradiated PCA.[3] The formation and stability of MC are vital to irradiation resistance in steels. MC behavior fits into the more general understanding of phase stability in irradiated steels that has developed recently.""

Previous work showed embrittlement resistance qualitatively via disk-bend testing, but did not combine optimum pretreatments for swelling and embrittlement resistance together. Therefore, the objective of this work is to evaluate the swelling and embrittlement resistance of a new, optimized microstructural variant of PCA, designated B3. The 83 microstructure was produced by aging solution annealed (SA) material for 8 h at 800°C to produce medium-coarse grain boundary MC prior to 25% cold working (CW). Mechanical properties were evaluated quantitatively by postirradiation tensile testing of larger, bar-type specimens.

3.4.4.2 Experimental

The PCA was fabricated into 5-mm-diam rod stock in either the 25% CW (A3), the B3, or the 50% CW condition. The *83* material was solution annealed for 30 min at 1100°C prior to aging and then 25% CW. Standard HFIR "sub-mini" buttonhead tensile specimens (gage lengths - 18.3 mm, gage diam - 2 mm) were machined from the rod stock. The 50% CW specimens were then annealed for 30 min at 1100°C to produce the SA (A1) microstructure.

Specimens were irradiated in experiments HFIR-CTR-42 and -43. Elevated temperatures were achieved via gas gaps that kept irradiation temperatures uniform over the shoulder and gage regions of the specimens.

Irradiation temperatures of 300, 400, 500, and 600°C were calculated, based on recent temperature measurements from similar gas-gap experiments.' Specimens were irradiated to neutron fluences producing *10.8* to 16.6 dpa and 1060 to 1371 at. ppm He, based on dosimetry and calculations by Greenwood."

The irradiated specimens were tensile tested on an in-cell instron universal testing machine at the irradiation temperature using a strain rate of 0.51 mm/min. Unirradiated controls were also tested at 300, 500, and 600°C, while aged PCA-A3 and 83 specimens (5000 h at 600°C) were also tested at 600°C.

Transmission electron microscopy (TEM) disks were sliced from the shoulders of several tested HFIR specimens and thinned via a remote TENUPOL unit and examined using a JEM 2000FX analytical electron microscope (AEM). Fractography was performed on a remote, modified AMRAY 12008 scanning electron microscope (SEM).

3.4.4.3 Results

Tensile properties

HFIR irradiation at 300 and 400°C produced considerable hardening, whereas there was less hardening at 500°C, and little or none at 600°C. Tensile properties for HFIR-irradiated specimens are listed in Table 3.4.1 and shown with unirradiated control data in Fig. 3.4.1. Properties on control specimens are listed elsewhere.[11,12] The PCA-Al was softest prior to irradiation and experienced the most strengthening during irradiation, The PCA-A1, -A3, and -83 all approached similar strength levels during irradiation, but PCA-A3 was slightly stronger than the others. Unirradiated PCA-B3 was the strongest material at 500 and 600°C. Irradiation caused PCA-A1 and -A3 to have equal and high (900–1000 MPa) values of yield and ultimate tensile strength (YS and UTS, respectively) at 300 and 400°C. The YS and UTS became measurably different in PCA-A3 and -83 at 500 and 600°C, but they remained nearly equal for PCA-A1.

Table 3.4.1. Postirradiation tensile data for PCA Irradiated in HFIR

Material condition	Irradiation temperature (°C)	Conditions[a]			Strength[b] MPa		Elongation, %	
		Fluence ($\times 10^{26}$ n/m²) (E > 0.1 MeV)	Displacement damage (dpa)	Helium level (at. ppm)	Yield	Ultimate	Uniform	Total
PCA-83	600	2.46	20.8	1370	508	579	3.2	3.8
PCA-A3	600	2.40	20.3	1335	539	570	1.0	1.1
PCA-A3	600	2.40	20.3	1335	513	548	1.2	1.7
PCA-A1	600	2.46	20.8	1370	468	473	0.3	0.6
PCA-B3	500	2.40	20.3	1335	659	745	5.3	8.6
PCA-A3	500	2.25	19.0	1234	692	771	3.4	6.2
PCA-A3	500	2.25	19.0	1234	767	842	2.0	3.9
PCA-A1	500	2.40	20.3	1335	765	793	1.4	3.3
PCA-A3	400	1.97	16.6	1060	950	951	0.2	4.4
PCA-A3	400	2.25	19.0	1234	935	938	0.3	4.1
PCA-A3	400	1.97	16.6	1060	976	980	0.3	4.1
PCA-A1	400	2.25	19.0	1234	896	897	0.1	5.5
PCA-A3	300	1.97	16.6	1060	973	973	0.2	5.3
PCA-A1	300	1.97	16.6	1060	851	851	0.3	7.3

[a]Displacement damage and helium were calculated from dosimetry measurements made by Greenwood.[..]

[b]Specimens were tested at the irradiation temperature.

Irradiation caused significant ductility loss in all specimens except PCA-B3, which actually had better ductility after irradiation at 500°C than unirradiated material (Fig. 3.4.1). The PCA-A1, which had the highest ductility among the pretreatment variants prior to irradiation, had the lowest ductility after irradiation. Ductility loss at 300 and 400°C correlated reasonably well with the general increase in strength caused by irradiation, for comparison of PCA-A1 and -A3. But progressively greater ductility losses at 500 and 600°C despite decreases in strength suggested embrittlement in both of these materials. Total elongation (TE) decreased monotonically with temperature for PCA-A1, from ~7% at 300°C to 0.6% at 600°C. Uniform elongation (UE), however, was very low (0.1–0.3%) at 300 and 400°C, and reached a maximum (1.4%) at 500°C and then became low (0.3%) again at 600°C. PCA-A1 and -A3 had parallel behavior of ductility with temperature, but PCA-A1 was less ductile. Decreased strength and ductility going from 500 to 600°C indicated that both PCA-A1 and -A3 were becoming brittle.

In contrast to PCA-A1 or -A3, PCA-B3 appeared to resist embrittlement altogether at 500°C and to resist it somewhat better than the others at 600°C. At 500°C, UE was low prior to irradiation, making its increase during irradiation quite significant. At 600°C, UTS decreased while UE again increased during irradiation. Aging at 600°C decreased the UE of unirradiated PCA-A3, whereas aging increased it for PCA-B3. Although PCA-B3 was also becoming brittle at 600°C, embrittlement was not as severe as in PCA-A1 or -A3.

SEM - fracture analysis

Unirradiated control specimens generally fractured via a ductile dimple-type failure mode up to 600°C, as confirmed for PCA-A3. However, after HFIR irradiation at 600°C, fracture became intergranular to varying

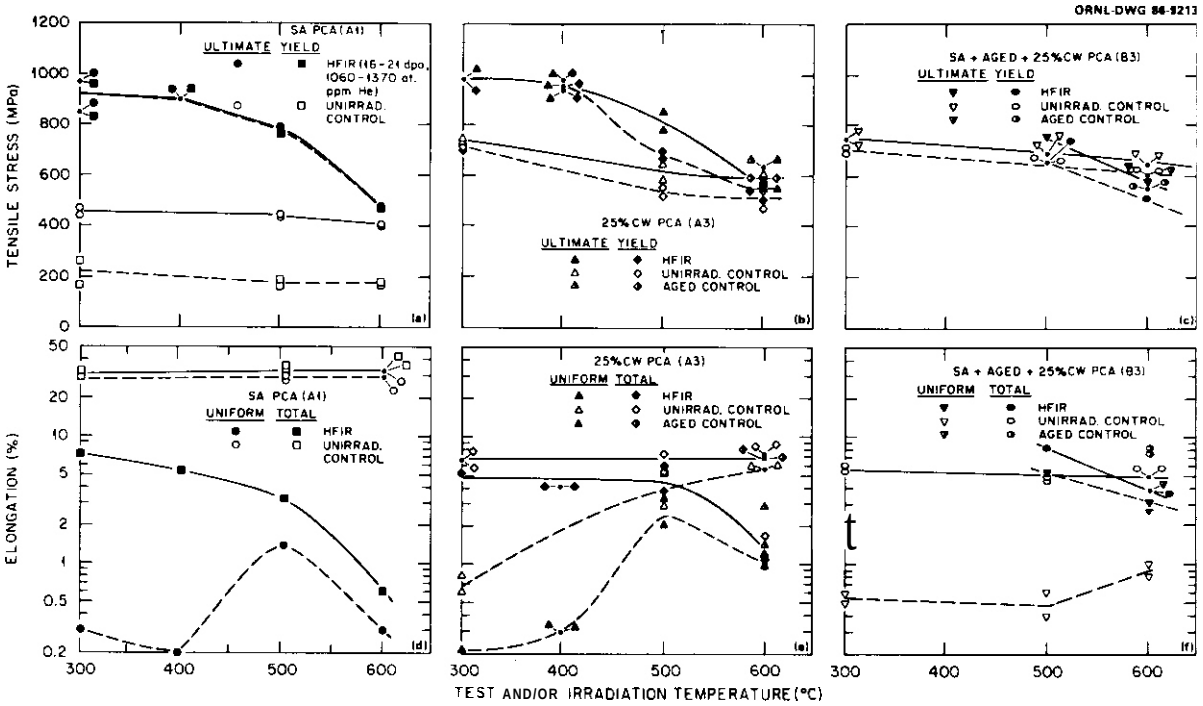

Fig. 3.4.1. Plots of yield and ultimate tensile stress and uniform and total elongation, respectively, for PCA-Al (*a,d*), PCA-A3 (*b,e*) and PCA-83 (*c,f*) as functions of test temperatures. HFIR irradiated specimens were tested at their irradiation temperatures. Data on unirradiated control specimens and specimens aged for 5000 h at 600°C are included for comparison from ref. 12.

degrees, depending upon alloy pretreatment. PCA-A3 failed intergranularly across the entire fracture surface after irradiation at 600°C, whereas PCA-B3 showed a mixture of ductile transgranular and intergranular failure modes. After irradiation at 500°C, the failure mode was ductile shear in the middle of the cross section for all samples, but varied near the outer edge. As shown in Fig. 3.4.2, PCA-B3 failed in a ductile mode at the specimen edge, whereas in PCA-Al, failure was intergranular near the specimen surface. Despite low ductilities after irradiation at 400°C, specimens were not brittle and failed via a ductile-dimple mode, similar to unirradiated material.

3.4.4.4 TEM - Microstructural Analysis

The microstructure was examined from the shoulders of PCA-A1 and -83 tensile specimens irradiated at 500 and 600°C. Previous work showed that HFIR irradiation at 300 and 400°C to 44 dpa produced similar microstructures of many Frank loops and fine bubbles in PCA-Al, -A3, and other pretreatments. However, microstructural evolution varied considerably with pretreatment at higher temperatures.[3,7]

Intragranularly. PCA-B3 had many fine bubbles at 500 and 600°C after ~20 dpa, with possibly a few voids at 500°C. The amount of fine MC increased with temperature, whereas dislocation and loop concentrations decreased. By comparison to PCA-83, A1 had many coarse voids together with fewer and coarser bubbles at 500 and 600°C. The A1 material also had more large loops and less MC with the additional formation of G and γ' phases. The PCA-B3 microstructures were similar to those found previously in HFIR irradiations of PCA-A3 at 500 and 600°C to 22 dpa.[3]

Intergranularly, PCA-B3 contained medium-coarse MC precipitation after irradiation at 500°C to ~20 dpa, whereas PCA-A1 did not (Figs. 3.4.3 and 3.4.6). The grain boundary MC produced in PCA-B3 prior to irradiation survived well at 500°C, but not at 600°C. Some coarse grain boundary $M_6C(\eta)$ [and/or either $M_{23}C_6$ (τ) or G] precipitated sporadically at 500°C in PCA-83, but more frequently at 600°C. Similar coarse particles were more abundant in PCA-Al at 500°C [see Fig. 3.4.3(*a*) and (*b*)]. Bubbles were larger and more concentrated at the precipitate-bare grain boundaries in PCA-A1 than in PCA-83, particularly at 500°C [see Fig. 3.4.4(*c*) and (*d*)]. Many of the finer bubbles in PCA-83 were attached to MC particles in the boundary. At 600°C, however, grain boundary regions in PCA-B3 that experienced MC dissolution were similar to those in PCA-A1.

Finally, we note that grain boundary regions were poorly defined in PCA-A1 at 500°C. The grain boundaries may have migrated to sweep up helium bubbles and leave trails of elongated precipitates and voids behind. Grain boundary regions are better defined and apparently more stable in PCA-83.

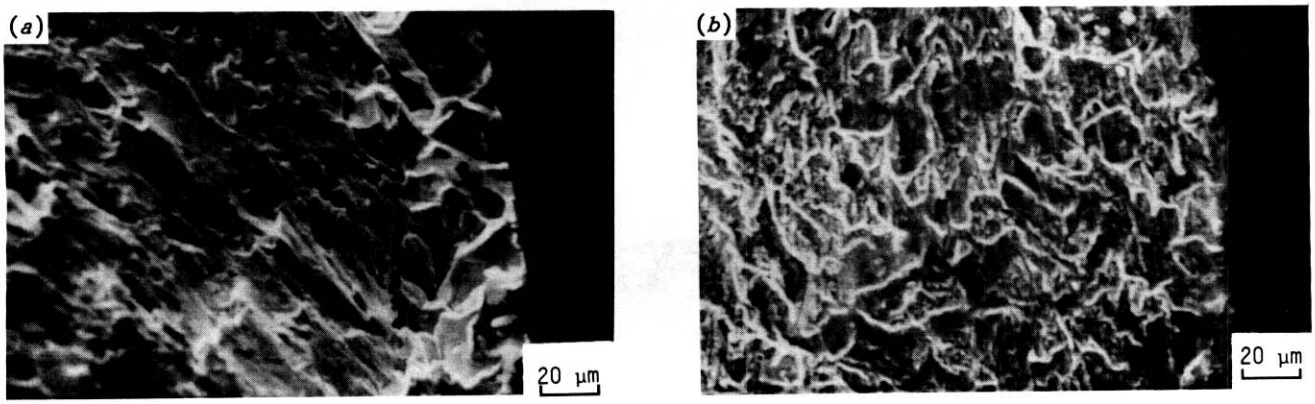

Fig. 3.4.2. SEM of fractures for (*a*) PCA-A1 (EJ-6) and (*b*) PCA-B3 (EL-7) irradiated in HFIR at 500°C to 20.3 dpa and 1335 at. ppm He. PCA-A1 shows some intergranular failure near the specimen surface where PCA-B3 shows ductile-shear failure throughout the gage cross section.

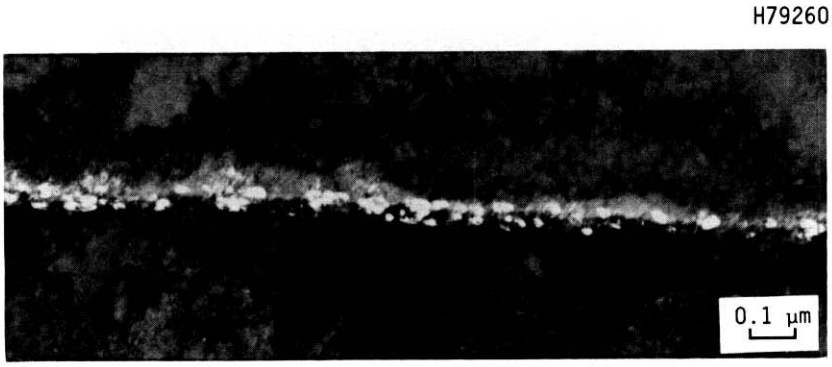

(*a*)

(*b*)

Fig. 3.4.3. TEM comparison of grain boundary MC precipitation via dark-field imaging for PCA-B3 *(a)* as-heat-treated prior to irradiation and (*b*) after HFIR irradiation at 500°C to 20.3 dpa and 1335 at. ppm He. Most of the MC particles survive during irradiation, despite some coarsening and/or dissolution.

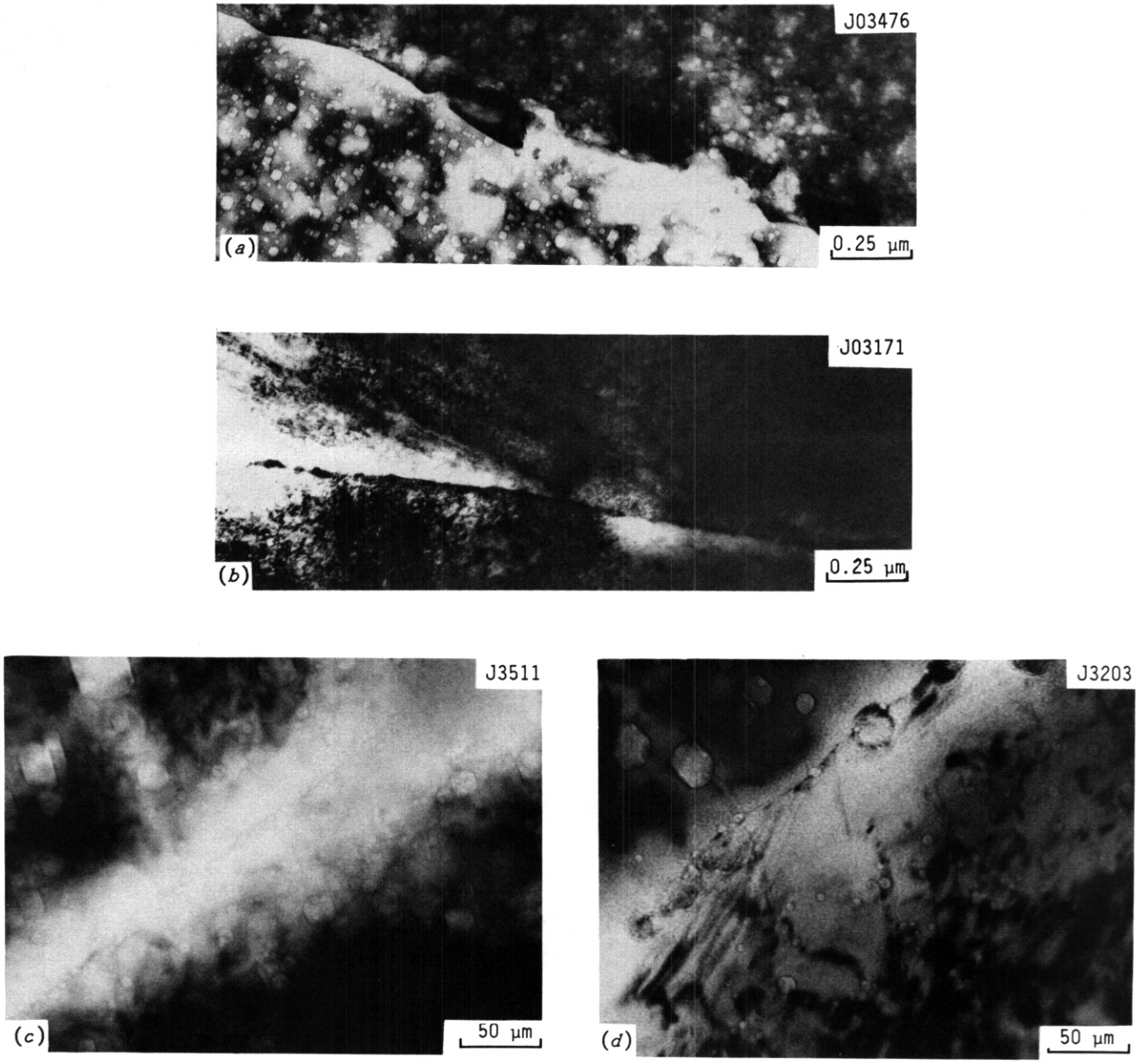

Fig. 3.4.4. TEM comparison of grain boundary precipitation at lower magnification (*a,b*) and grain boundary helium bubbles at higher magnification (*c,d*) for PCA-A1 (*a,c*) and -B3 (*b,d*) irradiated in HFIR at 500°C to 20.3 dpa and 1335 at. ppm He. Note the fine bubbles attached to MC particles in PCA-B3 (*d*).

3.4.5 Discussion

Within this data set, microstructures and properties correlate quite well. Loops appear to be the major source of matrix hardening, because temperature and pretreatment effects on strength correlated with their effects on Frank loop formation and stability. At 600°C it appears that fine MC particles and possibly bubbles pin the network dislocations to strengthen PCA-A3 and -B3 relative to -A1. At grain boundaries, coarser helium bubbles and lack of precipitation contribute to embrittlement at 500 and 600°C of PCA-A1 and -A3. Conversely, MC and bubble refinement at grain boundaries contribute to embrittlement resistance of PCA-B3.

Comparison with previous HFIR data at less than 20 dpa[13-15] shows that at 400 to 600°C the YS of the 25% CW PCA was 100 to 200 MPa higher than for 20% CW 316 or 316+Ti stainless steels, while SA PCA was 200 to 300 MPa stronger than the same SA steels. However, SA and 25% CW PCA were less ductile, particularly between 500 and 600°C.

The embrittlement resistance of PCA-B3 at 500 and 600°C was consistent with qualitative disk-bend testing on two pretreatment variants of PCA with similar grain boundary MC precipitation.' Bend test results were also qualitatively consistent with the present results on the embrittlement behavior of PCA-AI and -A3 at 400 to 600°C.

Grain boundary MC affects embrittlement resistance during neutron irradiation in several ways: (a) the effect of MC particles trapping helium and refining the bubble distribution at their interfaces, (b) the effects of the MC precipitation on grain-boundary behavior, and (c) the stability of the MC particles. For the first aspect, if embrittlement is related to critical bubble size at the grain boundaries,[16] then the benefits of MC to refine and pin bubbles to hinder their growth on coalescence are obvious. The second and third aspects are related. The oversized MC particles themselves may alter the sink nature of the grain boundary for helium as well as prevent boundary migration and sweeping. However, all benefits disappear if the MC becomes unstable due to segregation processes in the matrix.[5] Schroeder et al.[1] and Kesternich[2] identify MC stability during neutron irradiation as a key issue, whereas our results provide some information on the limits of that stability.

Finally, Schroeder et al.[1] and Kesternich[2] suggest that embrittlement resistance stems from the helium trapping of fine matrix MC particles, based on helium injection and thermal creep data. Our work differs because we ascribe the embrittlement resistance to MC particles within grain boundaries. Similar dispersions of fine matrix MC and bubbles form in PCA-A3 and -83 in HFIR, but better embrittlement resistance correlates with the grain boundary MC present in PCA-B3. Both mechanisms are valid, and further experiments are needed to truly evaluate them at in-reactor creep conditions relevant to fusion.

3.4.6 Conclusions

PCA-AI and -A3 become very strong and lose ductility after HFIR irradiation at 300 and 400°C to -19 dpa and 1230 at. ppm He, but do not become brittle. They do, however, become progressively more embrittled with increasing temperature at 500 and 600°C.

PCA-B3 is more resistant to embrittlement than either PCA-A1 or -A3 after HFIR irradiation at 500 and 600°C. At 500°C, irradiation actually improves the ductility. The embrittlement resistance appears directly related to the effects and stability of grain boundary MC produced via aging prior to irradiation.

3.4.7 Publication

This paper was presented as a contribution to the ICFRM-2 meeting, held in Chicago, Illinois, April 13-17, 1986, and will appear in the Proceedings; to be published in the *Journal of Nuclear Materials.*

3.4.8 References

1. H. Schroeder, W. Kesternich, and H. Ullmaier, *Nucl. Engin. and Design/Fusion* **2**, (1985) 65-95.

2. W. Kesternich, *J. Nucl. Mater.* **127**, (1985) **153-60.**

3. P. J. Maziasz and D. N. Braski, *J. Nucl. Meter.* **122** and **123**, (1984) 305-10.

4. P. J. Maziasz, *J. Nucl. Mater.* **138** and **134**, (1985) 134-40

5. P. J. Maziasz, *J. Nucl. Mater.* **122** and **123**, (1984) 472-86.

6. P. J. Maziasz and T. K. Roche, *J. Nucl. Mater.* **103** and **104**, (1981) 797-802.

7. P. J. Maziasz and D. N. Braski, *J.* Nucl. *Mater.* **122** and **123**, (1984) 311-16.

8. E. H. Lee, P. J. Maziasz, and A. F. Rowcliffe, pp. 191-278 in *Conf. Proc. Phase Stability Under Neutron Irradiation,* TMS-AIME, 1981.

9. M. L Grossbeck, J. W. Woods, and G. A. Potter, pp.36–44 in *ADIP Quart. Prog. Rept.,* DOE/ER-0045/4 (1980) Of-ice of Fusion Energy, U.S. Department of Energy.

10. L. R. Greenwood, pp. 13–17 in *ADIP Semiannu. Prog. Rept.,* DOE/ER-0045/13 (1984) Office of Fusion Energy, U. S. Department of Energy.

11. D. N. Braski and P. J. Maziasz, *J. Nucl. Mater.* **122** and **123** (1984) 338–342.

12. D. N. Braski and P. J. Maziasz, pp. 61–63 in *ADIP Semiannu. Prog. Rept.,* DOE/ER-0045/12 (1984) Office of Fusion Energy, U.S. Department of Energy.

13. M. L. Grossbeck and P. J. Maziasz, pp. 32-49 in *ADIP Quart. Prog. Rept.,* DOE/ER-0058/3 (1978) Office of Fusion Energy, U.S. Department of Energy.

14. M. L. Grossbeck and P. J. Maziasz, *J. Nucl. Mater.* **103** and **104** (1981) 827–832.

15. R. L. Klueh and M. L. Grossbeck, pp. 768-782 in *Effects of Radiation on Materials, Twelfth Inter. Symp.,* ASTM-STP-870, Amer. Soc. for Testing and Matls., Philadelphia, PA, 1985.

16. G. R. Odette, *J. Nucl. Mater.* **122** and **123** (1984) 435–441.

3.5 MICROSTRUCTURES OF TYPE 316 STAINLESS STEEL IRRADIATED TO 30 dpa AT 300 and 400°C IN HFIR – S. Hamada, M. P. Tanaka (Japan Atomic Energy Research Institute, assigned to ORNL), and P. J. Maziasz (Oak Ridge National Laboratory)

3.5.1 ADIP Task

ADIP Task I.C.1, Microstructural Stability.

3.5.2 Objectives

The objective of this experiment is to evaluate the change of microstructures in a Japanese heat of type 316 stainless steel irradiated in HFIR at 300 and 400°C, and to evaluate heat-to-heat variations in behavior by comparison with U.S. heats of type 316 stainless steel.

3.5.3 Summary

Type 316 stainless steel solution annealed (SA) and 20% cold-worked (20% CW) specimens were irradiated in HFIR at 300 and 400°C to fluences of ~33 dpa and 2250 at. ppm He. The swelling by bubbles was 0.3% at 300°C and 0.5% at 400°C, and was similar in SA and 20% CW material, respectively. A few fine and large precipitates with Moiré fringes were observed in the grains and along grain boundaries, but no γ' precipitates were observed.

3.5.4 Progress and Status

This work is a part of the U.S./Japan collaborative program.[1]

3.5.4.1 Experimental

The chemical composition of specimens used in the experiment is given in Table 3.5.1. Solution-annealed and 20% CW disks were irradiated in the JP-1 capsule at 300°C and in the JP-3 capsule at 400°C to ~33 dpa and 2250 at. ppm He in HFIR. After irradiation, these disks were electropolished and examined with a JEM 2000FX transmission electron microscope. Further details of experiments have been described previously.[2]

Table 3.5.1. Chemical composition of type 316 stainless steel

Composition,[a] wt %											
Cr	Ni	Mo	Mn	C	Ti	Si	P	S	N	B	Co
16.75	13.52	2.50	1.80	0.058	0.005	0.61	0.028	0.013	--	--	<0.01

[a]Balance iron.

3.5.4.2 Results and Discussion

A. Results on J-316

Small cavities (1–5 nm in diameter) were observed in specimens irradiated at both 300 and 400°C up to 30 dpa and 2250 at. ppm He in HFIR, as shown in Figs. 3.5.1 and 3.5.2. Following irradiation at 300°C, very fine cavities were distributed uniformly and in high concentration throughout the matrix in both SA and 20% CW. The size distributions of the cavities at 300°C are given in the right side of Fig. 3.5.1. The sharp, narrow peaks in these size distributions suggest that most of these fine cavities are subcritical bubbles. The swelling values at 300°C (calculated from TEM observations) were less than about 0.3% for both SA and 20% CW material.

Figure 3.5.2 shows cavity microstructure and size distribution of cavities at 400°C. Unlike those irradiated at 300°C, some larger cavities (4 to 8 nm in diameter) are present at 400°C among the many finer ones. The largest cavities are faceted, and may be voids. The histograms of size distribution show a broad tail as size increases and also indicate an incipient splitting into a bimodal distribution. This would suggest that the largest cavities are above their critical size and have converted into bias-driven voids. The size distributions would be consistent with a critical size of 4 to 5 nm. The swelling at 400°C was about 0.47%, which is slightly larger than in the case of 300°C irradiation (Table 3.5.2). The dislocation structure in all specimens consisted of a high concentration of network and Frank faulted loops. Dark-field images of Frank faulted loops are shown in Fig. 3.5.3. Frank faulted loops were imaged separately from the network, using a high-resolution dark-field method suggested by Okamoto and Harkness.[3] The quantitative

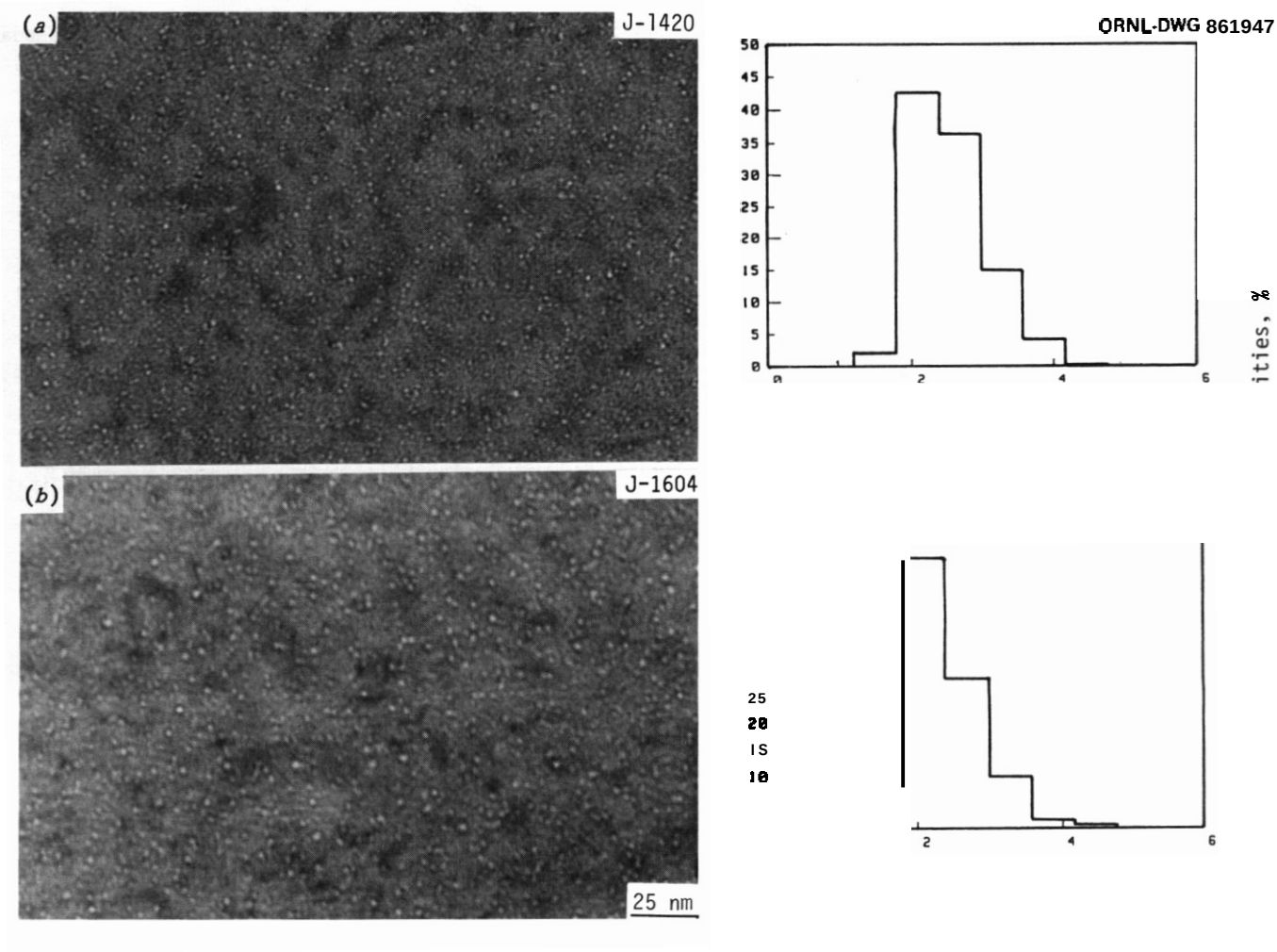

Fig. 3.5.1. Cavity microstructure observed in (e) SA and (*b*) 20% CW type 316 stainless steel after HFIR irradiation at 300°C to about 10 dpa. The cavity size distribution is given on the right side.

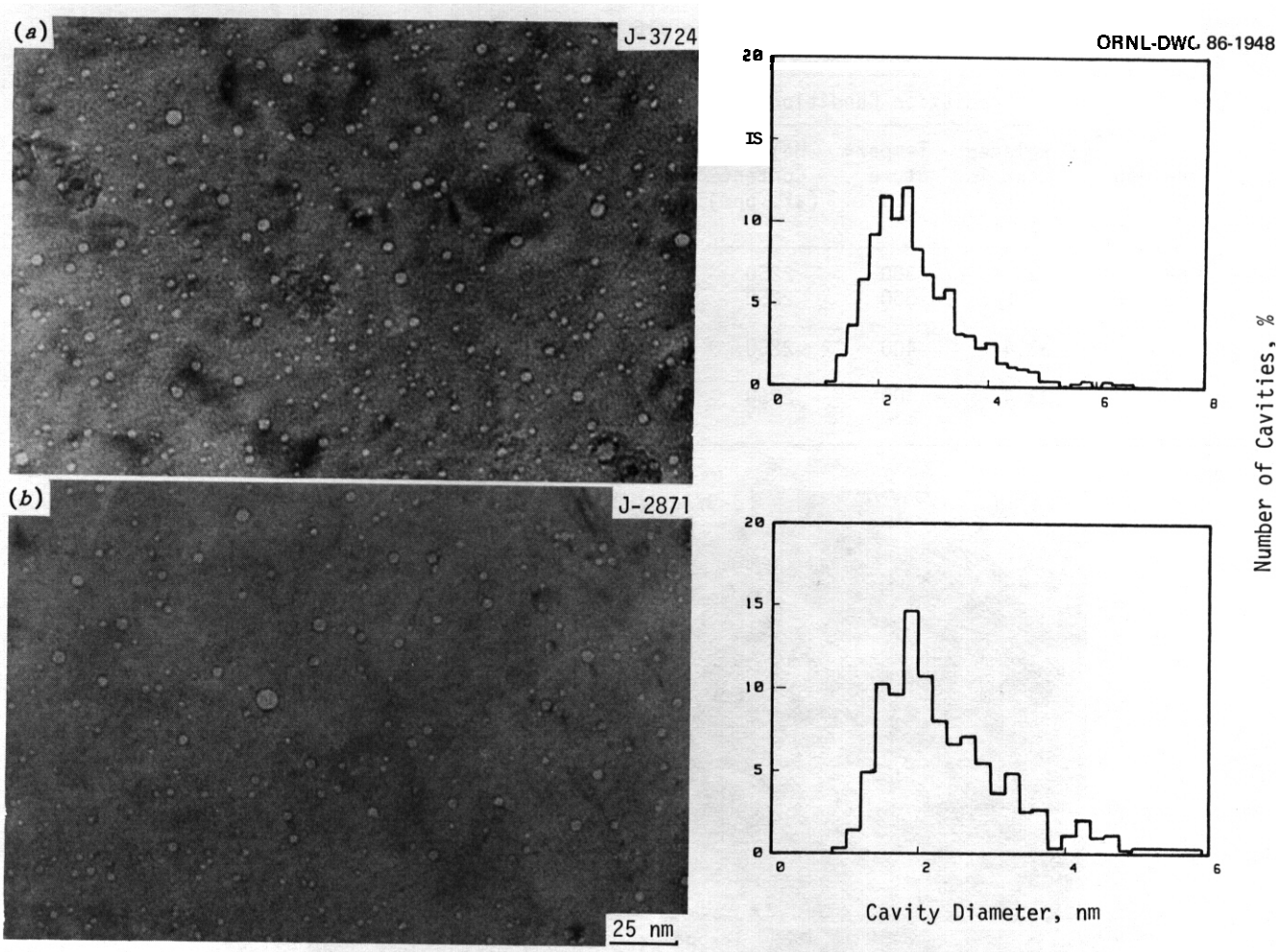

Fig. 3.5.2. Cavity microstructure observed in (*a*) SA and (*b*) 20% CW type 316 stainless steel after HFIR irradiation at 400°C to about 30 dpa. The cavity size distribution is given on the right side.

Table 3.5.2. Cavity data for type 316 stainless steel irradiated in HFIR

Specimen	Irradiation Conditions			Cavity Data			
	Displacement Damage (dpa)	Temperature (°C)	Helium Content (at. ppm)	Type	Average Diameter (nm)	Number Density (cavities/m³)	Cavity Volume Fraction (%)
SA	33.6	300	2250	Bubble	2.7	3.0×10^{23}	0.29
20% CW	33.6	300	2250	Bubble	2.5	3.5×10^{23}	0.28
SA	33.4	400	2250	Bubble (and void)	3.0	3.2×10^{23}	0.46
20% CW	33.4	400	2250	Bubble (and void)	2.7	4.6×10^{23}	0.48

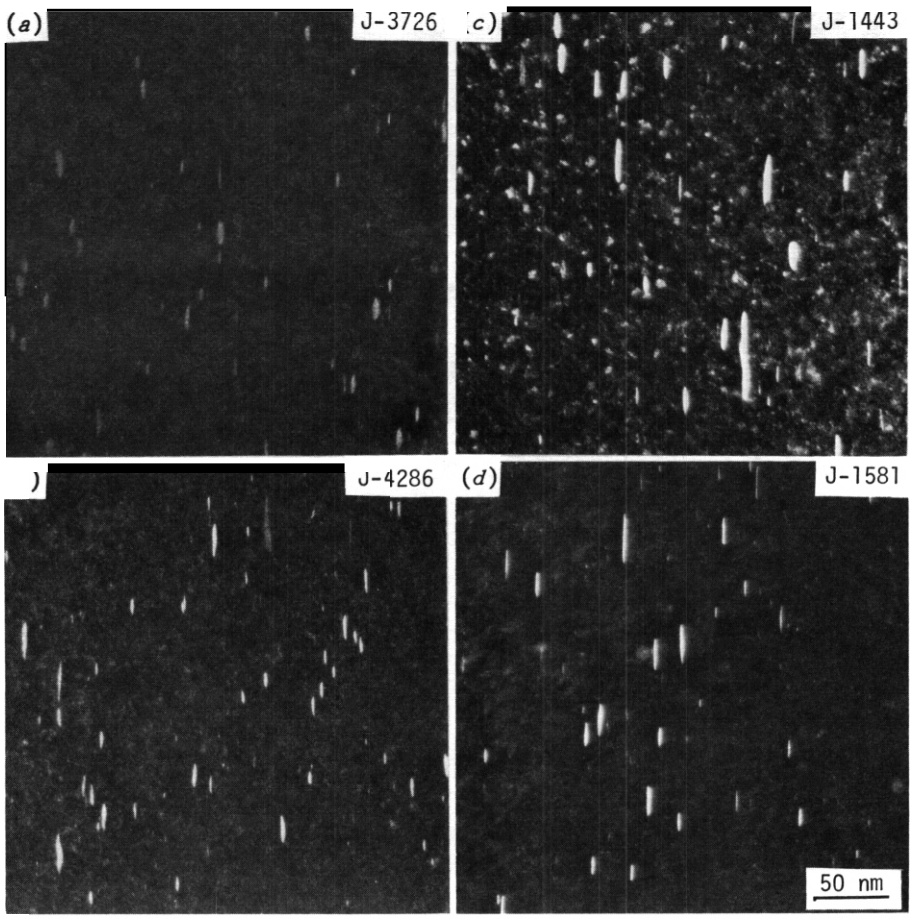

Fig. 3.5.3. Frank faulted loops observed in SA and 20% CW type 316 stainless steel irradiated in HFIR to about 30 dpa to about 2200 at. ppm He at irradiation temperature of 300°C (*a*) and (*b*), and 400°C (*c*) and (d).

results for the dislocation loops are given in Table 3.5.3. In general, the average diameter and the number density of Frank loops were larger at 400°C than at 300°C. The loops were larger in the SA compared to 20% CW material at 400°C, whereas there was no difference at 300°C.

Very few precipitates were observed in specimens irradiated at 300°C. Figures 3.5.4 through 3.5.6 show observations of fringes that suggest precipitates in SA (Figs. 3.5.4 and 3.5.5) and 20% CW (Fig. 3.5.6) specimens irradiated at 400°C within the grains of both materials. Some precipitates were also observed along the grain boundaries. The Moire fringes of these precipitates are perpendicular to the direction of the g vector, and their interval spacing would be consistent with tau ($M_{23}C_6$). Carbon extracted replicas will help to analyze the chemical compositions of these precipitates in the future. None of these precipitates appear associated with cavities. Gamma prime (Ni_3Si type) precipitates were not observed in any of the soecimens irradiated under these conditions.

Table 3.5.3. Frank faulted loop parameters for type 316 stainless steel irradiated in HFIR to ~33 dpa and 2250 at. ppm He

Specimen	Temperature (°C)	Average diameter (nm)	Number Density (loops/m³)
SA	300	10.3	1.3×10^{22}
20% CW	300	10.4	1.5×10^{22}
SA	400	16.0	2.5×10^{22}
20% CW	400	11.6	4.5×10^{22}

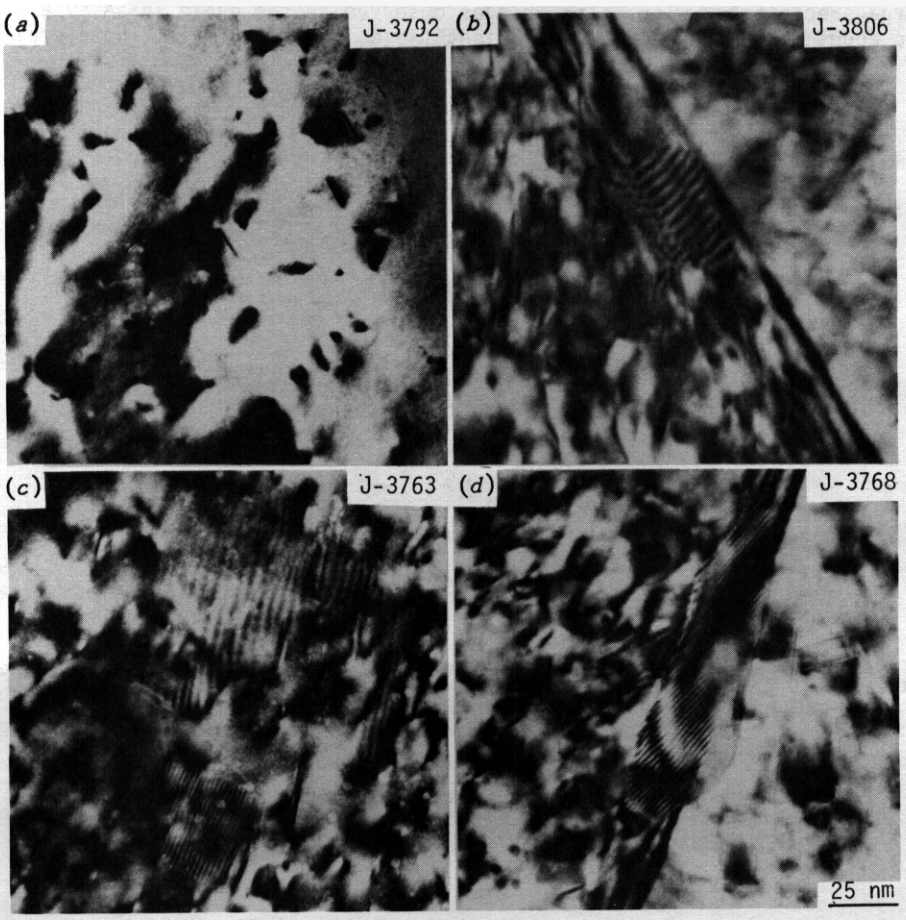

Fig. 3.5.4. Precipitates with Moiré fringe observed in SA type 316 stainless steel irradiated in HFIR to about 30 dpa at 400°C in the grain (*a*) and (*b*), and along the grain boundary (*c*) and (*d*).

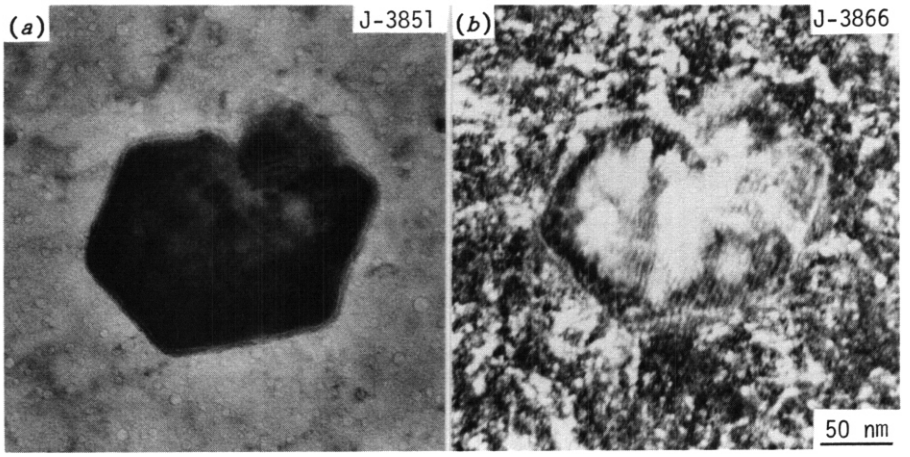

Fig. 3.5.5. Large precipitates with Moire fringes observed in the grain in SA type 316 stainless steel irradiated in HFIR to about 30 dpa at 400°C. (e) Bright field; (b) dark field. Note small fringes observed in the precipitate.

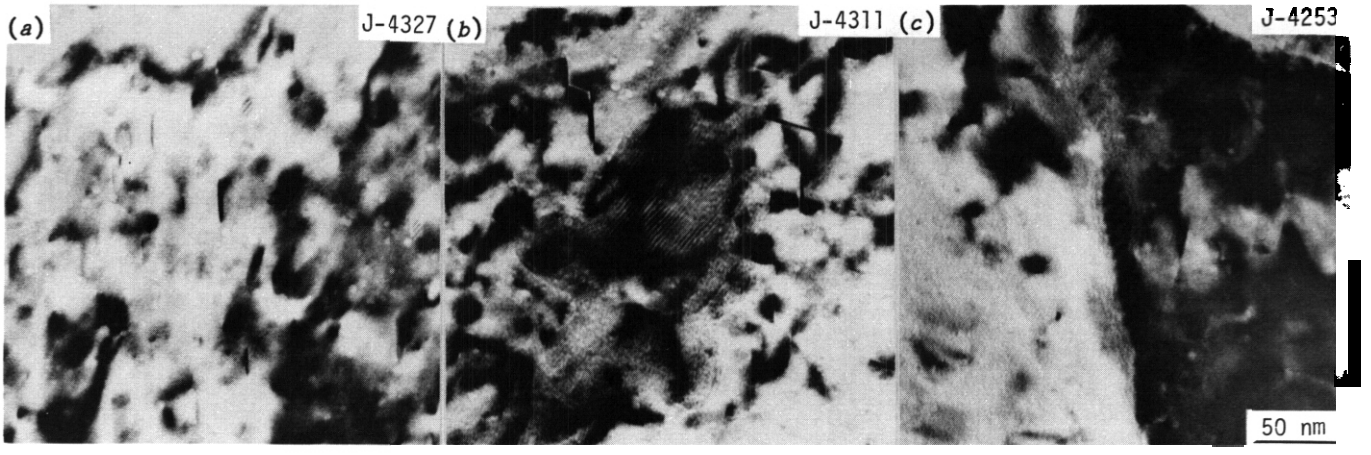

Fig. 3.5.6. Precipitates with Moiré fringes observed in 20% CW type 316 stainless steel irradiated in HFIR to about 30 dpa at 400°C in the grain (e) and (b), and along the grain boundary (c).

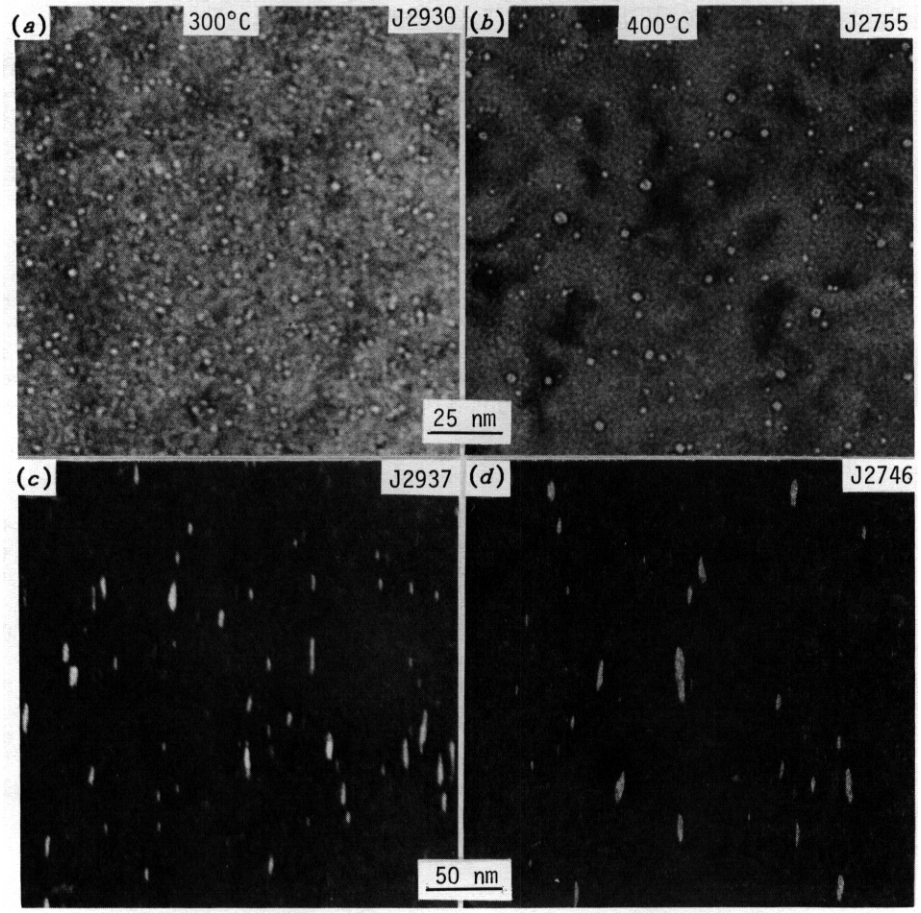

Fig. 3.5.7. Cavity and dislocation loop microstructure observed in the 20% CW (DO-heat) 316 irradiated in HFIR at 300 and 400°C to -33 dpa and -2250 at. ppm He.

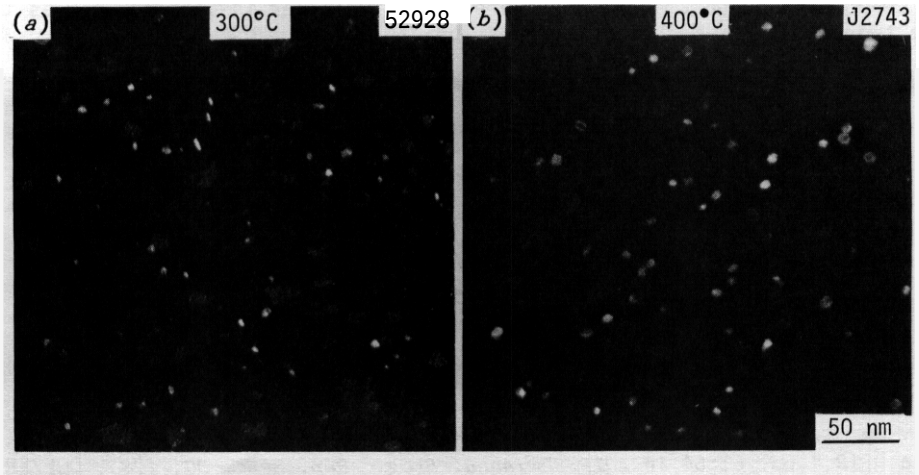

Fig. 3.5.8. Fine precipitates observed in the 20% CW (DO-heat) 316 irradiated in HFIR at 300 and 400°C to -33 dpa and -2250 at. ppm He.

B. Oualitative Comparison of 20% CW J316 and U.S. (DO-Heat) 316 Steel

A comparison of the U.S. 20% CW (DO-heat) 316 steel with the 20% CW Japanese heat of 316 stainless steel indicates qualitatively similar cavity and dislocation evolutions in HFIR at 300 and 400°C to –33 to 34 dpa and –2250 at. ppm He. Cavity and loop microstructures at 300 and 400°C can be seen for the 20% CW (DO-heat) 316 in Fig. 3.5.7 [cf. Figs. 3.5.1(*b*), 3.5.2(*b*), Fig. 3.5.3(*b*) and 3.5.3(*d*)]. The micrographs suggest that a slightly higher concentration of fine cavities exists in the Japanese 316 at 400°C, but the U.S. results remain to be quantified. Loop sizes appear similar between U.S. and Japanese 316s at both temperatures, but again it appears that there are less loops in the U.S. steel at 400°C.

Like the Japanese steel, the (DO-heat) 316 shows no evidence of I' at either 300 or 400°C. However, abundant fine precipitation was observed via dark-field imaging in the 20% CW (DO-heat) 316 at both temperatures, as shown in Fig. 3.5.8. Preliminary diffraction data do not suggest $M_{23}C_6$, but could be consistent with possibly G-phase, M_6C, or a vanadium-rich MC (HFIR irradiation produces vanadium via transmutations in all of these steels). Diffraction results do not indicate any simple or standard orientation relationship between matrix and precipitate planes, which would be consistent with very few displacement or rotational Moire fringes observed in the bright field. Such precipitation has not yet been observed in the Japanese steel, but further work is needed.

C. Discussion

From the standpoint of theoretical work on cavity evolution,[7,8] it appears that most of the samples observed here have cavity-sink-dominated microstructures, which makes the critical cavity size large and conversion of bubbles to voids difficult. Only at 400°C do the cavity microstructures hint at some cavities being supercritical in size. Data on 20% CW (N-lot) 316 reported by Maziasz and Braski' indicate a critical cavity size in HFIR at 600°C after –10 dpa that is consistent with that observed here at 400°C.

With regard to precipitation, I' has been observed in both SA and 20% CW (DO-heat) specimens irradiated in HFIR at 425 to 450°C after 9 to 14 dpa, but not at lower temperatures.[9,10] A review by Maziasz' of SA 316 data indicates that 1' is not observed at fluences less than –30 dpa or at temperatures below 400°C. Gamma prime is not observed in 20% CW (N-lot) 316 even after 44 dpa at 400°C in HFIR. Our data on the absence of 1' formation is therefore consistent with the data in the literature. However, the formation of fine precipitation at 300 and 400°C appears unusual compared to reported results for type 316 stainless steel irradiated in either EBR-II or HFIR.

3.5.5 Conclusions

1. Solution-annealed and 20% CW type 316 stainless steels have been irradiated up to 30 dpa and 2250 at. ppm He at 300 and 400°C in HFIR. Swelling was about 0.3% at 300°C and less than 0.5% at 400°C regardless of preirradiation treatment. In the 400°C irradiation', the cavities showed incipient splitting of sizes into a bimodal distribution.

2. At 300°C, there was not much difference in the average diameter and number density of Frank faulted loops in SA and 20% CW J316. At 400°C, the loops were slightly larger in SA 316, whereas the loop sizes were similar for the two conditions following irradiation at 300°C.

3. A low concentration of fine and large precipitates with Moire fringes was observed in the grain and along the grain boundary. No γ' precipitation was observed after HFIR irradiation at 300 and 400°C up to 30 dpa.

4. Cavity and loop evolution of the U.S. 20% CW (00-heat) 316 appears similar to 20% CW 5316 at 300 and 400°C in HFIR. Many fine precipitates were also found in the DO-heat 316. They do not appear to be γ' or $M_{23}C_6$, but could possibly be G, M_6C, or a vanadium-rich MC phase.

3.5.6 References

1. J. L. Scott and T. Kondo, "Introduction to U.S./Japan Collaborative Testing Program in HFIR and ORR," pp. 35–36 in *ADIP Semiannu.* Prog. *Rep. March 31, 1984,* DOE/ER-0045/12, U.S. DOE, Office of Fusion Energy.

2. S. Hamada, M. P. Tanaka, and P. J. Maziasz, "Microstructures of Type 316 Stainless Steel Irradiated to 30 dpa at 300°C in HFIR," pp. 61–64 in *ADIP Semiannu. Prog. Rep. Sept. 30, 1985,* DOE/ER-0045/15, U.S. DOE, Office of Fusion Energy.

3. P. R. Okamoto and S. D. Harkness, "Stress-Biased Loop Nucleation in Irradiated Type 316 Stainless Steel," *J. Nucl. Mater.* 48, (1973) 204–06.

4. G. R. Odette and M. W. Frei, "Potential Effects of Interactions Between Transmutants and Displaced Atoms in Controlled Thermonuclear Reactor First Wall," p. 485 in *Proc. First Topical Meeting on the Technology of Controlled Nuclear Fusion,* CONF-740402-P2 (August 1974).

5. G. R. Odette and C. S. Langley, "Modeling of Synergistic Effects of Displaced Atoms and Transmutant Damage in Fission and Fusion Environments," p. 395 in ***Radiation Effects and Tritium Technology for Fusion Reactors,*** CONF-750989, Vol. 1 (March 1976).

6. M. R. Hayns, "The Transition from Gas Bubbles to Void Growth," ***AERE Harwell Report,*** AERE-R8806 (May 1977).

7. L. K. Mansur and W. A. Coghlan, "Mechanisms of Helium Interaction with Radiation Effects in Metals and Alloys: A Review," ***J. Nucl. Mater.*** **119, (1983) 1-25.**

8. P. J. Maziasz and D. N. Braski, "Swelling of Path A PCA Irradiated to 10 dpa in HFIR," pp. 98-117 in ***ADIP Quart. Prog. Rep. March 31, 1982,*** DOE/ER-0045/8, U.S. DOE, Office of Fusion Energy.

9. P. J. Maziasz, "Effects of Helium Content on Microstructural Development in Type 316 Stainless Steel Under Neutron Irradiation," ORNL-6121, Oak Ridge National Laboratory (1985).

10. P. J. Maziasz and O. N. Braski, "Improved Swelling Resistance for PCA Austenitic Stainless Steel Under HFIR Irradiation Through Microstructural Control," ***J. Nucl. Mater.*** 122 and 123, (1984) 311-16.

4. HIGHER STRENGTH Fe-Ni-Cr ALLOYS

5. REACTIVE AND REFRACTORY ALLOYS

5.1 THE TENSILE PROPERTIES AND SWELLING OF SEVERAL VANADIUM ALLOYS AFTER IRRADIATION TO 40 dpa IN FFTF – D. N. Braski (Oak Ridge National Laboratory)

5.1.1 AOIP Task

ADIP Task I.B.15, Tensile Properties of Reactive and Refractory Alloys.

5.1.2 Objective

The goal of this research is to investigate the effects of displacement damage and helium generation on the properties of vanadium alloys.

5.1.3 Summary

The V-3Ti-1Si alloy exhibited better resistance to irradiation hardening and helium embrittlement than V-15Cr-5Ti or VANSTAR-7 after irradiation in the Fast Flux Test Facility (FFTF) to 40 dpa at 420, 520, and 600°C. All three alloys were low swelling except VANSTAR-7 which showed high swelling at 520°C. In all cases, the preimplanted helium enhanced swelling. The V-3Ti-1Si alloy clearly outperformed the other two alloys and should be investigated and developed further.

5.1.4 Progress and Status

5.1.4.1 Introduction

Specimens of V-15Cr-5Ti, VANSTAR-7, and V-3Ti-1Si were sealed in 'Li-filled TZM capsules and irradiated at 420, 520, and 600°C in the FFTF to 40 dpa. The effects of the irradiation and preimplanted helium on the tensile properties and microstructure of the alloys were evaluated.

5.1.4.2 Experimental

The source, heat number, chemistry, and final annealing treatment for each of the vanadium alloys are given in Table 5.1.1. Disks (3-mm in diameter) and miniature tensile specimens (SS-3 type) were sealed in 'Li-filled TZM capsules and irradiated at 420, 520, and 600°C in FFTF to 40 dpa. Some of the specimens were

Table 5.1.1. Vanadium alloy data

Alloy	Heat	Composition, wt %								Final Heat Treatment	^{3}He Content[c] (appm)
		Cr	Ti	Fe	Zr	Si	C	O	N		
V-15Cr-5Ti[a]	CAM-834-3	14.5	6.2				0.032	0.031	0.046	1 h Q 1200°C	74
VANSTAR-78	CAM-837-7	9.7		3.4	1.3		0.064	0.028	0.052	1 h Q 1350°C	70
V-3Ti-1Si[b]	11153		3.4	0.04		1.28	0.045	0.091	0.026	1 h Q 1050°C	82

[a]Source: Westinghouse Electric Corporation

[b]Source: KFK, Karlsruhe, West Germany (Dr. D. Kaletta)

[c]Analyses performed by Dr. B. M. Oliver, Rockwell International Corporation, Canoga Park, CA.

preimplanted with ~80 appm 'He using the "tritium trick" technique.' The actual amount of 'He measured in each alloy is given in Table 5.1.1. An equal number of vanadium alloy specimens were encapsulated in similar fashion and thermally aged at the respective irradiation temperatures for 257 days; these specimens served as control specimens. Both irradiated and control tensile specimens were tested under vacuum ($<10^{-4}$ Pa) at the irradiation/aging temperature in a tensile machine located in a hot cell. After testing, the fracture surfaces were examined using a scanning electron microscope (SEM) which was also located in a hot cell.[2] Microstructural details were studied by transmission electron microscopy (TEM) using disks that were jet-polished at −30°C in a solution of 12½ vol % conc. H_2SO_4 in methanol.

5.1.4.3 Results and Discussion

The results of the tensile tests of vanadium alloy starting material, controls, and irradiated specimens are listed in Tables 5.1.2, 5.1.3, and 5.1.4, respectively. With only one exception, the thermally-aged control specimens exhibited tensile behavior similar to the starting material. This result establishes

Table 5.1.2. Results of tensile tests of vanadium alloys in the as-annealed condition (starting material)

Alloy	1-h anneal Temperature (°C)	Test Temperature (°C)	Strength, MPa		Elongation, %	
			Yield	Ultimate Tensile	Uniform	Total
V-15Cr-5Ti	1200	420	392	517	17.1	28.2
V-15Cr-5Ti	1200	420	370	504	15.2	24.3
V-15Cr-5Ti	1200	520	334	513	13.5	23.3
V-15Cr-5Ti	1200	520	353	514	14.3	25.9
V-15Cr-5Ti	1200	600	323	521	13.6	22.0
V-15Cr-5Ti	1200	600	317	557	12.6	20.5
VANSTAR-7	1350	420	278	443	15.0	23.7
VANSTAR-7	1350	520	276	442	13.3	24.7
VANSTAR-7	1350	600	277	521	14.5	22.3
V-3Ti-1Si	1050	420	335	470	14.0	21.0
V-3Ti-1Si	1050	520	290	527	15.0	21.0
V-3Ti-1Si	1050	600	320	504	15.5	23.6

Table 5.1.3. Results of tensile tests of vanadium control specimens aged 257 days in 'Li

Specimen Number	Alloy	Helium Level (appm)	Aging/Test Temperature (°C)	Strength, MPa		Elongation, %	
				Yield	Ultimate Tensile	Uniform	Total
RD40	V-15Cr-5Ti	0	420	399	545	15.0	26.0
RD66	V-15Cr-5Ti	74	420	381	540	14.3	23.7
RA187	V-15Cr-5Ti	74	420	369	539	14.0	21.3
RD38	V-15Cr-5Ti	0	520	387	539	15.3	24.3
RA73	V-15Cr-5Ti	74	520	352	511	12.7	20.7
RA170	V-15Cr-5Ti	74	520	381	578	13.0	20.7
RD03	V-15Cr-5Ti	0	600	390	555	12.3	21.7
RA129	V-15Cr-5Ti	74	600	390	573	11.3	19.0
RA176	V-15Cr-5Ti	74	600	377	574	10.3	17.7
QA71	VANSTAR-7	0	420	256	398	16.0	26.3
QA73	VANSTAR-7	70	420	312	451	14.7	23.7
QA110	VANSTAR-7	70	420	302	448	12.7	22.3
QA08	VANSTAR-7	0	520	282	469	15.7	23.7
QA118	VANSTAR-7	70	520	283	469	13.0	20.7
QA119	VANSTAR-7	70	520	297	480	11.7	20.7
QA69	VANSTAR-7	0	600	298	490	12.3	20.0
QA80	VANSTAR-7	70	600	274	482	13.0	20.3
QA102	VANSTAR-7	70	600	261	473	14.0	22.0
RC54	V-3Ti-1Si	0	420	378	473	14.0	21.0
RC08	V-3Ti-1Si	82	420	444	550	10.7	17.3
RC42	V-3Ti-1Si	82	420	430	542	12.3	19.0
RC30	V-3Ti-1Si	0	520	454	595	11.0	20.0
RC33	V-3Ti-1Si	82	520	452	587	10.0	14.3
RC44	V-3Ti-1Si	82	520	446	570	14.0	20.0
RC55	V-3Ti-1Si	0	600	315	467	8.0	12.3
RC23	V-3Ti-1Si	82	600	300	495	13.3	20.0
RC57	V-3Ti-1Si	82	600	290	498	14.0	20.3

Table 5.1.4. Results of tensile tests and void swelling measurements for vanadium alloys irradiated to 40 dpa in FFTF (MOTA)

Specimen Number	Alloy	Helium Level (appm)	Irradiation/ Test Temperature (°C)	Strength, MPa		Elongation, %		Disk Number	ΔV/V (%)
				Yield	Ultimate Tensile	Uniform	Total		
RD14	V-15Cr-5Ti	0	420	825	913	0.8	0.8	RD18	0.003
RD64	V-15Cr-5Ti	74	420	--	793	0	0	RD52	0.005
RA34	V-15Cr-5Ti	74	420	692	834	0.8	0.8		
RD37	V-15Cr-5Ti	0	520	879	989	3.0	9.5	RD65	0.031
RA20	V-15Cr-5Ti	74	520	882	1003	1.8	1.8	RD38	0.046
RA108	V-15Cr-5Ti	74	520	868	956	1.5	1.7		
RD30	V-15Cr-5Ti	0	600	674	797	4.5	11.9	RD21	0.024
RA68	V-15Cr-5Ti	74	600	Broke during loading			--	RD16	0.283
RA139	V-15Cr-5Ti	74	600	Broke during loading			--		
QA19	VANSTAR-7	0	420	881	896	0.7	6.8	QB55	0.001
QA40	VANSTAR-7	70	420	978	997	0.9	6.0	QB38	0.004
QA71	VANSTAR-7	70	420	987	1002	0.6	5.7		
QA29	VANSTAR-7	0	520	1058	1138	1.5	4.0	QB60	0.958
QA87	VANSTAR-7	70	520	960	1016	1.3	1.3	QB39	5.940
QA91	VANSTAR-7	70	520	Failed at hole in shoulder					
QA53	VANSTAR-7	0	600	360	429	2.8	5.5	9857	0.014
QA83	VANSTAR-7	70	600	651	755	3.2	4.5	QB40	0.065
QA90	VANSTAR-7	70	600	722	790	3.5	5.2		
RC34	V-3Ti-1Si	0	420	692	780	3.4	4.8	RC40	0.079
RC35	V-3Ti-1Si	82	420	795	884	3.8	6.0	RC18	0.090
RC53	V-3Ti-1Si	82	420	717	880	6.3	11.8		
RC17	V-3Ti-1Si	0	520	541	682	8.2	13.3	Disk lost	
RC11	V-3Ti-1Si	82	520	632	758	6.3	10.3	RC15	0.002
RC29	V-3Ti-1Si	82	520	565	688	6.0	10.9		
RC27	V-3Ti-1Si	0	600	378	564	8.1	12.1	R12	0
RC41	V-3Ti-1Si	82	600	276	480	7.8	11.3	RC11	0.052
RC43	V-3Ti-1Si	82	600	369	583	8.8	12.3		

the technique of irradiating the vanadium alloys in lithium as a viable one, i.e., the exposure to lithium did not affect the tensile properties. The only exception was one aged V-3Ti-1Si specimen (0-He) tested at 600°C (Table 5.1.3). This was obviously a bad specimen because the two specimens with 82 appm tested at the same temperature had substantially higher elongations.

Neutron irradiation created defects in the microstructure of the vanadium alloys that impede the motion of dislocations and harden the material. Such hardening is evident in electron micrographs of the irradiated microstructure and in the increases in yield strength and accompanying ductility losses after irradiation (cf. Tables 5.1.2 and 5.1.3 with 5.1.4 for respective alloys), The VANSTAR-7 alloy was the most susceptible to irradiation hardening followed by V-15Cr-5Ti and V-3Ti-1Si (for more details, see ref. 3). Irradiation hardening was generally greater at 420°C for all three alloys, and decreased with increasing temperature. At 420°C, the hardening caused a V-15Cr-5Ti specimen to fail in a brittle cleavage mode at low elongation, as shown in Fig. 5.1.1.

In a fusion reactor, helium will be produced by the energetic neutrons; this helium production is simulated for experiments using a fission reactor by preimplanting helium. The helium, in turn, can form bubbles in the grain boundaries thereby weakening them and embrittling the material. Helium embrittlement affected the V-15Cr-5Ti, in particular, but had little or no effect on the other two alloys. The embrittlement is revealed by the drastic reductions in elongation from the unimplanted to the helium-implanted specimens, especially at the higher temperatures, as shown in Table 5.1.4 for V-15Cr-5Ti. The fracture mode characteristic of this type of embrittlement is intergranular separation, as shown in Fig. 5.1.2 for V-15Cr-5Ti containing 74 appm He.

Irradiation hardening and helium embrittlement may act together in reducing the ductility of a specimen and the relative contribution from each may be estimated by examination of the fracture surface. Figure 5.1.3 shows the fractograph for a V-15Cr-5Ti specimen containing 74 appm He that was irradiated and tested at 420°C. The effects of both mechanisms is seen – cleavage due to irradiation hardening and intergranular separation caused by helium embrittlement. The author believes that helium embrittlement is influenced by irradiation hardening in a manner similar to that suggested for irradiated high-strength Fe-Ni-Cr alloys.' The overall ductility of the specimen depends on the combined strengths of the grain matrices and the grain boundaries. However, hardening or strengthening of the matrices due to irradiation will accentuate the effects of any weaknesses in the boundaries and promote intergranular separation.

N230

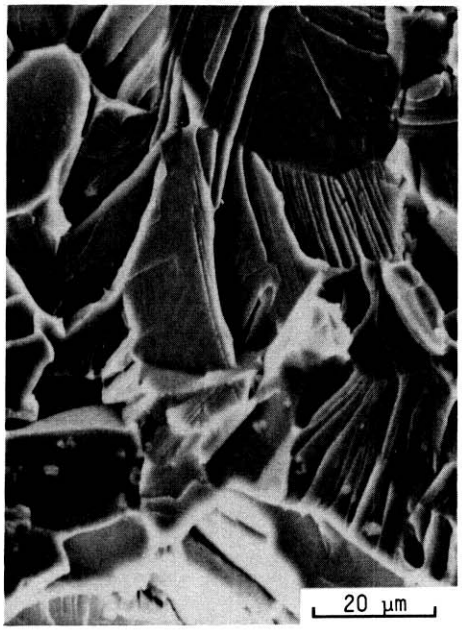

Fig. 5.1.1. Brittle cleavage fracture surface of V-15Cr-5Ti specimen, without preimplanted helium, after irradiation to 40 dpa at 420°C and tensile testing at 420°C.

N243

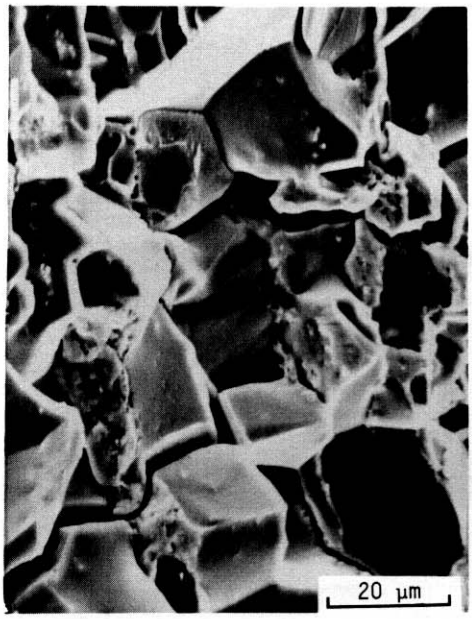

Fig. 5.1.2. Brittle intergranular fracture surface of V-15Cr-5Ti specimen, containing 300 appm He, after irradiation to 10 dpa at 420°C and tensile testing at 420°C.

N225

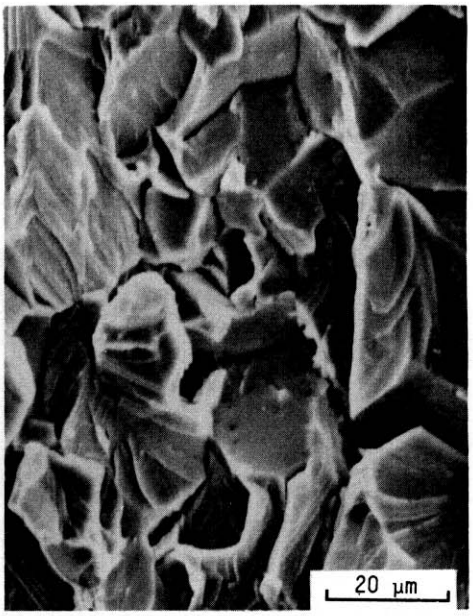

Fig. 5.1.3. Mixed cleavage and intergranular fracture of V-15Cr-5Ti, containing 74 appm He, after irradiation to 40 dpa at 410°C and tensile testing at 420°C.

Another effect of neutron irradiation on the materials is the creation of small cavities in the microstructure. The three vanadium alloys were, in general, quite low swelling as shown by the values listed in Table 5.1.4 for each specimen. Only the VANSTAR-7 alloy irradiated at 520°C showed significant swelling. The author speculates that zirconium (present in VANSTAR-7) may not be as effective as titanium in suppressing cavity formation. In every instance, the presence of helium enhanced swelling. Although this last observation may apply to true fusion reactor conditions in some general way, the reader is reminded that the continued production of helium (not all preimplanted from the start) may alter the amount of swelling produced compared to the present results.

The V-3Ti-1Si alloy outperformed both the V-15Cr-5Ti and VANSTAR-7, having better resistance to irradiation hardening and helium embrittlement, while maintaining good resistance to swelling. Therefore, it should be investigated further with development aimed at further improvement of irradiation resistance as well as other important properties such as corrosion and creep resistance.

5.1.5 Conclusions

1. The V-3Ti-1Si alloy had better resistance to irradiation hardening and helium embrittlement than V-15Cr-5Ti or VANSTAR-7.

2. All three vanadium alloys demonstrated low swelling under all test conditions except VANSTAR-7 which exhibited high swelling at 520°C. The preimplanted helium enhanced swelling.

3. The V-3Ti-1Si alloy clearly outperformed V-15Cr-5Ti and VANSTAR-7 and should be investigated and developed further.

5.1.6 References

1. D. N. Braski and D. W. Ramey, "A Modified Tritium Trick Technique for Doping Vanadium Alloys with Helium," in: *Effects of Radiation on Materials: Twelfth International Symposium,* ASTM STP **870**, pp. 1211–24, F. A. Garner and J. S. Perrin, eds., American Society for Testing and Materials, Philadelphia, 1985.

2. J. R. Gibson and D. N. Braski, *Scanning Electron Microscope Facility for Examination of Radioactive Materials*, ORNL/TM 9451 (February 1985).

3. D. N. Braski, "The Effect of Neutron Irradiation on the Tensile Properties and Microstructure of Several Vanadium Alloys," to be presented at 13th Int. Symp. on Effects of Radiation on Materials, Seattle, WA, June 23–25, 1986 and to be published in ASTM STP.

4. W.J.S. Yang and M. L. Hamilton, "The Ductility Behavior of Irradiated Path B Alloys," pp. 90–119. in *ADIP Semiannu. Prog. Rep. Sept. 30, 1982,* DOE/ER-0045/9, Office of Fusion Energy.

5.2 MICROSTRUCTURAL EVOLUTION AND COMPUTED YIELD STRESS INCREASE FOR ION-IRRADIATED V-15Cr-5Ti ALLOY -

B. A. Loomis and H. J. Kestel (Argonne National Laboratory)

5.2.1 ADIP Task

ADIP Task I.A.I. Define Material Property Requirements and Make Structural Life Predictions.

5.2.2 Objective

The objective of this work is to provide guidance on the applicability of vanadium-base alloys for structural components in a fusion reactor.

5.2.3 Sumnary

The effect of 4-MeV $^{58}Ni^{++}$ ion irradiation on the microstructure of the V-15Cr-5Ti alloy was determined for irradiation temperatures ranging fran 550°C to 750°C and for damage levels of 50 to 260 dpa. The swelling of the alloy that could be attributed to voids was negligible (< 0.1%). The principle effect of the irradiation was to induce the formation of disc-shape precipitates in the alloy microstructure. The increase of the yield stress for the alloy resulting from the irradiations was evaluated from the irradiation-produced dislocation density and the number density and size of irradiation-produced precipitates. These evaluations showed that the increase of yield stress for the alloy on irradiation has a maximum value at ~50 dpa, and the increase of yield stress decreases for irradiation temperatures above 600°C.

5.2.4 Progress and Status

5.2.4.1 Introduction

The V-15Cr-5Ti alloy is considered to be a candidate alloy for structural components in a magnetic fusion reactor (MFR). The production of displacement damage in the alloy during the reactor lifetime will have a significant influence on the alloy microstructure and, therefore, on the mechanical properties of the structural components. Observations of the microstructure in the V-15Cr-5Ti alloy after neutron or ion irradiation for damage levels up to 300 dpa have shown a remarkable absence of voids and the presence of irradiation-produced precipitates.[1-5] In this report, we show the evolution of the microstructure in the V-15Cr-5Ti alloy following 4.0-MeV $^{58}Ni^{++}$ ion irradiation at temperatures ranging from 550°C to 750°C and for damage levels of 50 to 260 dpa.

An increase in yield stress for the irradiated alloy can be expected due to the interaction of gliding dislocations with (1) small dislocation loops and black spot clusters, (2) large dislocation loops and networks, (3) voids, (4) gas-filled cavities, and (5) precipitates.[d] In this report, we also present the results of evaluations on the increase of yield stress for the alloy on ion irradiation. These evaluations are derived from determinations of the radiation-produced dislocation density and precipitate size and number density in the ion-irradiated V-15Cr-5Ti alloy.

5.2.4.2 Materials and Procedure

The V-15Cr-5Ti alloy was supplied in the form of 0.81-mn thick sheet from the Fusion Program Research Materials Inventory (melt number 834-6) at Oak Ridge National Laboratory. The chemical analysis for this material is presented in Table 5.2.1. The as-received sheet was reduced in thickness to 0.25 mm and annealed at 1125°C for one hour in a system evacuated to 6.7 x 10^{-7} Pa.

Specimens of the alloy, each with a diameter of 3.05 mn, were mounted in a tungsten holder for single-ion irradiation with 4.0-MeV $^{58}Ni^{++}$ ions. The irradiations of the specimens at temperatures ranging from 550°C to 750°C were conducted in a cryogenically pumped chamber evacuated to 1.3 x 10^{-6} Pa. The chamber was connected by a cryogenically pumped, ion-beam transport tube to the 2-MeV Tandem accelerator at Argonne National Laboratory. Following irradiation, the specimens were sectioned from the irradiated surface to a depth of 1050 nm, then thinned from the backside to perforation in an 80% CH_3OH-20% H_2SO_4 solution at ~5°C. Deposited energy densities as a function of ion range in the alloy from a

Table 5.2.1. Chemical Analysis of the V-15Cr-5Ti Alloy

Element	Concentration (a/o)
Cr	14.1
Ti	6.6
C	0.14
O	0.10
N	0.18

computerized TRIM code were converted to displacements per atom (dpa). The depth in the V-15Cr-5Ti alloy for peak irradiation damage during 4.0-MeV $^{58}Ni^{++}$ ion irradiation was computed to be 1150 nm. The specimens were irradiated to displacement damage levels of 50-260 dpa at a damage rate of ~5 x 10^{-3} dpals.

The microstructure of the unirradiated and irradiated alloy were observed by transmission electron microscopy (TEM) in a Philips EM 400T electron microscope operated at 120 keV. The thickness of the specimen for TEM was typically 80 nm.

5.2.4.3 Experimental Results

TEM for the alloy

The microstructure for the unirradiated V-15Cr-5Ti alloy is shown in Fig. 5.2.1. This microstructure was characterized by the presence of precipitates with diameters ranging from 2 to 6 μm and a number density of 3.6 x 10^{19} m^{-3}. The annealed, unirradiated material had an average grain diameter of 40 μm and contained ~10^{13} dislocations/m^2.

The dependence of the microstructural evolution in the irradiated alloy on the temperature of irradiation for a damage level of ~200 dpa is shown in Fig. 5.2.2. The dependence of the microstructural evolution in the alloy on the level of irradiation damage for an irradiation temperature of ~715°C is shown in Fig. 5.2.3. The dislocation density, precipitate number density and precipitate average diameter in the irradiated alloy are listed in Table 5.2.2. The dislocation density was determined from the equation

$$\rho_{dis} = 2NMF/Lt \qquad (1)$$

where N is the number of dislocations intersecting a line of length L, M is the magnification, F is a factor which allows for those dislocations out of contrast, and t is the dislocation layer thickness. The dislocation density, ρ_{dis}, in the alloy decreased significantly for irradiation temperatures above 600°C and for damage levels in excess of 50 dpa. The precipitate diameter, d_{ppt}, in the irradiated alloy increased on increasing the irradiation temperature above 625°C with a corresponding decrease in the precipitate number density, N_{ppt}.

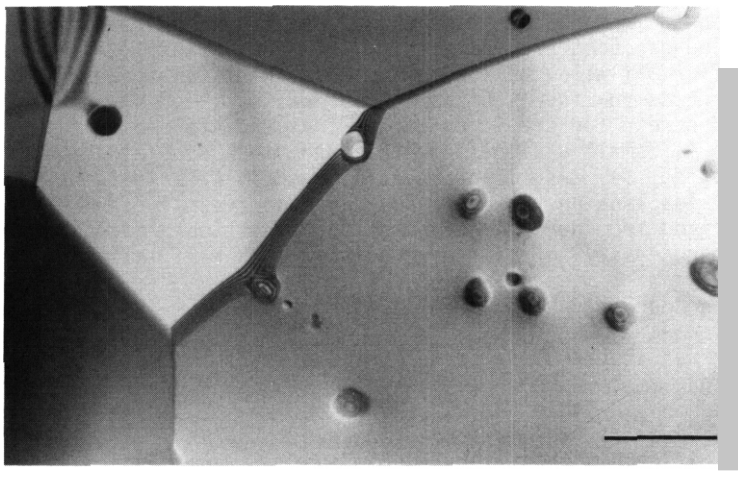

Fig. 5.2.1 . Microstructure of unirradiated V-15Cr-5Ti alloy (marker = 1.6 μm)

Increase of yield stress

The increase in yield stress for the ion-irradiated V-15Cr-5Ti alloy was evaluated by use of the equation

$$\Delta\tau_{total} = \alpha_p \mu b\sqrt{\rho} + \beta_p \mu b\sqrt{N_p d_p} \qquad (2)$$

In Eq. (2), a and β_p are the interaction parameters between gliding dislocations and forest dislocations and precipitates, respectively. For the purpose of this paper we shall use α_p = 0.5 and β_p = 0.2.[6] Also, in Eq. (2) μ is the shear modulus and b is the Burgers-vector for vanadium with values of 4.67 x 10^4 MPa and 0.26 nm, respectively.[6] Contributions to the increase in yield stress from loops, voids, and cavities are not included in Eq. (2) since these defect clusters were not visible in the microstructures. The results of computations of the increase in yield stress for the irradiated V-15Cr-5Ti alloy using Eq. (2) and the data in Table 5.2.2 are shown in Figs. 5.2.4 and 5.2.5 and are also tabulated in Table 5.2.2. These computations show that the increase of yield stress for the V-15Cr-5Ti alloy on irradiation has a maximum value at ~50 dpa, and the increase of yield stress decreases for irradiation temperatures above 600°C.

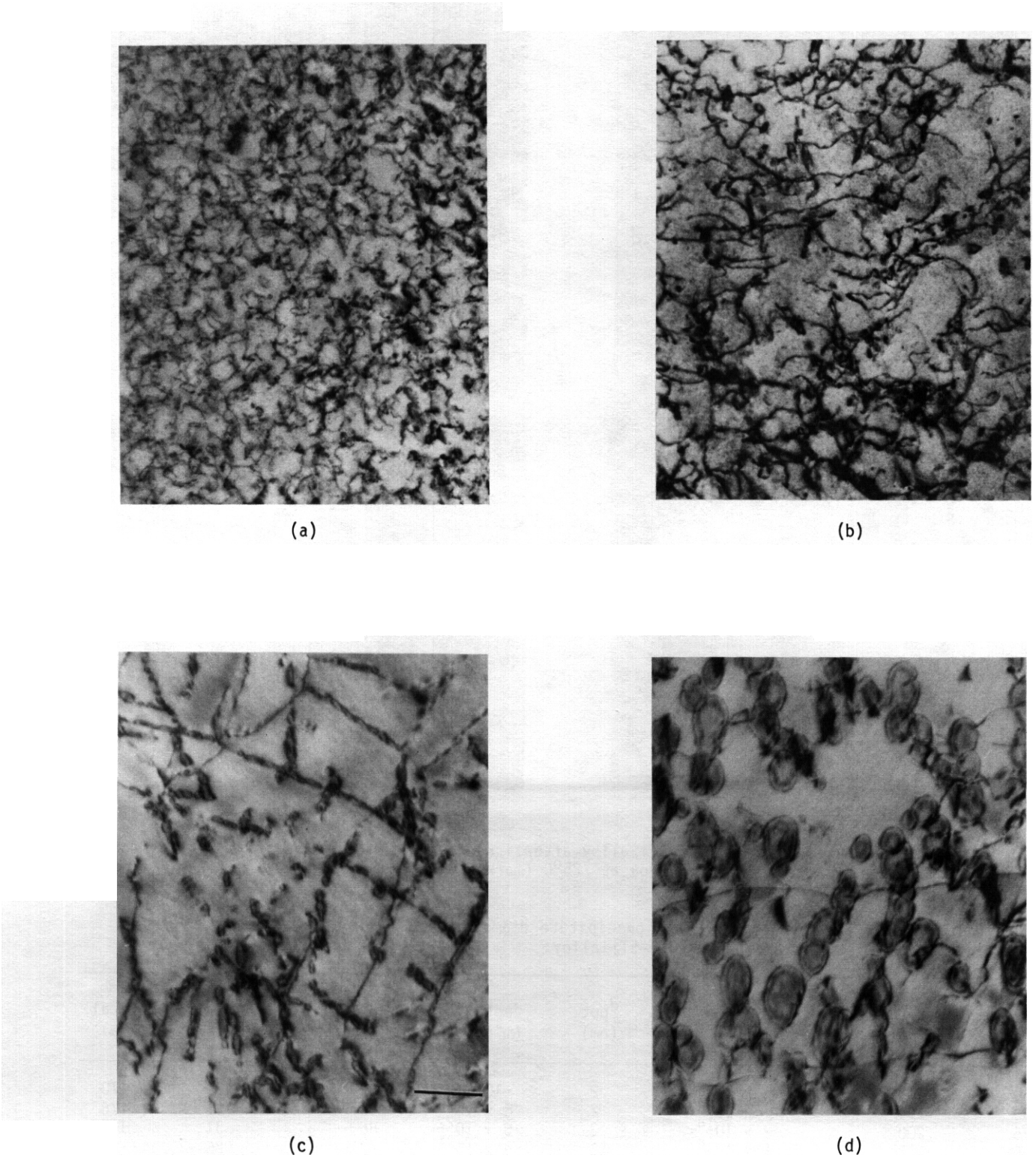

Fig. 5.2.2. Microstructures of the V-15Cr-5Ti alloy after irradiation to: 203 dpa at 550°C (a), 194 dpa at 600°C (b), 203 dpa at 714°C (c), and 200 dpa at 750°C (d) (marker = 200 nm).

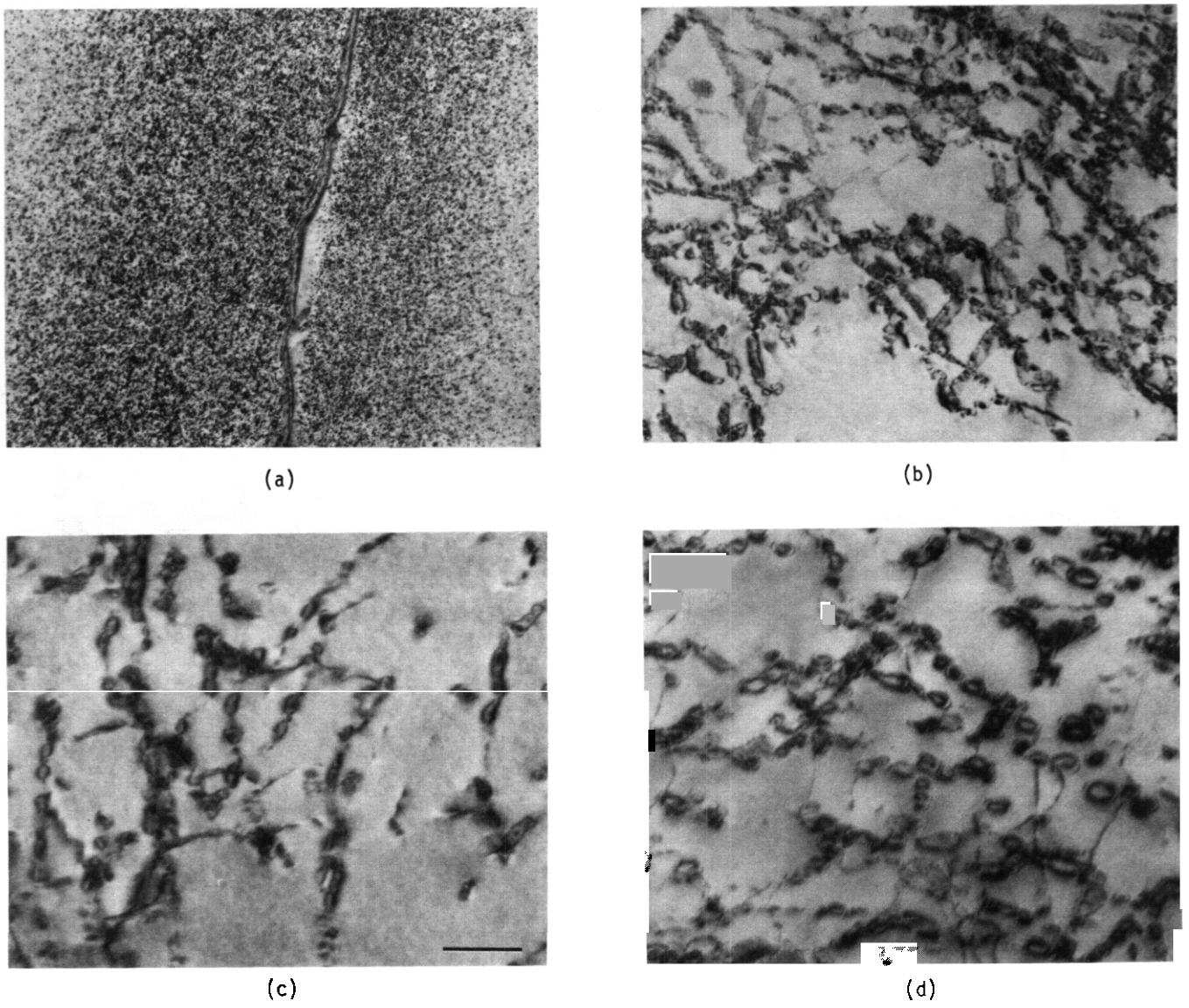

Fig. 5.2.3. Microstructures of the V-15Cr-5Ti alloy after irradiation to: 50 dpa at 725°C (a), 125 dpa at 714°C (b), 203 dpa at 714°C (c), and 260 dpa at 725°C (marker = 200 nm).

Table 5.2.2. Dislocation density, precipitate diameter and density, and yield stress increment for ion-irradiated V-15Cr-5Ti alloy.

Temperature (°C)	Damage (dpa)	ρ_{dis} (m^{-2})	d_{ppt} (nm)	N_{ppt} (m^{-3})	$\Delta\tau_{dis}$ (MPa)	$\Delta\tau_{ppt}$ (MPa)	$\Delta\tau_{Total}$ (MPa)
550	203	5×10^{14}	2	$\sim 10^{23}$	139	31	170
600	194	6×10^{14}	2	8×10^{22}	145	31	176
625	200	2×10^{14}	2	8×10^{22}	86	31	117
650	195	1×10^{14}	12	9×10^{21}	72	26	98
714	203	1×10^{14}	25	2×10^{21}	72	17	89
7sp	200	1×10^{14}	79	8×10^{20}	72	19	91
725	50	5×10^{14}	3	7×10^{22}	137	31	174
714	125	3×10^{14}	23	5×10^{21}	98	27	125
714	203	1×10^{14}	25	2×10^{21}	72	17	89
725	260	2×10^{14}	35	2×10^{21}	77	21	98

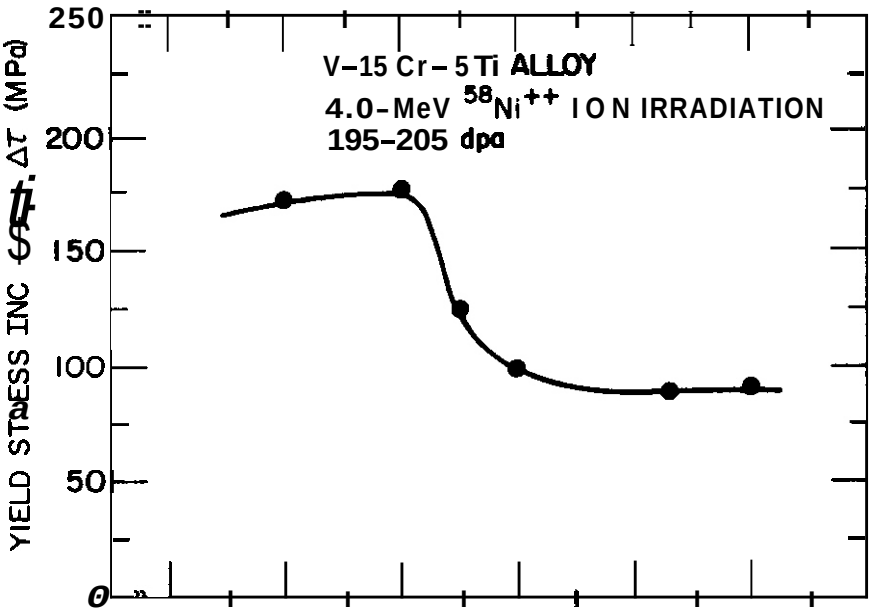

Fig. 5.2.4. Temperature dependence of the yield stress increase for the V-15Cr-5Ti alloy on 4.0-MeV $^{58}Ni^{++}$ ion irradiation to 195-205 dpa.

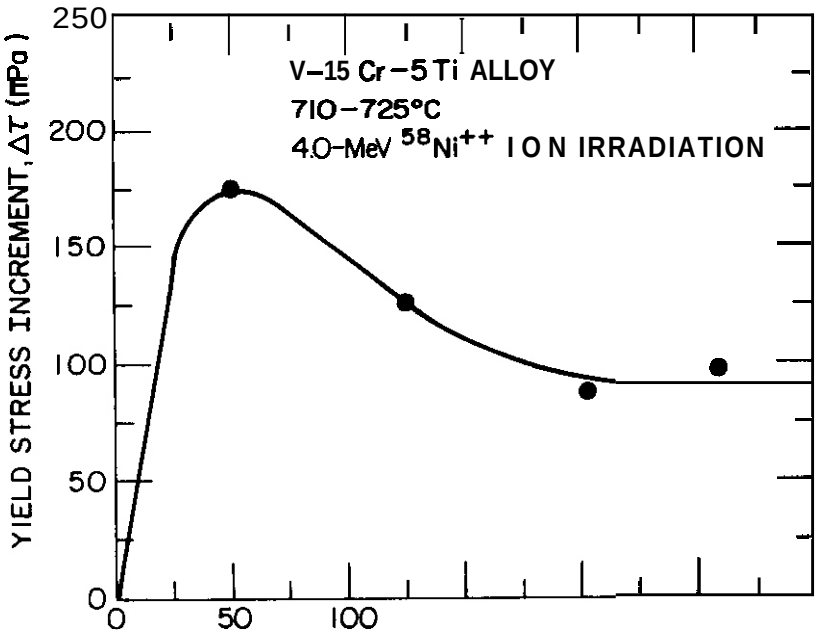

Fig. 5.2.5. Oependence of the yield stress increase on damage level for the V-15Cr-5Ti alloy irradiated at 710-725°C with 4.0-MeV $^{58}Ni^{++}$ ions.

5.2.5. Oiscussion

Swelling of the V-15Cr-5Ti on 4.0-MeV $^{58}Ni^{++}$ ion irradiation at temperatures ranging from 550°C to 750°C and to damage levels ranging fran 50 dpa to 260 dpa was negligible. Thus, these results together with previous results on the simultaneous ion irradiation and implantation of helium[5] suggest that swelling of the V-15Cr-5Ti alloy should not be a concern in a MFR. However, the formation of the irradiation-produced precipitates and dislocation network may result in embrittlement of the alloy.

Grossbeck and Horak have reported that the yield stress of the V-15Cr-5Ti alloy increased approximately 350 MPa on irradiation at 625 and 700°C to ~30 dpa in the EBR-II reactor.[4] Braski has reported that the yield stress of the alloy increased 492 MPa on irradiation at 520°C to 40 dpa and 284 MPa on irradiation at 600°C to 40 dpa in the FFTF reactor.[3] The ductility of the alloy after irradiation in EBR-II was very limited (< 1% uniform elongation)[4], whereas the alloy after irradiation in the FFTF showed 3-5% uniform elongation in tensile tests.[3] In the present study, the computed increase in the yield stress of the alloy on ion irradiation at ~725°C to 50 dpa was ~175 MPa. However, it is expected that the computed value for the increase of yield stress will increase with the use of more accurate parameters for F in Eq. (1) and α_p and β_p in Eq. (2). Nevertheless, the experimental results obtained in this study suggest that the potential for embrittlement of the V-15Cr-5Ti alloy will be highest for damage levels of ~50 dpa and irradiation temperatures of less than 650°C.

5.2.6. Conclusions

1. Swelling of the V-15Cr-5Ti alloy on 4-MeV $^{58}Ni^{++}$ ion irradiation at temperatures ranging from 550°C to 750°C and damage levels of up to 260 dpa is negligible.
2. The principle effect of ion irradiation is to induce the formation of disc-shape precipitates.
3. The formation of precipitates and dislocation networks results in an increase of the yield stress for the irradiated alloy.
4. The increase of yield stress for the alloy on irradiation has a maximum value at ~50 dpa.
5. The increase of yield stress decreases for irradiation temperature above 600°C.

5.2.7. References

1. R. Carlander, S. D. Harkness, and A. T. Santhanam, "Effects of Fast-Neutron Irradiation on Tensile Properties and Swelling Behavior of Vanadium Alloys", pp. 399-414 in Effects of Radiation on Substructure and Mechanical Properties of Metals and Alloys, ASTM-STP-529, American Society for Testing and Materials, 1973.
2. A. F. Bartlett, J. H. Evans, B. L. Eyre, E. A. Terry, and T. M. Williams, "High Temperature Irradiation Damage Structures in Fast Reactor Irradiated Niobium and Vanadium Alloys", pp. 122-219 in: Radiation Effects and Tritium Technology for Fusion Reactors, Vol. I, J. S. Watson and F. W. Wiffen, Eds., 1976.
3. O. N. Braski, "The Effect of Neutron Irradiation on the Tensile Properties and Microstructure of Several Vanadium Alloys", to he published in: The proceedings of the Second International Conference on Fusion Reactor Materials, April 13-17, 1986, Chicago.
4. M. L. Grossbeck and J. A. Horak, "Tensile and Fracture Properties of EBR-II Irradiated V-15Cr-5Ti Containing Helium", to be published in: The proceedings of the Second International Conference on Fusion Reactor Materials, April 13-17, 1986, Chicago.
5. B. A. Loomis and O. L. Smith, "Swelling of V-15Cr-5Ti Alloy on Single- and Dual-Ion Irradiation", pp. 66-71 in: Alloy Development for Irradiation Performance Semiannual Prowess Report, Period Ending March 31, 1984, DOE/ER-0045/12, U. S. Department of Energy, Office of Fusion Energy.
6. J. Moteff, D. J. Michel and V. K. Sikka, "The Influence of Irradiation Temperature on the Hardening Behavior of the Refractory BCC Metals and Alloys", pp. 198-211 in: Defects and Defect Clusters in B.C.C. Metals and Their Alloys, ed. R. J. Arsenault, 1973.

5.3 ENVIRONMENTAL AND CHEMICAL EFFECTS ON THE PROPERTIES OF VANADIUM-BASE ALLOYS -- D. R. Oiercks and D. L. Smith (Argonne National Laboratory)

5.3.1 ADIP Task

ADIP Task I.A.3, Perform Chemical and Metallurgical Compatibility Analyses.

5.3.2 Objective

The objective of this task is to experimentally evaluate the corrosion behavior of selected vanadium-base alloys in aqueous, liquid-metal, and gaseous environments and to investigate chemical effects on the mechanical and physical properties of the alloys. The results of these investigations will be used in the selection of appropriate vanadium-base alloys for structural applications in fusion reactors.

5.3.3 Summary

The susceptibility of V-15Cr-5Ti to stress corrosion cracking in high-purity water at 288°C is being evaluated by means of constant extension rate tensile (CERT) tests. No stress corrosion cracking was observed in tests conducted at a strain rate of 1×10^{6} s^{-1} and dissolved oxygen levels in the range <0.005 to 7.7 wppm.

5.3.4 Progress and Status

The results of a series of experiments to determine the corrosion behavior of selected vanadium-base alloys in pressurized water at 288°C (550°F) and 8.3 MPa (1200 psi) containing various levels of dissolved oxygen in a refreshed autoclave system have been reported previously.[1-4] During the present reporting period, a related series of experiments has been initiated to determine the susceptibility of the V-15Cr-5Ti alloy to stress corrosion cracking in oxygenated water. Previous work conducted by investigators at the U. S. Bureau of Mines determined that unalloyed vanadium was generally resistant to stress corrosion cracking in a variety of organic and inorganic acid solutions and inorganic salt solutions at near ambient temperature.[5] However, U-bend specimens showed evidence of transgranular stress corrosion cracking in 6-N HCl and 18-N H_2O_4 solutions.

In the present experiments, the stress corrosion cracking susceptibility of V-15Cr-5Ti was determined by means of CERT tests in 288°C water containing various concentrations of dissolved oxygen. The tests were performed using a loading system consisting of a worm gear Jactuator, gear reducer, and variable-speed motor. The test specimen was enclosed in a small-diameter autoclave and once-through water system. The dissolved oxygen level in the autoclave water was controlled by bubbling the appropriate nitrogen-oxygen gas mixture through deoxygenatedIdeionized feedwater (conductivity $\leq$0.2 µS/cm) in a 120-L stainless steel tank. A flow rate of –10 mL/s was maintained in the autoclave. An external silver chloride (0.1M KCl) reference electrode and a thermocouple were located at the outlet of the autoclave, along with platinum and V-15Cr-5Ti electrodes to establish the redox and open-circuit corrosion potentials, respectively. Commercial instruments were used to monitor the pH, conductivity, and dissolved oxygen concentrations at the influent and effluent lines of the autoclave. The dissolved oxygen concentration was verified by the colorimetric (CHEMetrics ampules) method.

The CERT test specimens were fabricated from 0.635-cm (0.25-in.) dia. V-15Cr-5Ti rod material obtained from the Fusion Program Materials Inventory (Heat No. CAM 835 B-2). A chemical analysis supplied with the as-fabricated rod indicated the following composition (in wt %): 15.3% Cr, 5% Ti, 0.017% C, 0.023% O, and 0.052% N. Cylindrical tensile specimens with 0.41-cm (0.161-in.) diameters and 1.91-cm (0.75-in.) gage lengths were machined from the rod material. The material was tested in the as-received, cold-worked condition without prior annealing. The gage sections of the specimens were wet abraded with 600-grit metallographic paper in the circumferential direction immediately before insertion into the autoclave. The specimens were exposed to the oxygenated water environment at 288°C before straining.

Results of the CERT tests and electrochemical potential measurements completed to date are summarized in Table 5.3.1. All of these tests were conducted at a strain rate of 1×10^{-6} s^{-1}, and dissolved oxygen concentrations varied from <0.005 to 7.7 wppm. No significant effect of oxygen concentration on ductility was observed, and for all four tests the fracture mode was found to be 100% ductile. These results indicate that the alloy V-15Cr-5Ti is not susceptible to stress corrosion cracking over the wide range of dissolved oyxgen concentrations and values of open-circuit corrosion potential evaluated. Tortorelli[6] recently obtained similar results for this alloy at 300°C and a strain rate of 6×10^{-5} s^{-1} and for V-3Ti-1Si at strain rates of 6×10^{-5} and 1×10^{-5} s^{-1} in a static autoclave system. Tortorelli also found that a hydrogen overpressure of 90 kPa appeared to have no effect on the ductility of V-15Cr-5Ti when tested under the conditions described.

Table 5.3.1. Results obtained from CERT tests conducted at a strain rate of 1×10^{-6} s^{-1} on V-15Cr-5Ti in pressurized water containing various concentrations of dissolved oxygen at 288°C

Dissolved Oxygen (wppm)	Conductivity (μS/cm)	Failure Time (h)	Maximum Stress (MPa)	Total Elongation (%)	Reduction in Area (%)	Fracture Mode	Potentials [mV(SHE)] V-15Cr-5Ti	Pt	Type 304 SS
<0.005	0.07	32.0	846	12	48	ductile	-422	-398	-419
0.025	0.08	32.5	847	12	49	ductile	-428	-410	-427
0.20	0.20	32.9	833	12	50	ductile	-351	83	-39
7.7	0.09	31.7	834	11	48	ductile	23	150	80

Additional CERT tests will be conducted on V-15Cr-5Ti at slower strain rates and possibly with dissolved $SO_4^=$ additions to the water to verify that this alloy retains its resistance to stress corrosion cracking under these more aggressive conditions.

5.3.5 Conclusions

Results from CERT tests conducted at 1×10^{-6} s^{-1} on V-15Cr-5Ti at 288°C in pressurized water containing dissolved oxygen concentrations ranging from <0.005 to 7.1 wppm indicate that this alloy is not susceptible to stress corrosion cracking under the conditions evaluated. Further tests at slower strain rates and possibly with $SO_4^=$ additions to the water are planned.

5.3.6 References

1. D. R. Oiercks and D. L. Smith, "Environmental Effects on the Properties of Vanadium-base Alloys," pp. 15-79 in Alloy Development for Irradiation Performance: Semiannual Progress Report for Period Ending March 31, 1984, DOE/ER-0045/12, Oak Ridge National Laboratory, Oak Ridge, TN, July 1984.
2. O. R. Diercks and D. L. Smith, "Environmental Effects on the Properties of Vanadium-base Alloys," pp. 209-213 in Alloy Development for Irradiation Performance: Semiannual Progress Report for Period Ending September 30, 1984, DOEIER-0045113, Oak Ridge National Laboratory, Oak Ridge, TN, March 1985.
3. D. R. Diercks and D. L. Smith. "Environmental Effects on the Prooerties of Vanadium-base Alloys," pp. 177-181 in Alloy Developnent for Irradiation Performance: Semiannual Progress Report for Period Ending March 31, 1985, DOE/ER-0045/14, Oak Ridge National Laboratory, Oak Ridge, TN, July 1985.
4. D. R. Diercks and D. L. Smith, "Environmental and Chemical Effects on the Properties of Vanadium-base Alloys," pp. 159-166 in Alloy Oevelopment for Irradiation Performance: Semiannual Progress Report for Period Ending September 30, 1985, DOE/ER-0045/15, Oak Ridge National Laboratory, Oak Ridge, TN, February 1985.
5. J. P. Carter, C. 8. Kenahan, and O. Schlain, "Stress Corrosion Cracking of Vanadium, Molybdenum, and a Titanium-Vanadium Alloy," U. S. Bureau of Mines Report of Investigation 6680 (1966).
6. P. F. Tortorelli, "Compatibility of Vanadium Alloys in High Temperature Water," pp. 193-194 in Alloy Development for Irradiation Performance: Semiannual Progress Report for Period Ending September 30, 1985, DOE/ER-0045/15, Oak Ridge National Laboratory, Oak Ridge, TN, February 1986.

5.4 PREPARATION AND FABRICATION OF VANADIUM BASE ALLOYS -- A. G. Hins and H. R. Thresh (Argonne National Laboratory)

5.4.1 ADIP Task

I.D.1 materials Stockpile for MFE Programs (Path C).

5.4.2 Objective

Previous fabrication efforts established a stockpile quantity of Path C Scoping Study vanadium and niobium alloys. These materials were used to evaluate the potential of the alloys for fusion reactor applications. The vanadium alloy supply has been depleted to the point where additional stock must be produced to support further work in the scoping studies. A current objective is to produce 50 pounds of the V-15Cr-5Ti ternary alloy in 0.020" and 0.050" flat stock form to replenish the refractory alloy inventory.

5.4.3 Summary

Fabrication of V-15Cr-5Ti alloy has begun to replenish the inventory of vanadium ternary alloy for Path C Scoping Studies. A process flowsheet has been devised to generate alloy material having optimum properties. Process operations are designed to minimize the pickup of interstitial elements O, N, H and C for R&D requirements.

Pure vanadium, chromium and titanium feedstock materials have been prepared for alloy consolidation melting. Primary and secondary plasma arc melting of 350 g ingots has begun. Two flat stock rolling experiments were conducted on as-cast material. Alloy sheet delivery is planned to begin early in the third quarter.

5.4.4 Progress and Status

5.4.4.1 Introduction

An extensive review was made of unpublished fabrication file records from the 5-lot V-15Cr-5Ti alloy production campaign conducted at ANL in 1967. Details of the basic steps of alloy consolidation, consumable arc melting, breakdown extrusion and finish rolling were studied to determine which operations required modification to meet the current ternary alloy production objectives. The current interest is to generate allay material with essentially no interstitial impurities pickup. The fabrication process is required to be generally reproducible, cost effective and should have a better materials recovery percentage than the 45% obtained during the earlier work.

A decision was made to substitute button arc melting of bulk feedstocks far the formerly used particulate metal compacting and melting operation. This is done to reduce impurities pickup and processing cost. In the current case four melting steps -- two copper mold arc melts and 2 consumable electrode arc melts --were deemed to provide adequate alloy homogeneity. Formerly, two breakdown extrusions of round stock were used to prepare the stock for final metalworking operations. Current plans are to produce rectangular flat stock in one extrusion step for final rolling of the sheet material. An extrusion temperature of 1125°C, rolling temperatures of 900°C-500°C-R.T., and a stress relief temperature of 900°C will be used as developed before. A higher, 1200°C, processing temperature will be avoided because of this alloy's tendency for grain coarsening and precipitate formation at grain boundaries at the higher temperatures. The basic alloy processing operations are shown in Table 5.4.1.

5.4.4.2 Process Development

Two hot rolling experiments were run to evaluate the breakdown characteristics of as-cast V-15Cr-5Ti material by rolling mill techniques. The first experiment was conducted directly an a 1" x 0.7" x 4-1/2" arc-cast bar. After the bar was vacuum heat treated at 1050°C for 2 h, it was canned into a stainless steel picture frame assembly. The compact was hot pressed at 1050°C (10% reduction) to enable subsequent rolling mill entry. Hot rolling was begun at 1050°C and the rolling temperature was gradually lowered to 900°C where a reduction of approximately 50% was reached. The ternary alloy piece was removed from the stainless steel can and was found to exhibit significant edge cracking.

The second hot rolling experiment was conducted on a rectangular casting of 3" x 4-1/2" x 3/8" size. This ternary alloy piece was also clad in a GTAW welded stainless steel picture frame assembly. No prerolling heat treatment was performed. Initially the compact was rolled at 1050°C to a 20% reduction. Here the temperature was decreased to 900°C and the compact was rolled until a total reduction of 50% was reached. The compact was further cooled to 500°C and warm rolling continued for an additional 50% reduction. Upon decanning the alloy piece was found to have edge cracking similar to that found in the first test sample.

A conclusion was drawn that the hot breakdown of this alloy in the cast state should employ a compressive approach such as hot extrusion to generate the maximum yield.

Table 5.4.1. V-15Cr-5Ti *Sheet* Fab for Fusion Power.

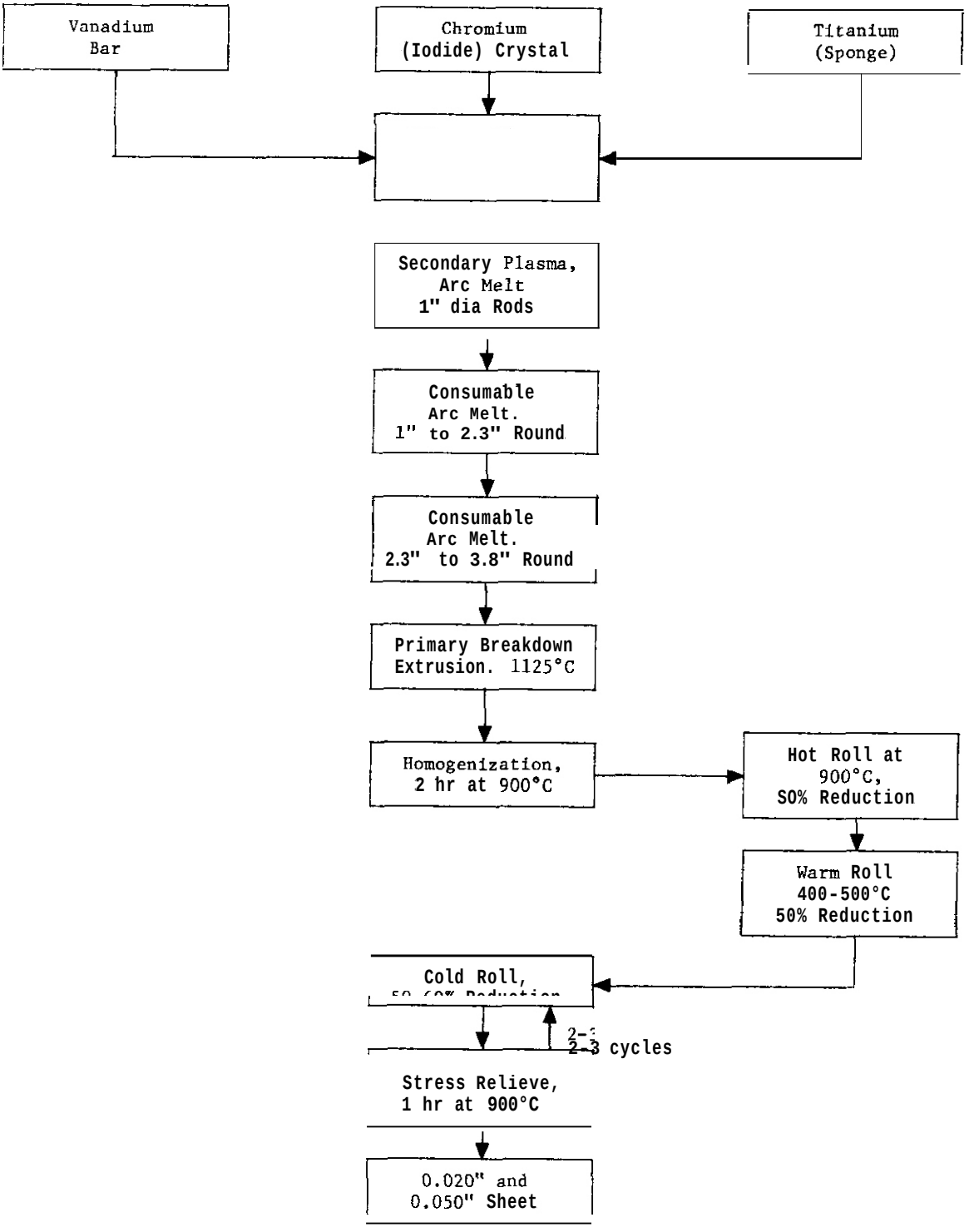

5.4.4.3 Current Status

Preparations were made for the processing of V-15Cr-5Ti alloy in three 31 pound lots. Each lot is identified as the alloy material in one extrusion billet.

Vanadium metal feedstock was prepared by cutting 1" slices from Wah Chang heat 820305 forged bar. The slices were cold rolled to 0.100" and 0.020" thick sheet for melt charge cutting. Chromium (Iodide) crystal stock, lot 463996, was fractured to provide multisized pieces for melt charge makeup. Sponge titanium pieces from lot 507391 were prepared in a similar manner. Forty-two melt charges of 350 g material were weighed to the fallowing tolerances: V = 280.0 ± 0.3 g, Cr = 52.50 ± 0.05 g, and Ti = 17.50 ± 0.02 g. Each charge was loaded into a copper 2-1/4" x 2-1/4" x 3/8" plate mold far primary plasma arc melting. The furnace was evacuated and backfilled to 2 psig with a 70-30 mixture of helium and argon gas. The charge was melted using a tungsten tipped nonconsumable electrode. Melting currents ranged from 200-1000 amps with a voltage range of 20-30 volts. Weight losses during melting were controlled to generally less than 0.25 g of alloy. This allowed the use of feedstock melt charges without weight compensation for Cr or Ti losses. A primary melt charge and the resultant alloy plate are shown in Figure 5.4.1.

The primary alloyed plates were sheared into strips on an industrial shear. Each secondary melt charge was loaded in 2 layers into a copper 1.0" x 0.7" x 4-1/2" bar mold as shown in Figure 5.4.1. After half of the Secondary charge was melted, the furnace electrode was used remotely to position the second layer of feedstock in the mold cavity. Another arc melting cycle followed. A typical arc melted alloy bar is shown in the figure. Weight losses during secondary melting were controlled to less than 0.20 g.

Finished alloy bars are joined by GTAW welding in an argon atmosphere glovehox as shown in Figure 5.4.2. Each electrode contains up to 9 bars and is joined to a vanadium adaptor at the top end. The V-15Cr-5Ti alloy electrode is fixed in the melting furnace by use of the 11" stainless steel extension rod that is also shown in the figure.

The 1" welded electrode is consumable arc melted into a 2.3" diameter water cooled copper mold. A 70-30 mixture of helium and argon at 6.5 psia provides the cover gas. A vanadium, or V-Cr-Ti alloy, starter block and V-15Cr-5Ti arc starter turnings are used to maintain ingot alloy purity. Melting is accomplished by applying 1400-1500 amps to the electrode at 39 volts. To date two of the necessary 5 consumable arc melt ingots have been produced for the first lot of ternary alloy.

5.4.4.4 Future Plans

Processing of the first lot of V-15Cr-5Ti ternary alloy will continue through completion of the steps given in the flowsheet. At the same time, work will begin on the initial processing steps of the second lot of material. Ternary alloy sheet stock of 0.020" and 0.050" thickness will be delivered in the third quarter of 1986.

5.4.5 References

1. H. R. Thresh, "Preparation and Fabrication of Vanadium Base Alloys," Fig. 5.3.1, p. 88 in Alloy Development for Irradiation Performance: Semiannual Progress Report for Period Ending September 30, 1985, DOE/ER-0045/15, Oak Ridge National Laboratory, Oak Ridge, Tennessee, February 1986.

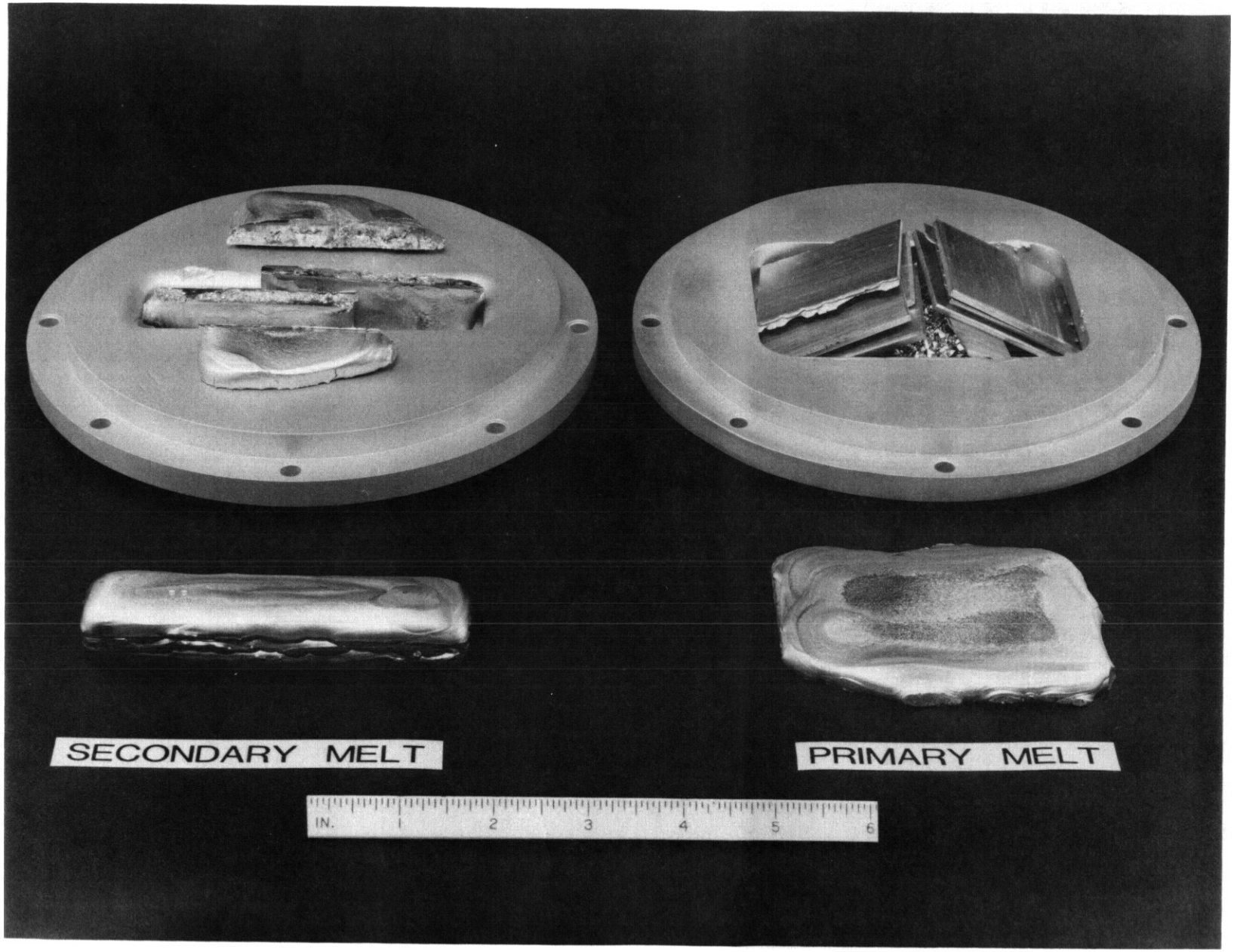

Fig. 5.4.1. Primary and Secondary Alloy Consolidation Arc Melt Molds with Feedstock Charges and Typical Finished Ingots.

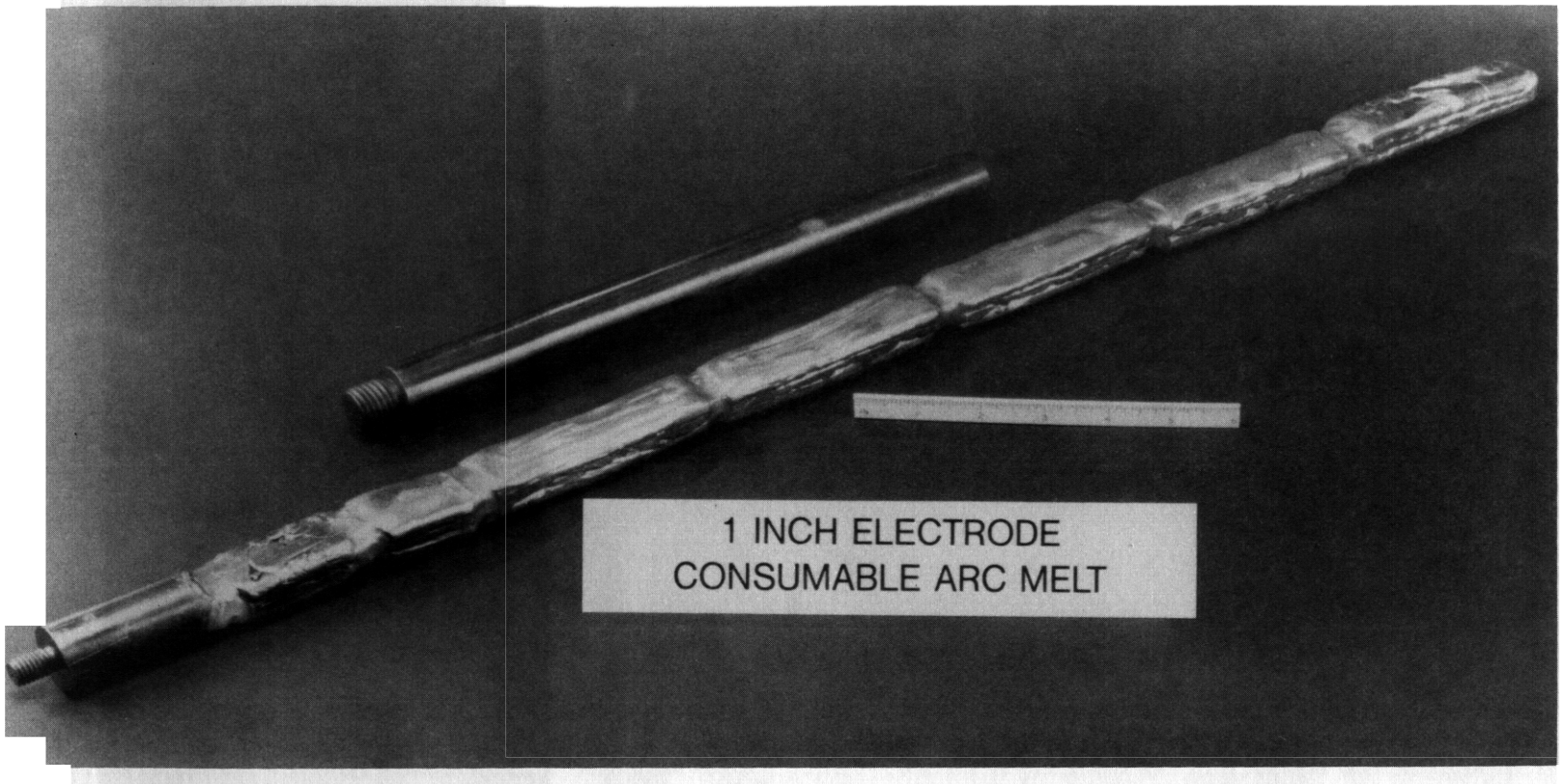

Fig. 5.4.2. V-15Cr-5Ti Alloy Bar Electrode for 1"-2.3" Consumable Arc Melting.

6. INNOVATIVE MATERIAL CONCEPTS

6.1 THE EFFECTS OF STRAIN RATE AND LONG-TERM AGING ON THE PROPERTIES OF IRON-BASE LRO ALLOYS - H. T. Lin and B. A Chin (Auburn University)

6.1.1 ADIP Task

ADIP Task I.B. 16, tensile properties of special and innovative materials.

6.1.2 Objective

This study was undertaken to investigate the effects of strain rate and long-term thermal exposure on the mechanical properties of the $(Fe,Ni)_3V$ LRO alloys.

6.1.3 Summary

Tensile tests covering strain rates from 10^{-6} to 10^{0} per sec were performed on the ordered alloys at room temperature. The results indicate that there is little or no effect of strain rate on the tensile strength and ductility. The long-term thermal exposure at 600°C does not cause any significant change in tensile properties. The deformation and fracture characteristics along with controlling mechanisms change as a function of strain rate and aging time.

6.1.4 Progress and Status

6.1.4.1 Introduction

Long-range-ordered alloys offer potential advantages over conventional alloys for high-temperature structural applications [1-4]. Atomic ordering produces a pronounced increase in the rate of work hardening [4-8] and improves the fatigue resistance [9]. As a result of stronger binding and closer packing of atoms, most kinetic processes such as creep and grain growth, are slower in the ordered structure [10]. Also, the unique dislocation dynamics associated with the ordered lattices give the LRO alloys excellent high-temperature strength and fatigue resistance [11]. The main disadvantaae of the LRO alloys is their tendency to be brittle in the ordered state. The newly developed LRO alloys based on the general composition $(Fe,Ni)_3(V,Ti)$ show an elongation in excess of 30% [12,13]. This has been achieved by controlling the ordered lattice structure through use of the e/a ratio or average electron density per atom outside the inert gas shell.

The excellent mechanical properties exhibited by these ordered alloys have led them to be considered as structural materials in fusion reactors and steam turbine systems. Before these alloys can be used widely for high-temperature applications, the major challenge is to improve and maintain the

ductility of LRO alloys in the ordered state. In an effort to clarify the deformation and failure mechanisms, and to optimize the ductility of the iron-base LRO alloys, this study investigates the effects of strain rate and long-term thermal aging on the tensile properties, structural stability and fracture mechanism of the LRO alloys.

6.1.4.2 Experimental

Two series of tensile specimens, LRO-37 and LRO-42, of iron-base LRO alloys were received from Oak Ridge National Laboratory. The chemical composition analysis of ingots is given in reference [15]. The specimens were solution-treated for 20 minutes at 1100 C, followed by an ordering treatment involving step cooling from 600 C to 500 C. The ordered specimens were aged at 600 C for three months and six months respectively. All specimens were electro-polished in a solution of 40% water, 40% nitric acid and 20% hydrofluoric acid. The specimens were polished between 15 and 30 seconds, with voltage and current settings at 0.7 volts and 0.3 amperes respectivity.

Room temperature tensile tests were performd with an MTS hydraulic testing machine at strain rates of 2.8 x 10^{-6} to 2.8 x 10^{-} per sec. To investigate deformation and fracture mechanisms, selected specimens were examined in detail with an ISI-SS 40 scanning electron microscope operated at 20 KV. Additionally, the microstructure of the LRO alloys before and after long-term thermal aging was examined using a Zeiss photomicroscope.

6.1.4.3 Results

Optical Microscopy

Figure 1 shows optical micrographs of the LRO alloys in their ordered state before and after different aging treatments. Annealing twins are visible together with some inclusions which were analyzed to be VC particles. These two LRO alloys, LRO-37 and LRO-42, were given identical heat treatment processes, but the significantly different grain sizes were obtained as a result of minor difference in chemical composition. The results show that the grain size of the LRO-42 is approximately half of the LRO-37 alloys. Also, it reveals that the microstructure of LRO alloys is not affected by the long-term thermal exposure at 600°C.

Tension Test

Figures 2 and 3 show the characteristic stress versus strain curves for the LRO alloys in the aged and unaged conditions respectively. All the LRO-42 six months aged specimens exhibited a sharp yield point, characterized by the classical upper and lower yield point, while none of the control group specimens showed the sharp yield point phenomenon. For the LRO-37 alloys, the sharp yield point behavior is not discernible in either the three months aged or the control specimens.

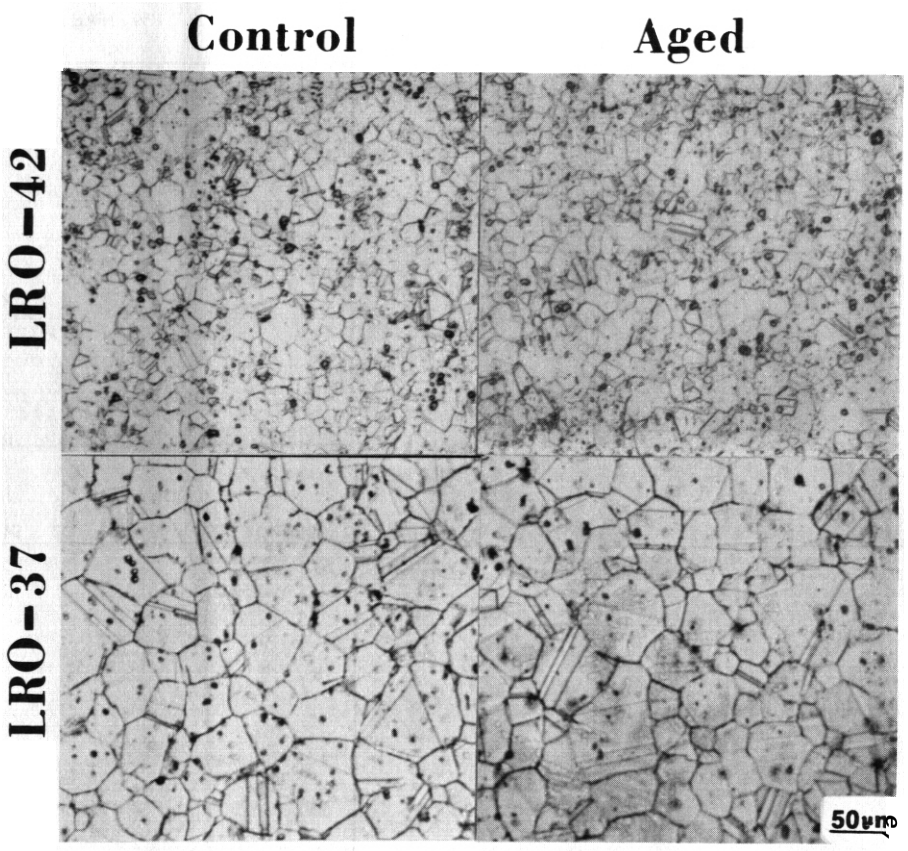

Figure 1. Optical Microstructure of LRO Alloys.

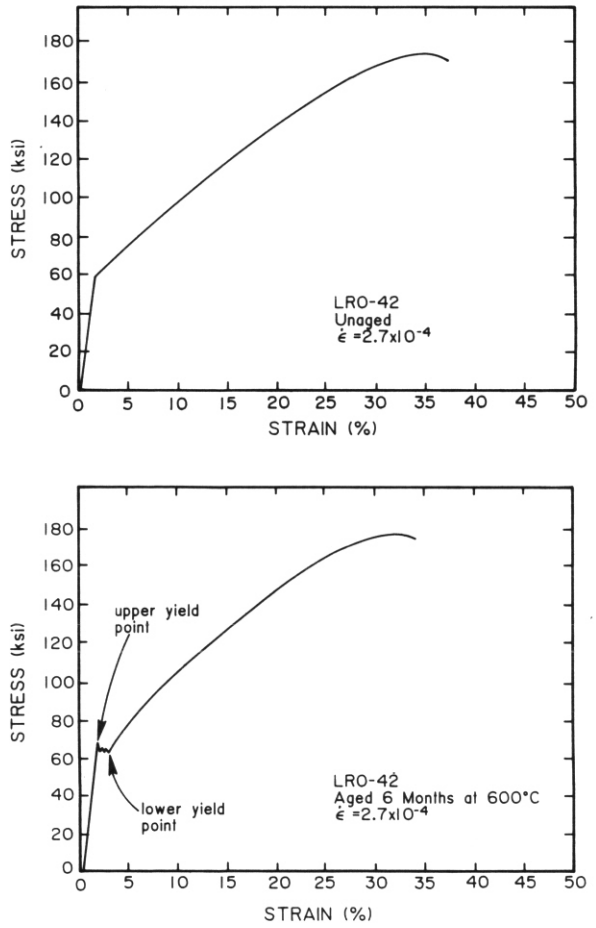

Figure 2 Stress-Strain Curves of LRO-42 Alloys.

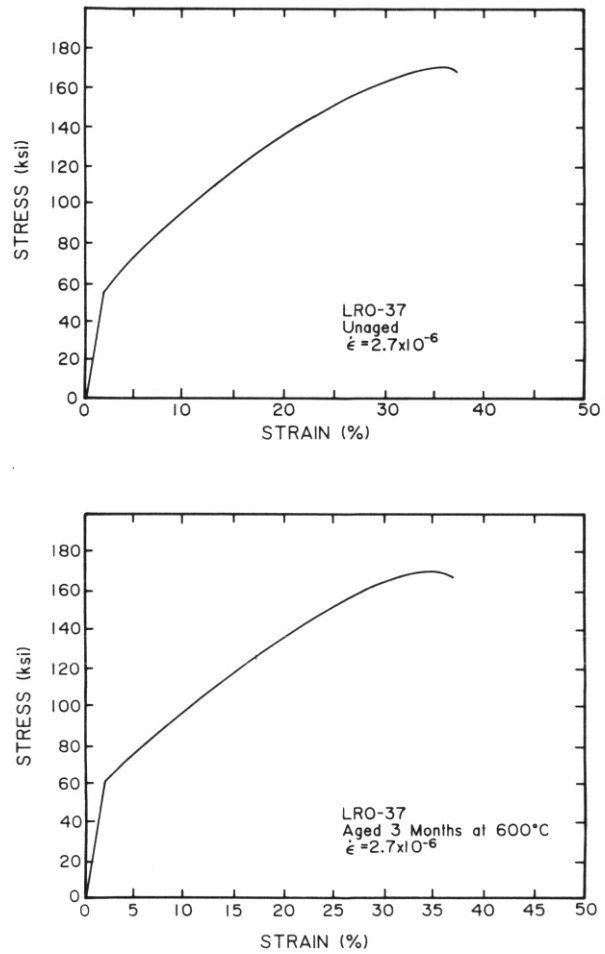

Figure 3. Stress-Strain Curves of LRO-37 Alloys.

Figure 4 shows the effect of strain rate on the ultimate tensile strength for both the LRO alloys. From the figure, there is a trend toward increasing tensile strength with increasing strain rate for the LRO-37 alloys, while the LRO-42 control group behaves in the opposite way. The tensile strength of the LRO-42 six months aged group is insensitive to strain rate up to 2.8 x 10^{-1} sec^{-1}. The results also indicate that the LRO-42 six months aged group displays a higher UTS than its control group, and there is a small difference between the aged and control specimens of LRO-37 alloys. The results show that the strain rate and long-term aging have little effect on the room temperature tensile strength.

The yield strength as a function of strain rate is shown in Figure 4. There is no apparent effect of strain rate on the yield strength. The yield strengths of the LRO-42 six months aged group differ from those of its control group by 10% to 20%. For LRO-37 alloys, no significant difference in yield strength was found between the aged and control group. Additionally, there is no detectable effect of long-term aging on the yield strength.

Gage section elongation was found to be insensitive to both strain rate and aged condition, as shown in Figure 4. A small amount of necking was observed in samples prior to final failure. As a result of high strain hardening exponent, a minor deformation of the holes on the grip section were observed.

The strain-hardening exponent versus strain rate is plotted in Figure 4. The figures show that the strain hardening exponent of these LRO alloys is insensitive to strain rate up to 2.8 x 10^{0} sec . The results also indicate that long-term thermal aging has a little effect on the strain hardening characteristics of the material.

Scanning Electron Microscopy

Macroscopically, the fracture surfaces of all room temperature tested specimens are nearly identical. The fracture propagated at an angle of about 90 degrees with respect to the tensile axis (Figure 5). In spite of the similarity in macroscopic fracture surface features, there were identifiable differences in the microscopic deformation and fracture mechanisms. These differences were discernible using scanning electron microscopy.

Figure 6 compares the deformation mechanism of six selected specimens in the different aged and strain rate conditions. The photomicrographs indicate that the transgranular slip band density is seen to be both a function of strain rate and aged condition. The unaged specimens have a much higher slip band density than either of the aged specimens. Also, the unaged and aged specimens, tested at high strain rate, have a much higher slip band density than those tested at lower strain rate. These phenomena suggest that the deformation within the grains increases with increasing strain rate and decreases with increasing exposure time at 600°C.

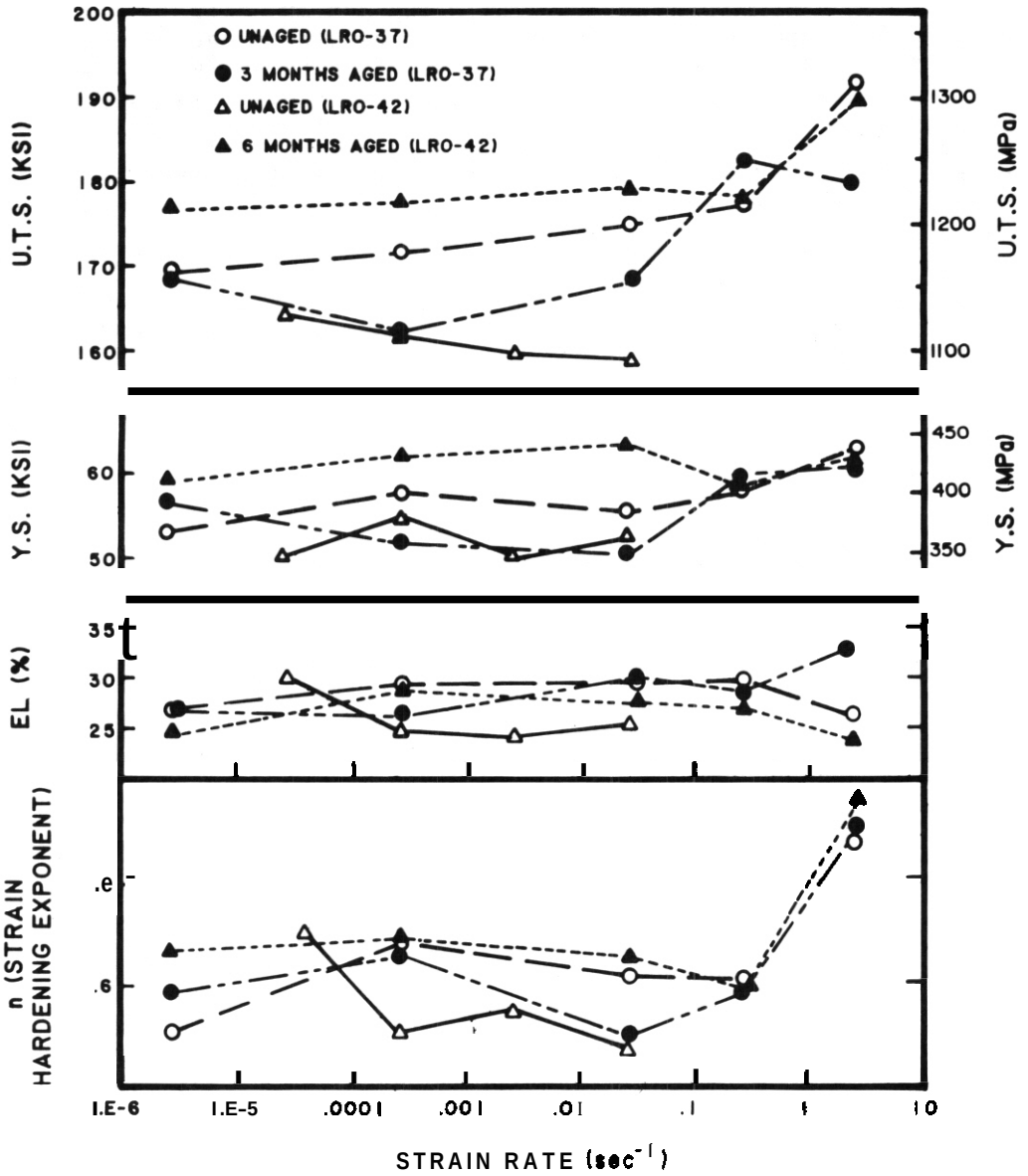

Figure 4. Strain Rate Dependence of Tensile Properties of LRO Alloys.

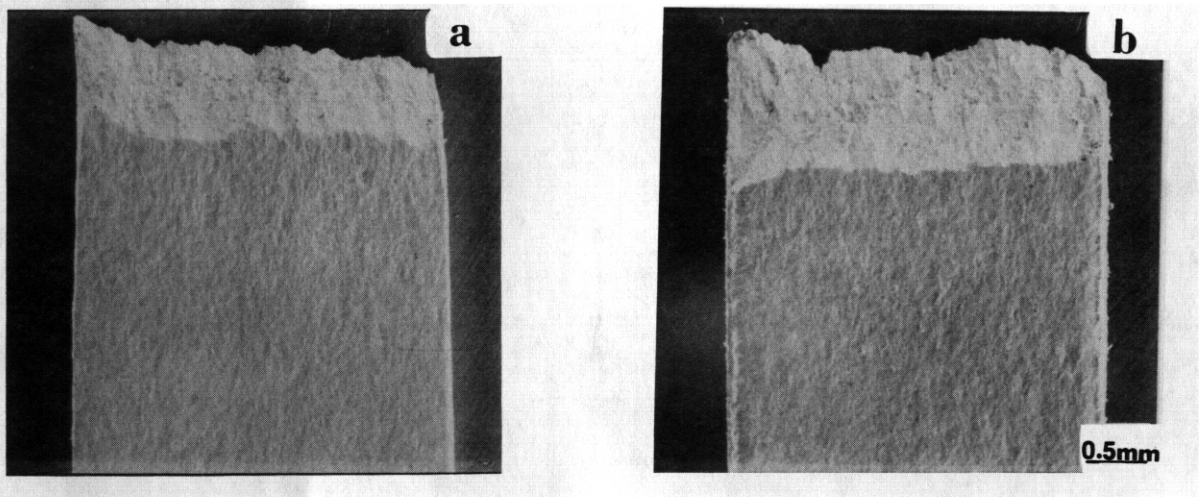

Figure 5. Macroscopic Fracture Features of LRO Alloys. a). Specimen Tested at Low Strain Rate b). Specimen Tested at High Strain Rate.

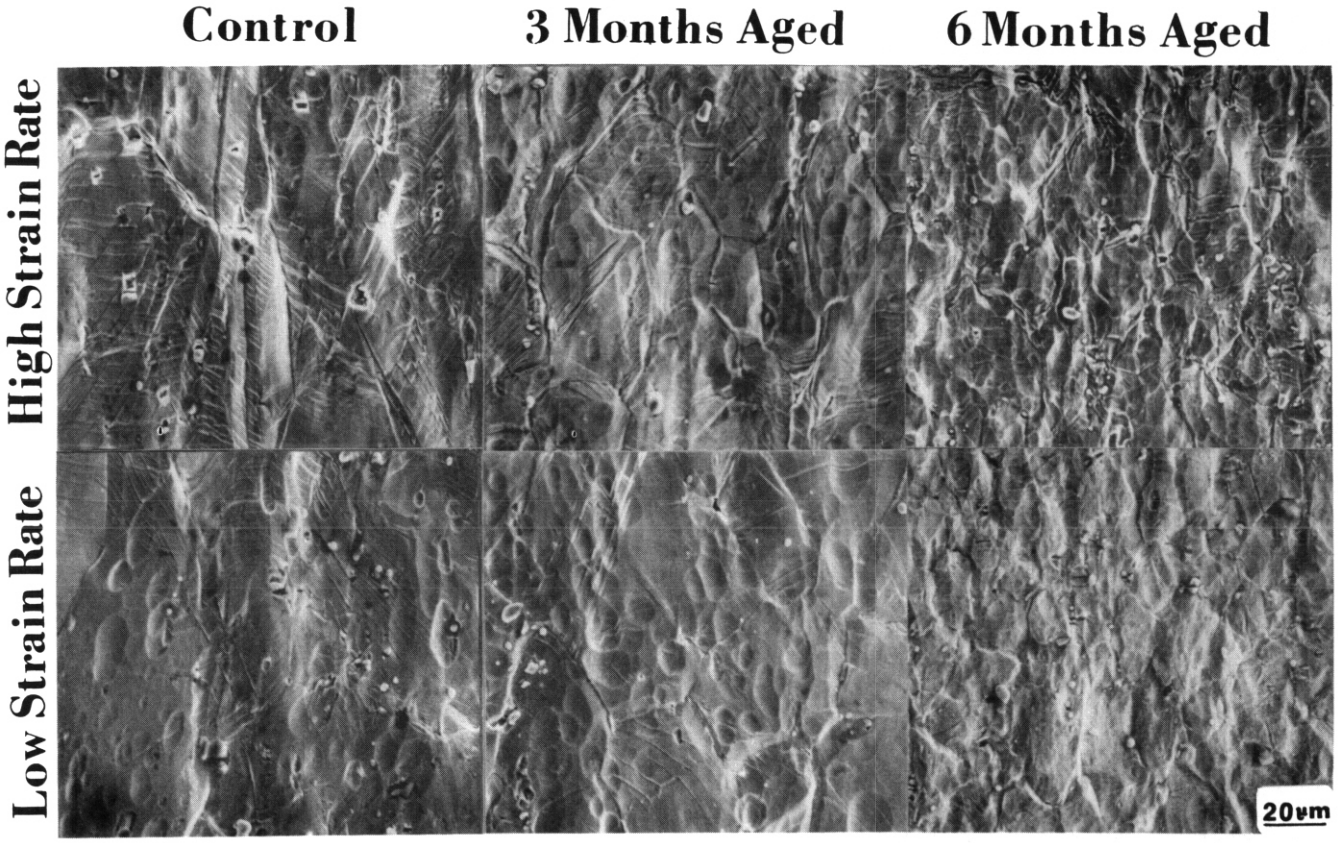

Figure 6. Microscopic Slip Band Features. Density of Slip Band Increases with Increasing Strain Rate and with Decreasing Aging Time.

Correspondingly, the fracture mechanism as a function of strain rate and aged condition is shown in Figure 7. The fracture surface features for all the tested specimens show ductile rupture, characterized by dimples, at these strain rates. The unaged specimens exhibited mixed mode fracture, intergranular and transgranular fracture, through the tested strain rate range. Some holes, which probably are inclusion sites, are visible on the grain boundary facets. For three months aged and six months aged specimens, the fracture mode is predominantly ductile. Also, the dimples of aged samples are finer than those in the unaged condition. Generally, specimens tested at lower strain rate have a greater tendency to failure by dimple rupture than those tested at high strain rate. The aged specimens show a much higher degree of dimple rupture than the unaged specimens.

6.1.4.4 Discussion

From observation of the microstructure of the iron-base LRO alloys, the grain size of these ordered materials is not affected by long-term thermal aging. This suggests that the impurities or precipitates pin grain boundaries to impede grain growth, or the kinetics of grain growth of the ordered alloys is very slow which may be attributed to the strong binding and closer packing of atoms. In addition, the experimental results at room temperature indicate that long-term thermal exposure at 600^{0}C does not cause any significant change in the mechanical properties of the iron-base LRO alloys demonstrating the structural stability of the ordered alloys.

The room temperature tensile properties of the iron-base LRO alloys are insensitive to strain rate over six orders of magnitude. The photomicrographs (Figures 6-7), however, indicate that both the deformation and fracture mechanisms change as a function of strain rate and aged condition. These features show that with decreasing strain rate and increasing aging time there is a decrease in the deformation of the matrix. This shift in matrix deformation should result in a significant decrease in ductility. However, the lower matrix deformation was compensated by an increase in the grain boundary ductility. This compensation is manifested by the presence of more dimple rupture on the grain boundary facets in the aged material (Figure 7). These analyses indicate that long-term aging reduces the matrix deformation significantly. This is probably due to the formation of VC type solute atmospheres which inhibit the motion of dislocations [14]. The appearance of upper and lower yield point associated with lüders band phenomenon in the aged samples supports this conclusion. The present study suggests that, for iron-base LRO alloys, reduction in matrix solute impurities will be effective in increasing the ductility of the ordered materials. This can be achieved by controlled melting practices to reduce solute impurities or by the addition of dopants to tie up impurities as harmless precipitates.

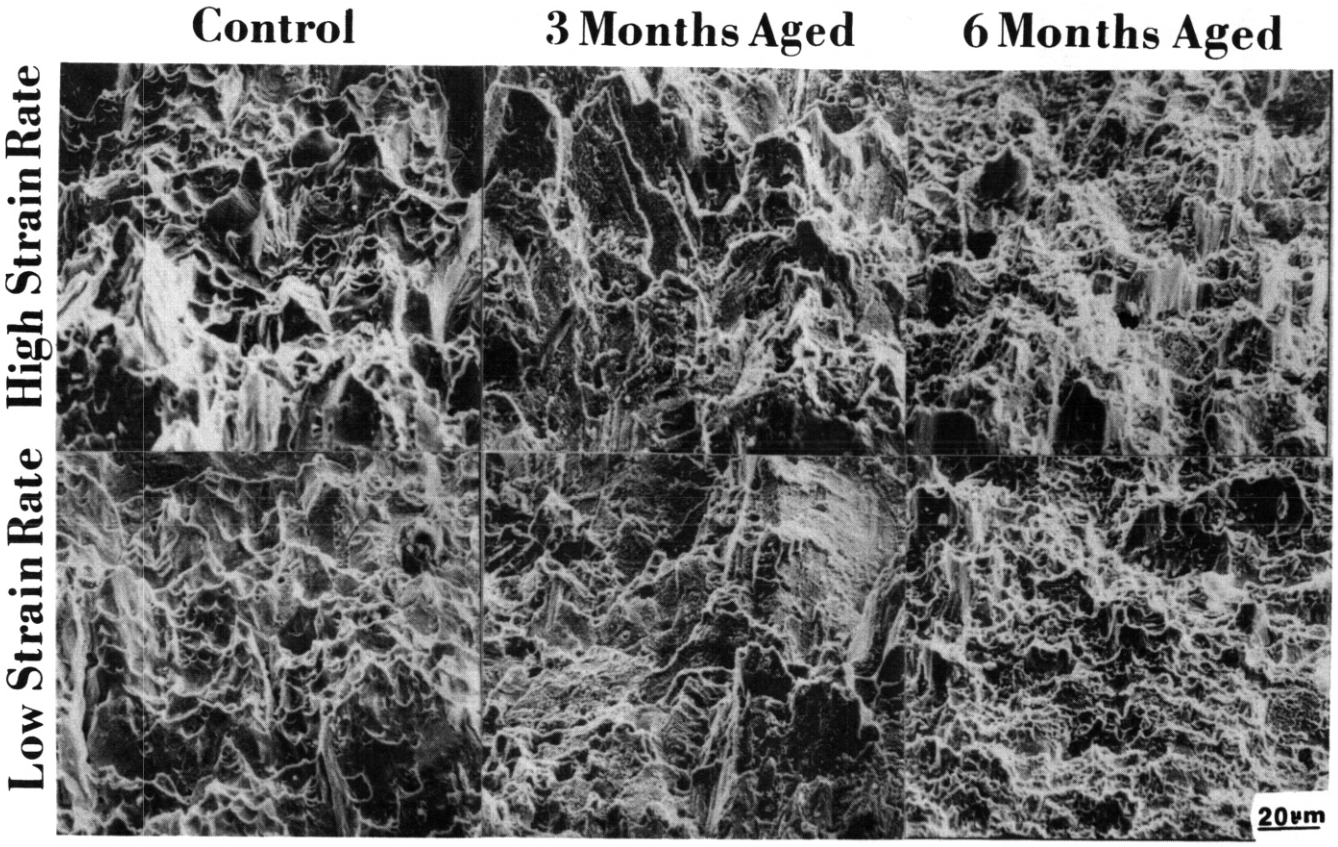

Figure 7 Microscopic Fracture Surface Features. Fracture Surfaces Generally Show a MIxed Failure Mode of Intergranular and Transgranular Fracture. Dimple Rupture Increases with Increasing Aging Time and with Decreasing Strain Rate.

6.1.5. Conclusions

The following conclusions were drawn from the experiment and analysis:

1. The mechanical properties of the LRO alloys are insensitive to strain rate over six order of magnitude.

2. Long-term aging at 600°C does not cause any significant change in the tensile properties which demonstrates the structure stability of the LRO alloys.

3. The scanning electron microscopy investigation indicates that slip band density increases with strain rate and decreases with aging time. Correspondingly, the ductile grain boundary fracture increases with a decrease in strain rate and increase of aging time.

6.1.6 References

1. N. S. Stoloff and R. G. David. "The Mechanical Properties of Ordered Alloys," Progress in Materials Science, 13 (1), (1966) p. 1.
2. B. H. Kear, C. F. Sims, N. S. Stoloff and J. H. Westbrook, Eds., Ordered Alloys Structure and Physical Metallurgy, Proc. 3rd., Bolton Landing Conf., Lake George, N. Y., Claiter's Pub. Div. (1970).
3. M. A. Krivoglaz and A. A. Smirinov, The Theory of Order-Disorder in Alloys, American Elsevier Pub. Co., New York (1964).
4. F. Muto and Y. Takagi, The Theory of Order-Disorder Transformations in Alloys, Academic Press, New York (1956).
5. L. E. Popov and N. A. Koneva, Order Disorder Transformation in Alloys, J. Warlimant, Ed.. Springer-Verlag. New York (1974), p. 404.
6. M. J. Marcinkowski, Order Disorder Transformation, J. Warlimant, Ed., Springer-Verlag. New York (1974), p. 364.
7. A. E. Vidoz, D. P. Lazarenio and R. W. Chan, Acta Met, Vol. 11 (1963), p. 17.
8. B. H. Kear and H. Wilsdorf, Trans AIME, Vol. 224 (1962), p. 382.
9. R. C. Boetler, N. S. Stoloff and R. G. Davis, Trans AIME, Vo1.236 (1966), p. 131.
10. E. M. Schuison, "Order Strengthening as a Method for Reducing Irradiation Creep: An Hypothesis," Journal of Nuclear Materials, 66 (1977), p. 322.
11. A. H. Cottrell, in Relation of Properties to Structure, Seminar Series, Am. Society of Metals, Cleveland, Ohio (1954).
12. C. T. Liu, "Development of Long Range Ordered Alloys," Alloys Development for Irradiation Performance, Proceedings of Program Review Meeting, Sep. 30-Otc. 1, 1980, p. 354.
13. C. T. Liu, and H. Inouye, " Control of Ordered Structure and Ductility of $(Fe,Co,Ni)_3V$ Alloys," Met. Trans A, Vol. 10 (1979), p. 1515.
14. E. O. Hall, Yield Point Phenomena in Metals, Plenum Publishing Company, New York, (1970).
15. C. T. Liu, "Development of Fe-Base Long Range Ordered (LRO) Alloys for Fusion Reactor First Wall and Blanket Applications, " Proceedings of the Second Topical Meeting of Fusion Reactor Materials, Seattle, WA, Aug. 9-12, 1981, Session 5c.

7. FERRITIC STEELS

7.1 HELIUM EFFECTS ON VOID FORMATION IN 9Cr-1MoVNb AND 12Cr-1MoVW IRRADIATED IN HFIR – P. J. Maziasz, R. L. Klueh, and J. M. Vitek (Oak Ridge National Laboratory)

7.1.1 ADIP Task

ADIP Tasks are not defined for Path E, ferritic steels in the 1978 Program Plan.

7.1.2 Objective

Ferritic 9Cr-1MoVNb and 12Cr-1MoVW steels have been doped with up to 2 wt % Ni to increase helium production during HFIR irradiation. The goals of this work are to examine the microstructural evolution of bubbles and voids in response to increased helium concentrations, as well as to study the precipitation behavior during irradiation via analytical electron microscopy (AEM).

7.1.3 Summary

Up to 2 wt % Ni was added to 9Cr-1MoVNb and 12Cr-1MoVW ferritic steels to increase helium production by transmutation during HFIR irradiation. The various steels were irradiated to -39 dpa. Voids were found in all the undoped and nickel-doped steels irradiated at 400°C. Voids developed in most of the steels at 500°C, but not in any of them at 300 or 600°C. Bubble formation, however, was increased at all temperatures in the nickel-doped steels. Maximum void formation was found at 400°C, but swelling remained less than 0.5% even with up to 440 appm He. Irradiation at 300 to 500°C caused dissolution of as-tempered $M_{23}C_6$ precipitates and coarsening of the lath/subgrain structure in the 9-Cr steels, whereas the microstructure generally remained stable in the 12-Cr steels. Irradiation in this temperature range also caused compositional changes in the as-tempered MC phase in all the steels, and produced combinations of fine M_6C, G, and M_2X precipitates in various steels. The subgrain boundaries appear to be strong sinks that enhance resistance to void formation. Higher helium production during irradiation appears to shorten the incubation period for void formation. The effects of helium on steady state void swelling behavior, however, remain unknown.

7.1.4 Prowess and Status

7.1.4.1 Introduction

In 1971, Harkness et al.[1] observed that the void swelling resistance of bcc ferrite was better than fcc austenite in a duplex steel. Based on this and several later investigations of void formation in ferritic steels,[2-5] various national fast breeder reactor (FBR) alloy development programs' began studying ferritic steels for fuel cladding in 1976. The U.S. magnetic fusion reactor (MFR) materials program included these steels as structural candidates in 1979.' Void swelling resistance has been demonstrated more recently for various ferritic steels irradiated in FBRs to doses as high as 120 to 150 dpa (refs. 8–12). However, helium generation in ferritic steels is very low (-0.1 appm He/dpa) in FBRs such as EBR-II, as seen in Fig. 7.1.1.

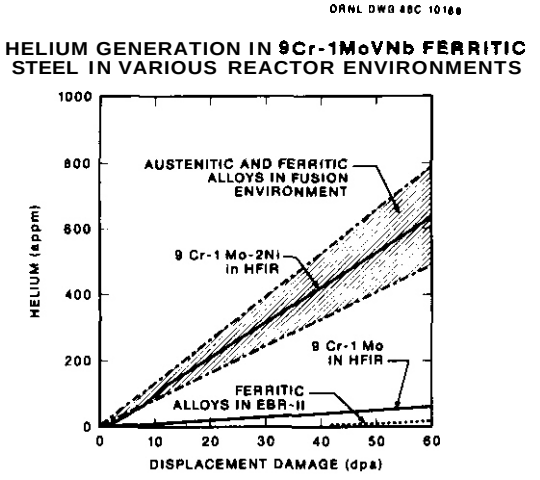

Fig. 7.1.1. Helium generation platted versus displacement damage level for undoped and 2 wt % Ni-doped 9Cr-1MoVNb irradiated in FFTF, HFIR, and a fusion first wall.

The effect of higher helium generation on void swelling resistance is therefore a major question when considering ferritic steels for use in an MFR environment,[13-15] where helium generation rates will be 8 to 13 appm He/dpa.

Recent work by Vitek and Klueh[16,17] and by Gelles[18] has demonstrated that, when helium generation was increased, void formation also increased in 9- and 12-Cr ferritic steels at 400°C after ~39 dpa. The higher helium generation was obtained by irradiating 9Cr-1MoVNb and 12Cr-1MoVW steels in HFIR instead of EBR-II (Fig. 7.1.1). HFIR has more thermal neutrons that produce helium from a two-step transmutation reaction with nickel. Neutron irradiation studies of austenitic stainless steels have demonstrated that large amounts of helium can either increase or decrease void formation.[19,20] Horton and Bentley[21] have shown that helium co-injected during heavy-ion irradiation of high-purity Fe-10Cr increased both the concentration of cavities and their spreading into a bimodal size distribution, indicative of subcritical cavities converting into bias-driven cavities or voids. Moreover, single and dual-beam heavy-ion irradiation studies in 12Cr-1MoVW by Ayrault[22] have shown that the presence of helium was necessary for void formation.

The purpose of this work is to further examine the effects of increased helium generation on void formation and microstructural evolution in the 9- and 12-Cr ferritic steels during neutron irradiation. Greater helium generation during HFIR irradiation was achieved by doping the steels with up to 2 wt % Ni (ref. 23), as shown for 9Cr-1MoVNb-2Ni in Fig. 7.1.1.

7.1.4.2 Experimental

The compositions of the nickel-doped and undoped heats of 9Cr-1MoVNb and 12Cr-1MoVW steels are given in Table 7.1.1. The various normalization and tempering heat treatment conditions are listed in Table 7.1.2. The 2% Ni-doped steels were tempered longer" at lower temperatures than the undoped alloys because previous studies showed that nickel lowered the A_C (lowest critical austenite-forming) temperature. However, the 12Cr-1MoVW-1Ni had the same tempering treatment as the undoped 12-Cr steel.

Table 7.1.1. Compositions of 9Cr-1MoVNb and 12Cr-1MoVW heats of steel with and without nickel doping

Alloy designation	Heat number	Concentration* (wt %)										
		Cr	Mo	Ni	Mn	C	Si	V	Nb	Ti	W	N
9Cr-1MoVNb	(XA 3590)	8.6	1.0	0.1	0.36	0.09	0.08	0.21	0.063	0.002	0.01	0.05
9Cr-1MoVNb-2Ni	(XA 3591)	8.6	1.0	2.2	0.36	0.064	0.08	0.22	0.066	0.002	0.01	0.05
12Cr-1MoVW	(XAA 3587)	12.0	0.9	0.4	0.5	0.2	0.18	0.27	0.018	0.003	0.54	0.02
12Cr-1MoVW-1Ni	(XAA 3588)	12.0	1.0	1.1	0.5	0.2	0.13	0.31	0.015	0.003	0.53	0.02
12Cr-1MoVW-2Ni	(XAA 3589)	11.7	1.0	2.3	0.5	0.2	0.14	0.31	0.015	0.003	0.54	0.02

[a]Balance iron.

Alloys were irradiated side by side in HFIR CTR-30 in the form of standard 3-mm-diam transmission electron microscopy (TEM) disks punched from 0.254-mm-thick sheet stock. Irradiation temperatures ranged from 300 to 600°C and have been verified by analysis of temperature monitors.[24] Displacement damage (including dpa due to nickel recoils) and helium generation levels were calculated by L. R. Greenwood based on dosimetry performed for this experiment.[25] HFIR neutron fluences produced 36 to 39 dpa and helium levels of ~33 appm in 9Cr-1MoVNb, ~410 appm in 9Cr-1MoVNb-2Ni, ~87 appm in 12Cr-1MoVW, ~217 appm in 12Cr-1MoVW-1Ni, and ~440 appm in 12Cr-1MoVW-2Ni. A specimen of 9Cr-1MoVNb-2Ni irradiated in FFTF at 407°C to a fluence producing 47 dpa and ~5 appm He was included in this work to separate the effects of nickel doping from those of helium on microstructural evolution under irradiation.

Table 7.1.2. Normalizing and tempering conditions for various steels

Alloy designation	Normalization	Tempering
9Cr-1MoVNb	0.5 h @ 1040°C	1 h @ 760°C
9Cr-1MoVNb-2Ni	0.5 h @ 1040°C	5 h @ 700°C
12Cr-1MoVW	0.5 h @ 1050°C	2.5 h @ 780°C
12Cr-1MoVW-1Ni	0.5 h @ 1050°C	2.5 h @ 780°C
12Cr-1MoVW-2Ni	0.5 h @ 1050°C	5 h @ 700°C

TEM disks were examined on a JEM 100C TEM equipped with a special objective lens polepiece designed to lower the magnetic field at the specimen. Carbon film extraction replicas were produced from as-tempered material and from selected irradiated specimens prepared in a special, shielded, hands-on facility because of the highly radioactive HFIR specimens.[20] Precipitates were studied by means of analytical electron microscopy (AEM), using either a Philips EM400 microscope equipped with a field emission gun (FEG) for very high electron intensity at small probe sizes or a JEM 2000FX microscope with an LaB_6 filament.

7.1.4.3 **Results**

7.1.4.3.1 Cavitv Microstructure

A. 9Cr-1MoVNb and 9Cr-1MoVNb-2Ni steels. HFIR and FFTF

A few fine (2–5 nm in diameter) bubbles were found at 400°C in the matrix, and at 600°C along subgrain boundaries in 9Cr-1MoVNb irradiated in HFIR to ~38 dpa and ~32 appm He. Larger matrix voids (9–18 nm in diameter) were found only at 400°C [Fig. 7.1.2(*a,b*)]. Bubbles are cavities smaller than their critical size whose growth is gas-driven. Conversely, voids are cavities larger than their critical size whose growth is bias-driven. Some experimental guidelines for determining whether cavities are bubbles or voids have been suggested.[20] Voids formed in patches that were several microns in size, while similar adjacent patches were void-free. Cavity swelling was about 0.2%. No bubbles were observed at either 300 or 500°C.

By contrast, HFIR irradiation of 9Cr-1MoVNb-2Ni to ~38 dpa and ~410 appm He produced significantly more fine bubbles at 300 to 600°C relative to 9Cr-1MoVNb, and also produced voids at both 400 and 500°C [Figs. 7.1.2(*c,d*) and 7.1.3]. At 400°C, void formation was spatially more uniform throughout the matrix and up to several times greater in 9Cr-1MoVNb-2Ni than in the 9Cr-1MoVNb, but void sizes were similar. Void swelling appeared to be 0.3 to 0.4% in the 9Cr-1MoVNb-2Ni. At 500°C, large (20–70 nm diam) voids in 9Cr-1MoVNb-2Ni were found only inside very coarse, irradiation-produced precipitate particles [Fig. 7.1.2(*d*)] tentatively identified as χ phase. Swelling appeared to be 0.1 to 0.3% in 9Cr-1MoVNb-2Ni at 500°C, whereas no void swelling was found in 9Cr-1MoVNb.

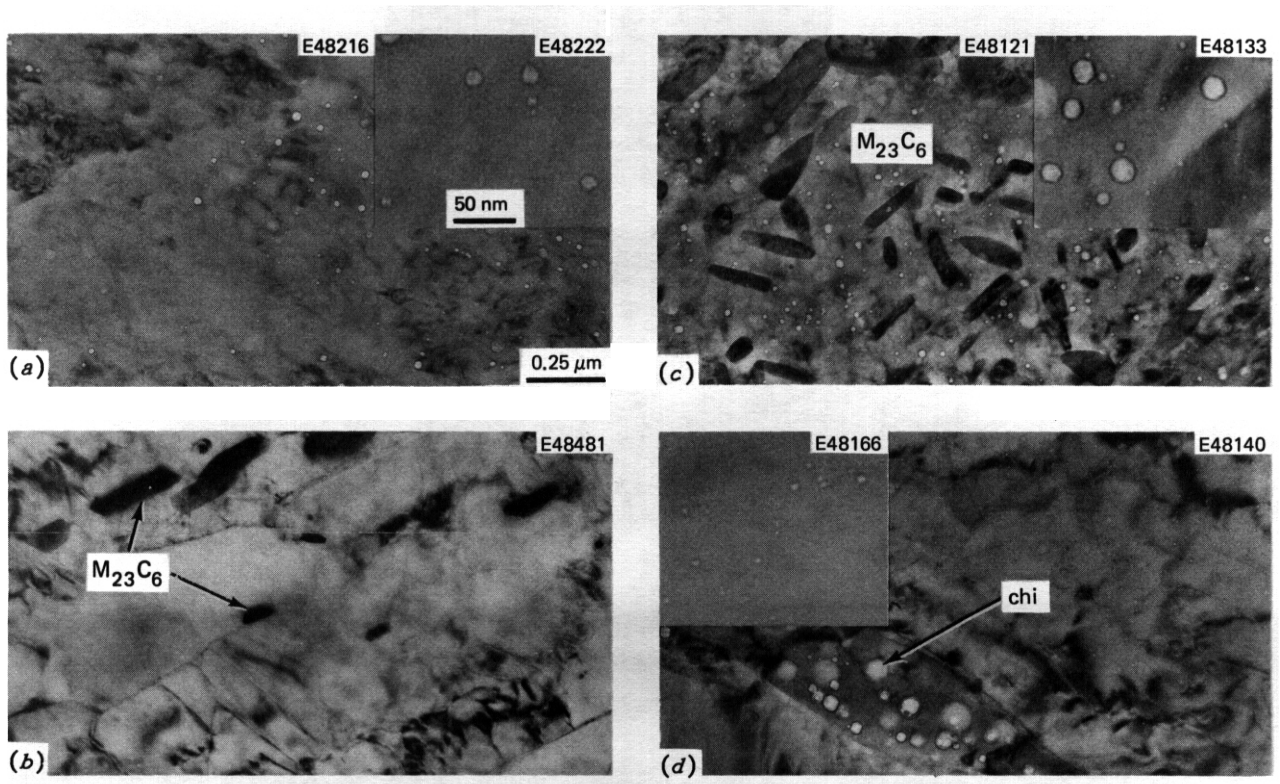

Fig. 7.1.2. **Microstructures of (*a,b*) 9Cr-1MoVNb (~32 appm He) and (*c,d*) 9Cr-1MoVNb-2Ni** (410 appm He) irradiated in HFIR at 400 and 500°C to ~37 to 39 dpa. High magnification insets show bubbles in (c) and (*d*), but almost none in (a).

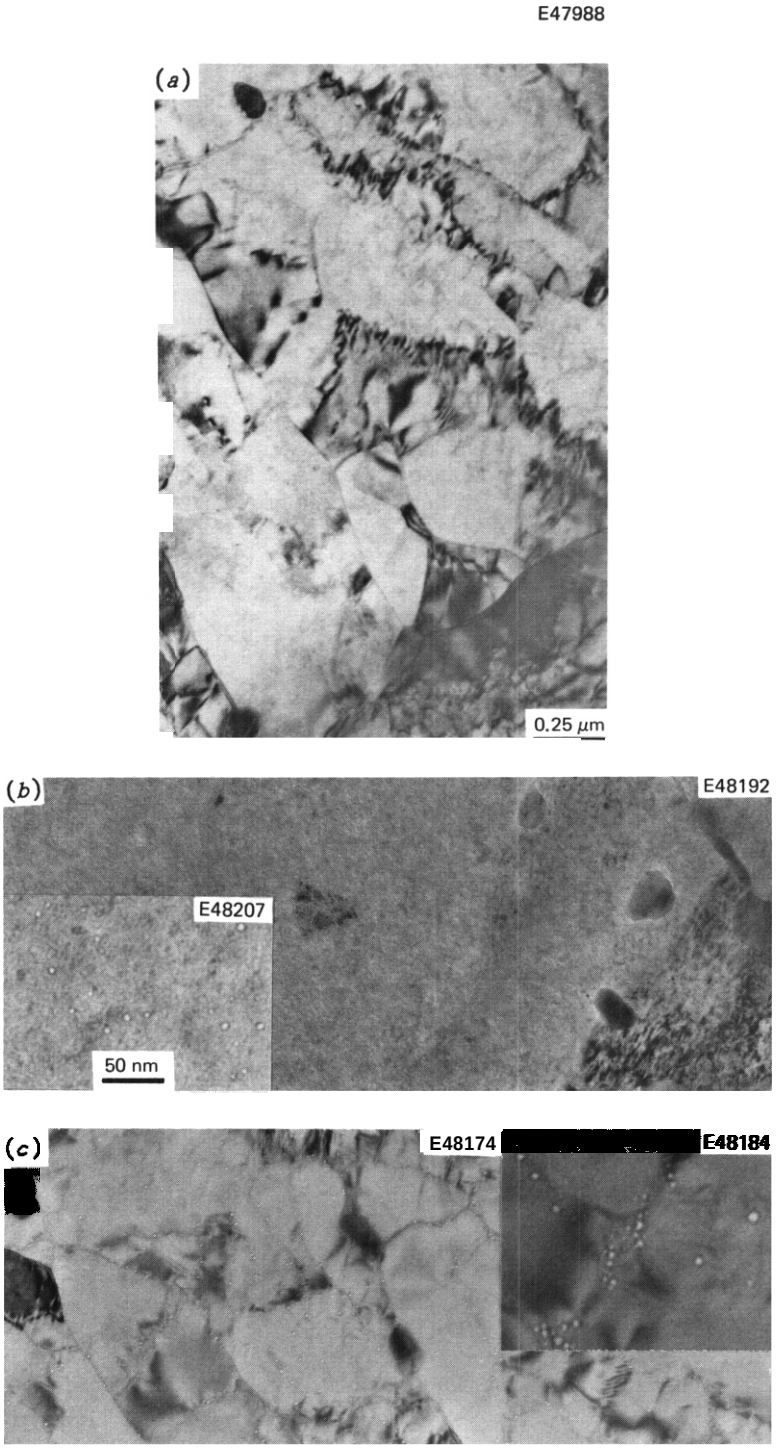

Fig. 7.1.3. Microstructural comparison of the subgrain structure of 9Cr-1MoVNb-2Ni (e) as-tempered and after HFIR irradiation to ~37 to 39 appm and 410 appn He at (b) 300°C, and (c) 600°C. High magnification insets show bubbles in (b) and (c).

There is an obvious difference in precipitation behavior of the nickel-doped 9-Cr steel as compared to the undoped steel after HFIR irradiation at 400°C [cf Fig. 7.1.2(*a*) and (*c*)]. It raises the question of whether or not increased helium generation alone causes increased void formation. However, irradiation of the same 9Cr-1MoVNb-2Ni alloy in FFTF at 407°C to 47 dpa and ~5 appm He produced nearly the same precipitation as found during HFIR irradiation but with no matrix bubbles or voids [cf Fig. 7.1.2(*c*) and Fig. 7.1.4]. This comparison suggests that the increased helium generation in HFIR is primarily responsible for the increased bubble and void formation, independent of the precipitation produced in 9Cr-1MoVNb-2Ni by irradiation at about 400°C.

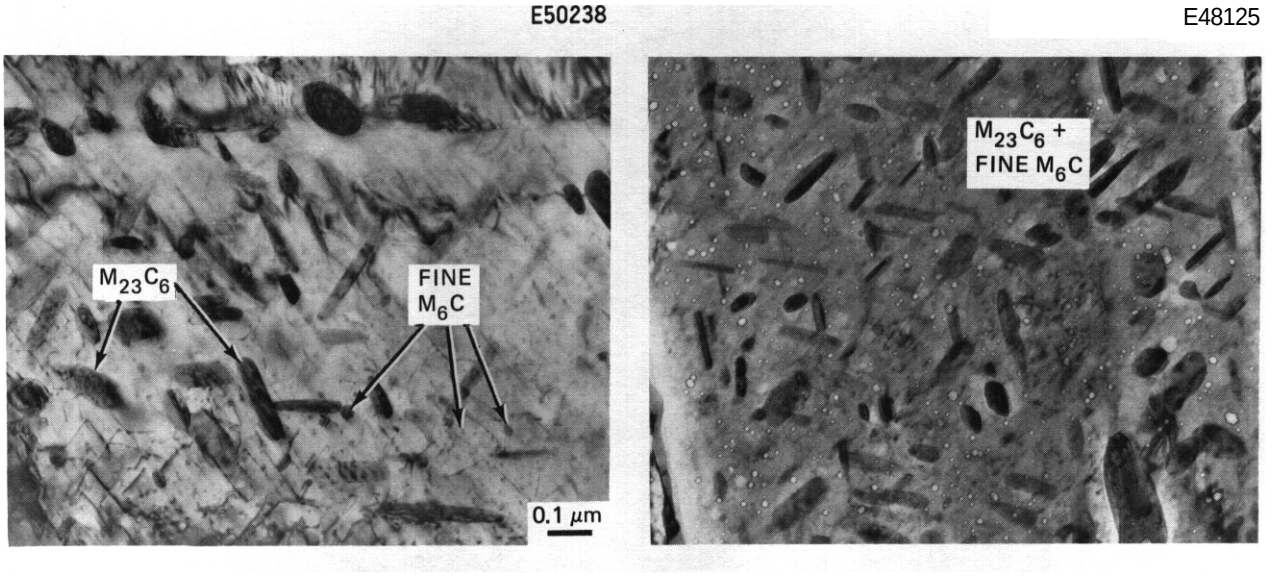

Fig. 7.1.4. Microstructures of 9Cr-1MoVNb-2Ni irradiated in (*a*) FFTF at 407°C to 47 dpa and 5 appm He and (*b*) HFIR at 400°C to ~37 dpa and 410 appm He. Precipitate and dislocation microstructures about the same for both samples, but void formation increases with helium content.

B. 12Cr-1MoVW, 12Cr-1MoVW-1Ni and 12Cr-1MoVW-2Ni steels. HFIR

Some fine (2–5 nm in diameter) bubbles were found in the grain boundaries of 12Cr-1MoVW irradiated in HFIR at 400 to 600°C to ~37 dpa and ~87 appm He. Larger matrix voids were found at both 400 and 500°C (10–25 nm and 20–40 nm in diameter, respectively). Void formation was spatially nonuniform at both 400 and 500°C and usually occurred in the coarsest regions of the subgrain structure (Figs. 7.1.5 and 7.1.6). Many more voids were found at 400°C than at 500°C. Void swelling was about 0.1% at 400°C and less than 0.1% at 500°C. No voids or bubbles were observed at 300°C.

As with the 9-Cr steels, abundant fine bubble formation was greater at all temperatures in the nickel-doped 12-Cr steels, but voids still formed only at 400 and 500°C. At 500°C, large voids (20–80 nm in diameter) within the coarse X phase particles of the 12Cr-1MoVW-1Ni instead of in the matrix (the 12Cr-1MoVW-2Ni has not yet been examined). At 400°C, matrix void formation was more uniform in the nickel-doped 12-Cr steels, but swelling appeared to be similar or less than in the undoped steel (Fig. 7.1.5). The matrix void size was refined in 12Cr-1MoVW-1Ni (7–19 nm in diameter) relative to 12Cr-1MoVW, but void size and distribution in 12Cr-1MoVW-2Ni were similar to the undoped steel. The as-tempered subgrain structure of the 12Cr-1MoVW-2Ni was finer than the other 12-Cr steels and at 400°C the smallest subgrains had fewer and smaller voids than the largest subgrains. The general correlation of void formation with subgrain size for all the 12-Cr steels suggests that subgrain boundaries may be strong sinks which hinder void formation.

7.1.4.3.2 Subgrain Structure and Precipitate Microstructure. 9- and 12-Cr Steels

A. As tempered

The 9Cr-1MoVNb steel contained polygonized, fairly dislocation-free ferrite subgrains after normalizing and then tempering for 1 h at 760°C. Coarse $M_{23}C_6$ particles were distributed along prior austenite grain boundaries and along some of the subgrain boundaries. Finer MC particles were found along subgrain boundaries and within subgrains. AEM analysis of relative phase fractions revealed ~85% $M_{23}C_6$ and 15% MC. The 9Cr-1MoVNb2Ni showed less recovery after tempering for 5 h at 700°C, with lenticular subgrains and more dislocations. There were no differences in precipitation relative to 9Cr-1MoVNb.

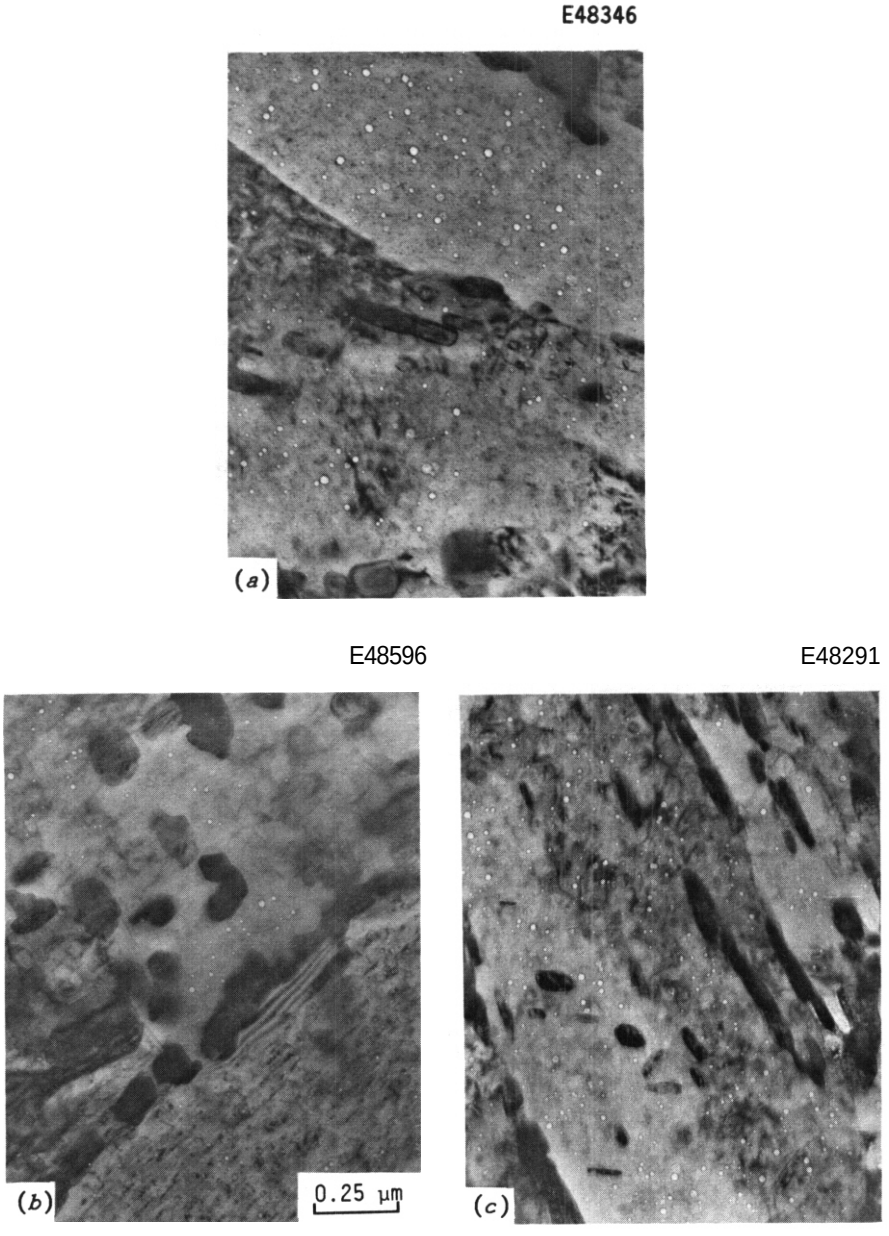

Fig. 7.1.5. Microstructures of (a) 12Cr-1MoVW (87 appm He), (b) 12Cr-1MoVW-1Ni (217 appm He), and (c) 12Cr-1MoVW-2Ni (440 appm He) irradiated in HFIR at 407°C to 36 to 39 dpa.

The 12Cr-1MoVW steel tempered for 2.5 h at 780°C had dislocation-free subgrain structure similar to the 9Cr-1MoVNb although the subgrains were finer. Because the 12Cr-1MoVW steel had more carbon than the 9Cr-1MoVNb steel, it contained more carbide precipitation [3.5 as compared to 1.4 wt % (refs. 16,17)], which was analyzed to be 99% $M_{23}C_6$ and 1% MC. This same tempering treatment produced a similar structure in the 12Cr-1MoVW-1Ni. However, in the 12Cr-1MoVW-2Ni steel, a 5-h temper at 700°C produced a finer subgrain structure with more dislocations and some refinement of the $M_{23}C_6$ precipitation. Again, nickel-doping did not affect the precipitate phases produced in the 12-Cr steels during tempering.

B. HFIR irradiated

HFIR irradiation of 9Cr-1MoVNb and -2Ni at 300 to 500°C produced a dense dislocation structure, considerable coarsening of the subgrain structure, and apparently some dissolution of the as-tempered precipitate structure. These effects were more pronounced at the lower temperature (Fig. 7.1.3). By contrast, at 600°C, both doped and undoped 9-Cr steels had subgrain and precipitate structures that were similar to or finer than the as-tempered structure (Fig. 7.1.3). Most of the smallest as-tempered MC particles appeared to dissolve at 300 to 500°C, while many coarser ones were found after irradiation in both doped and undoped

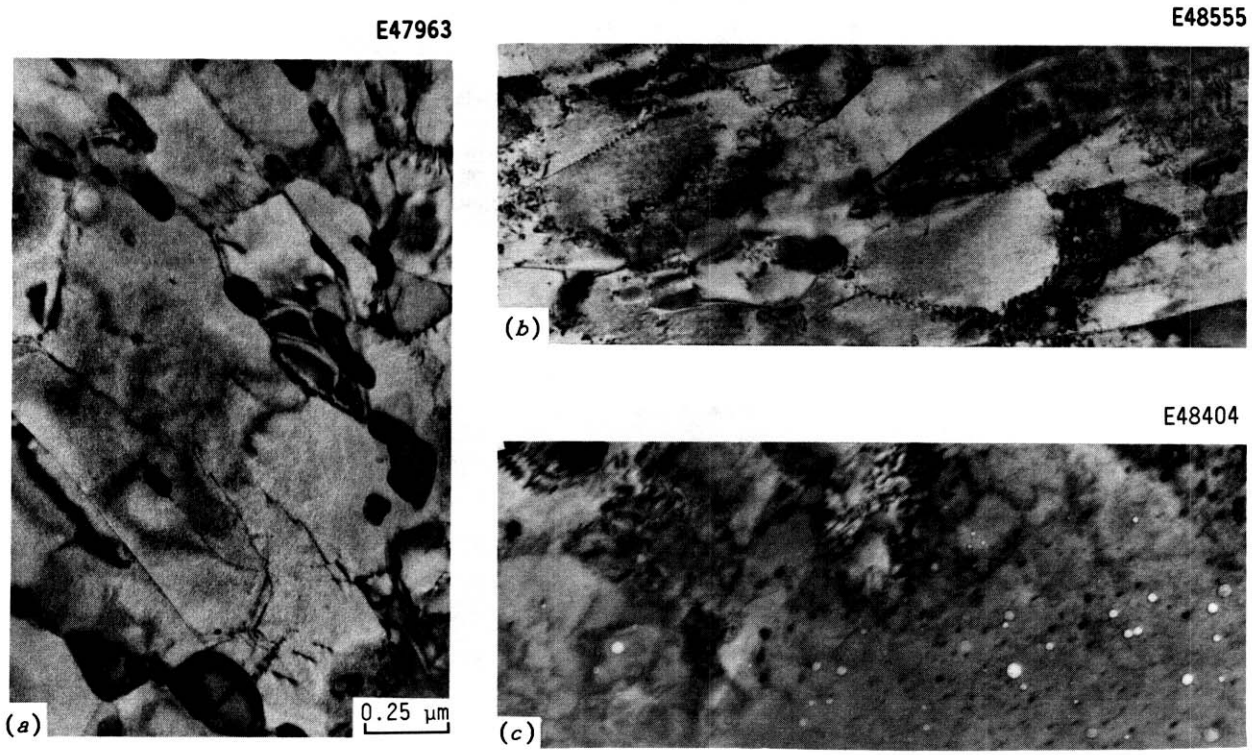

Fig. 7.1.6. Microstructures of the subgrain structure of 12Cr-1MoVW (*a*) as-tempered and after HFIR irradiation at (*b*) 300°C, and (*c*) 500°C to 37 to 39 dpa and ~87 appm He.

9-Cr steels (Fig. 7.1.7). Irradiation produced additional precipitation in the 9Cr-1MoVNb-2Ni steel at 400 and 500°C but not in the 9Cr-1MoVNb steel. Irradiation of 9Cr-1MoVNb-2Ni at 400°C produced copious amounts of coarse $M_{23}C_6$ [Fig. 7.1.2(*c*)] and fine M_6C (η) particles [Fig. 7.1.8(*a*)], some fine M_2X rods, and a few coarse χ particles (with internal voids). Irradiation at 500°C produced many more coarse χ phase particles with internal voids [Fig. 7.1.2(*d*)], together with abundant, fine M_6C and a few fine M_2X rods.

ORNL PHOTO 1841-86

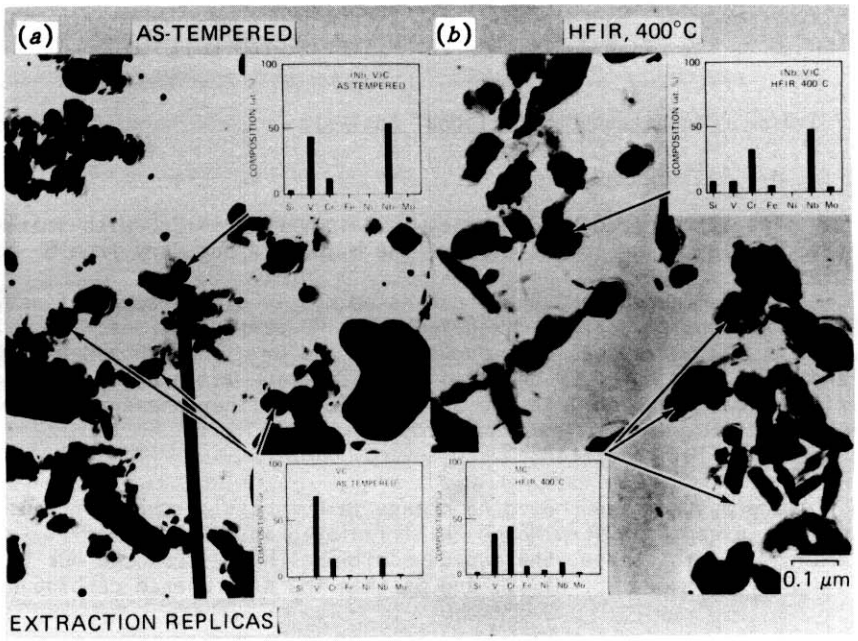

Fig. 7.1.7. Micrographs of precipitate extraction replicas of 9Cr-1MoVNb (*a*) as-tempered and (*b*) HFIR irradiated at 400°C to 37 dpa and 32 appm He. Compositional histograms of MC phase particles determined by quanitative XEDS analysis are included for each specimen. Note the particle coarsening and compositional evolution for (*b*) compared to (*a*).

By contrast, the as-tempered $M_{23}C_6$ carbide and subgrain structures of the doped and undoped 12-Cr steels remained stable during irradiation at various temperatures, with the exception of 12Cr-1MoVW at 500°C. Irradiation produced dislocation loops and/or networks at 300 to 500°C in all steels. But at 500°C, there was considerable coarsening of the subgrain and precipitate structure of the 12Cr-1MoVW during irradiation, as well as replacement of the coarse, as-tempered $M_{23}C_6$ with irradiation-produced M_6C. Fine MC evolved and coarsened during irradiation at 300 to 500°C for all of the 12-Cr steels, and copious amounts of fine M_6C was produced at 400 and 500°C. Similar to the 9-Cr steels, nickel doping caused additional formation of a few coarse χ phase particles (with internal voids) at 400°C, but many more at 500°C. Fine M_2X rods and occasional, fine G-phase particles have thus far been found only in 12Cr-1MoVNb irradiated at 500°C (Fig. 7.1.8).

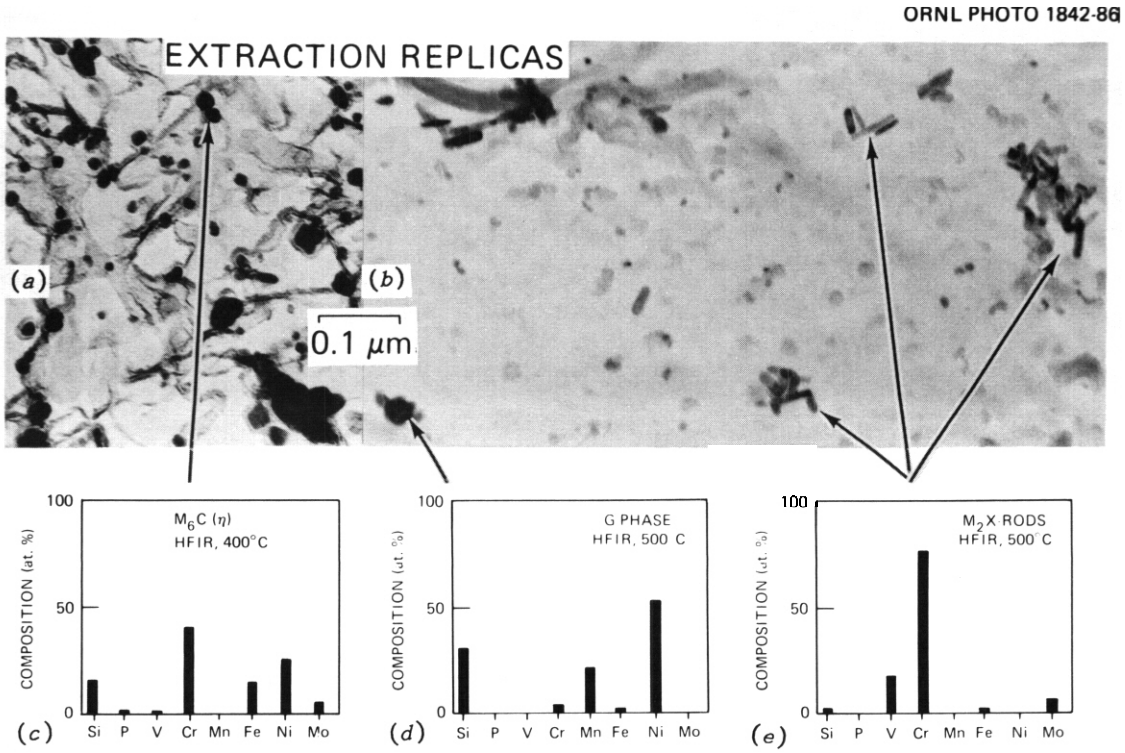

Fig. 7.1.8. Micrographs of precipitate extraction replicas from (a) 9Cr-1MoVNb-2Ni irradiated in HFIR at 400°C to 37 dpa and 410 appm He, and (*b*) 12Cr-1MoVW irradiated in HFIR at 500°C to 38 dpa and 87 appm He. Histograms show phase compositions determined from quantitative XEOS for fine (*c*) M_6C (η) particles from (a), and (*d*) G-phase, and (e) M_2X rods from (*b*).

7.1.3.3 Precipitate Compositional Analysis

A. As-tempered

The as-tempered $M_{23}C_6$ phase was mainly rich in Cr, with smaller concentrations of Fe, V, and Mo (Fig. 7.1.9). The composition of the $M_{23}C_6$ did not vary from 9- to 12-Cr steels or change with nickel doping.

The as-tempered MC phase consisted mostly of coarse and fine vanadium-rich MC (VC) particles, with a lesser amount of coarse, mixed V/Nb-rich MC particles [see Fig. 7.1.7(*a*)]. The VC phase was very rich in V (~75 at. %), with smaller amounts of Nb and Cr. The (Nb,V)C had, on average, >50 at. % Nb, a little less V, and small amounts of Cr and Si. The VC carbide was present in all the 9- and 12-Cr steels, but the niobium-rich MC was found only in the 9-Cr steels. Neither phase was affected by nickel doping.

B. HFIR irradiated

The $M_{23}C_6$ phase showed no change in composition during irradiation at 300 to 500°C in any of the steels, except for 9Cr-1MoVNb-2Ni irradiated at 400°C. Samples irradiated at 600°C have not yet been examined. In this case, the copius additional $M_{23}C_6$ produced during irradiation contained less Cr and Mo, and slightly more Fe, Nb, Ni, V, and Si than the as-tempered carbide (Fig. 7.1.9).

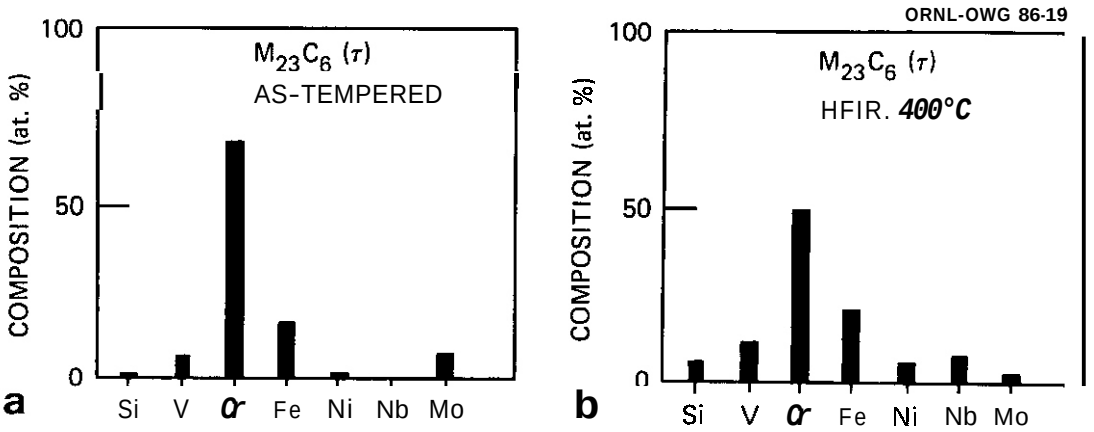

Fig. 7.1.9. Comparison of $M_{23}C_6$ phase compositions for particles analyzed via quantitative XEDS on extraction replicas from 9Cr-1MoVNb-2Ni (*a*) as-tempered and (*b*) after irradiation at 400°C to 37 dpa and 400 appm He.

Both the V- and Nb-rich MC phases showed compositional changes during HFIR irradiation at 300 to 500°C which were similar in all the 9- and 12-Cr steels, nickel-doped and undoped. The V-rich MC was dominant after irradiation and contained much less V and slightly less Nb while having much more Cr and traces of Si, Ni, Fe, and Mo relative to the as-tempered phase (Fig. 7.1.7). The mixed V/Nb-rich MC phase, which was more abundant after irradiation, also was much richer in Cr and poorer in V while picking up traces of Mo, Fe, and Si, relative to the as-tempered phase.

During irradiation at 400 and 500°C, the M_6C (η) was the dominant fine precipitate phase produced. Although identification by diffraction analysis is incomplete, the composition of this phase was similar to that found in precipitates in type 316 stainless steel irradiated in HFIR at 425 to 450°C which were positively identified as η phase.[illegible] The η phase was primarily rich in Cr, Ni, and Si, as shown in Fig. 7.1.8, while containing some Fe and traces of Mo, P, and V. The phase composition was identical in nickel-doped 9- and 12-Cr steels, but apparently was enriched only in Si and Cr in the 12Cr-1MoVW steel irradiated at 400°C. Only very coarse η was found in 12Cr-1MoVW steel irradiated at 500°C, but it had the same composition as the fine Cr/Ni/Si-rich η phase shown in Fig. 7.1.8.

Traces of fine G-phase were found in 12Cr-1MoVW irradiated at 500°C. This phase was enriched in Si, Ni, and Mn (Fig. 7.1.8). The fine M_2X rods found in 9Cr-1MoVNb-2Ni at 400 and 500°C and 12Cr-1MoVW at 500°C contained mainly Cr and some V, with traces of Mo, Si, and Fe (Fig. 7.1.8).

The large, void-containing χ phase particles observed in the thin foils of the nickel-doped 9- and 12-Cr steels were not found on the extraction replicas for analysis.

7.1.4.4 Discussion

Increased void and bubble nucleation in the irradiated nickel-doped steels appears to be a direct consequence of the increased helium generation rather than an artifact caused by the addition of nickel to the alloys. Although nickel doping had no detectable effect on the phase nature and composition in the as-tempered condition, it does seem to influence the phase evolution in the 9Cr-1MoVNb steel during irradiation at 400 and 500°C. In particular at 400°C in HFIR, the 9Cr-1MoVNb-2Ni steel had abundant irradiation-produced $M_{23}C_6$ and M_6C precipitation whereas the 9Cr-1MoVNb steel did not. However, the comparison of HFIR- and FFTF-irradiated 9Cr-1MoVNb-2Ni steels showed no difference in radiation-produced $M_{23}C_6$ and M_6C precipitation, suggesting that the difference in void evolution clearly correlates with the increased helium generation in HFIR. The fact that nickel-doping does not affect precipitation significantly in the 12-Cr steels with a stable as-tempered structure suggests that the instability of the as-tempered structure in the 9-Cr steel plays some role in subsequent phase evolution during irradiation.

Our data suggest that helium bubble (gas-driven cavities) formation is a crucial, but not sufficient, step in nucleating voids (bias-driven cavities), consistent with a critical-cavity-size theoretical approach to void formation.[26] Further, our data suggest a balance of dislocation and cavity sink strength for matrix void formation only at 400°C. Ideas to explain void resistance of the ferritics based on solute trapping' or dislocation loop induced[27,28] reductions in vacancy supersaturation do not seem to explain helium-enhanced void formation. Our data does not entirely support the intrinsically low steady-state void swelling rates and low biases claimed for the ferritic steels,[26,30] because it appears that void nucleation is occurring. Finally, we see abundant voids together with copious fine precipitation, which seem contrary to the idea that such fine precipitates may contribute to swelling resistance.[illegible]

Our data are consistent with the idea suggested by Ayrault[30] for ion-irradiated 9Cr-1MoVNb – that subgrain boundaries are strong point-defect sinks in the ferritic steels and that they contribute to void formation resistance when subgrains are small and stable. However, our reactor data at low damage rates and long times indicate far more subgrain instability than he observed during ion irradiation. This may signal the need for caution when looking at ion data to predict void-swelling resistance during neutron irradiation

Finally, our data indicate that irradiation has strong effects on phase formation and stability coincident with void formation and/or subgrain instability and coarsening. The data further suggest that niobium, silicon, nickel, and especially chromium, are segregating toward precipitates. By contrast, chromium primarily diffuses away from precipitates in irradiated austenitic stainless steels.[20] Our observation of M_6C, χ, and M_2X rods produced during irradiation are consistent with the findings of others.[2,31] However, our observation of M_6C as the primary fine precipitate with only traces of G-phase found at 400 to 500°C differs with Gelles and Thomas," who found primarily G-phase and no M_6C. Our observations of irradiation-induced composition modification of $M_{23}C_6$ and MC phases as well as the formation of a silicon/chromium-rich η phase appear to be new findings.

For fusion applications, our results suggest that helium could shorten the incubation period for void formation from projected doses of 150 dpa based on FBR data."" With higher helium levels, it is also possible that even more voids may form during the incubation period. The effects of helium on the steady-state void swelling behavior are not known from these experiments, which are still in the low-swelling transient regime, and must be assessed by higher fluence irradiations.

7.1.5 Conclusions

1. Increased helium (up to 450 appm) enhanced bubble (gas-driven cavity) formation at 300 to 600°C in nickel-doped 9- and 12-Cr steels irradiated in HFIR to ~38 dpa, but voids (bias-driven cavities) formed only at 400 and 500°C.

2. Void formation was maximum at 400°C and greater in 9Cr-1MoVNb-2Ni than the other 9- and 12-Cr steels. However, void swelling was still below 0.5% at ~38 dpa.

3. The absence of bubbles or voids in 9Cr-1MoVNb-2Ni irradiated in FFTF at 407°C to ~47 dpa and ~5 appm He indicates that the void formation of the same steel with a similar microstructure in HFIR at 400°C was due to increased helium generation.

4. As-tempered $M_{23}C_6$ dissolved and the subgrain structures coarsened in the 9-Cr steels irradiated at 300 to 500°C, whereas the microstructure generally remained stable in the 12-Cr steels.

5. Irradiation produced a compositional evolution of the MC phase at 300 to 500°C and produced fine precipitation of primarily M_6C with traces of M_2X and G-phases at 400 and 500°C in the 9- and 12-Cr steels.

7.1.6 Publication

This paper was presented as an invited contribution to the ICFRM-2 meeting, held in Chicago, Illinois, April 13–17, 1986, and will appear in the Proceedings, to be published in the ***Journal of Nuclear Materials.***

7.1.7 References

1. S. D. Harkness, B. J. Kestel, and P. Okamoto, Prepared Discussion, p. 334 in: ***Inter. Conf. Radiation-Induced Voids in Metals,*** eds. J. W. Corbett and L. C. Ianniello, CONF-710601 (USAEC, 1972).

2. E. A. Little, ***Rad. Effects*** 16 (1972) 135

3. K. R. Garr, C. G. Rhodes, and D. Kramer, p. 109, in: ***Effects of Radiation on Substructure and Mechanical Properties of Metals and Alloys,*** ASTM-STP-529 (1973).

4. W. G. Johnston et al., ***J. Nucl. Mater.*** **54** (1974) 24.

5. F. A. Smidt et al., p. 227 in: ***Irradiation Effects on the Microstructure and Properties of Metals,*** ASTM-STP-611 (1976).

6. ***Radiation Effects in Breeder Reactor Structural Materials,*** eds. M. L. Bleiberg and J. W. Bennett (The Metallurgical Society of AIME, 1977).

7. R. E. Gold et al., ***Nucl. Technol./Fusion*** **1** (1981) 169

8. J. I. Bramman et al., ***Radiation Effects in Breeder Reactor Structural Materials,*** eds M. L. Bleiberg and J. W. Bennett (The Metallurgical Society of AIME, 1977) 479.

9. J. J. Huet et al., p. 5 in: ***Irradiation Behavior of Metallic Materials for Fast Reactor Core Components,*** Ajaccio, France (CEA, 1979).

10. J. Erler et al., p. 11 in: ***Irradiation Behavior of Metallic Materials for Fast Reactor Core Components,*** Ajaccio, France (CEA, 1979).

11. D. S. Gelles and L. E. Thomas, p. 559 in: *Proc. Topical Conf. on Ferritic Alloys for Use in Nuclear Energy Technologies.* eds. J. W. Davis and D. J. Michel (The Metallurgical Society of AIME, 1984).

12. D. S. Gelles, *J. Nucl. Mater.* **122** and **123** (1984) 207

13. R. L. Klueh, *Nucl. Eng. and Design* **72** (1982) 329.

14. T. Lechtenberg, *J. Nucl. Mater.* **133** and **134** (1985) 149.

15. R. L. Klueh and M. P. Tanaka, *J. Metals* **37** (Oct. 1985) 16.

16. J. M. Vitek and R. L. Klueh, p, 551 in: *Proc. Topical Conf. on Ferritic Alloys for Use in Nuclear Energy Technologies,* eds. J. W. Davis and D. J. Michel (The Metallurgical Society of AIME, 1984).

17. J. M. Vitek and R. L. Klueh, *J. Nucl. Mater.* **122** and **123** (1984) 254.

18. D. S. Gelles, p. 129 in: *ADIP Semiannu. Prog. Rept., March 31, 1985,* DOE/ER-0045/14, Office of Fusion Energy, U.S. Department of Energy.

19. P. J. Maziasz, *J. Nucl. Mater.* **122** and **123** (1984) 472.

20. P. J. Maziasz, "Effects of Helium Content on Microstructural Development in Type 316 Stainless Steel under Neutron Irradiation," Oak Ridge National Laboratory report, DRNL-6121 (November 1985).

21. L. L. Horton and J. Bentley, p. 569 in: *Proc. Topical Conf. on Ferritic Alloys for Use in Nuclear Energy Technologies,* eds. J. W. Davis and D. J. Michel (The Metallurgical Society of AIME, 1984).

22. G. Ayrault, p. 182 in: *DAFS Quart. Prog. Rept., February 1982,* DOE/ER-0046/8, Vol. 1, USDOE, Office of Fusion Energy.

23. R. L. Klueh, J. M. Vitek, and M. L. Grossbeck, p. 648 in: *Effects of Irradiation on Materials; Eleventh Conf.,* ASTM-STP-782, eds. H. R. Brager and J. S. Perrin (American Society for Testing and Materials, 1982).

24. M. L. Grossbeck, J. W. Woods, and G. A. Potter, p. 36 In: *ADIP Quart. Prog. Rept., Sept. 30, 1980,* DOE-ER-0045/4, Office of Fusion Energy, U.S. Department of Energy.

25. L. R. Greenwood, p. 22 in: *ADIP Semiannu. Prog. Rept., March 31, 1985,* DOE/ER-0045/14, Office of Fusion Energy, U.S. Department of Energy.

26. L. L. Horton and L. K. Mansur, p. 344 in: *Effects of Radiation on Materials: Twelfth International Symposium,* ASTM-STP-870, eds. F. A. Garner and J. S. Perrin (American Society for Testing and Materials, 1985).

27. E. A. Little, R. Bullough, and H. M. Wood, *Proc. Royal Soc.* **A372** (1980) 565.

28. R. Bullough, H. M. Wood, and E. A. Little, p. 593 in: *Effects of Irradiation on Materials: Proc. Tenth International symposium,* ASTM-STP-725, eds. D. Kramer, H. R. Brager, and J. S. Perrin (American Society for Testing and Materials, 1981).

29. J. J. Sniegowski and W. G. Wolfer, p. 579 in: *Proc. Topical Conf. on Ferritic Alloys for Use in Nuclear Energy Technologies,* eds. J. W. Davis and O. J. Michel (The Metallurgical Society of AIME, 1984) 34.

30. G. Ayrault, *J. Nucl. Mater.* **114** (1983) 34.

31. L. P. Stoter and E. A. Little, p. 369 in: *Conf. Proc. Advances in Physical Metallurgy and Applications of Steels* (The Metals Society, London, 1981).

7.2 ON THE SATURATION OF THE DBTT SHIFT OF IRRADIATED 12Cr-1MoVW WITH INCREASING FLUENCE – J. M. Vitek, W. R. Corwin and R. L. Klueh (Oak Ridge National Laboratory), and J. R. Hawthorne (Materials Engineering Associates)

7.2.1 ADIP Task

ADIP tasks are not defined for Path E, Ferritic Steels, in the 1978 Program Plan.

7.2.2 Objective

The objective of this work is to determine whether or not the amount of irradiation damage in 12Cr-1MoVW steel, as measured by the shift in the ductile to brittle transition temperature, saturates with increasing fluence, and if so at what fluence.

7.2.3 Summary

Identical subsize Charpy specimens of 12Cr-1MoVW steel were irradiated at 300°C to a fluence of 0.86 × 10^{24} n/m² (E > 0.1 MeV) and at 300 and 400°C to a fluence of ~1 × 10^{26} n/m² (E > 0.1 MeV). Impact testing indicated the DBTT was increased by irradiation at 300°C by 36 and 164°C, respectively, for the low and high fluences. Irradiation at 400°C led to an increase in the DBTT of 217°C. Aging alone has an insignificant effect on the impact properties. The major portion of the irradiation embrittlement at 300°C occurs for fluences beyond 1 × 10^{24} n/m².

7.2.4 Introduction

Ferritic/martensitic steels are considered one of the prime candidate materials for structural applications in fusion reactors.' This class of steels provides many advantages including excellent swelling resistance and high thermal conductivity. A review of current results on the suitability of ferritic/martensitic steels reveals their corrosion behavior and postirradiation properties are, in general, quite promising.' However, a major concern is the existence in these steels of a ductile-to-brittle transition temperature (DBTT), below which the steel has limited ductility and fails in a brittle mode. Although the DBTT, as measured in a Charpy impact test, may be below room temperature in the unirradiated condition, irradiation can increase the DBTT significantly and the increase depends on the irradiation temperature.[3-6] Increases in the DBTT of greater than 100°C have been measured following irradiation at 400°C and below.

The potential applications for ferritic steels in a fusion reactor would involve very high irradiation fluences. Therefore, it is necessary to know how the postirradiation properties vary as a function of fluence and, in particular, how the degradation of impact properties behaves with increasing fluence. Earlier work on low-alloy pressure vessel steels has shown rapid embrittlement with increasing fluence at low fluences, but a marked decrease in the rate of embrittlement (as measured by the upward shift in DBTT) beyond fluences of approximately 2 × 10^{23} n/m² (E > 0.1 MeV).' Such results suggest the shift in DBTT may saturate at some low fluence, with only minor changes for higher fluences. It is necessary to determine if such a saturation of the DBTT shift occurs in the Cr-Mo ferritic steels of interest. Furthermore, it is necessary to evaluate the shift in DBTT at considerably greater fluences since even a small rate of embrittlement above 10^{23} n/m² would result in a large additional shift of the DBTT when extrapolated several orders of magnitude to fusion-relevant fluences of 10^{26} n/m² and greater. Unfortunately, the data available in the literature do not allow for such an assessment of impact properties as a function of fluence.

The change in DBTT following irradiation is expected to be a function of several variables, including the following: alloy, heat chemistry, heat treatment, specimen geometry and orientation, irradiation flux and spectrum, temperature, fluence, helium production rate during irradiation, and experimental method of evaluation. To date, the data available are difficult to compare because all of these parameters have varied from experiment to experiment. The present experiment was undertaken to address more directly the question of a saturation of radiation-induced embrittlement with increasing fluence. Samples of the same alloy, heat number, heat treatment, specimen geometry and orientation were tested under identical conditions following irradiation in two different reactors. By examining specimens irradiated to two different fluences, it was hoped an assessment of the fluence dependence of Charpy impact properties could be made.

7.2.5 Experimental Procedures

The 12Cr-1MoVW steel was hot-rolled plate from an electroslag-remelted heat (National Fusion heat 9607-R2). The alloy composition is given in Table 7.2.1. The alloy was normalized and tempered as follows: 1050°C/0.5 h/air cool + 780°C/4 h/air cool. Miniature Charpy V-notch (C_v) specimens were machined from the heat-treated plate in the longitudinal (LT) orientation. Figure 7.2.1 shows the specimen geometry and dimensions. Such miniature specimens, used because of space limitations in the reactor, show irradiation effects similar to those found in full-sized C_v specimens.'

Samples were irradiated in two reactors. The irradiation to a low fluence of 0.86 × 10^{24} n/m² (E > 0.1 MeV) (ref. 5) was performed in the light water cooled and moderated test reactor at the State University of New York at Buffalo (UBR). The higher fluence irradiation was conducted in the High Flux Isotope Reactor (HFIR) at Oak Ridge National Laboratory and reached 0.5 to 1.2 × 10^{26} n/m² (E > 0.11 MeV) (ref. 9). The

Table 7.2.1. Composition (wt %) of 12Cr-1MoVW Alloy Investigated (HT 9607-R2)

Element	Weight Percent	Element	Weight Percent
Cr	12.1	Si	0.17
Mo	1.04	P	0.016
Ni	0.51	S	0.003
Mn	0.57	N	0.027
V	0.28	Ti	0.001
W	0.45	Al	0.006
C	0.20	cu	0.07

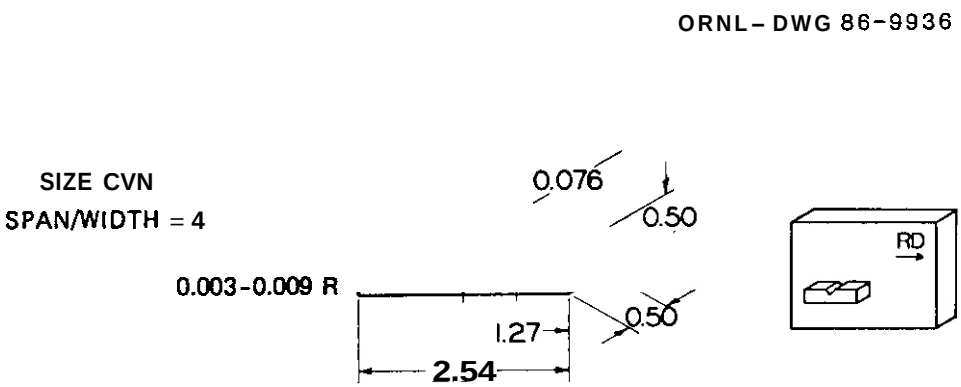

Fig. 7.2.1. Specimen geometry and dimensions used for miniature Charpy V-notch samples. Dimensions given in cm.

exact fluence depended on the position of the sample within the experimental assembly. The flux in HFIR was approximately 40 times greater than that in UBR. Corresponding displacement damage levels are <0.1 dpa (UBR) and 4 to 9 dpa (HFIR). Specimens were irradiated at 300°C in the UBR, and at both 300 and 400°C in HFIR (in a single experiment). In order to assess the effect of exposure at elevated temperatures alone, control specimens were aged at 300 and 400°C for times equivalent to the irradiation period in HFIR (2500 h). During irradiation in HFIR, continuous helium production resulted from a transmutation reaction between nickel and the thermal neutrons. For the fluences achieved, a maximum helium concentration of ~25 at. ppm He was produced.[9]

Samples were tested in a pendulum-type impact machine specially modified to accommodate the miniature specimens. The details of the test equipment are given elsewhere.[10] Impact energy versus test temperature curves were generated by fitting a hyperbolic tangent function to the data. Due to the limited number of specimens available, the upper-shelf energy (USE) could not always be determined accurately. The DBTT was chosen at a fixed energy level of 9.2 J, corresponding to the frequently used criterion of 68 J in a full-size specimen.

7.2.6 Results

The results of impact tests following irradiation at 300°C are presented in Fig. 7.2.2. Also shown are the impact properties for the unirradiated controls and the controls aged 2500 h at 300°C. The values for the USE and the DBTT are given in Table 7.2.2. The results show that aging at 300°C has no effect on the impact behavior. The low-fluence irradiation resulted in a modest increase in the DBTT of 36°C and a concurrent decrease in the USE of 3 J (13%). In contrast, the impact properties were degraded considerably more by the high-fluence (4 to 9 dpa) irradiation in HFIR. The increase in DBTT was 164°C and the USE dropped 8 J (33%) to a value of 16 J.

Impact properties following irradiation at 400°C are given in Fig. 7.2.3, along with results on unirradiated controls and aged samples. Irradiation at 400°C was only conducted in HFIR. Values for the USE and DBTT are given in Table 7.2.2. As was the case for aging at 300°C, aging at 400°C resulted in no significant change in either the USE or the DBTT. However, irradiation at 400°C resulted in a substantial drop in the USE of 12 J (50%) and a large increase in the DBTT of 217°C.

7.2.7. Discussion

Before evaluating the results on the miniature samples in detail, it is of interest to confirm the reliability of these smaller specimens. As noted earlier, tests on unirradiated 12Cr-1MoVW (a different heat) showed good agreement between results for the two specimen sizes.[8] However, a direct comparison of

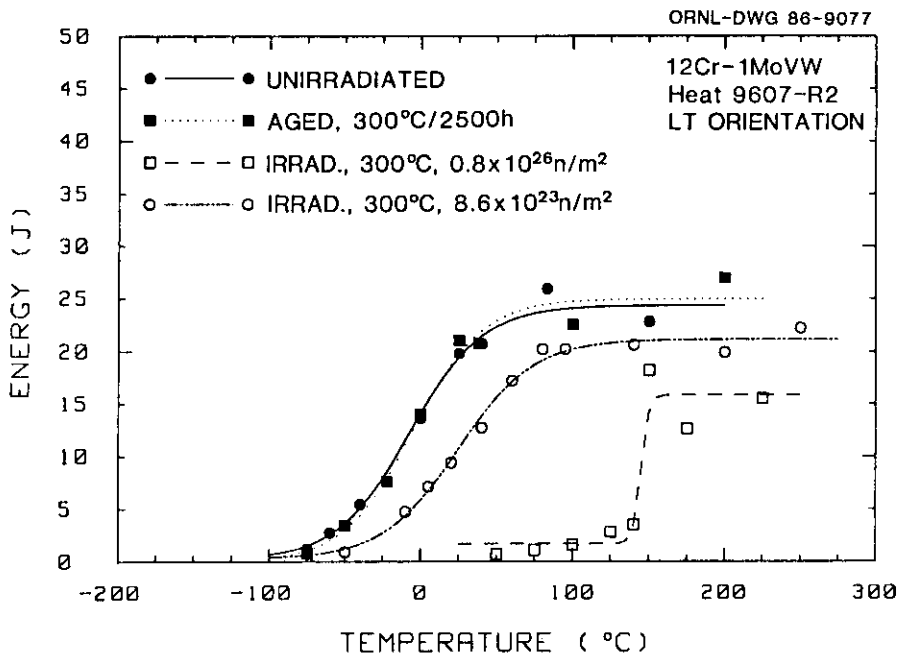

Fig. 7.2.2. Charpy impact properties of controls and samples aged or irradiated at 300°C.

the irradiated 12Cr-1MoVW used in this experiment is also possible. Results on full-size specimens taken from the same heat-treated plate and orientation as those used in the present tests have been published.[5] These specimens were irradiated in the same UBR experiment at 300°C to the identical fluence. An increase in DBTT of 47°C was found, in good agreement with the 36°C increase found for the miniature specimens. A drop of 13% in the USE was found for the full-size specimens, which was identical to that found for the miniature specimens. Thus, the miniature specimens are a reliable means for measuring the impact properties of irradiated specimens as well as unirradiated specimens, at least for the 12Cr-1MoVW steel.

Considering first the results after irradiation at 300°C, it is clear from Fig. 7.2.2 that a substantial additional degradation of impact properties occurred after the higher fluence irradiation in HFIR compared to the lower fluence irradiation in UBR. The shift in DBTT was 350% greater, and the decrease in USE was 170% more. Data are unavailable to determine whether the UBR irradiation was to a fluence beyond the value at which a marked decrease in the degradation rate occurs. If the irradiation to 0.86×10^{24} n/m² was beyond such a transition point (saturation fluence), the data indicate a modest rate of degradation still exists resulting in a significant additional embrittlement when extrapolated two orders of magnitude to a fluence of $\sim 1 \times 10^{26}$ n/m². However, several factors may be responsible for simply shifting the saturation fluence beyond the fluence of the UBR irradiation. The fluence at which the rate of embrittlement decreases dramatically may be a function of the alloy and the irradiation temperature, and may be higher than the

Table 7.2.2. Charpy Impact Properties[a] of Unirradiated, Aged, and Irradiated 12Cr-1MoVW

	DBTT[b] (°C)	ADBTT (Irrad) (°C)	USE (J)
Unirradiated	−19	--	24
Aged 300°C/2500 h	−17	--	25
Irradiated 300°C to 0.86 × 10^{24} n/m²	17	36	21
Irradiated 300°C to 0.5–1.0 × 10^{26} n/m²	145	164	16
Aged 400°C/2500 h	−19	--	25
Irradiated 400°C to 1.0–1.2 × 10^{26} n/m²	198	217	12

[a]Miniature-size specimens.

[b]At 9.2 J.

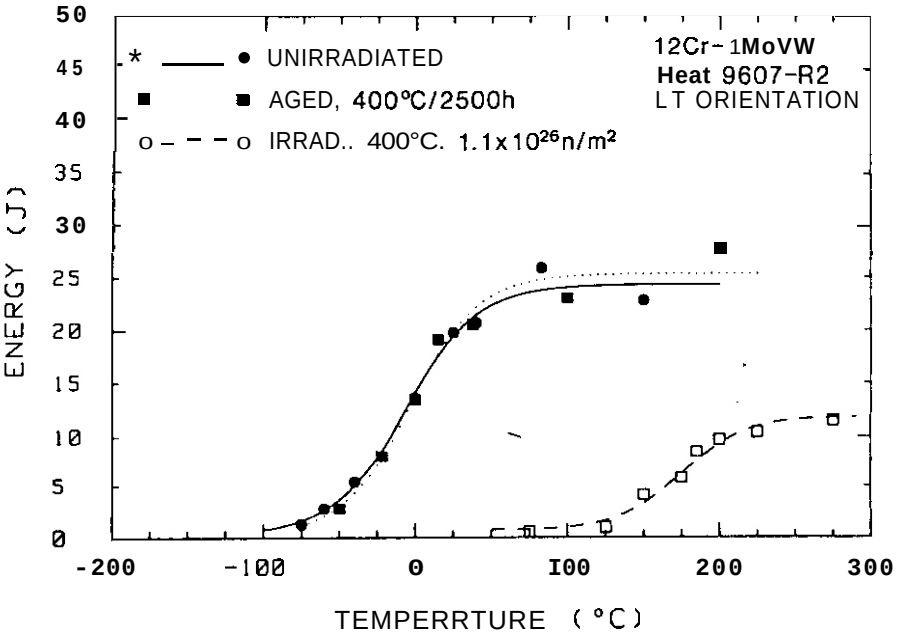

Fig. 7.2.3. Charpy impact properties of controls and samples aged or irradiated at 400°C.

value of 2 × 10^{23} n/m² found for pressure vessel steels. Furthermore, if a saturation in the DBTT shift does exist, the saturation level may be a function of the displacement damage rate and helium concentration (see later discussion). Therefore, the saturation level may be different for the irradiation conditions in the two reactors. More work is needed to separate these effects. Such details are, however, secondary to the major point that the fluence difference between the HFIR and UBR irradiation leads to significantly different degrees of embrittlement. Furthermore, the HFIR irradiation conditions are more relevant to expected fusion reactor irradiation conditions with regard to both fluence and displacement damage rates.

The next consideration is whether an additional shift in DBTT occurs beyond a fluence of ~1 × 10^{26} n/m². Data at higher fluences are not available on heat 9607-R2. Results on another heat of 12Cr-1MoVW irradiated in the EBR-II reactor at 390°C to fluences of 3 and 6 × 10^{26} n/m² have been reported recently.[3,4] Although impact tests on these samples involved different experimental parameters, a comparison of the shift in DBTT with increasing fluence is informative. An additional shift of 20° from 124 to 144°C, was found upon increasing the fluence from 3 to 6 × 10^{26} n/m². However, this difference is very

likely to be within the experimental error since only four specimens were tested at each fluence. This conclusion is supported by the fact that a decrease in the DBTT shift with increased fluence (from 3 to 6 × 10^{26} n/m²) was found after irradiation at 550°C.[4] It may be concluded, therefore, that the shift in DBTT does not change significantly with increasing fluence from 3 to 6 × 10^{26} n/m². It is assumed that little, if any, additional shift in DBTT occurs between ~1 × 10^{26} n/m² (examined in this study) and 3 × 10^{26} n/m².

The change in Charpy impact properties can also be examined as a function of irradiation temperature. The results of several investigators are combined in Fig. 7.2.4. Only qualitative comparisons can be made

ORNL-DWG 86-9217

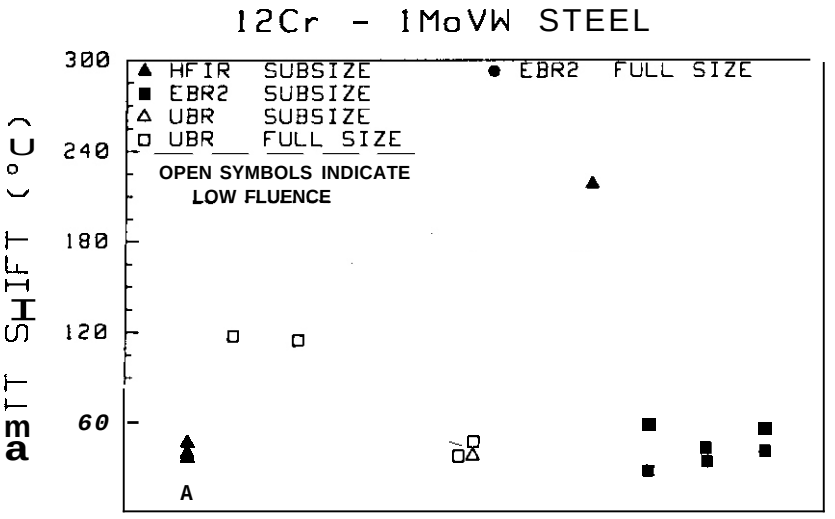

Fig. 7.2.4. Composite of Charpy impact properties of 12Cr-1MoVW versus irradiation temperature, taken from present results and refs. 3-6, 11-13.

since the results shown in Fig. 7.2.4 represent different experimental conditions. The data for fluences greater than ~0.5 × 10^{26} n/m² (to a maximum of ~6 × 10^{26} n/m²) are considered first. As noted above, it is reasonable to assume that for these fluences the dependence of the shift in DBTT (ADBTT) on fluence is small. The results from the present study as well as from the literature[3,4,6,11,12] on 12Cr-1MoVW indicate that ADBTT increases with increasing temperature for irradiation temperatures from room temperature to ~400°C. Above 400°C, the shift in DBTT decreases with increasing temperature. This behavior is represented by the broad shaded band in Fig. 7.2.4. However, this trend seemingly contradicts the data of Hawthorne et al.,[5] which showed a larger shift in DBTT at irradiation temperatures from UBR of 93 and 149°C than at 288 and 300°C. It is possible to reconcile these findings by realizing that the shift in DBTT results from a balance between damage production and recovery. At higher temperatures, the recovery rate will be greater, and for a given fluence and fixed flux, the net damage should be smaller. Therefore, for the data from UBR irradiations at 93 to 300°C, where the flux and total fluence are essentially constant, less net damage at the higher temperature is expected and this corresponds to the smaller ADBTT observed. Such a simple explanation does not explain the decrease in DBTT shift with decreasing irradiation temperature below ~400°C found for the high fluence data. Some other mechanism must be involved and probably will require extensive structural examination by electron microscopy.

The shift in DBTT for HFIR irradiation at 400°C is substantially higher than the shift measured after irradiation of specimens with the same geometry and orientation at 390°C in EBR-II[6] (ADBTT of 217 versus 166°C). This may be due to heat-to-heat variations, although unirradiated control specimens showed similar behavior for the different heats. Differences in heat treatment may also be responsible, but previous results[11] have indicated the 12Cr-1MoVW impact properties are not sensitive to heat treatment for the range of thermal treatments employed. An alternative explanation may be the difference in helium concentrations produced during irradiation. As noted earlier, the HFIR-irradiated samples contain more irradiation-induced helium and perhaps the relatively low levels present are sufficient to have an effect on the impact properties. Although the low-helium concentrations produced (~25 at. ppm He) were not expected to be significant, the additional 51°C shift in DBTT following HFIR irradiation seems to be beyond the experimental uncertainty. It is possible that the helium may result in a hardening of the matrix, either directly or through an interaction with the dislocation structure, and thereby raise the DBTT. However, evaluation of tensile properties of 12Cr-1MoVW alloys after low-temperature irradiation has not shown any hardening effect attributable to helium.[15] Should the helium concentration be important, the saturation behavior of impact properties following HFIR irradiation may be noticeably different as helium is continually produced with increasing exposures.

Finally, possible long-term effects should be considered. Whether true saturation ever occurs is questionable because of changes that occur during long-term irradiation. The microstructure and precipitation character may change, and evidence for such microstructural instabilities is becoming available following detailed evaluation of long-term irradiated materials.[16] In addition, even if helium has little influence on the properties at the levels examined in the current work, a hardening effect might be expected as the helium concentration increases during longer HFIR irradiation exposures, resulting in a further shift of the DBTT. Although little change in impact properties at temperatures above 400°C has been found to date (in the absence of helium), the effect of larger concentrations of helium may be greatest at higher temperatures where cavity formation at boundaries has been shown to occur after higher fluence irradiations in HFIR.[11] An accumulation of helium at the boundaries may result in a change in the fracture mode to one of intergranular failure, and thereby lead to embrittlement. Thus, even if the degradation rate is low beyond some damage level, higher fluence and higher temperature irradiations must be carried out to insure that other effects do not begin to play a role.

7.2.8 Summary and Conclusions

The Charpy impact properties of a 12Cr-1MoVW alloy were measured after irradiation in the UBR and HFIR to determine the effect of fluence on the degradation of impact properties. Identical specimens were irradiated at 300°C to fluences of 0.86×10^{24} and -1×10^{26} n/m². Additional samples were irradiated at 400°C to a fluence of -1×10^{26} n/m². Unirradiated aged specimens were also evaluated. In combination with other data on post-irradiation Charpy impact properties, the following conclusions can be reached:

1. The major shift in DBTT produced by irradiation at 300°C occurs at fluences beyond 10^{24} n/m².
2. Aging at 300 or 400°C for 2500 h has essentially no effect on the impact properties of 12Cr-1MoVW.
3. The shift in DBTT following irradiation at 400°C is larger after HFIR irradiations than after EBR-II irradiations and may indicate an influence of helium at concentrations as low as 25 at. ppm.
4. The decrease in DBTT shift with decreasing temperature found for irradiation temperatures below 400°C does not follow conventional saturation behavior and further work is required to explain these results.

7.2.9 References

1. R. L. Klueh, ***Nucl. Eng. and Design* 72** (1982) 329–44.

2. T. Lechtenberg, ***J. Nucl. Mater.* 133** and 134 (1985) 149–55.

3. W. L. Hu and D. S. Gelles, ***Proc. Topical Conf. on Ferritic Alloys for Use in Nuclear Energy Technologies,*** eds. J. W. Davis and D. J. Michel (TMS-AIME, Warrendale, PA, 1984), 631–46.

4. W. L. Hu, ***ADIP Semiannu. Prog. Rep. Sept. 30, 1984,*** DOE/ER-0045/13 (USDOE, Office of Fusion Energy, Washington), 106–19.

5. J. R. Hawthorne, J. R. Reed, and J. A. Sprague, ***Effects of Radiation on Materials: Twelfth Inter Symp.***, ASTM STP ***870,*** eds. F. A. Garner and J. S. Perrin (ASTM, Philadelphia, 1985), 580–604.

6. W. R. Corwin, R. L. Klueh, and J. M. Vitek, ***ADIP Semiannu. Prog. Rep. Sept. 30, 1984,*** DOE/ER-0045/13 (USDOE, Office of Fusion Energy, Washington), 120–27.

7. J. R. Hawthorne, ***Treatise on Materials Science and Technology,*** Vol. 25 (Academic Press, New York, 1983), 461–524.

8. W. R. Corwin, R. L. Klueh, and J. M. Vitek, ***J. Nucl. Mater.* 122** and **123** (1984) 343–48.

9. L. R. Greenwood, ***ADIP Semiannu. Prog. Rep. Mar. 31, 1985,*** DOE/ER-0045/14 (USDOE, Office of Fusion Energy, Washington), 22–26.

10. W. R. Corwin and A. M. Hougland, "Effect of Specimen Size and Material Condition on the Charpy Impact Properties of 9Cr-1MoVNb Steel," pp. 325–38 in ***The Use of Small-Scale Specimens for Testing Irradiated Material,*** ASTM STP ***888,*** eds. W. R. Corwin and G. E. Lucas, American Society for Testing and Materials, Philadelphia, 1986.

11. W. R. Corwin, Oak Ridge National Laboratory, unpublished results, 1985

12. D. S. Gelles, W. L. Hu, F. H. Huang, and G. D. Johnson, pp. 115–17 in *ADIP Semiannu. Prog. Rep. Sept. 30, 1983,* DOE/ER-0045/11 (USDOE, Office of Fusion Energy, Washington).

13. F. A. Smidt, Jr., J. R. Hawthorne, and V. Povenzano, *Effects of Radiation on Materials: Tenth Conference,* ASTM STP 725, eds. D. Kramer, H. R. Brager, and J. S. Perrin (ASTM, Philadelphia, 1981), 269–84.

14. B. A. Chin and R. C. Wilcox, *Proc. Topical Conf. on Ferritic Alloys for Use in Nuclear Energy Technologies,* eds. J. W. Davis and D. J. Michel (TMS-AIME, Warrendale, PA, 1984), 347–56.

15. R. L. Klueh, J. M. Vitek, and M. L. Grossbeck, *J. Nucl. Mater.* 103 and 104 (1981) 887–92.

16. P. J. Maziasz, R. L. Klueh, and J. M. Vitek, pp. 91–101 in *ADIP Semiannu. Prog. Rep. Sept. 30, 1985,* DOE/ER-0045/15 (USDOE, Office of Fusion Energy, Washington).

17. J. M. Vitek and R. L. Klueh, *Proc. Topical Conf. on Ferritic Alloys for Use in Nuclear Energy Technologies,* eds. J. W. Davis and D. J. Michel (TMS-AIME, Warrendale, PA, 1984), 551–58.

7.3 THE DEVELOPMENT OF FERRITIC STEELS FOR FAST INDUCED-RADIOACTIVITY DECAY – R. L. Klueh (Oak Ridge National Laboratory)

7.3.1 ADIP Task

ADIP Task I.A.5, Perform Fabrication Analysis, and I.C.1, Microstructural Stability

7.3.2 Objectives

During the operation of a fusion reactor. the structural material of the first wall and blanket structure will become highly radioactive from activation by the high-energy fusion neutrons. A difficult radioactive waste problem will be involved in the disposal of this material after service. One way to minimize the disposal problem is to use structural materials in which the induced radioactivity decays rather quickly to levels that allow for simplified disposal techniques. We are exploring the development of ferritic steels to meet this objective.

7.3.3 Summary

Tensile studies were continued on eight heats of normalized-and-tempered chromium-tungsten steel that contained variations in the composition of chromium, tungsten, vanadium, and tantalum. The results were compared to results for analogous chromium-molybdenum steels.

7.3.4 Prosress and Status

7.3.4.1 Introduction

We have continued the studies to characterize eight heats of ferritic steels designed for fast induced-radioactivity decay (FIRD).' These steels were patterned on the chromium-molybdenum steels that are of interest for fusion-reactor applications – namely, 2.25Cr-1Mo, 9Cr-1MoVNb, and 12Cr-1MoVW steels. The major changes from the chromium-molybdenum steels involve the replacement of molybdenum with tungsten, the use of vanadium in the 2.25% Cr steels, and the replacement of niobium with tantalum in the 9% Cr steel. (Although tantalum can be used in a FIRD steel, the decay of its transmutation products immediately after irradiation in a fast- or mixed-spectrum reactor makes such a steel difficult to study. Therefore, few, if any, irradiated studies will be performed on steels *containing* tantalum.) The composition of the eight steels is given in Table 7.3.1.

We previously reported on the tempering characteristics of these steels and on their tensile behavior after one normalizing-and-tempering heat treatment.' In the present report, tensile results on specimens given a different heat treatment are presented.

Table 7.3.1. Chemical composition of fast induced-radioactivity decay (FIRD) ferritic steels

Alloy	Chemical composition,[a] (wt %)						
	Cr	W	V	Ta	C	Mn	Si
2 1/4 CrV	2.36		0.25		0.11	0.40	0.17
2 1/4 Cr-1WV	2.30	0.93	0.25		0.10	0.34	0.13
2 1/4 Cr-2W	2.48	1.99	0.009		0.11	0.39	0.15
2 1/4 Cr-2WV	2.42	1.98	0.24		0.11	0.42	0.20
5 Cr-2WV	5.00	2.07	0.25		0.13	0.47	0.25
9 Cr-2WV	8.73	2.09	0.24		0.12	0.51	0.25
9 Cr-2WVTa	8.72	2.09	0.23	0.075	0.10	0.43	0.23
12 Cr-2WV	11.49	2.12	0.23		0.10	0.46	0.24

[a]P = 0.014–0.016, S = 0.005-0.006. Ni ≤ 0.01. Mo ≤ 0.01. Nb < 0.01, Ti < 0.01, Co = 0.005–0.008; Cu = 0.02'0.03, Al = 0.02–0.03, B < 0.001, bal Fe.

7.3.4.2 Experimental Procedure

Tensile tests were made on SS-1 specimens taken from 0.76-mm-thick sheet of the eight heats given in Table 7.3.1. The SS-I tensile specimens have a reduced gage section 20.3 mm long by 1.52 mm wide by 0.76 mm thick. All specimens were machined with gage lengths parallel to the rolling direction. Tensile tests were made in vacuum on a 44-kN-capacity Instron universal testing machine at a crosshead speed of 8.5 μm/s, which results in a nominal strain rate of 4.2×10^{-4}/s.

7.3.4.3 Results and Discussion

We previously reported on the tensile behavior of the eight heats in Table 7.3.1 after austenitizing all but the 2.25Cr-2W steel for 0.5 h at 1050°C prior to cooling in helium.[2] The 2.25Cr-2W was austenitized 0.5 h at 900°C. Tempering treatments were chosen by referring to the treatments for the analogous Cr-Mo steels that are being studied in the fusion program. To better compare the results of the effect of tempering on the tensile behavior, the steels were given the same normalizing treatment as before' and then tempered at 700 or 750°C, depending on the tempering treatment they had previously received. That is. the

2.25CrV, 2.25Cr-1WV, and 2.25Cr-2W steels, which were tempered for 1 h at 700°C before,* were tempered 1 h at 750°C, and the other five steels, which were tempered 1 h at 750°C before,[2] were tempered 1 h at 700°C.

Tensile tests were conducted over the temperature range from room temperature to 600°C, and the results are given in Tables 7.3.2 and 7.3.3. Data from these tests and from the previous tests' have been combined in Figs. 7.3.1 to 7.3.4. Figures 7.3.1 and 7.3.2 show the data for all eight heats after the 700°C tempering treatment, and Figs. 7.3.3 and 7.3.4 show the data for these heats after the 750°C tempering treatment. In comparing the results, it should be recalled that the 2.25Cr steels form bainite when normalized and the 5- and 12-Cr steels form martensite. The 12-Cr steel contains about 26% delta-ferrite, with the balance martensite.'

Table 7.3.2. Tensile properties of normalized-and-tempered low-chromium FIRD steels[a,b]

Test temperature (°C)	Strength (MPa)		Elongation (%)	
	Yield	Ultimate	Uniform	Total
		2 1/4 CrV		
22	557	640	5.9	9.4
200	500	571	4.3	7.3
300	496	582	5.1	8.1
400	471	553	4.0	5.9
500	472	552	3.0	6.4
600	394	413	1.1	6.0
		2 1/4 Cr-1WV		
22	579	653	6.6	8.8
200	-	-	-	-
300	527	608	4.8	7.9
400	540	624	4.3	6.9
500	504	589	3.3	6.4
600	401	421	1.3	5.0
		2 1/4 Cr-2W		
22	554	618	9.6	13.5
200	542	581	8.1	12.0
300	531	570	7.1	10.0
400	474	555	6.9	9.9
500	430	609	7.4	10.4
600	372	484	4.6	9.1
		2 1/4 Cr-2WV		
22	904	964	5.3	8.5
200	860	925	5.0	8.0
300	848	911	4.1	7.0
400	803	882	3.4	6.6
500	789	871	3.5	6.4
600	708	760	1.9	5.6

[a]All but the 2.25Cr-2W steel were austenitized 0.5h at 1050°C; the 2.25Cr-2W was austenitized 1 h at 900°C.

[b]All but the 2.25Cr-2WV steel were tempered 1 h at 750°C; the 2.25Cr-2 WV was tempered 0.5h at 700°C.

Table 7.3.3. Tensile properties of normalized-and-tempered high-chromium FIRD steels[a]

Test temperature (°C)	Strength (MPa)		Elongation (%)	
	Yield	Ultimate	Uniform	Total
		5Cr-2WV		
22	715	811	4.5	8.0
200	695	784	3.6	6.8
300	673	756	3.3	6.6
400	676	753	2.8	5.5
500	629	706	2.0	4.6
600	538	565	1.2	5.6
		9Cr-2WV		
22	790	910	4.4	7.5
200	760	865	3.4	6.5
300	710	825	3.3	6.1
400	711	797	2.6	5.4
500	660	734	1.9	4.3
600	599	644	1.6	6.3
		9Cr-2WVTa		
22	823	942	3.8	6.6
200	-	-	-	-
300	782	873	2.8	5.0
400	761	840	2.3	5.0
500	707	779	1.6	4.1
600	651	696	1.4	4.8
		12Cr-2WV		
22	708	859	5.4	8.4
200	668	804	4.5	7.5
300	649	777	4.4	7.4
400	650	703	3.4	6.1
500	601	698	2.5	5.0
600	500	528	2.3	6.6

[a]All specimens were heat treated as follows: 0.5 h at 1050°C, air cool; 1 h at 700°C, air cool.

The previous results indicated the effect of tungsten, and vanadium on the tensile properties;' they also showed that the chromium content did not contribute significantly to the strength of the steels with vanadium and tungsten.

The recent results allow for more detailed comparisons. At 700°C, the 2.25Cr-2WV steel has the highest strength over the entire temperature range. The 9-Cr steel with tantalum is next, followed by the 9-Cr steel without tantalum. For tests up to 500°C, the 5-Cr steel is the next strongest, although there is little difference between the strength of this steel, the 12 Cr-2WV steel, and the 2.25Cr-1WV steel.

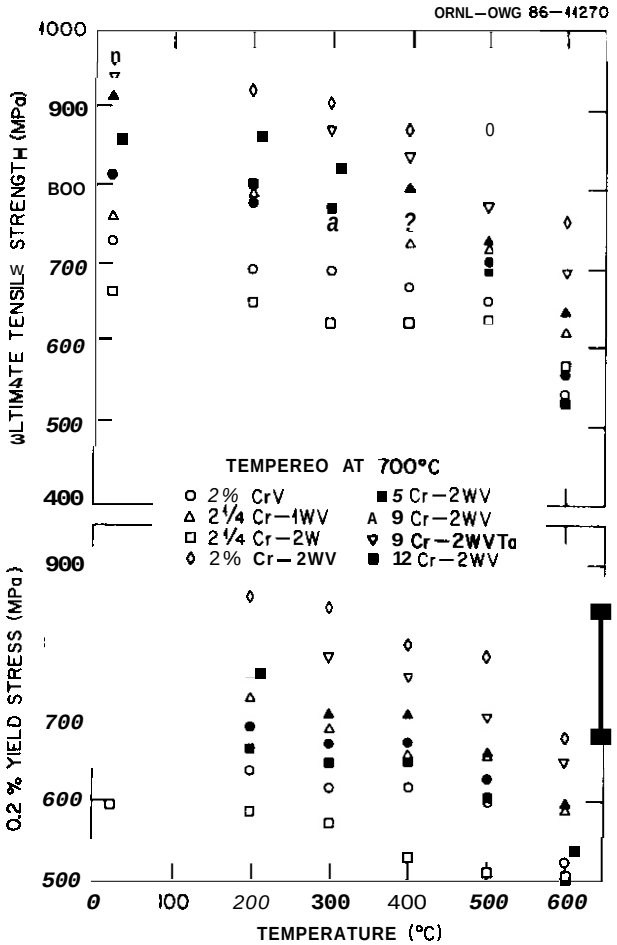

Fig. 7.3.1. The 0.2% yield stress and ultimate tensile strength plotted against test temperature for eight experimental heats of FIRD steel. After normalizing, all steels were tempered for 1 h at 700°C.

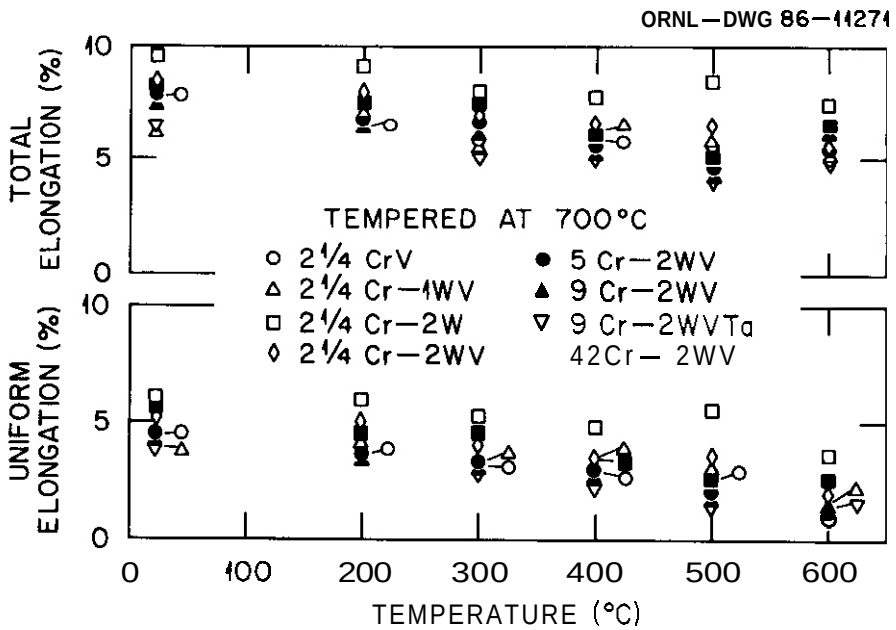

Fig. 7.3.2. The uniform and total elongation plotted against test temperature for eight experimental heats of FIRD steel. After normalizing, all steels were tempered for 1 h at 700°C.

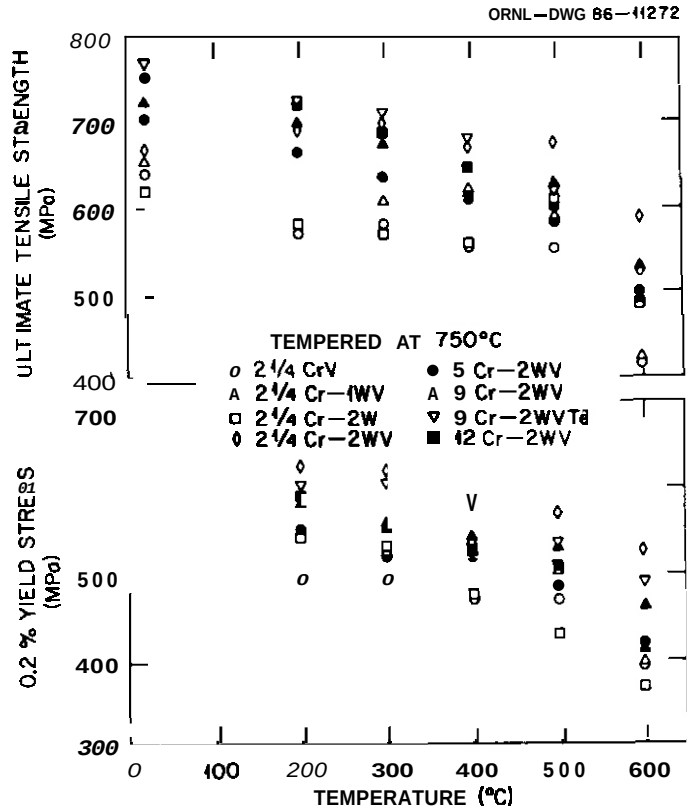

Fig. 7.3.3. The 0.2% yield stress and ultlmate tensile strength plotted against test temperature for eight experimental heats of FIRD steel. After normalizing. all steels were tempered for 1 h at 750°C.

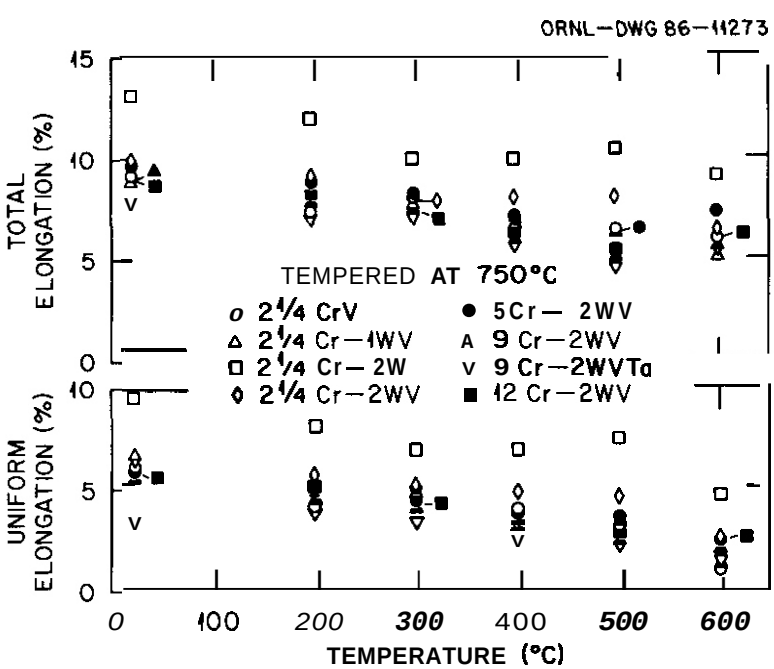

Fig. 7.3.4. The uniform and total elongation plotted against test temperature for eight experimental heats of FIRD steel, After normalizing, all steels were tempered for 1 h at 750°C.

Up to 500°C, the 2.25Cr-2W steel is the weakest steel, while the 2.25Cr-2V steel falls between the weakest steel and the remainder of the steels. At 600°C, the 12-Cr steel with the 26% delta-ferite becomes the weakest. The 5-Cr steel is one of the weakest steels at 600°C, along with the 2.25CrV and 2.25Cr-2W steels. The 2.25Cr-1WV maintains a relatively good strength at this temperature.

After the steels were tempered at 750°C, the relative strengths were similar to those after tempering at 700°C, with the exception that 2.25Cr-2WV did not have the highest UTS at temperatures below 500°C. There was less difference in the 9Cr, 12Cr, and the 2.25Cr-2WV steels at temperatures up to 500°C than after the 700°C temper. At the 600°C test temperatures, the 2.25Cr-2WV steel had the highest strength, with the 9-Cr steels next, followed by the 5- and 12-Cr steels. The low-chromium steels with 0 and 1%W and the one without vanadium were, in general, the weakest.

The ductilities of the different steels were not substantially different, regardless of the composition. The 2.25Cr-2W steel, which was generally the weakest, always had the highest uniform and total elongations. The 9Cr-2 WVTa steel nearly always had the lowest uniform and total elongation. Although the 2.25Cr-2WV steel was generally the strongest, it generally had the highest ductility of the steels containing vanadium. The ductilities of the steels given the 750°C temper had higher ductilities than those tempered at 700°C, although the difference was quite small, considering the difference in strength.

Previous work[4] has shown that the chromium composition does not affect the strength of Cr-Mo steels for chrominum compositions beyond about 2.25% if *similarly tempered materials* are compared. That is, if a tempered bainite microstructure of 2.25Cr-1 Mo steel is compared with a tempered martensite structure of 9Cr-1 Mo steel (the higher hardenability of the latter steel results in martensite when typical section sizes are normalized, while it is very difficult to obtain martensite in the 2.25Cr-1 Mo steel), the elevated-temperature strenghts are similar.' Note that neither of these steels contains any strong carbide-forming elements, such as vanadium or niobium. The results of the present work indicate that for the Cr-W steels under discussion, the chromium can affect the strength of the steels, at least when they all contain the same amount of vanadium. Furthermore, the effect appears to go through a local minimum, since the strength of the 5-Cr steel is less than that of either the 2.25 or 9-Cr steels. It should also be noted that the 2.25-Cr steel with vanadium and tungsten had the higher strength even though it had a bainitic microstructure, compared to the martensitic microstructures in the high chromium steels.

7.3.5 Future Work

The steels will be examined by electron microscopy to determine if differences in the microstructures of the different steels can be detected to determine the source of the differences in the strengths for the different steels. Results of charpy impact tests on these steels will also be reported.

7.3.6 References

1. R. L. Klueh and E. E. Bloom, "The Development of Ferritic Steels for Fast Induced-Radioactivity Decay for Fusion Reactor Applications," *Nucl. Eng. Design/Fusion* **2** (1985) 383–89.

2. R. L. Klueh, "The Development of Ferritic Steels for Fast Induced-Radioactivity Decay for Fusion Reactor Applications," pp. 117–23 in *ADIP Semiann. Prog. Rep., Sept. 30, 1985,* DOE/ER-0045/15, U.S. DOE, Office of Fusion Energy.

3. R. L. Klueh and J. M. Vitek, "The Development of Ferritic Steels," pp. 141–45 in *ADIP Semiennu. Prog. Rep., Sept. 30, 1984,* DOE/ER-0045/13, U.S. DOE, Office of Fusion Energy.

4. J. Orr, F. R. Beckitt, G. D. Fawkes, "The Physical Metallurgy of Chromium-Molydenum Steels for Fast Reactor Steam Boilers," pp. 91–109 in *Ferritic Steels for Fast Reactor Steam Generators,* Vol 1, British Nuclear Energy Society, London 1978.

7.4 FATIGUE BEHAVIOR OF IRRADIATED HELIUM-CONTAINING FERRITIC STEELS FOR FUSION REACTOR APPLICATIONS — M. L. Grossbeck, J. M. Vitek, and K. C. Liu (Oak Ridge National Laboratory)

7.4.1 ADIP Task

ADIP task for ferritic alloys not defined.

7.4.2 Objective

This research evaluates the effect of fatigue on irradiated ferritic steels containing helium

7.4.3 Summary

The martensitic alloys 12Cr-1MoVW and 9Cr-1MoVNb have been irradiated in the High Flux Isotope Reactor (HFIR) and subsequently tested in fatigue. In order to achieve helium levels characteristic of fusion reactors, the 12Cr-1MoVW was doped with 1 and 2% Ni, resulting in helium levels of 210 and 410 at. ppm at damage levels of 25 dpa. The 9Cr-1MoVNb was irradiated to a damage level of 3 dpa and contained <5 at. ppm He. Irradiations were carried out at 55°C and testing at 22°C. No significant changes were found in 9Cr-1MoVNb upon irradiation at this damage level, but possible effects of helium were found in 12Cr-1MoVW. Alloys with 210 and 410 at. ppm He showed cyclic strengthening of 29 and 34% over unirradiated, helium-free nickel-doped materials, respectively. This cyclic hardening, which may be caused by helium, resulted in a degradation of the cyclic life. However, the fatigue life remained comparable to or better than that of unirradiated 20%-cold-worked 316 stainless steel.

7.4.4 Progress and Status

7.4.4.1 Introduction

Ferritic, or martensitic, steels have attracted attention far fusion reactor applications due to their radiation resistant properties. Variations of alloys based on 12Cr-1Mo and 9Cr-1Mo compositions have been shown to exhibit low swelling and low irradiation creep rates.' These alloys have further appeal for fusion reactor first wall and blanket structures because they have higher thermal conductivity and lower thermal expansion coefficients than austenitic stainless steels. The consequence is reduced thermal stress and increased thermal fatigue life, provided the unirradiated fatigue properties remain unchanged by irradiation. Transmutation-induced helium could alter fatigue life, and it is this point that is addressed in this report.

The helium production rate in a fusion reactor is dependent on reactor design as well as alloy composition. A range of expected helium levels for a stainless steel wall and a lithium-cooled blanket is given in Fig. 7.4.1 based on calculations by Gabriel et al.[2] Figure 7.4.1 also shows the helium concentrations generated in ferritic and austenitic alloys as a function of dpa for several experimental reactors: the Oak Ridge Research Reactor (ORR), High Flux Isotope Reactor (HFIR), and Experimental Breeder Reactor (EBR-II). The helium formed in these reactors results primarily from the reaction $^{58}Ni(n,\gamma)$ followed by $^{59}Ni(n,\alpha)$, both of which occur with thermal neutrons. In a given reactor, the helium production rate can be chosen by adjusting the nickel content. This approach was used in the present research, where the nickel concentration of two ferritic steels was varied from 0.5 to 2%. As can be seen in Fig. 7.4.1, an alloy with 2% wt Ni results in a He:dpa ratio after HFIR irradiation comparable to that of a fusion reactor.

7.4.4.2 Experimental Procedure

In this investigation HFIR irradiation of fatigue specimens was followed by low cycle fatigue testing to evaluate the effect of neutron irradiation and helium on the fatigue life of the alloys.

Two fusion reactor candidate alloys were studied: the Sandvik alloy HT-9, often designated 12Cr-1MoVW, which contains nominally 0.5% Ni, and 9Cr-1MoVNb. Three electroslag-remelted (ESR) heats of 12Cr-1MoVW and one ESR heat of 9Cr-1MoVNb were prepared by Combustion Engineering, Inc. The compositions appear in Table 7.4.1. One 12Cr-1MoVW alloy (HT-3587) was prepared to match the composition of commercial HT-9. The remaining two were doped with 1 and 2% Ni. A fourth ESR heat (91353) prepared by Carpenter Technology Corp. was also irradiated; this heat has been tested extensively in the United States breeder reactor program. One heat of 9Cr-1MoVNb, not doped with nickel, was studied.

The specimens were normalized and tempered using the heat treatments shown in Table 7.4.2. The result was a tempered martensite structure described by Klueh et al.[3,4]

The specimens were encapsulated in aluminum tubes that were hydrostatically collapsed onto the specimens. The sealed tubes were irradiated in the HFIR with reactor coolant in direct contact with the collapsed tubes. The 12Cr-1MoVW type alloys were irradiated in an irradiation vehicle designated HFIR-MFE-T1 which was irradiated in the peripheral target position of the HFIR to a fluence of 1.4 to 3.4 × 10^{26} neutrons/m^2 (E > 0.1 MeV) corresponding to a damage level of 10 to 25 dpa. The 9Cr-1MoVNb was irradiated in HFIR-MFE-RB1 which was irradiated in the beryllium reflector of the HFIR to a fluence of 0.38 to 0.51 × 10^{26} neutrons/m^2 (E > 0.1 MeV), corresponding to a damage level of 2.5 to 3.3 dpa. The displacement damage and helium levels are provided in Table 7.4.3.

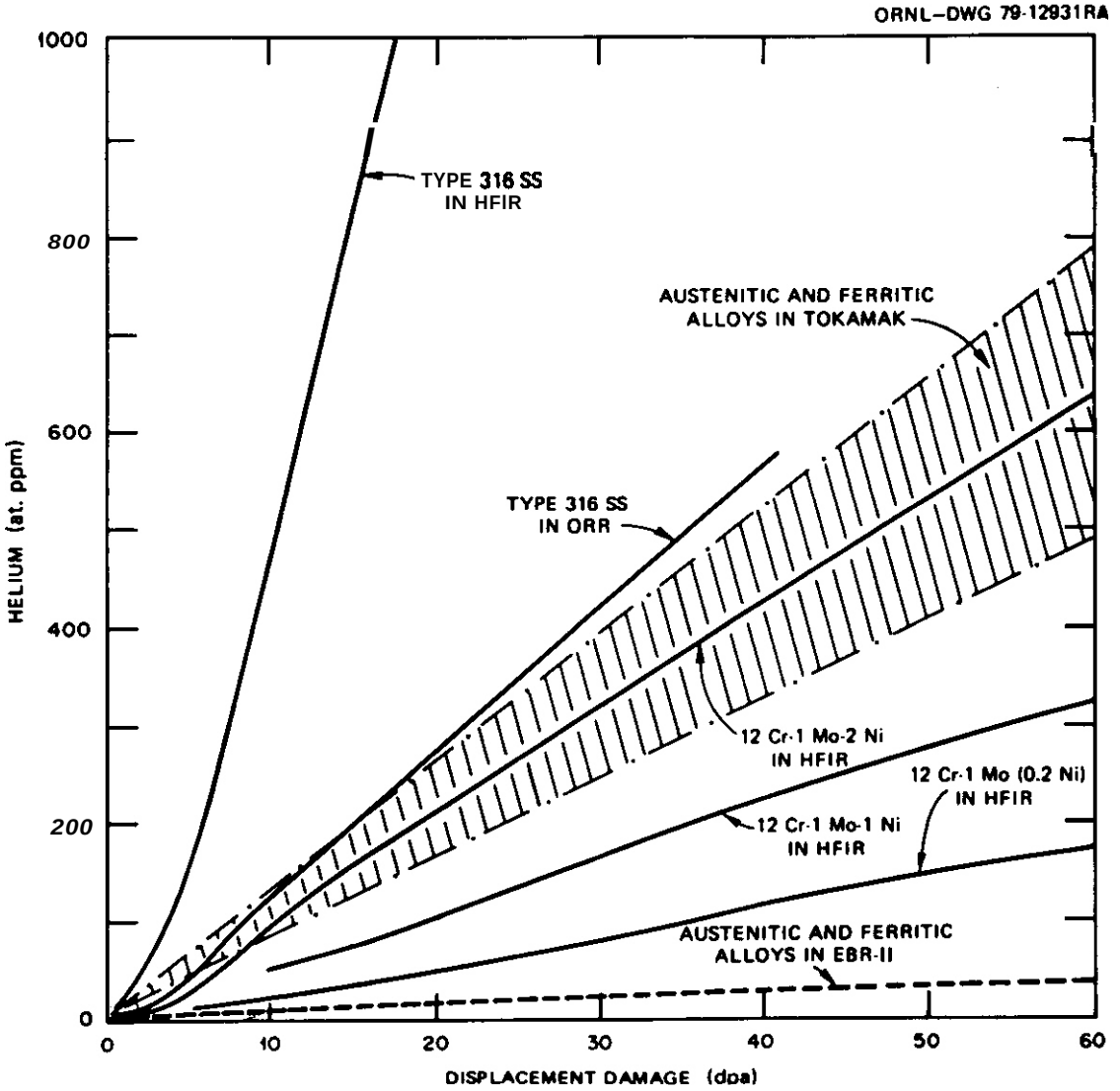

Fig. 7.4.1. Helium as a function of displacement damage for alloys with varying levels of nickel irradiated in experimental reactors. The cross-hatched portion shows levels expected in a tokamak fusion reactor.

Table 7.4.1. Compositions of martensitic steels investigated

Element	Alloy Content, wt %				
	12Cr-1MoVW (91353)	12Cr-1MoVW (3587)	12Cr-1MoVW + 1 Ni (3588)	12Cr-1MoVW + 2 Ni (3589)	9Cr-1MoVNb (3590)
C	0.21	0.21	0.20	0.20	0.09
Mn	0.50	0.50	0.47	0.49	0.36
P	0.007	0.011	0.010	0.011	0.008
S	0.003	0.004	0.004	0.004	0.004
Si	0.22	0.18	0.13	0.14	0.08
Ni	0.58	0.43	1.14	2.27	0.11
Cr	11.80	11.99	11.97	11.71	8.62
Mo	1.02	0.93	1.04	1.02	0.98
V	0.32	0.27	0.31	0.31	0.209
Nb		0.018	0.015	0.015	0.063
Ti	0.003	0.003	0.003	0.003	0.002
co	0.02	0.017	0.015	0.021	0.013
Cu	0.04	0.05	0.05	0.05	0.03
Al	0.028	0.030	0.017	0.028	0.013
B	<0.001	<0.001	<0.001	<0.001	<0.001
W	0.50	0.54	0.53	0.54	0.01
As	<0.001	<0.001	0.002	<0.002	<0.001
Sn	0.01	0.002	0.001	0.002	0.003
Zr		<0.001	<0.001	<0.001	'0.001
N		0.020	0.016	0.017	0.050
O	<0.006	0.005	0.007	0.007	0.007

Table 7.4.2. Heat treatment of alloys

Alloy	Heat	Heat treatment
12Cr-1MoVW	91353	1038°C – 10 min AC 760°C – 30 min AC
12Cr-1MoVW	3587	1050°C – 0.5 h 780°C – 2.5 h AC
12Cr-1MoVW + 1 Ni	3588	1050°C – 0.5 h 780°C – 2.5 h AC
12Cr-1MoVW + 2Ni	3589	1050°C – 0.5 h 700°C – 5 h AC
9Cr-1MoVNb	3590	1040°C – 0.5 h 760°C – 1 h AC

Table 7.4.3. Irradiation parameters and fatigue data

Specimen	Alloy	Heat	Damage Level (dpa)	Helium (at. ppm)	Strain Range (%)	Stress Range $\Delta\sigma$ at $N_f/2$ (MPa)	Cycles to Failure (N_f)
SB01	12Cr-1MoVW	3587	0		2.0	1338	1,807
SB11	12Cr-1MoVW	3587	0		1.0	1104	22,814
SB12	12Cr-1MoVW	3587	0		0.5	924	644,665
SB03	12Cr-1MoVW	3587	10	34	1.0	1268	30,908
SB10	12Cr-1MoVW	3587	15	53	0.5	993	227,652
SJ02	12Cr-1MoVW	91353	0		2.0	1324	4,029
SJ01	12Cr-1MoVW	91353	0		1.0	1117	45,762
SJ07	12Cr-1MoVW	91353	0		0.5	972	719,759
SC02	12Cr-1MoVW-1Ni	3588	0		1.0	1172	26,362
SC04	12Cr-1MoVW-1Ni	3588	24	210	1.0	1517	15,581
SD02	12Cr-1MoVW-2Ni	3589	0		1.0	1393	22,010
SD01	12Cr-1MoVW-2Ni	3589	25	410	1.0	1862	10,539
TA17	9Cr-1MoVNb	3590	0		2.0	1186	1,315
TA14	9Cr-1MoVNb	3590	0		0.5	883	204,235
TA19	9Cr-1MoVNb	3590	0		0.3	641	4,983,360
TA20	9Cr-1MoVNb	3590	3.3	4	1.0	1089	13,225
TA09	9Cr-1MoVNb	3590	2.5	2	0.5	938	247,907
TA11	9Cr-1MoVNb	3590	3.3	4	0.3	703	17,859,711

The fatigue specimens were of the miniature hourglass type with a minimum diameter of 3 mm and 45.2 mm in length. The specimens incorporated threaded ends with conical guides to aid in alignment. Further details are provided by Liu and Grossbeck.[5] The specimens were tested on a fully remote servo-hydraulic fatigue testing system installed in a radiation hot cell. Strain was measured by a diametral extensometer. The tests were performed at room temperature in air. A triangular strain versus time function beginning with compression at a strain rate of 4×10^{-3} s^{-1} was used. For low-cycle fatigue (total strain range $\geq$ 0.5%), tests were controlled on the basis of axial strain calculated by a strain computer from diametral strain, which was measured directly at the minimum gage section. For high-cycle tests, the same strain control was used until a stable hysteresis loop was achieved, at which time, control was switched to load, and the frequency was increased by a factor of 10 to reduce test duration. Both the irradiated and unirradiated specimens were loaded remotely using the same procedure in order to avoid differences in alignment.

7.4.4.3 Results

Results for the 12Cr-1MoVW type alloys appear in Table 7.4.3 and Figs. 7.4.2 and 7.4.3. Figure 7.4.2 is a plot of cyclic stress as a function of total strain range. Stress range was measured at half the cyclic life where a stable hysteresis loop had been achieved. Each point on the curves represents a separate specimen. For unirradiated 12Cr-1MoVW (0.5% Ni), both heats were plotted on the same curve and not separately identified since the results are indistinguishable. The curve for the irradiated 12Cr-1MoVW lies above the unirradiated curve as a result of the expected radiation hardening at low temperatures. Although only one specimen for each nickel-doped alloy was irradiated, the results were consistent and were, therefore, plotted in Fig. 7.4.2 along with corresponding unirradiated specimens. The most important comparison to be made is that between the irradiated specimens and their corresponding unirradiated counterparts. The strength of the undoped 12Cr-1MoVW increased 14% upon irradiation, but the 1% Ni-doped material increased 29% in strength upon irradiation and the 2% Ni-doped material increased 34% in strength.

The curves of total strain range as a function of cyclic life are plotted in Fig. 7.4.3. Although data are sparse, where possible the data were fit to an equation of the form (using the method of least squares),

$$\Delta\epsilon_T = AN_f^{-0.12} + BN_f^{-b} \quad , \qquad (1)$$

where

$\Delta\epsilon_T$ = total strain range,

N_f = cycles to failure,

A,B,b = constants.

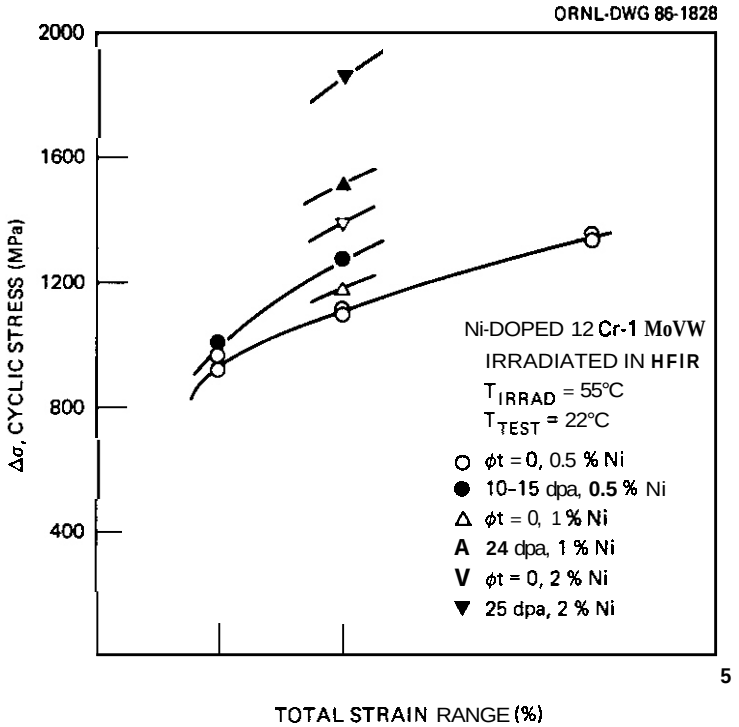

Fig. 7.4.2. Cyclic stress-strain curve for 12Cr-1MoVW type alloys tested at room temperature showing effects of irradiation and helium. Each point represents an individual specimen.

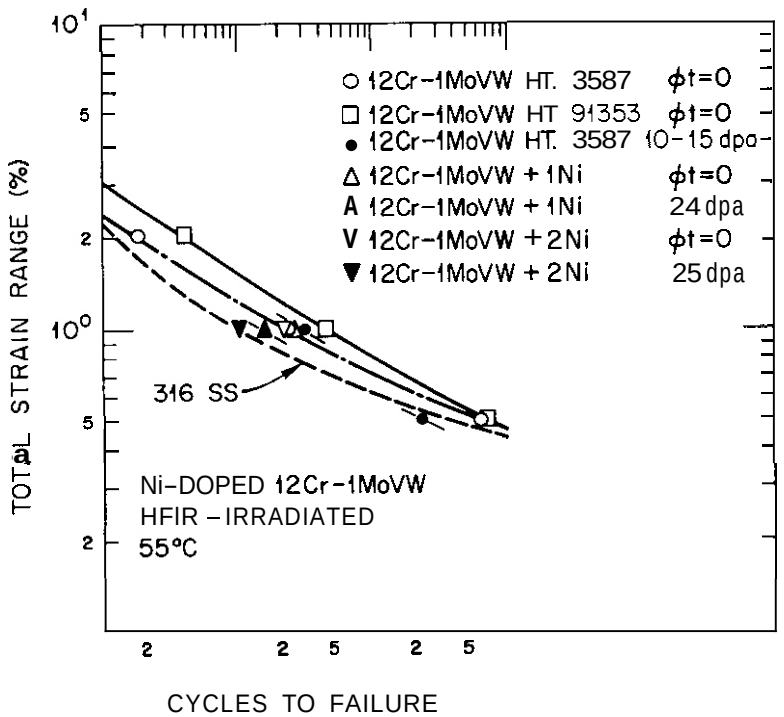

Fig. 7.4.3. Cyclic life of 12Cr-1MoVW type alloys tested at room temperature showing effects of irradiation and helium. A curve for 20%-cold-worked type 316 stainless steel is shown for comparison.

The results appear in Table 7.4.4.

Table 7.4.4. Relations for room temperature fatigue life

Alloy	Condition	Equation
12Cr-1MoVW	Unirradiated	$\Delta\epsilon_T = 0.9\ N_f^{-0.12} + 15.7\ N_f^{-0.29}$
9Cr-1MoVNb	Unirradiated	$\Delta\epsilon_T = 1.82\ N_f^{-0.12}\ \ 59.6\ N_f^{-0.54}$
9Cr-1MoVNb	Irradiated	$\Delta\epsilon_T = 2.11\ N_f^{-0.12} + 91.7\ N_f^{-0.6}$
AISI 316	Unirradiated	$\Delta\epsilon_T = 2.25\ N_f^{-0.12} + 134\ N_f^{-0.68}$

The curves for 12Cr-1MoVW, which appear in Fig. 7.4.3, show heat 91353 to have a slightly longer fatigue life than heat 3587 in the unirradiated condition. The irradiated 12Cr-1MoVW shows essentially the same cyclic life as the unirradiated material. The curves for nickel-doped alloys, although based on one specimen each, show fatigue lives similar to undoped material in the unirradiated condition. The irradiated nickel-doped alloys exhibited shorter fatigue lives than their unirradiated counterparts, but the differences are small.

It should be noted that, despite the observed effects, the fatigue life of all of the variants of 12Cr-1MoVW remained as good or better than that of unirradiated 20%-cold-worked type 316 stainless steel (20% C.W. 316). Cyclic life of 20% C.W. 316 at room temperature is also plotted in Fig. 7.4.3 for comparison purposes.

The cyclic stress curves for 9Cr-1MoVNb appear in Fig. 7.4.4. Again, radiation strengthening is evident, but the effect is slight because of the low damage level of only 2 to 4 dpa. Nonetheless, this result is significant since these damage levels are two or three orders of magnitude greater than the embrittling damage level for pressure vessel steels. The cyclic life curves in Fig. 7.4.5 also show only a small effect of irradiation. The data for fatigue life of this alloy were again fit to a power law equation of the form of Eq. (1). The results also appear in Table 7.4.4. This alloy behaves similarly to unirradiated 20% C.W. 316 but slightly worse than 12Cr-1MoVW.

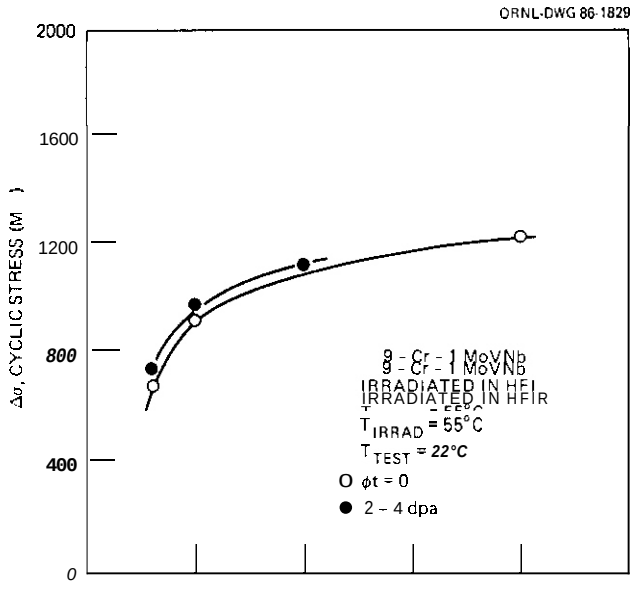

Fig. 7.4.4. Cyclic stress-strain curve for 9Cr-1MoVNb tested at room temperature showing effects of irradiation. Each datum represents an individual specimen.

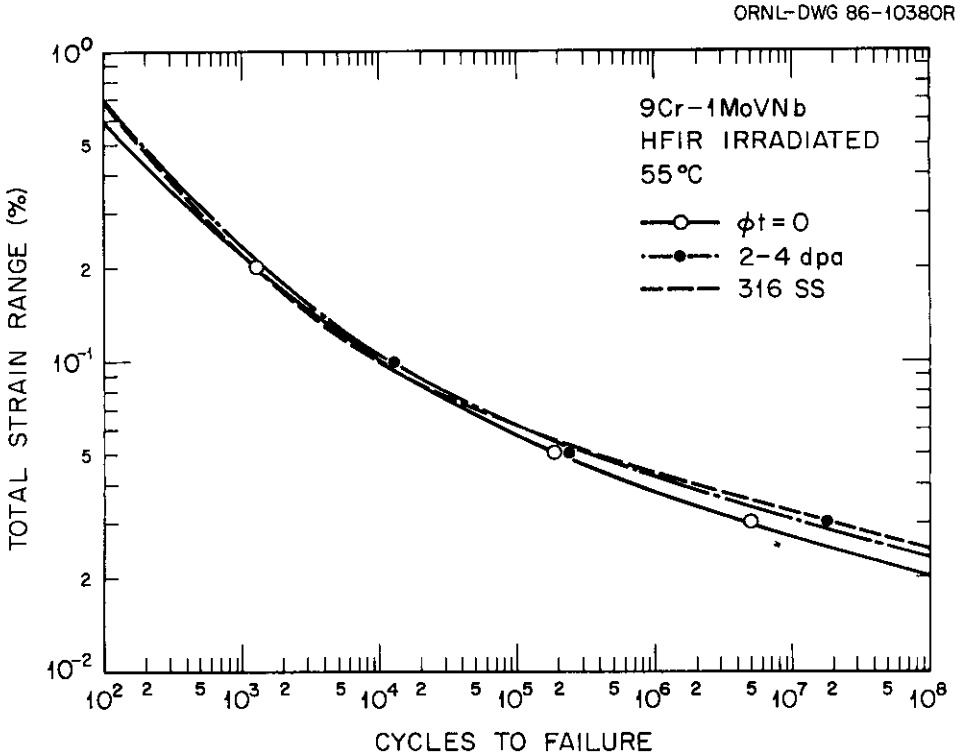

Fig. 7.4.5. Cyclic life of 9Cr-1MoVNb tested at room temperature showing effects of irradiation. A curve for 20%-cold-worked type 316 stainless steel is shown for comparison.

7.4.4.4 Discussion

The blanket and perhaps the first wall of any fusion reactor that produces useful energy must operate at elevated temperatures. However, in the present series of scoping experiments, the material was irradiated at only 55°C and tested at room temperature. Elevated temperatures were not chosen because experimental research on pressure vessel steels, consisting of mostly fracture toughness-type-tests, indicated that low-temperature irradiation and testing would provide the most adverse conditions.[6] The lowest temperature attainable in the HFIR is 55°C. Fatigue testing was done at 22°C since no significant differences in performance were expected between room temperature and 55°C.

Normal scatter in fatigue life data makes it difficult to draw conclusions from the sparse data presented. However, cyclic stress-strain curves are more reproducible and normally yield more consistent results. Therefore, they will be discussed first.

The cyclic strength for the 12Cr-1MoVW type steels (Fig. 7.4.2) does not differ significantly between the two heats of undoped 12Cr-1MoVW. The unirradiated nickel-doped material shows a small increase in cyclic strength for the 1% Ni-doped alloy and a 26% increase for the 2% Ni-doped alloy. The effects of nickel on the unirradiated steels have been discussed by Klueh et al.[3,4] They found two primary effects: lowering of the A_{c_1} temperature, and lowering the martensite start (M_s) and finish (M_f) temperature. If the nickel-doped steel is tempered above the A_{c_1} temperature, partial austenitization occurs, which leads to martensite formation upon cooling. This leads to untempered martensite in the nickel-doped material. If the new M_f temperature is below room temperature, the alloy will contain retained austenite following normalization. When a steel with retained austenite is tempered, precipitation of carbon results in an increase in M_s and M_f. Upon cooling, the austenite can transform to martensite.

To prevent austenite formation when tempering, the 2% Ni-doped material was tempered at 700°C, determined by Klueh et al.[4] to be below the A_{c_1} temperature. For the 1% Ni-doped alloy, the previously developed tempering temperature of 780°C was determined to be below the A_{c_1} temperature and was therefore used. The M_s and M_f temperatures were determined by Klueh et al.[3] to remain above room temperature even for the 2% Ni-doped alloy so that no difficulties were expected. The problem remaining is to develop a heat treatment that produces equivalent microstructures for the doped and undoped alloys. The 5 h heat treatment at 700°C was developed for this purpose, but the high cyclic strength is evidence that this was not fully achieved. Apparently the tempering resulting from the 700°C treatment was not as complete as that achieved by the 780°C heat treatment.[3,4]

Keeping in mind that the unirradiated microstructures are similar but not the same, the effects of irradiation will now be addressed. In undoped 12Cr-1MoVW, irradiation strengthening is apparent. The effect of irradiation-induced defects on hardening at low temperatures is well known, and the increase in cyclic strength is expected. The increase in cyclic strength at 1% total strain is 14% upon irradiation. To evaluate the effect of irradiation and helium, the ratio of the cyclic strength for irradiated material to that for unirradiated material will be examined. For 1% Ni-doped material the ratio is 1.29 and for 2% Ni-doped material it is 1.34. These are to be compared with 1.14 for the undoped alloy. If we can assume that the effects of irradiation for the three alloys are similar and that strengthening by displacement damage is the same, then the additional strengthening observed in the nickel-doped alloys is attributable to helium, 210 and 410 at. ppm for 1% and 2% Ni, respectively. Clearly there are insufficient data to draw strong conclusions, but the additional strengthening observed in the nickel-doped alloys is significant, and the starting microstructures of the doped and undoped alloys appear similar."' The differences in microstructure, evidenced by the differences in unirradiated cyclic strength, are expected to become even less significant upon irradiation. If the increments in cyclic strength are due to hardening by helium, then the increment in strength should increase as $C^{1/2}$, where C is the concentration of helium.' Since there is much hardening already present from dislocation loops and point defects as well as dislocation networks from fatigue, a quantitative approach has limited physical meaning. However, if an equation of the form,

$$\Delta\sigma = A(N + C)^{1/2} \quad ,$$

where

$\Delta\sigma$ = increment in cyclic stress in MPa,

C = helium concentration in at. ppm,

N,A = constants,

is used then the data may be used to determine N and A. The result is

$$\Delta\sigma = 23(18 + C)^{1/2}$$

This empirical equation fits the data remarkably well, lending support to the hypothesis that the hardening is caused by point defects such as an interstitial solute, in particular helium. The constant N represents an artificial defect concentration producing strengthening equivalent to the strengthening resulting from all other sources besides helium. By using the same value of N for all alloys, it is assumed that the point defect contribution to strengthening is not strongly influenced by the differences in the initial microstructures.

The cyclic strength observations may now be used to interpret the cyclic life curves of Fig. 7.4.3. The curves for the two heats of 12Cr-1MoVW show a heat-to-heat variation that cannot be attributed to strength since cyclic strengths were similar. This variation should be used as a guide and serve as a caution in evaluating the significance of small changes in cyclic life. The decreases in fatigue life observed for the nickel-doped alloys are indeed small and comparable to the heat-to-heat variation. Nonetheless the decrease is consistent with the observed cyclic hardening, the stronger alloy, containing more helium, has the shorter life. Strengthening is predicted to reduce low-cycle fatigue life.' It is, therefore, likely that the loss of fatigue life is a consequence of hardening from helium. It is also noteworthy that the strengthening resulting from incomplete tempering in the nickel-doped alloy did not adversely affect fatigue life.

The 9Cr-1MoVNb also shows cyclic hardening due to irradiation. However, the low fluence produces a small change, insufficient to produce a measurable effect on cyclic life.

7.4.4.5 Conclusions

1. The low-cycle fatigue behavior of 12Cr-1MoVW steel is similar to or better than that of 20% C.W. 316 at room temperature. Irradiation to 10 to 25 dpa does not degrade fatigue life below that of unirradiated 20% C.W. AISI 316 stainless steel.

2. Helium concentrations up to 410 at. ppm produce strengthening in 12Cr-1MoVW steel at room temperature; a possible reduction in fatigue life was also observed.

3. The fatigue life of 9Cr-1MoVNb steel is not significantly altered by irradiation to 2 to 4 dpa, although the cyclic life is slightly lower than that of 12Cr-1MoVW steel.

The results indicate that nickel doping may be used to produce fusion reactor levels of helium in martensitic steels. The effects of the nickel are reasonably well understood so that the effects of helium may be separated. The results indicate that the martensitic steels may be used at low temperatures to damage levels of 25 dpa without appreciable degradation of the fatigue life. Nonetheless, since a possible helium effect was observed, it is prudent to perform a similar investigation at elevated temperatures.

7.4.4.6. References

1. F. A. Smidt, Jr., P. R. Malmberg, J. A. Sprague, and J. E. Westmoreland, "Swelling Behavior of Commercial Ferritic Alloys, EM-12 and HT-9, as Assessed by Heavy Ion Bombardment," ***Irradiation Effects on the Microstructure and Properties of Metals,*** ASTM STP 611 (1976) 227-41.

2. T. A. Gabriel, B. L. Bishop, and F. W. Wiffen. ***Calculated Irradiation Response of Materials Using a Fusion-Reactor First-Wall Neutron Spectrum,*** ORNL/TM-5956 (Oak Ridge National Laboratory), June 1977.

3. R. L. Klueh, J. M. Vitek, and M. L. Grossbeck, "Effect of Low-Temperature Irradiation with (n,α) Helium Production on Tensile Properties of 12Cr-1MoVW-Type Steels," ***J. Nucl. Mater.*** 103 and 104 (1981) 887-92.

4. R. L. Klueh, J. M. Vitek, and M. L. Grossbeck, "Nickel-Doped Ferritic (Martensitic) Steels for Fusion Reactor Irradiation Studies: Tempering Behavior and Unirradiated and Irradiated Tensile Properties," ASTM STP 782 (1983) 648-64.

5. K. C. Liu and M. L. Grossbeck, "Use of Subsize Fatigue Specimens for Reactor Irradiation Testing," The Use of Small-Scale Specimens for Testing Irradiated Material, ASTM STP-888 (1986) 276-89.

6. D. A. Canonico, Oak Ridge National Laboratory, Private Communication, 1980.

7. J. P. Hirth and J. Lothe, ***Theory of Dislocations,*** McGraw-Hill Book Co., New York (1968) 625

8. S. I. Sandor, ***Cyclic Stress and Strain,*** The University of Wisconsin Press, Madison, Wisconsin (1972) 149.

7.5 EFFECTS OF IRRADIATION ON FERRITIC ALLOYS AND IMPLICATIONS FOR FUSION REACTOR APPLICATIONS - O. S. Gelles (Westinghouse Hanford Company)

7.5.1 ADIP Task

The United States Department of Energy (DOE) Office of Fusion Energy (OFE) has cited the need to investigate ferritic alloys under the ADIP Program task, Ferritic Steels Development [Path E).

7.5.2 Objective

The objective of the work is to provide guidance on the applicability of martensitic steels for fusion reactor structural components.

7.5.3 *Summary*

The ADIP irradiation effects data base on ferritic [martensitic) alloys is reviewed in order to provide reactor design teams with an understanding of how such alloys will behave for fusion reactor first wall applications. Irradiation affects dimensional stability, strength and toughness. Dimensional stability is altered by precipitation and void swelling. Swelling as high as 25% may occur in some ferritic alloys at 500 dpa.

Irradiation alters strength both during irradiation and following irradiation. Irradiation at low temperatures lead to hardening whereas at higher temperatures and high exposures, precipitate coarsening can result in softening. Toughness can also be adversely affected by irradiation. Failure can occur in ferritics in a brittle manner and irradiation induced hardening causes brittle failure at higher temperatures. Even at high test temperatures, toughness is reduced due to reduced failure initiation stresses.

Ferritic alloys should provide an attractive material for structural applications in a fusion reactor but the temperature regime over which they are used must be limited.

7.5.4 Progress and Status

7.5.4.1 Introduction

The Alloy Development for Irradiation Performance [ADIP) element of the DOE Office of Fusion Energy has been assessing the applicability of ferritic (martensitic) alloys [Path E) for fusion reactors since October 1979. The candidate alloy for study in that program is HT-9, a 12% chromium martensitic stainless steel containing 0.2% C, 0.5% Ni, 0.5% W, 0.6% Mn, 0.3% V and 0.2% Si. The applicability of such a steel can now be assessed and the ADIP program is moving in new directions. The intent of this paper is therefore to review the irradiation effects data base on ferritic alloys generated by ADIP to inform reactor design teams how such alloys behave in a fusion reactor, with particular emphasis on first wall applications. Several other ADIP efforts are not included in this review such as weld procedure development, liquid metal corrosion and hydrogen charging effects which are described elsewhere in this proceedings or in previous conference proceedings.[1]

ADIP objectives are to develop structural materials to withstand the hostile environment of a fusion first wall.[2] The expected irradiation requirements were survival to 40 $MW\text{-}y/m^2$ at a temperature of at least 600°C. Note that for ferritic alloys, 40 $MW\text{-}y/m^2$ corresponds to ~480 displacements per atom (dpa). Generation of materials data and the formulation of property design equations for lower performance intermediate fusion systems was also required. When it became apparent that ferritic alloys could possibly satisfy these goals, Path E or a ferritic alloy development effort was initiated. However, budgetary constraints required that the OOE liquid metal reactor (LMR) data base should be applied whenever possible. The ADIP effort therefore concentrated on developing a data base for weld metal since base metal properties were well characterized by the LWR Program. Fast neutron irradiation testing were used as opposed to ion or electron simulation studies. The irradiation facilities available were the Experimental Breeder Reactor-I1 (EBR-II) in Idaho Falls, ID, the Oak Ridge Reactor [ORR) and the High Flux Irradiation Reactor (HFIR) in Oak Ridge, TN, and the Fast Flux Test Facility [FFTF) in Richland, WA. The temperatures and fluences obtained to date in these facilities for Path E experiments are diagramed in Figure 7.5.1. Figure 7.5.1 emphasizes the fact that fast neutron experiments are considerably short of goal fluence objectives. Therefore, any attempts to predict materials properties at goal fluence require considerable extrapolation. The materials properties considered to be performance limiting and therefore requiring irradiation testing were swelling, irradiation creep, high cycle fatigue, postirradiation tensile, Charpy impact and fracture toughness (J_{IC}). Composition effects such as chromium variation, phase [microstructural) stability and helium generation were also investigated. The major tool relied on for studying helium effects was the nickel two step reaction for which special alloys with intentional nickel additions were prepared for irradiation in the mixed spectrum HFIR facility.

7.5.4.2 Results

Swelling. AOIP experiments confirm that swelling is low in ferritic and martensitic alloys. A series of commercial alloys covering the range Fe-5Cr to Fe-22.5Cr irradiated in EBR-II showed a maximum of 0.6% swelling as measured by density change following irradiation to fluences as high as 125 dpa over the temperature range 400 to 650°C.[3] Void swelling and dislocation evolution were identified in several alloys but only below 500°C and the peak swelling temperature was generally in the range 400 to 425°C.[4,5]

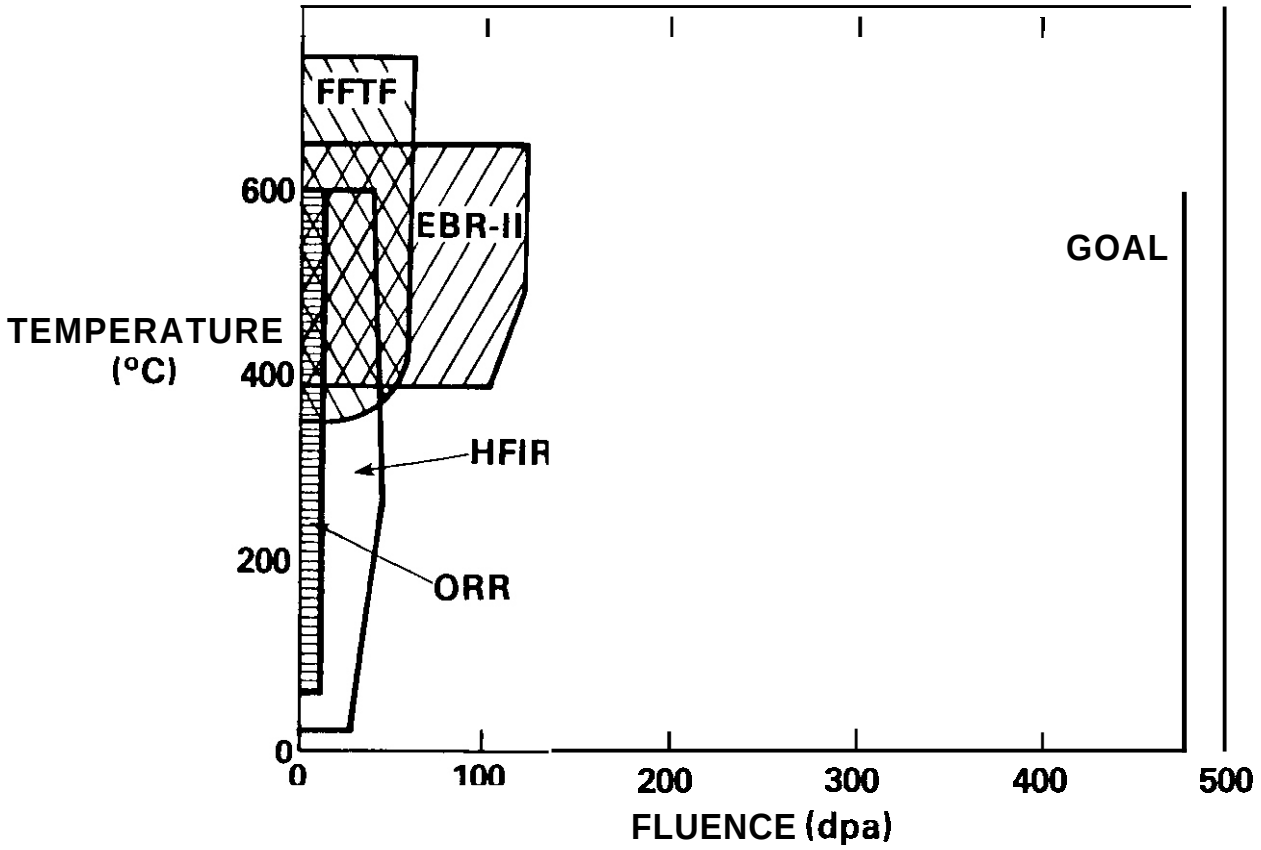

Fig. 7.5.1. The fluence and temperature limits of the ADIP neutron irradiation data base for Path E in comparison with program goals.

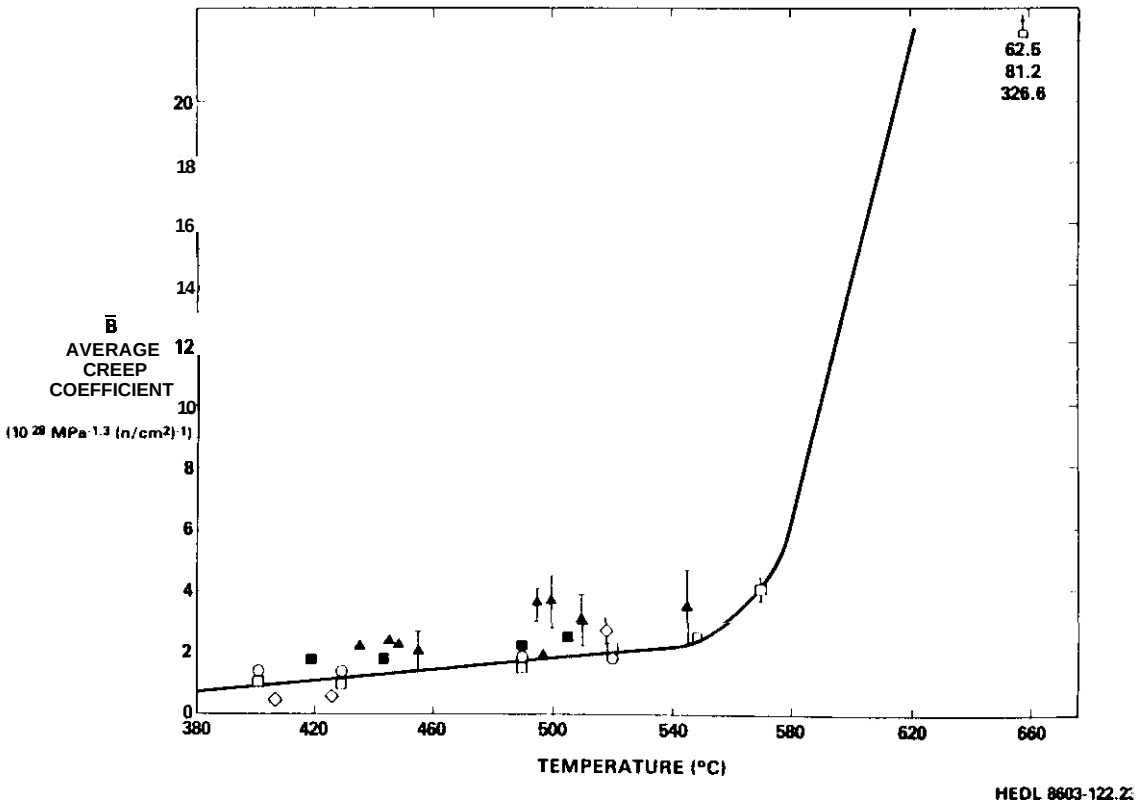

Fig. 7.5.2. The temperature dependence for the average creep coefficient, B, for HT-9 as taken from Reference 17.

Similar results were obtained for 2¼Cr-1Mo.[6] However, one of the most swelling resistant alloys was HT-9[7] in which no radiation induced voids were found. This swelling resistance does not appear to be maintained in a helium generating environment.[8,9] Void formation was found after 35 dpa when helium generation levels reached -100 appm in HFIR. Therefore, it is likely that in a fusion environment, HT-9 will swell at goal fluence as will most ferritic or martensitic alloys.

Swelling in HT-9 at goal fluence in a fusion reactor can be estimated based on swelling response in simple alloys.[10] Swelling measurements on binary Fe-Cr alloys irradiated in EBR-II to fluences as high as 105 dpa showed the temperature dependence of swelling to be similar to that of commercial alloys and showed peak swelling of 4.7% at 425°C and 95 dpa in Fe-12Cr. The results can be interpreted to show that unless saturation occurred, a steady state swelling rate on the order of 0.06%/dpa applied for temperatures between 400 and 450°C and for alloys ranging from Fe-6Cr to Fe-12Cr. Such a value is in reasonable agreement with most other data on ferritic alloys[11-14] with one exception which is a factor of 2 higher.[15] Based on the approach recommended by Garner for austenitic alloys[16] this value for steady state swelling with an appropriate swelling incubation parameter can be applied to HT-9 to predict swelling at goal fluence.[10] A maximum of 24% swelling at 500 dpa is obtained. A more accurate prediction requires high fluence data using the correct Hefdpa ratio.

Irradiation Creep. Pressurized tube specimens of HT-9 9Cr-1Mo and 2¼Cr-1Mo have been irradiated in EBR-II and FFTF to fluences as high as 51 dpa.[17,18] Diameter change measurements show that irradiation creep for HT-9 is relatively insensitive to temperature for irradiation temperatures below 500°C whereas above 500°C creep increases non-linearly with increasing temperature. Fluence increases from 14 to 23 dpa in EBR-II do not significantly alter creep rates below 500°C and decrease creep rates slightly above 500°C. The behavior is best demonstrated by comparison of the average creep coefficient (B) behavior where B is defined by

$$E = B\,\Phi t\,\sigma^{n} \qquad [1]$$

E is the effective creep strain, Φt is the fast fluence, σ is the effective stress, and n is the stress exponent where $1 \leq n < 2$.

Using an average value for n of 1.5, the HT-9 results from EBR-II for the average creep coefficient B as a function of temperature are shown in Figure 2. The average creep coefficient is 8-9 x 10^{-29} $MPa^{-1.5}$ cm^2/n for temperatures below 500°C whereas it increases to =20 10^{-29} at 580°C and to 40 x 10^{-29} for temperatures below 500°C whereas it increases to =20 x 10^{-29} $MPa^{-1.5}$ cm^2/n at 580°C and above 40 x 10^{-29} $MPa^{-1.5}$ cm^2/n at 660°C. The behavior above 500°C corresponds to thermal behavior. Therefore, irradiation alters creep behavior only below 500°C in a fast reactor environment. Behavior for 9Cr-1Mo and 2¼Cr-1Mo is similar except that thermal creep is more rapid for 2¼Cr-1Mo above 500°C. Irradiation creep in ferritic alloys is in fact lower than that for AISI 316 despite more rapid diffusion response.

Fatigue. High cycle fatigue crack growth rate measurements in helium have been made on miniature center cracked HT-9 tension specimens following irradiation in EBR-II to 26 dpa at 390 and 550°C.[19] Results shown in Figure 7.5.3 indicate that no effect of irradiation can be determined within the scatter of the data. These results are in agreement with results on other ferritic and martensitic alloys.[20] Therefore, based on presently available results, irradiation is not expected to significantly alter fatigue crack propagation in HT-9.

Postirradiation tensile behavior. Effects of irradiation on tensile strength have been obtained from four related ADIP experiments, two using EBR-II and two using HFIR.[21-24] They are part of an ongoing effort intended to determine the effect of Heldpa ratio on mechanical properties. Fluences achieved were in the range 10 to 20 dpa. The results may be generalized as follows. Following irradiation at 390°C or below, irradiation hardening occurs within -10 dpa which results in a strength increase of 20 to 30% and a corresponding decrease in ductility. Following irradiation between 450 and 500°C, negligible change was found and following irradiation at 550°C, slight softening was found. However, in all cases where Hefdpa effects could be assessed, variations in helium generation did not alter tensile properties. These results are shown in Figure 7.5.4 which provides values for the ratio of irradiated to unirradiated ultimate tensile strength as a function of irradiation temperature. A sharp increase in strength can be noted between the 450-550°C data and the 390°C data with the 55°C strength values even higher. Of particular concern is the fact that the temperature of maximum increase in strength has not yet been determined. Irradiation tests in HFIR at 200 and 300°C are in progress.

These results are in good agreement with the LMR data base for HT-9.25 That data base to a peak fluence of 1.1 x 10^{23} nfcm2 or 53 dpa has shown that significant hardening occurs rapidly in-reactor at low temperatures (390 to 425°C) with strength increases on the order of 25%. Above 500°C, HT-9 is found first to soften and then to harden so that following irradiation to 50 dpa, hardening has occurred at all temperatures below 600°C.

Charpy impact behavior. As with all body centered cubic metals, martensitic steels undergo a transition to brittle fracture at low temperatures. Fast neutron irradiation degrades performance in two ways: the ductile to brittle transition temperature (DBTT) is increased and the upper shelf energy (USE) or the energy required for ductile fracture is reduced. Typical response is shown in Figure 7.5.5 which compares Charpy impact fracture energy for third-sized specimens of HT-9 as a function of test temperature following irradiation in EBR-II to two fluence levels.[26] Other experiments confirm this

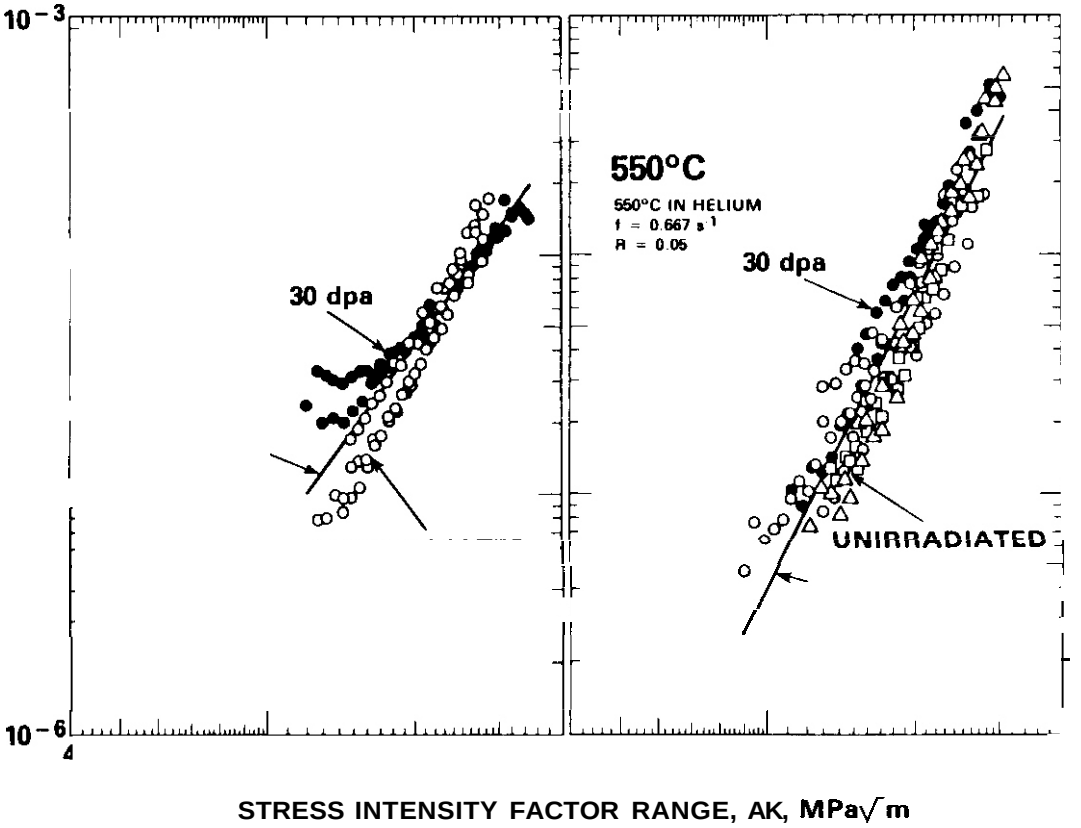

Fig. 7.5.3. High cycle fatigue crack growth rates for HT-9 irradiated to 26 dpa in EBR-II in comparison with unirradiated values: (a) irradiated and tested at 390°C, and (b) irradiated and tested at 550°C.

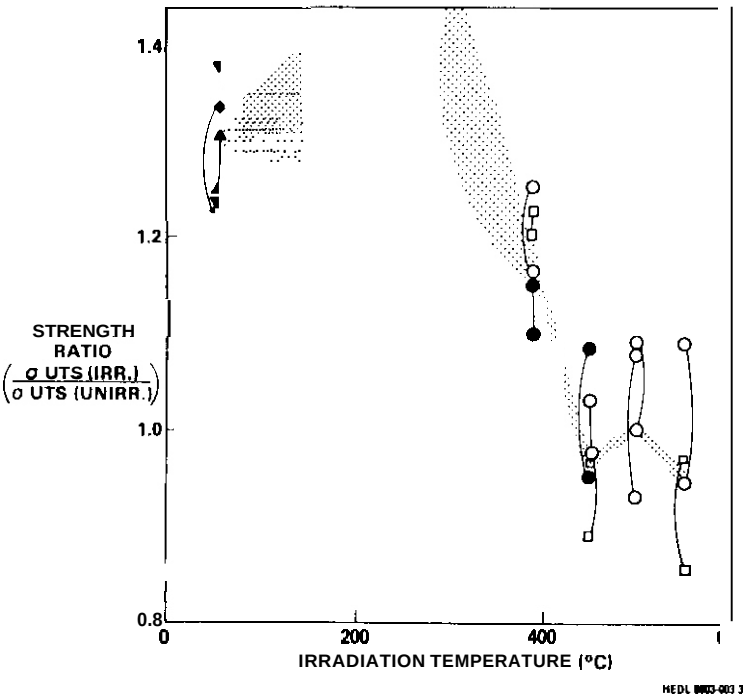

Fig. 7.5.4. Effect of irradiation temperature on strength for HT-9 in the fluence range 10 to 20 dpa. The connected points compare testing at room temperature with testing at the irradiation temperature. The behavior trend is unclear between 50 and 350°C.

behavior.[25,27-29] In all cases, the DBTT is increased and the USE is reduced. The greatest effect occurs following irradiation to 13 dpa; irradiation at 390°C results in ~120°C shift in DBTT, over twice that for hioher irradiation temperatures. Further irradiation to hioher fluence tends to collapse the higher temperature response, bringing the USE for higher irradiation temperatures down to the 390°C level. Similar tests on 9Cr-1Mo qive Significantly smaller OBTT shifts at 390°C and neqligible changes at higher temperatures. Therefore, composition can alter changes in impact properties due to irradiation. Saturation of the shift in DBTT can occur rapidly with fluence as shown in Figure 7.5.6. Tests following irradiation at ~420°C to 5.3 dpa[28] gave similar shifts to those found at higher fluence. Saturation occurs more slowly both at higher temperatures and at lower temperatures. In fact, irradiations done in HFIR at 55°C gave steady increases in DBTT with fluence to 10 dpa with no evidence for saturation [29]. Also, as shown in Figure 7.5.6, the 9Cr-1Mo alloy gave significantly higher shifts in DBTT following irradiation at 55°C than did HT-9, a reverse of response compared to higher irradiation temperature behavior.[29]

In comparison, weld metal and heat affected zone (HAZ) metal specimens which had been tempered following welding were found to give very similar results.[30] Therefore, fracture under impact loading is not controlled by the coarseness of the compositional segregation inherent in weldments. Welded fusion reactor components of HT-9 can be expected to serve as effectively as base metal parts provided that they are tempered following welding.

Fracture toughness. Charpy impact test results are not readily useful for engineering design. Most useful are fracture toughness measurements such as K_{Ic} or J_{Ic} which provide materials properties. The ADIP program has included an effort to determine effects of irradiation on J_{Ic} for HT-9 and 9Cr-1Mo by using single specimen electropotential methods on miniature compact tension specimens. Both J_{Ic} and tearing modulus information can be obtained. The results to a maximum fluence of 26 dpa indicate that fracture toughness degradation due to irradiation is not large enough to cause concern.[25,31-32] J_{Ic} results for HT-9 base metal specimens as a function of test temperature are shown in Figure 7.5.7. Each data point for irradiated specimens has been identified by irradiation temperature and fluence. As the strain rate is considerably below impact rates, an apparent DBTT is found at ~65°C for unirradiated specimens.[33] Low J_{Ic} values for unirradiated specimens are also found at 300°C. However, measurements of J_{Ic} for irradiated Hi-9 all remain above the 300°C unirradiated values. This includes both base metal and weld metal conditions. The largest effect on the fracture toughness of HT-9 was the reduction in tearing modulus, 80% in base metal irradiation at 55°C to 5 dpa for standard material and 75% due to irradiation at 390°C for large orain size material (ASTM 3-41 when tested at 205°C. Weld metal behaved similarly to the large grained material.

Irradiation at low temperatures in HFIR gave fracture toughness reduction in specimens of 9Cr-1Mo which were larger than decreases in HT-9. J_{Ic} for 9Cr-1Mo following irradiation to 5 dpa at 55°C was between 31 and 35 kJ/m^2 for test temperatures between 90 and 450°C. Tearing modulus values were also below the values for HT-9. Therefore, fracture toughness results reflect the Charpy impact results, the major difference being the low values found for unirradiated HT-9 in the 300°C range. This difference could be a consequence of strain rate. However, tests to date have not been able to confirm a Suzuki effect due to impurity atmospheres on dislocation drag in this strain rate and temperature regime.

Microstructural basis for observed behavior. Microstructural and fractographic examinations can provide a basis for understanding the irradiation effects behavior. Radiation induced dislocation loops and voids were onlv found following neutron irradiation at 500°C and below.[7,12] Therefore, response above 500°C should be similar to thermal behavior provided the dose rate *is* on the order of 30 dpa **per** year. Below 500°C, the density of voids, perfect dislocation loops, dislocation tangles and precipitate particles only increased significantly for irradiation temperatures of 425°C and below. Precipitation consisted of many phases (carbides, sigma, ***a'***, G-phase and chi, depending on the alloy composition)[7,34,3] and the dislocation structure included evolution of both a <100> and a/2 <111> Burgers vectors, often simultaneously.[7] Therefore, a major consequence of irradiation is the effect of void, dislocation and precipitate structures on postirradiation mechanical properties and fracture toughness. The cause of reduced swelling in ferritic alloys may in part be due to the martensite lath boundary spacing [7,35], **or** the complex dislocation evolution but the major factor appears to be due to the body centered cubic crystal structure which provides low relaxation volumes for interstitials and leads to reduced net bias in comparison with austenitic alloys.[12,36]

Implications for fusion reactor applications. HT-9 provides several advantages over an austenitic PCA material for first wall applications. In particular swelling and thermally induced fatigue crack growth are significantly lower. (Also, the opportunities for development of low activation alloy counterparts appears to be better.[37-38]) However, designers should be aware of high temperature strength limitations and significant degradation in mechanical properties following irradiation at temperatures below 400°C. Although mechanical properties remain attractive based on the presently available data base, **it** must be emphasized that the most severe degradation is expected to occur for irradiation temperatures in the range 100 to 300°C and results are now too limited to predict behavior in that temperature range. **It** is therefore recommended that until the data base is expanded, reactor designers avoid the use of HT-9 and similar allovs in irradiation environments below ~350°C.

Design equation development. A part of the AOIP effort has been the compilation of the Materials Handbook for Fusion Energy Systems, DOE/TIC-10122.[39] The Handbook includes peer review of submitted property design eauations. **It** is intended to orovide materials property information for fusion reactor systems design and includes Section AA, Ferritic Steels, based primarily on the HT-9 data base. A

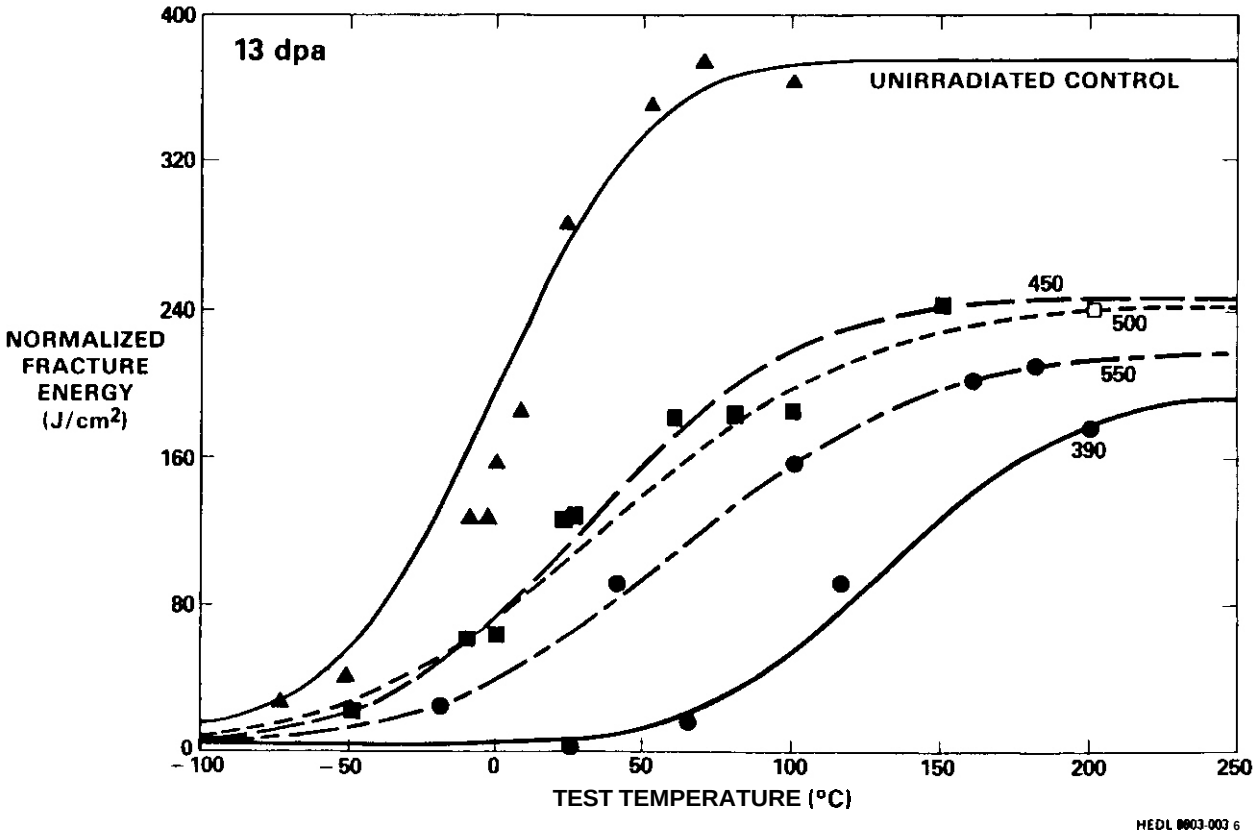

Fig. 7.5.5. Charpy impact curves for irradiated HT-9 base metal miniature samples: [a) to 13 dpa, and (b) to 26 dpa.

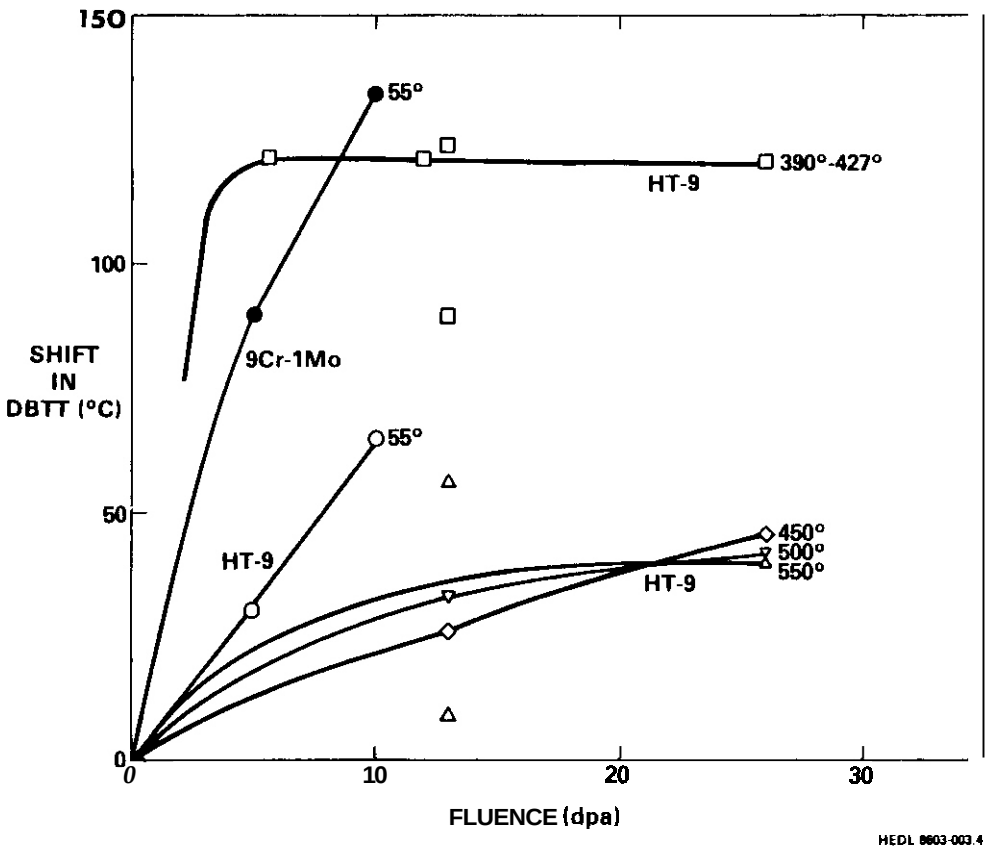

Fig. 7.5.6. Shift in DBTT as a function of fluence for HT-9 and 9Cr-1Mo. The 390-427°C irradiated specimens show saturation at the lowest fluence.

tentative swelling equation should be available by the time of this conference and future equations are under review for irradiation creep and planned for fatigue, fracture toughness and tensile strength. Reactor designers are therefore encouraged to make use of this information source.

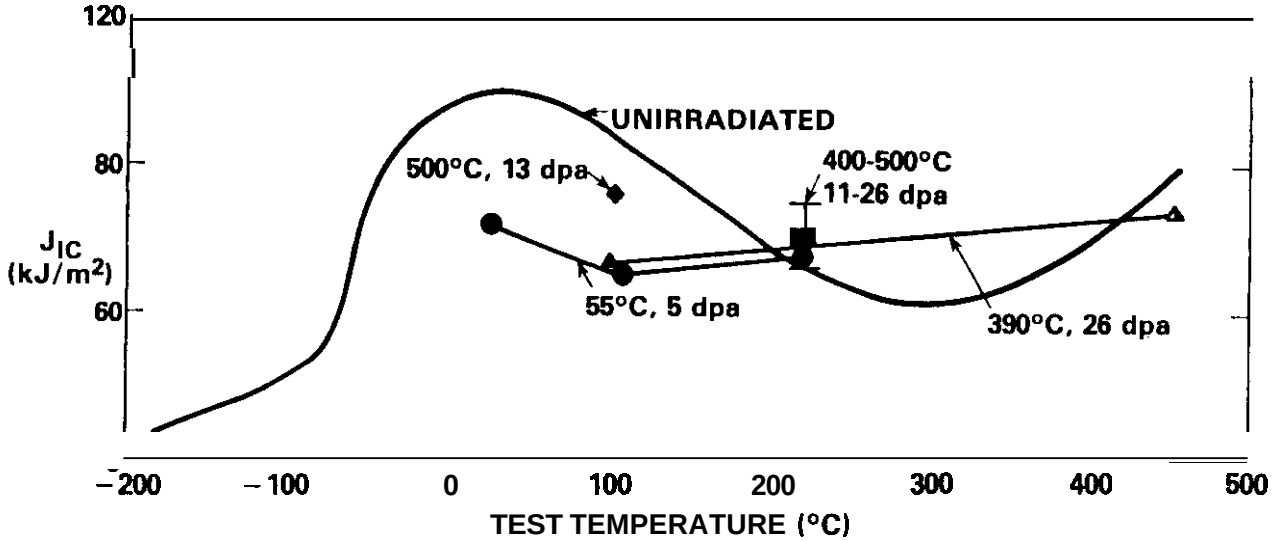

HEDL 8603-003.1

Fig. 7.5.7, Fracture toughness (J_{IC}) as a function of test temperature comparing unirradiated specimen results with irradiated specimen conditions (as marked).

7.5.5 Conclusions

Ferritic alloys should provide an attractive material for structural applications in a fusion reactor but the temperature regime over which they are used must be limited.

7.5.6 Future Work

This work will be continued as more data becomes available.

7.5.6 References

1. See J. Nucl. Mater. 85 & 86 (1979); 103 & 104 (1981); 122 & 123 (1984); and 133 & 134 (1985).
2. The Fusion Reactor Materials Program Plan. Section 1, Alloy Development for Irradiation Performance, DOE/ET-0032/1 (1978).
3. D.S. Gelles, J. Nucl. Mater. 122 & 123 (1984) 207.
4. D.S. Gelles, J. Nucl. Mater. 103 & 104 (1981) 975.
5. D.S. Gelles, "Microstructural Examination of Several Commercial Alloys Neutron Irradiated to 100 dpa," Proceedings of the Section International Conference on Fusion Reactor Materials, April 13-17, 1986, Chicago, IL.
6. D.S. Gelles and R.J. Puigh in Effects of Radiation on Materials, ASTM-STP 870, eds. F.A. Garner and J.S. Perrin (ASTM, Philadelphia, PA, 1985) 19.
7. D.S. Gelles and L.E. Thomas in Proc. of Topical Conf. on Ferritic Alloys of Use in Nuclear Energy Technologies, Snowbird 1983, eds. J.W. Davis and O.J. Michel (AIME, Warrendale, PA, 1984).
8. J.M. Vitek and R.L. Klueh, ibid, 551.
9. D.S. Gelles in ADIP Semiannual Progress Report, DOE/ER-0045/14 (ORNL, 1985) 129.
10. D.S. Gelles and R.L. Meinecke, ibid, DOE/ER-0045/11 (DRNL, 1984) 103.
11. E.A. Little and D.A. Stow., Met. Sci. (1980) 89.
12. L.L. Horton and J. Bentley, ibid reference 7, 569.
13. F.A. Smidt, Jr., P.R. Malonberg, J.A. Sprague and J.E. Westmoreland in Irradiation Effects on the Microstructure and Properties of Metals, ASTM-STP 6711, eds. F.R. Shober and J.A. Sprague (ASTM, Philadelphia, PA, 1976) 227.
14. E.A. Little, Phys. Stat. Sol. (a) 87 (1985) 441.
15. W.G. Johnston, T. Lauritzen, J.H. Rosolowski and A.M. Turkalo in Effects of Radiation on Materials. ASTM-STP 782, eds. H.R. Brager and J.S. Perrin (ASTM, Philadelphia, PA, 1982) 809.
16. F.A. Garner, J. Nucl. Mater. 122 & 123 (1984) 459.
17. R.J. Puigh, ibid reference 6, 7.
18. R.J. Puigh, "In-Reactor Creep Behavior of the Fusion Heats of HT-9 and Modified 9Cr-1Mo," Proceedings of the Section International Conference on Fusion Reactor Materials, April 13-17, 1986, Chicago, IL.

19. A.M. Ermi, to be published, reported in ADIP Path E Review Meeting held March 8, 1985 in San Diego, CA.
20. L.A. James, J. Eng. Mater. & Tech. 102 (1980) 187.
21. R.L. Klueh and J.M. Vitek, ibid reference 9, DOE/ER-0045/10 (ORNL, 1983) 104.
22. R.L. Klueh, P.J. Maziasz and J.M. Vitek, ibid, DOE/ER-0045/14 (ORNL, 1985) 87.
23. R.L. Klueh, J.M. Vitek and M.L. Grossbeck, J. Nucl. Mater. 103 & 104 (1981) 887.
24. R.L. Klueh and J.M. Vitek, ibid reference 7, 615.
25. J.L. Straalsund and D.S. Gelles, oral presentation reference 7, HEDL-SA-2771 FP.
26. W.L. Hu, ibid reference 9, DOE/ER-0045/13 (ORNL, 1985) 106.
27. W.R. Corwin, J.M. Vitek and R.L. Klueh, ibid, 120.
28. F.A. Smidt, Jr., J.R. Hawthorne and V. Provenzano, Effects of Radiation on Materials: Tenth Conf. ASTM-STP 725, eds. D. Kramer, H.R. Brager and J.S. Perrin (ASTM, Philadelphia, PA, 1981) 269.
29. D.S. Gelles, W.L. Hu, F.H. Huang and G.D. Johnson, ibid reference 10, 115.
30. W.L. Hu and D.S. Gelles, ibid reference 7, 631.
31. F.H. Huang, ibid reference 10, 180.
32. F.H. Huang, ibid reference 26, 156.
33. F.H. Huang, ibid reference 10, 172.
34. E.A. Little and L.P. Stater, ibid reference 15, 207.
35. P.J. Maziasz, R.L. Klueh and J.M. Vitek, ibid reference 9, DOE/ER-0045/15 (ORNL, 1986) 91.
36. J.J. Sniegowski and W.G. Wolfer, ibid reference 7, 579.
37. D.S. Gelles and M.L. Hamilton, Proceedings of the Section International Conference on Fusion Reactor Materials, April 13-17, 1986, Chicago, IL.
38. H. R. Brager and F.A. Garner, "High Fluence Neutron Irradiation of Commercial and Developmental Fe-Cr-Mn Austenitic Alloys for Reduced Activation Fusion Materials," Proceedings of the Section International Conference on Fusion Reactor Materials, April 13-17, 1986, Chicago, IL.
39. Materials Handbook for Fusion Energy Systems, DOE/TIC-10122 (McDonnell Douglas Astronautics Company, St. Louis, MD, beginning 1980).

7.6 EFFECTS OF IRRADIATION ON LOW ACTIVATION FERRITIC ALLOYS TO 45 dpa - D. S. Gelles and M. L. Hamilton (Westinghouse Hanford Company)

7.6.1 ADIP Task

The U. S. Department of Energy (DOE) Office of Fusion Energy (OFE) has cited the need to investigate ferritic alloys under the ADIP Program task, Ferritic Steels Development (Path E). The tasks involved are akin to task numbers 1.B.13, Tensile Properties of Austenitic Alloys, l.C.l, Microstructural Stability and 1.C.2, Microstructures and Swelling in Austenitic Alloys.

7.6.2 Objective

The objective of the work is to provide guidance on the applicability of low activation bainitic and martensitic steels for fusion reactor structural components.

7.6.3 *Summary*

Nine low activation ferritic alloys covering the range 2 to 12Cr with alloying additions of tungsten and/or vanadium have been irradiated to intermediate fluences of 30 to 45 dpa and tensile tested or examined by transmission electron microscopy in order to determine the effect of increasing neutron dose on properties and microstructure. Changes in properties and microstructure are for the most part completed within 10 dpa but swelling and dislocation evolution continue with increasing dose at 420°C and subgrain coarsening occurs at 600°C.

7.6.4 Progress and Status

7.6.4.1 Introduction

In a previous report,[1] results of postirradiation tensile tests and microstructural examinations were described for a series of low activation ferritic alloys following irradiation in the FFTF MOTA 18 test to 15 dpa. The alloy series consisted of three Fe-2Cr-0.1C bainitic alloys with varying additions of vanadium, four Fe-9Cr-0.1C martensitic alloys with tungsten andlor vanadium additions for strengthening and either carbon or manganese added for austenite stabilization and two Fe-12Cr-0.1C martensitic alloys with tungsten andlor vanadium additions for strengthening and manganese added for austenite stabilization. The present effort is intended to provide preliminary results for the same specimen conditions following irradiation in the MOTA 1C test to 45 dpa. Tensile tests on specimens irradiated at 420 and 585°C and microstructural examinations on specimens irradiated at 420 and 600°C have now been performed and are reported herein. Specimens irradiated at 520°C remain to be examined and miniature Charpy specimens irradiated at 365°C remain to be tested. Duplicate specimens continue to be irradiated in MOTA 1D and 1E, and are to be removed at approximately 100 dpa. The reader should refer to reference 1 for details concerning alloy design, fabrication, testing and lower fluence results.

7.6.4.2 Experimental Procedure

SS-3 type tensile specimens were irradiated at 426°C in MOTA 1C basket 2C and received a peak fluence as high as 1.0×10^{23} n/cm^2 (E > 0.1 MeV) or 46.3 dpa. In MOTA 18, they had been at 407°C, and therefore the average temperature was 417°C. Other specimens were irradiated at 585°C in MOTA 1C basket 1E and received a peak fluence as high as 8.7×10^{22} n/cm^2 (E > 0.1 MeV) or 39.3 dpa. In MOTA 18, the specimens had been at 580°C and therefore, the average temperature was 583°C. TEM specimens were either irradiated in packet FF from basket 2C4 of MOTA 1C which ran at 426°C and accumulated a fluence of 9.5×10^{22} n/cm^2 (E > 0.1 MeV) or 43.3 dpa (in MOTA 18, the temperature had been 407°C giving an average of 417°C), or were irradiated at 600°C in packet FE01 from basket 283 and accumulated a fluence of 1.4×10^{22} n/cm^2 or 33.8 dpa. The MOTA 18 dose estimates for packet FF have been revised from 7.7 to 9.8 dpa and the values given above include that revision. Fluence and temperature estimates are from reference 2. Specimen handling was identical to that previously described1 except that identification of engraving codes on specimens from packet FF proved to be difficult. Examinations followed routine procedures.[1]

7.6.4.3 Results

Tensile Properties

Sixteen SS-3 tensile specimens irradiated in MOTA 1C were tested at room temperature. The test results are included in Table 7.6.1 along with previous results. The results show that increasing the dose from approximately 10 dpa to approximately 40 dpa changes tensile properties very little. This is demonstrated in Figure 7.6.1 which shows yield strength and total elongation as a function of dose for eight of the nine low activation alloys (alloy 8, Fe-12Cr-6.5Mn-1W-0.3V-0.1C was not included in the test matrix). Figures 7.6.1a and 7.6.1b show results for specimens irradiated at 420°C. Each class of alloys (2Cr, 9Cr or 12Cr) shows a minimal decrease in strength with increasing dose from 10 to 40 dpa and only minor variations in strength within a given class. In all but one case, total elongation increased moderately with increasing dose, the exception being alloy 2. The results from alloy 3, specimen TZ02,

Table 7.6.1. Results of Low Activation Alloy Tensile Tests at Room Temperature with Comparison of Results for Commercial Alloys

$\dot{\epsilon} = 4 \times 10^{-4}$/sec

Alloy	Specimen ID	Dose (dpa)	Nominal Irrad. Temp. (°C)	Yield Strength (MPa)	Ultimate Strength (MPa)	Uniform Elongation (%)	Total Elongation (%)
2¼Cr-1Mo*	---	---	---				
2¼Cr-1Mo*		12	400				
2¼Cr-1Mo*		12	550				
1	TE 07	---	---	778	900	5.3	13.9
	08	---	---	792	902	6.1	13.9
	01	8.4	420	1248	1279	0.8	8.3
	02	43.7	420	992	1014	1.1	7.6
	05	39.3	585	204	319	21.6	>32.5
2	TH 07	---	---	288	566	16.6	28.5
	08	---	---	335	544	13.4	24.9
	03	11.5	420	1055	1086	1.0	8.1
	02	42.6	420	1110	1121	23.9	8.0
	04	14.1	585	146	351	23.9	38.9
	05	39.3	585	204	319	21.6	>32.5
3	TZ 08	---	---	297	477	12.3	24.4
	01	8.4	420	706	755	1.7	6.1
	02	43.7	420	Failed at 179 MPa and 0.0017 Strain			
	04	14.3	585	180	367	16.9	25.7
	05	37.2	585	199	346	10.4	16.4
9Cr-1Mo	---	---	---	575	690	---	-10
4	TM 07	---	---	565	666	4.6	16.6
	08	---	---	567	664	4.0	14.9
	01	11.5	420	660	698	2.2	12.0
	02	46.3	420	550	626	5.7	16.1
	04	14.3	585	310	460	12.8	22.7
	05	37.2	585	348	491	16.6	23.9
5	TP 07	---	---	565	673	5.1	14.8
	08	---	---	600	677	6.5	16.9
	01	9.8	420	599	670	5.9	15.8
	02	43.3	420	544	652	8.9	18.6
	04	13.7	585	343	419	17.8	33.5
	05	34.7	585	348	542	20.9	32.2
6	TN 07	---	---	553	712	6.4	>10.5
	08	---	---	578	731	6.8	17.6
	01	11.5	420	622	730	5.5	15.9
	02	43.3	420	581	718	9.2	18.6
	04	13.7	585	367	562	18.3	30.2
	05	34.7	585	362	597	16.4	28.9
7	TR 07	---	---	587	716	5.6	15.8
	01	9.8	420	608	714	5.8	15.8
	02	43.3	420	564	693	10.0	19.1
	05	39.3	585	463	626	15.1	25.9
HT-9	---	---	---	610	760	---	-12
9	TU 08	---	---	822	1002	2.3	10.1
	01	8.4	420	848	942	6.0	14.7
	02	43.7	420	684	853	9.3	16.1
	04	14.3	585	531	749	9.3	19.4
	05	37.2	585	449	744	18.0	21.2

*Tested at 205°C.

are not included in these figures; the results suggest premature failure and may therefore be fallacious, but it is quite possible that severe embrittlement has occurred in this condition. Visual examination at 10X showed a brittle fracture with the fracture surface normal to the stress axis. Figures 7.6.1c and 7.6.1d show results for specimens irradiated at 585°C. Again, the results can be grouped according to allow class and only minimal changes in yield strength occur with increases in dose. Of considerable note is the data point for alloy 7 which provides strength values very similar to alloy 9. This represents the first comparison of 9 vs. 12Cr alloys containing 1%W following irradiation since alloy 7 was not tested following irradiation to 14 dpa at 585°C. Therefore, the band defining 9Cr alloy behavior may be misleading, and previous conclusions that 12Cr alloys were superior to 9Cr steels are now in doubt. Also of note is the reduction in total elongation with increasing dose found for alloy 3 shown in Figure 7.6.1d. Apparently, embrittlement is occurring in this alloy following irradiation at 585°C which suggests that the data obtained from 420°C test specimen TZ02 which had failed prematurely are in fact valid.

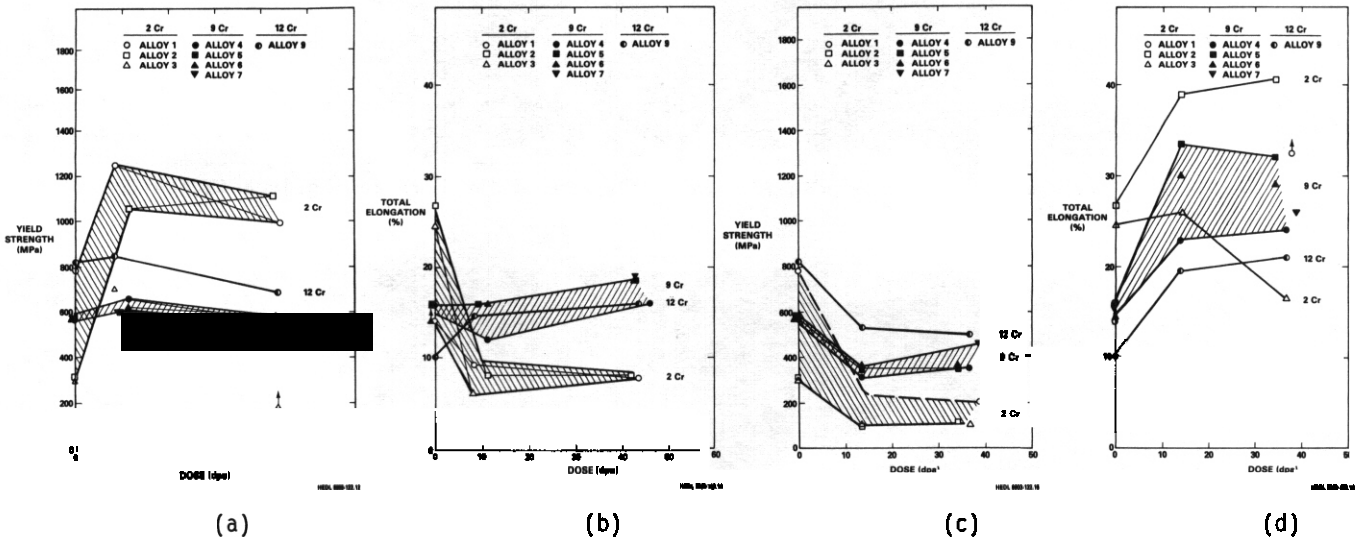

Fig. 7.6.1. Low activation alloy tensile properties as a function of dose. Yield strength (a) and total elongation (b) following irradiation at 420°C and yield strength (c) and total elongation (d) following irradiation at 585°C.

Nicrostructures

Nicrostructural examinations were performed using transmission electron microscopy on all low activation alloys irradiated at 420 and 600°C and in general showed microstructures similar to those observed at lower fluence. The major differences which could be identified were: (1) increased void swelling due to continued irradiation at 420°C, (2) coarsening of precipitates and subgrain structure following irradiation at 600°C, and (3) development of fault structures in alloys containing high manganese following irradiation at 600°C.

420°C irradiations. The microstructural features found following irradiation to 9.8 dpa were retained following irradiation to 43.3 dpa. However, void and dislocation evolution were more advanced. In the 2Cr alloys, alloys containing 0.5 and 1.0V were found to be void free and precipitate and dislocation structures qualitatively appeared to be more complex. An example is given in Figure 7.6.2 which allows comparison of the dislocation structures of alloy 1 with 0.5V at 9.8 and 43.3 dpa. Loop structures have approximately doubled in size, but the density of the dislocation structures and the consequences of the precipitate structures make quantitative evaluations very difficult. The 1.5V alloy differed in that voids were uniformly distributed through the specimen and had grown as large as 30 nm after 43.3 dpa. An example is given in Figure 7.6.3 which shows alloy 3 with 1.5V at 9.8 and 43.3 dpa under similar imaging conditions [$\bar{g}$= 110 near (001)]. At 9.8 dpa (Figure 7.6.3a), loop sizes are nonuniform and voids are nonuniformly distributed whereas at 43.3 dpa (Figure 7.6.3b), both voids and loops are uniformly distributed and are larger in size. Void swelling measurements for alloy 3 at 43.3 dpa indicate 0.072% swelling, with a void density of 3.8 x 10^{14} voids/cm^3 and a mean void size of 17 nm.

In the 9Cr alloys, all alloys contained void swelling. The voids were nonuniformly distributed within martensite laths with size distributions including very small sizes. all indicative of material in the incubation stage of void development. Examples of the void structures in alloys 5 and 6 (0.5V with 2.5Mn and 1.5V with 0.2C and 1.0Mn) are shown in Figure 7.6.4. The voids appear as sharply defined white features with facetted sides, whereas the poorly defined light features are surface pits probably associated with voids that were attacked during electropolishing. It may be noted that the larger voids in alloy 6 all differ in shape. Although this is usually the result of void-precipitate association

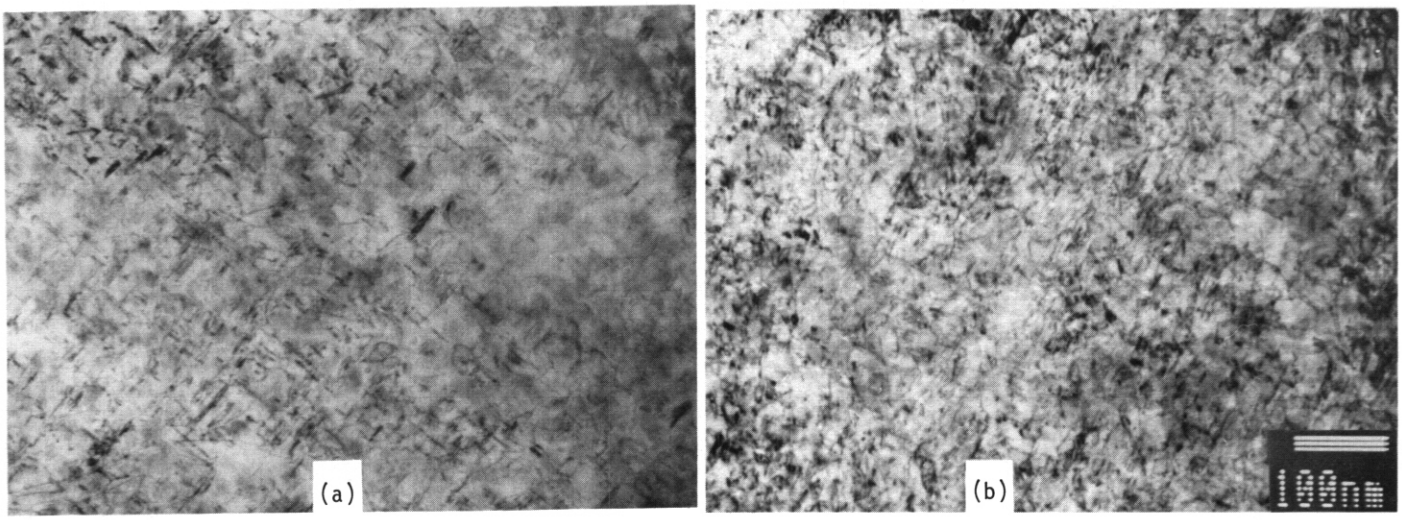

Fig. 7.6.2. Dislocation structures in 2Cr low activation alloy 1 following irradiation to (a) 9.8 and (b) 43.3 dpa at 420°C.

Fig. 7.6.3. Dislocation and void structures in 2Cr low activation alloy 3 following irradiation to (a) 9.8 and (b) 43.3 dpa at 420°C.

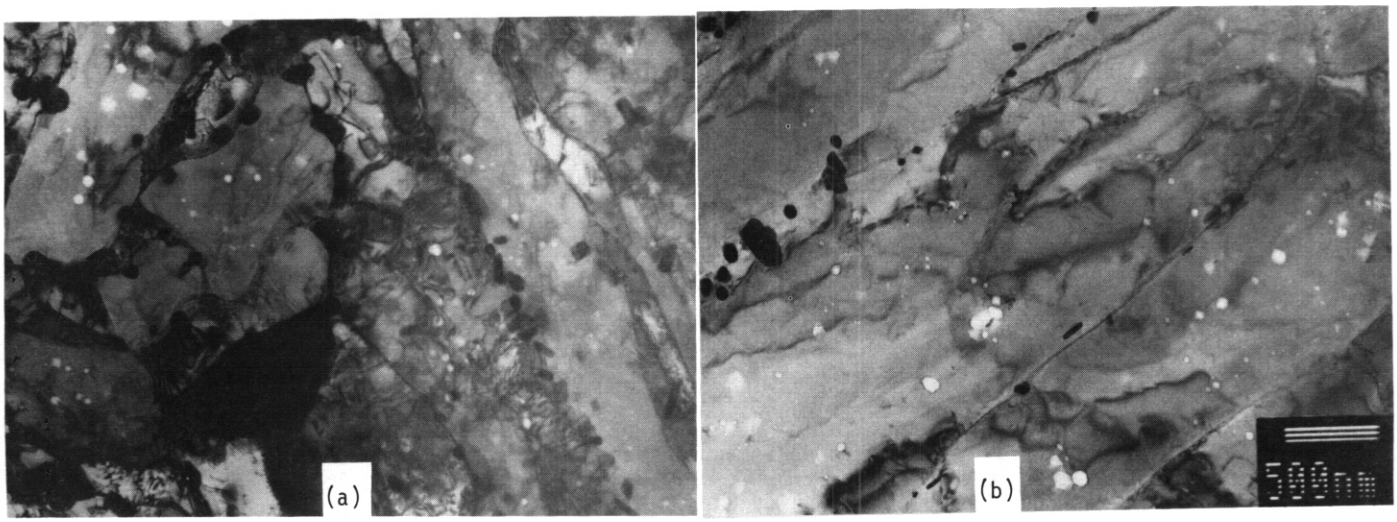

Fig. 7.6.4. Void swelling in 9Cr low activation alloys following irradiation to 43.3 dpa at 420°C, (a) alloy 5 and (b) alloy 6.

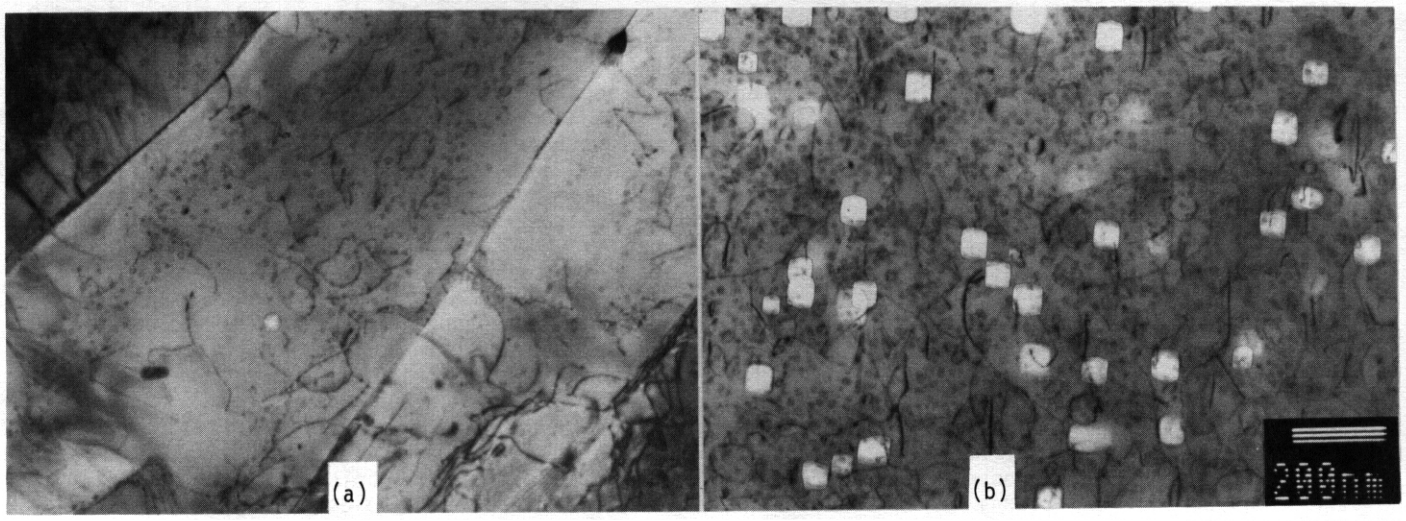

Fig. 7.6.5. Void swelling in 12Cr low activation alloy 8 following irradiation to 43.3 dpa at 420°C, (a) in martensite laths and (b) in ferrite.

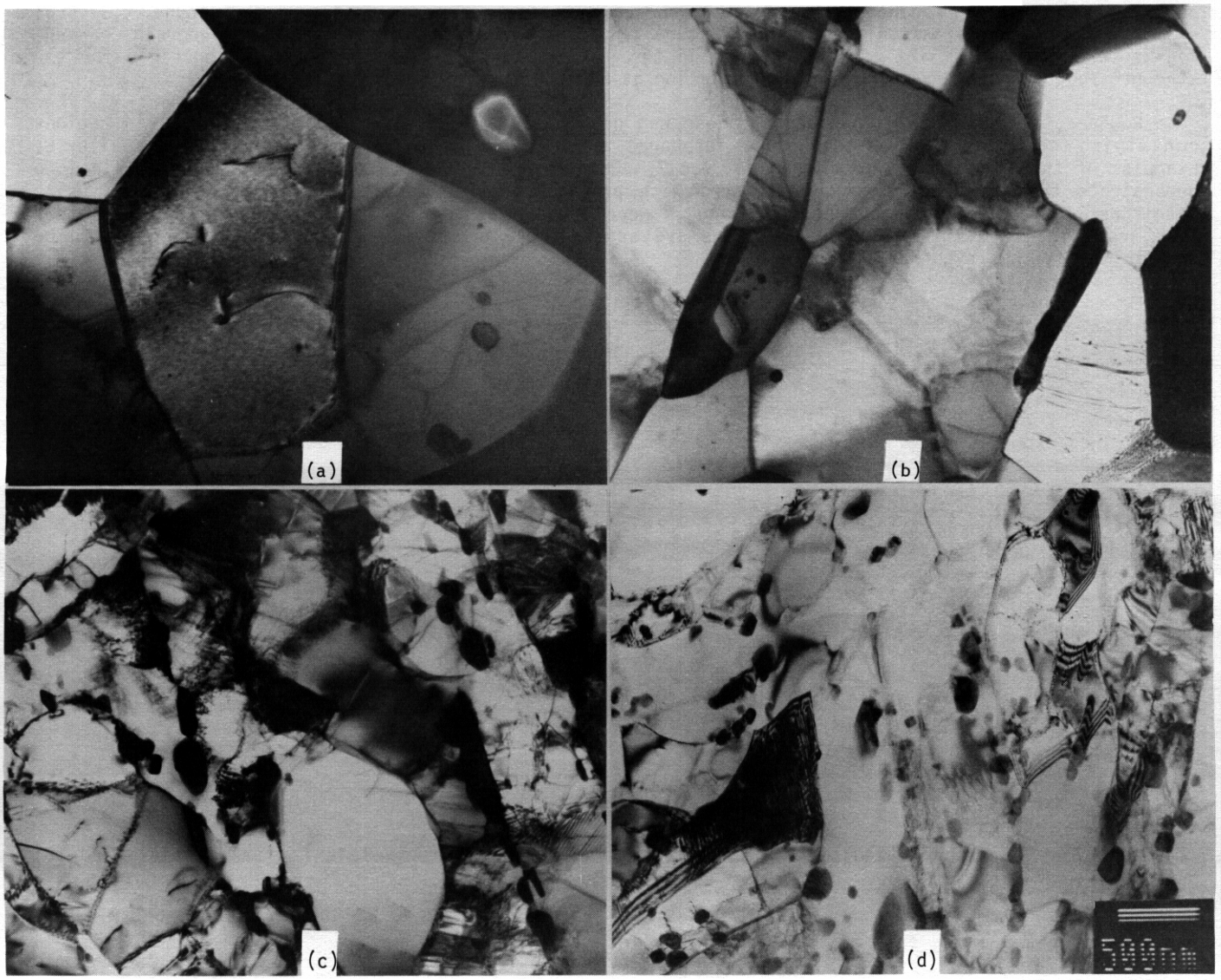

Fig. 7.6.6. Subgrain structure in low activation alloys following irradiation to 33.8 dpa at 600°C, (a) 2Cr alloy 2, (b) 9Cr alloy 5, (c) 9Cr alloy 7, and (d) 12Cr alloy 9.

inspection at higher magnification did not reveal the presence of any precipitation. Only alloys 6 and 8 (12Cr with 1V and 3.5Mn, respectively) displayed this behavior and therefore it may be associated with high vanadium concentrations. The dislocation structure consisted of dislocation tangles between martensite lath walls in all specimens and precipitation appeared to be limited to blocky carbides at grain and lath boundaries. Therefore, the major effects of increased dose from 9.8 to 43.3 dpa in the 9Cr alloys were due to evolution of void and dislocation structures.

The 12Cr alloys behaved similarly to the 9Cr alloys except that void evolution within martensite laths was reduced. The major results of irradiation on microstructure at lower dose were retained: dislocation evolution and α' precipitation. The dislocation structure had evolved to a combination of individual loops and dislocation tangles, but the a' precipitation appeared to be stable with little apparent change in particle size. Examples are given in Figure 7.6.5 which show martensite and ferrite regions in alloy 8. Figure 7.6.5a shows a region of martensite laths containing a single void in g = 110 contrast and Figure 7.6.5b shows a ferrite region in g = 200 contrast. In both figures, the a' precipitates can be seen as small equiaxed particles, quite non-uniformly distributed within the laths. Of particular note is the dislocation distribution in the ferrite. In g = 200 contrast, only one set of a [001] dislocation loops are visible and they appear almost edge on whereas all a12 [111] loops are visible and they are less steeply inclined. Figure 7.6.5b therefore shows that both a [001] and a12 [111] Burgers vectors are present in the ferrite but a/2 [111] are in the majority. Swelling in alloy 9 (12Cr with 1W, 0.3V and 6.5Mn) was similar to that in alloy 8 except that voids were generally smaller indicating that swelling incubation in alloy 9 is longer than in alloy 8.

600°C irradiations. All alloy microstructures were altered considerably due to irradiation at 600°C to 33.8 dpa. The major effect was rearrangement of martensite lath boundaries into more equiaxed subgrain structure with concurrent subgrain coarsening. Carbide coarsening was also found. Several examples at low magnification are given in Figure 7.6.6. As shown in Figure 7.6.6, the subgrain coarsening is more advanced in the 2Cr alloys than in the 9Cr alloys. This coarsening is responsible for the strength reduction observed Following irradiation at 600°C.

However, alloys containing high manganese had developed stacking fault structures often in regions containing carbides. These structures appeared to be more prevalent in alloy 9 than in alloy 8. Examples of the faults are shown in Figure 7.6.7. Unfortunately, no diffraction spots were obtained to demonstrate that the faults were associated with precipitates; the faults could only be imaged using matrix reflections. The fact that these faults were found only in high manganese alloys suggests that they are related to the manganese additions and are probably precipifaults. Further work needs to be done to verify this hypothesis.

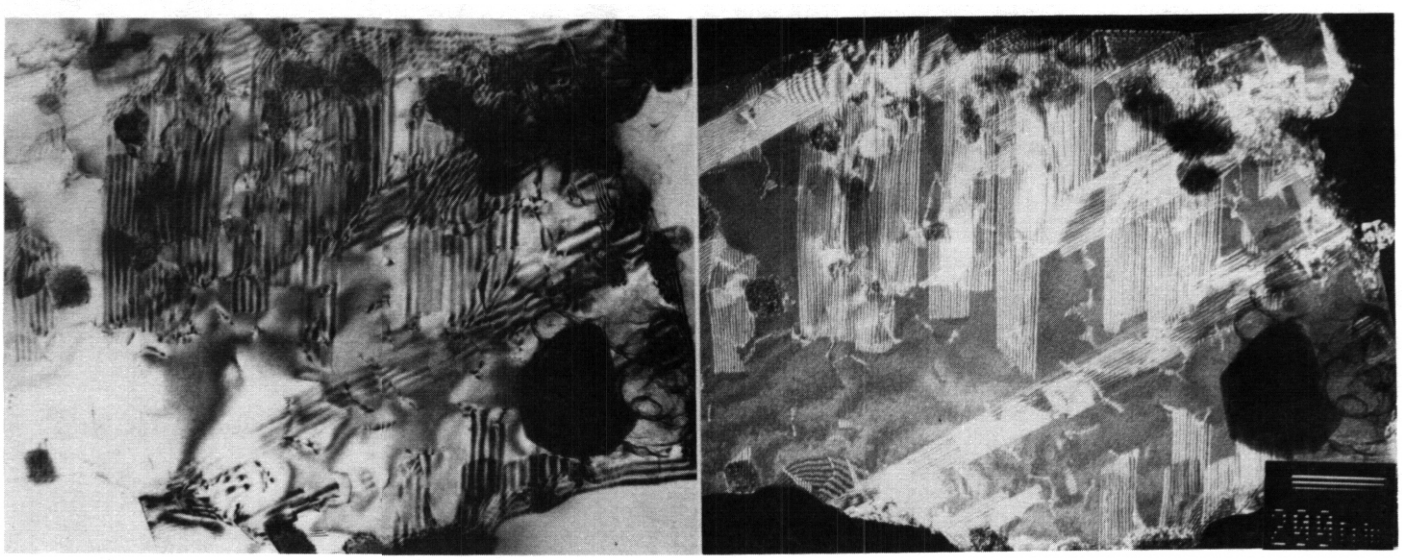

(a) (b)

Fig. 7.6.7. Stacking fault features in 12Cr low activation alloy 9 in (a) bright field and (b) matrix dark field contrast.

Precipitate Compositions

Extraction replicas were prepared from all TEM specimen conditions irradiated at 420 and 600°C. The results of energy dispersive x-ray analysis (EDX) on particles in those replicas are given in Table 7.6.2. The results can be summarized as follows. Phase stability is more complex at 420 than at 600°C.

Table 7.6.2. Metal compositions in weight percent of extracted precipitate particles

Allov	Metal Composition	Irradiation Conditions	Fe	Cr	Mn	V	W	Other	#	I.D
1	2Cr-0.5V	625°C,43.3 dpa	.7-4.1	0-18	.7-2.6	76-96	---	---	10	V_4C_3
			4-21	42-62	0-6	24-50	---	---	4	?
			39-51	45-61	0-1	4-5	---	---	7	M_7C_3
			6-16	34-50	.5	46-60	---	---		?
		600°C,33.8 dpa	0-3	0-9	0-2	78-98	---		16	V_4C_3
			.3-.5	.5-1	.5-1.5	.5-1.5	---	Si:94-96 (Ti: 0-1	1	SiO_2
2	2Cr-1.0V	425°C,43.3 dpa	2-5	3-23	0-1	71-95	---		7	V_4C_3
			0-20	30-55	0-5	32-62	---		10	?
			2	4	---	4	---	Si:90	1	SiO_2
		600°C,33.8 dpa	3-18	0-9	---	72-97	---		15	V_4C_3
			23-67	0-10	---	0-46	---	Si:15-23		
3	2Cr-1.5V-0.3Mn	425°C,43.3 dpa	1-6	0-20	0-2	72-98	---		10	V_4C_3
			7-19	40-60	0-7	22-50	---		11	?
				9	37	19		Si:35	1	MnS
		600°C,33.8 dpa	2-6	.3-4	0-.7	91-97	---	Si:0-1		V_4C_3
4	9Cr-0.5V	625°C,43.3 dpa	0-9	8-28	0-.8	67-87	---	Si:0-16	11	V_4C_3
			0-25	33-51	0-2	30-59	---		6	?
			0-5	3-5	22-24	0-1	---	Si:55-59 Ti:2-7 Al:7-10	3	SiO_2
		600°C,33.8 dpa	22-27	71-78	---	2-3	---			$M_{23}C_6$
5	9Cr-1.3V-1Mn	425°C,43.3 dpa	18-26	62-74	---	8-16	---			$M_{23}C_6$
		600°C,33.8 dpa	22-27	66-72	---	3-12	---		14	$M_{23}C_6$
			2-6.5	3-5	0-1	89-93	---		4	V_4C_3
6	9Cr-0.5V-2Mn	425°C,43.3 dpa	18-33	61-74	1-9	0-8	---			$M_{23}C_6$
		600°C,33.8 dpa	20-34	65-73	3-5	1-2	---			$M_{23}C_6$
7	9Cr-0.3V-1W-2.5Mn	425°C,43.3 dpa	28-62	48-57	2-7	0-1	7-13		14	$M_{23}C_6$
			43-64	28-43	3	0-1.5	5-9		2	x or Laves
		600°C,33.8 dpa	17-28	45-64	1-3	1-2	10-20		18	$M_{23}C_6$
			0-4	18-40	37-48	4-6	0-2	Al:4-8 Ti:7-13	6	E?
8	12Cr-1V-6.5Mn	425°C,43.3 dpa	17-28	51-68	5-24	0-7	---			$M_{23}C_6$
		600°C,33.8 dpa	14-21	69-83	.5-5	3-5	---			$M_{23}C_6$
9	12Cr-0.3V-1W-6.4Mn	625°C,43.3 dpa #1	16-24	55-60	5-14	0-2	8-18			$M_{23}C_6$
		#2	25-38	55-67	0-2	0-1	4-ii	Ni:0-2	14	$M_{23}C_6$
			9	3-7	7-11	0	38-46	Ni:31-38	2	?
		600°C,33.8 dpa	12-21	61-68	2-4	0-2	9-19			$M_{23}C_6$

In the 2Cr alloy range, 0.5V leads to phase instability whereas alloys with 1.0 and 1.5V are stable. In the 9Cr composition range, 1.3V promotes some V_4C_3 but V_4C_3 appears to be absent for lower levels. For alloys containing 1W, precipitates with approximate composition 30%Fe, 60%Cr and 10%W were found following irradiation at 420°C. Tungsten based Chi phase is expected to have composition of 45% Fe, 45% Cr and 10% W[3] but diffraction information is not yet available to confirm this identification. Manganese levels appear to be higher in $M_{23}C_6$ following irradiation at 420°C. Table 7.6.2 includes results from two replicas taken from alloy 9 following irradiation at 420°C. The results are somewhat different and are included to provide a measure of the uncertainties of the technique. The most probable cause of the discrepancies was differences in etching technique which extracted different particle compositions. For example, different voltage settings may give different amounts of matrix material coating each particle. Also, extracted particles can in fact consist of two or more different precipitates and measurements would average the different compositions. Therefore, the results of Table 7.6.2 have been compiled to show ranges of particle composition measurements, with the actual precipitate composition expected to within those ranges.

7.6.4.4 Discussion

This effort raises several topics for discussion. Swelling can apparently occur in low activation ferritic alloys. Phase instabilities are found and a brief review of the results as they apply to alloy design is pertinent. Finally, an explanation can be envisioned to account for severe embrittlement in irradiated ferritic alloys which may explain the behavior of specimen TZOZ.

Void Swelling

It has been shown that commercial ferritic alloys can develop void swelling following irradiation below 500°C.[4-6] Therefore, observation of swelling is not unexpected in low activation ferritic alloys. A more important concern is whether swelling rates will be higher in low activation alloys than in simple Fe-Cr binary alloys.7 The microstructures found in the present effort are similar to those of binary alloys. For example, both a [001] and a12 [111] Burgers vectors are present and void distributions are normal for the given irradiation temperatures. Therefore, it is anticipated that steady state swelling rates will not exceed 0.06% per dpa[7] and swelling at 500 dpa will not exceed 28% in any of the low activation alloys.

Low Activation Alloy Design

Sufficient results are now available to allow criticism of alloy design criteria. This section will address that issue. The carbide phase stability diagram for Fe-Cr-V alloys at 700°C given in reference 1 applies quite well for low activation alloy design, at least at high temperatures. The major exceptions found involved alloys 1 and 5. In alloy 1, evidence for M_7C_3 was found in extraction replicas of specimens irradiated at 420°C. Therefore, the two-phase field for V_4C_3 and M_7C_3 is somewhat larger at 420°C due to expansion of the M_7C_3 region, a phenomenon which is perhaps unrelated to the irradiation environment. In alloy 5, V_4C_3 was found after irradiation at K00'C which indicates that the two phase field is slightly larger than shown. This may be due to the lower temperature or to the manganese present in the alloy. However, following irradiation at 420°C, extraction replicas provide evidence for precipitates of approximate composition 45% Cr, 45% V and 10% Fe. The phase is as yet unidentified; it may be of an intermetallic or carbide type compound. However, diffraction evidence supports an identification of $(Cr,V)_4C_3$ which is difficult to comprehend.

Concern was raised regarding formation of tungsten based chi phase.[1] Precipitates similar in composition to chi or Laves phase have been found on extraction replicas, hut tensile properties of the irradiated specimens indicate that tungsten additions on the order of 1% do not degrade properties and microstructural examinations do not reveal excessive precipitation.

Manganese additions were made to low activation alloys for austenite stabilization. It was expected that the manganese would be inert with regard to precipitation. The present results indicate that this may not be the case. Stacking fault structures were found only in alloys containing high manganese levels following irradiation at K00'C. Their origin is probably due to manganese containing precipites. Such a hypothesis is compatible with recent Charpy impact test results on manganese stabilized martensitic steels irradiated at 365°C.[8] There it was found that an Fe-12Cr-1Mo-0.1C alloy with 3% Mn gave DBTT behavior similar to that for HT-9 whereas a similar alloy with 6.5% Mn produced shifts in DBTT which were considerably higher than those for HT-9. Therefore, it is anticipated that manganese additions may be detrimental to in-reactor alloy phase stability.

Embrittlement

It has been shown that ferritic alloys may be susceptible to channel fracture induced by void swelling.') It is possible that the test results on tensile specimen TZ02 alloy 3 are related to void induced embrittlement. Alloy 3 was found to contain the highest amount of void swelling of the low activation alloys examined. Although the fracture appearance was not compatible with channel fracture, it is apparent that the possibility of void induced embrittlement in ferritic alloys must be examined with care.

7.6.5 Conclusions

Effects of irradiation on the mechanical properties of low activation alloys saturate rapidly with dose in the temperature range 420 to 585°C. Both 9 and 12Cr alloys containing 1% W have similar high strength properties following irradiation at 585°C to 40 dpa whereas 9Cr alloys with only V additions are weaker and and 2 Cr alloys are weaker still. Microstructural examinations reveal void swelling in most alloys irradiated at 420°C but the swelling remains low after 40 dpa. Based on these results, the most promising alloy class appears to be 9 to 12Cr alloys containing tungsten.

7.6.6 Future Work

This work will be continued and expanded to include postirradiation Charpy impact testing

7.6.7 References

1. D. S. Gelles and M. L. Hamilton, "Effects of Irradiation on Low Activation Ferritic Alloys", p. 128 in AOIP Semiannu. Prog. Rep., Sept. 30, 1984, DOE/ER-0045/13, U.S. DOE, Office of Fusion Energy.

2. A. M. Ermi, Letter, to Distribution, "Fusion Materials Specimens from MOTA-IC FFTF Cycles 5-6", October 11, 1985.

3. H. J. Goldschmidt, "Discussion on Interstitial Compounds", J. Inst. Met. 97 (1969) p. 173.

4. D. S. Gelles, "Swelling in Several Commercial Alloys Irradiated to Very High Neutron Fluence", J. Nucl. Mat. 122 & 123 (1984) p. 207.

5. D. S. Gelles, "Microstructural Examination of Several Commercial Alloys Irradiated to 100 dpa", ibid ref. 1, p. 161.

6. J. M. Vitek and R. L. Klueh, "Microstructure of HFIR-Irradiated 12Cr-1MoVW Ferritic Steel", p. 551 in Proceedings of Topical Conference on Ferritic Alloys for Use in Nuclear Energy Technologies, J. W. Davis and D. J. Michel, eds., The Metallurgical Society of AIME, Warrendale, PA, 1984.

7. D. S. Gelles and R. L. Meinecke-Ermi, "Swelling in Simple Ferritic Alloys Irradiated to High Fluence", p. 103 in AOIP Semiannu. Prog. Rep., Sept. 30, 1983, DOE/ER-0045/11, U.S. DOE, Office of Fusion Energy.

8. W. L. Hu and D. S. Gelles, "Charpy Impact Behavior of Manganese Stabilized Martensitic Steels", Section 7.7 of this document.

9. D. S. Gelles, "Microstructural Examination of Fe-Cr Binary Ferritic Alloys Following Irradiation to 15 dpa in FFTF", p. 54 in ADIP Semiannu. Prog. Rep., Dec. 31, 1985, DOE/ER-0046/24, U.S. DOE, Office of Fusion Energy.

7.7 CHARPY IMPACT BEHAVIOR OF MANGANESE STABILIZED MARTENSITIC STEELS - W. L. Hu and D. S. Gelles (Westinghouse Hanford Company)

7.7.1 ADIP Task

The Office of Fusion Energy/Department of Energy has established the need to determine the fracture toughness of ferritic alloys (Path E).

7.7.2 Objective

The objective of this work is to evaluate the ductile-to-brittle transition temperature (DETT) behavior of manganese stabilized martensitic steels as a function of neutron exposure.

7.7.3 Summary

Tests were conducted to evaluate the irradiation-induced shift in ductile-to-brittle transition behavior of two manganese stabilized martensitic steels. Miniature Charpy specimens were fabricated from two heats of steel similar in composition to HT-9 but with 0.1% C and Mn contents ranging from 3.3 to 6.6%. The 3.3% Mn steel showed a transition temperature similar to that of HT-9 in both the unirradiated condition and in specimens irradiated to 11.3 dpa. The steel containing 6.6% Mn exhibited a higher transition temperature after irradiation than the steel containing 3.3% Mn. The upper shelf energy (USE) after irradiation for the manganese stabilized alloys was much higher than for HT-9.

7.7.4 Progress and Status

7.7.4.1 Introduction

Considerable progress has been made in recent years in the development of heat resistant martensitic stainless steels by carefully controlling the vanadium. niobium and carbon contents, as for example T91 (modified 9Cr-1Mo).[1] The composition range over which this could be applied, however, had been limited to alloys with chromium contents on the order of 9 percent and it was of interest to apply the concepts to steels containing 12 percent chromium. The carbon level in HT-9 was established as 0.2 percent in order to maintain a fully martensitic microstructure. Since carbon contents on the order of 0.2 percent were not required to maintain high temperature strength, a simultaneous objective was to improve the DBTT response by reducing the carbon content. Additions of other austenite stabilizers were required to compensate for reduced carbon levels. Nickel and manganese were the most likely candidates.[2] Nickel additions were shown to promote precipitation in irradiated 12-Cr steels,[3] whereas manganese additions are relatively stable and remained in solution. A series of alloys were manufactured to determine the ideal manganese content for a 12-Cr base alloy. Metallographic examination of the alloys following a treatment of 1100°C/0.5h/AC + 700°C/1h/AC showed that all alloys contained less than 15 percent delta ferrite and that alloys F2 with 3.3% Mn and F4 with 6.6% Mn should provide an adequate test of the effect of manganese on mechanical properties.

7.7.4.2 Specimen Preparation and Irradiation History

The manganese stabilized alloys were manufactured by Carpenter Technology, Inc. as previously described.[4] The compositions are listed in Table 7.7.1 together with the composition of HT-9 for comparison. The major composition difference is in the manganese content, which varied from 1.94 to 6.57 weight percent.

Table 7.7.1. Chemical composition of manganese stabilized as supplied by the vendor

Allov Elements	HT-9 Heat 9607R2	F1 Heat 10995	F2 Heat 10996	F3 Heat 10997	F4 Heat 10998	F5 Heat 10999
C	0.20	0.12	0.10	0.11	0.11	0.15
Mn	0.57	1.94	3.33	4.73	6.57	3.46
Si	0.17	0.12	0.12	0.10	0.10	0.11
P	0.016	0.007	0.007	0.007	0.007	0.008
S	0.003	0.005	0.005	0.005	0.006	0.005
Cr	12.1	11.95	11.8	11.79	12.0	11.90
Ni	0.51	<0.01	0.01	<0.01	<0.01	<0.01
Mo	1.04	0.98	0.96	0.96	0.96	0.97
W	0.45	<0.01	<0.01	<0.01	<0.05	0.23
V	0.28	0.25	0.21	0.25	0.20	0.26
N	0.027	0.003	0.003	0.002	0.003	0.003
Nb	<0.001	0.15	0.16	0.16	0.15	0.15
cu	0.07	0.01	0.01	0.01	0.012	0.013
Fe	Bal.	Bal.	Bal.	Bal.	Bal.	Bal.

Half-size Charpy impact specimens were fabricated from 2.5" x 0.5" forged plate stock with the specimen oriented in the T-L direction. Post-fabrication heat treatment consisted of 1000°C/16h/AC + 1100°C/0.5h/AC + 700°C/2h/AC. Specimens were precracked prior to irradiation.

Specimens of F2 and F4 were irradiated at FFTF in the below core canister of the MOTA assembly. They were discharged at the completion of MOTA 1B having received a neutron exposure of 5.4 dpa. Six new unirradiated specimens of each of the F2 and F4 alloys were then inserted in the below core canister of the MOTA 1C experiment and were removed at the end of cycle six having received a neutron exposure of 11.3 dpa. The irradiation temperature for both batches of specimens was 365°C.[4] Charpy impact tests were conducted with an automated drop tower. The details of the test system and procedures are reported elsewhere.[5]

7.7.4.3 Results and Discussions

The test results are tabulated in Table 7.7.2. The fracture energies, normalized by the fracture area, are plotted as a function of test temperature in Figure 7.7.1. The DBTTs for each alloy at various irradiation conditions are shown in the figure by the numbers enclosed in symbols which correspond to the data plotting symbols. The results show that both of the unirradiated manganese stablized alloys, F2 and F4, have a DBTT of -17°C, slightly above the value for unirradiated HT-9, which has a OETT of 5°C. After irradiation at 365°C to a fluence of 5.4 dpa, the DBTTs increase to 115°C for alloy F2 and to 150°C for alloy F4. The USE, on the other hand, shows an unexpected increase of approximately 30% for both alloys. Further irradiation at the same temperature to 11.3 dpa shifted the DETT and USE still higher, to 130°C and 60 J/cm^2 for alloy F2 and 225°C and 73 J/cm^2 for alloy F4. As a comparison, HT-9 fabricated from wrought bar stock and irradiated at 390°C to 13 dpa exhibits a DETT of 129°C and a USE of only 26 J/cm^2. Alloy F2 shows a similar transition temperature but a much improved USE. Although the USE of alloy F4 is still higher, the high DBTT suggests a less desirable transition behavior. Figures 7.7.2 and 7.7.3 show the DBTTs and USEs of alloys F2 and F4 as a function of neutron exposure.

The drastic increase in USE in both alloys after irradiation indicates a possibly high fracture toughness. A previous study[6] showed that the reduction of USE in irradiated HT-9 is caused mainly by thermal aging in sodium. The addition of manganese to the alloy appears to suppress this thermal aging effect.

7.7.5 Conclusions

Charpy impact tests were performed on two heats of manganese stabilized martensitic stainless steels in three conditions: unirradiated, irradiated at 365°C to 5.4 dpa, and irradiated at 365°C to 11.3 dpa. The alloy containing 3.3% Mn gave DBTT results similar to those of HT-9, while the alloy containing 6.6% Mn showed a larger shift in DBTT due to irradiation. Both alloys, however, developed significantly higher upper shelf energies than HT-9 following irradiation. Therefore manganese additions to martensitic steels have been shown to result in degradation of the DETT but improvement in the upper shelf response following irradiation.

7.7.6 Future Work

Fractographic and microstructural examinations of selected specimens from this study will be performed to identify the possible microstructural changes that lead to the high upper shelf fracture energies.

1.1.7 References

1. D. S. Gelles., "Qotimization of Martensitic Stainless Steels for Nuclear Reactor Aoolications.," in Optimizing Materials for Nuclear Applications, F. A. Garner, D. S. Gelles and F. W. 'Wiffen, eds. (AIME., Uarrendale, PA 1985) pp. 63-71.

2. F. E. Pickering, Physical Metallurgy and the Design of Steels, Chapter 12 (Applied Science Publishers, London, 1978).

3. D. S. Gelles and L. E. Thomas. "Effects of Neutron Irradiation on Microstructure in Experimental and Commercial Ferritic Alloys," in Proceedings of Topical Conference on Ferritic Alloys for use in Nuclear Energy Technologies, (AIME, Uarrendale, PA, 1984) pp. 559-568.

4. A. M. Ermi. "FFTF Fusion Irradiations - FFTF Cycles 4 - 6," AOIP Semi-annual Progress Report for Period Ending March-1983, DOEIER-0045113, pp. 21-40, ORNL, Oak Ridge, TN.

5. U. L. Hu and D. S. Gelles, '"Miniature Charpy Impact Test Results for the Irradiated Ferritic Alloys HT-9 and 9Cr-1Mo," ibid reference 3, pp. 631-646.

6. U. L. Hu, "Change of Charpy Impact Fracture Behavior of Precracked Ferritic Specimens Due to Thermal Aging in Sodium," ADIP Semi-annual Progress Report for Period Ending March 1986, DOE/ER-0045/15, ORNL, Oak Ridge, TN.

Table 7.7.2. Charpy impact test results on manganese stabilized alloys

Specimen I. D.	Test Temperature (°C)	Total Fracture Energy (J/cm2)	Normalized Fracture Energy (J/cm^2)
UNIRRADIATED			
F213	-20	0.698	4.79
F214	0	2.152	14.56
F225	22	4.077	27.78
F216	42	5.267	36.45
F218	60	6.095	41.29
F217	75	5.749	39.49
F417	-20	1.179	8.05
F425	0	2.283	15.21
F416	22	5.029	33.43
F418	42	4.830	32.65
F427	60	4.633	31.22
F426	70	4.909	33.03
IRRADIATED TO 5.4 DPA			
F201	24	0.356	2.49
F204	80	1.013	7.11
F203	110	3.496	23.73
F202	150	7.665	52.67
F206	200	7.538	52.43
F401	22	0.147	1.03
F406	100	0.748	5.05
F402	130	1.627	11.19
F403	150	2.869	19.66
F404	170	4.349	30.03
F405	220	6.016	40.87
IRRADIATED TO 11.3 DPA			
F219	50	0.345	2.30
F220	100	1.349	9.23
F224	125	1.740	12.27
F223	125	2.395	16.53
F221	150	6.963	47.36
F222	200	8.587	59.03
F419	S0	0.144	0.99
F420	100	0.260	1.77
F421	150	0.545	3.70
F422	200	2.807	19.31
F423	250	4.933	33.24
F424	300	10.626	73.04

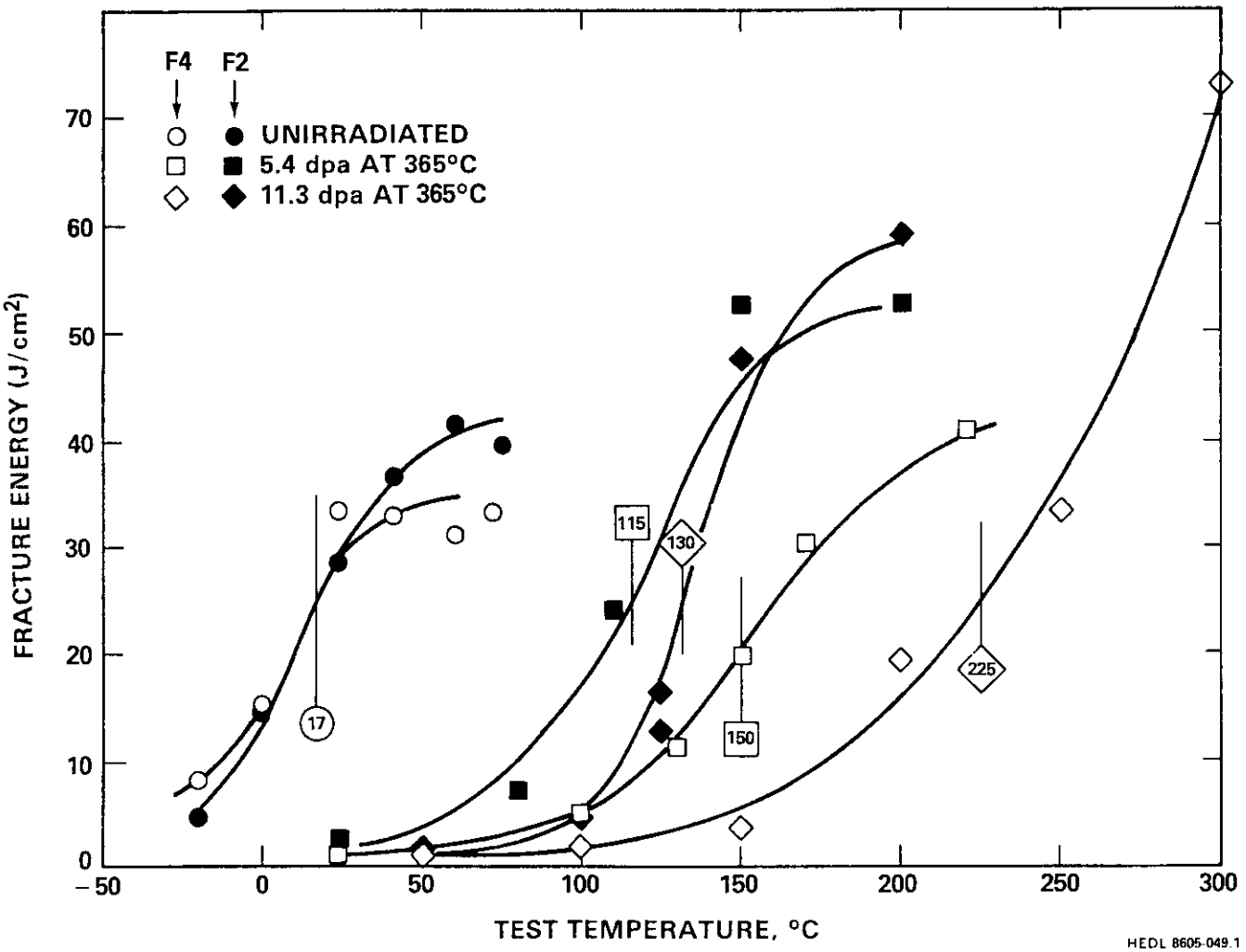

Fig. 7.7.1. Charpy impact fracture energy as a function of test temperature for manganese stabilized martensitic steels.

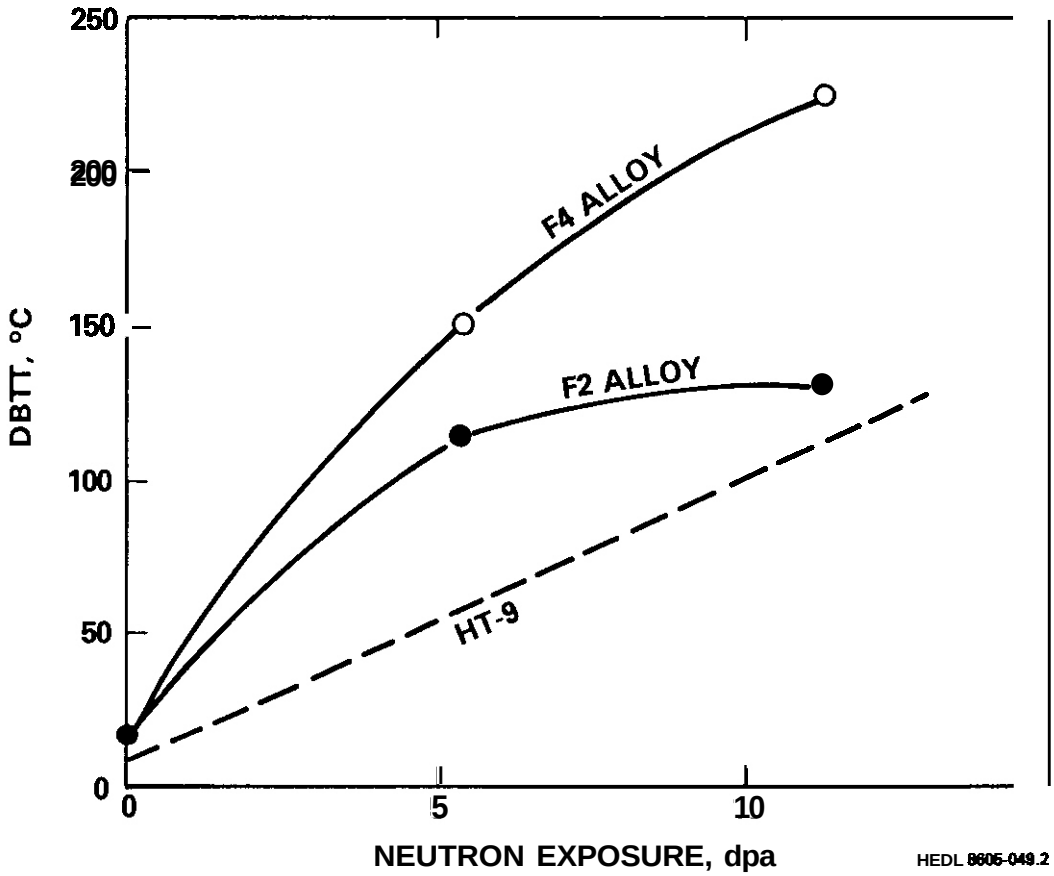

Fig. 7.7.2. Comparison of DBTT's as a function of neutron exposure for HT-9, F2, and F4 alloys.

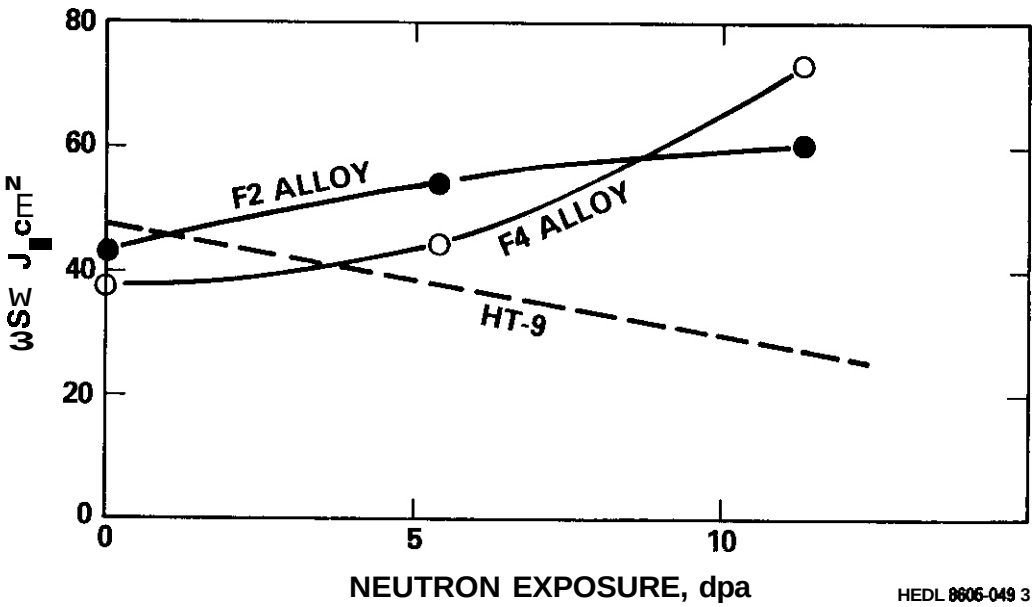

Fig. 7.7.3. Comparison of USE's as a function of neutron exposure for HT-9, F2, and F4 alloys

7.8 FRACTURE TOUGHNESS OF FERRITIC ALLOYS IRRADIATED IN FFTF - F. H. Huang (Westinghouse Hanford Company)

7.8.1 AOIP Task

The Department of Energy/Office of Fusion Energy (DOEIOFE) has cited the need to investigate ferritic alloys under the ADIP program task Ferritic Steels Development (Path E).

7.8.2 Objective

The objective of this work is to evaluate the effectss of neutron irradiation on the fracture behavior of HT-9 and 9Cr-1Mo, which are candidate materials for fusion first wall applications.

7.8.3 *Summary*

Ferritic compact tension specimens loaded in the Material Open Test Assembly (MOTA) for irradiation during FFTF Cycle 4 were tested at temperatures ranging from room temperature to 428°C. The electric potential single specimen method was used to measure the fracture toughness of the specimen. Results showed that the fracture toughness of both HT-9 and 9Cr-1Mo decreases with increasing test temperature and that the toughness of HT-9 was about 30% higher than that of 9Cr-1Mo. In addition, increasing irradiation temperature resulted in an increase in tearing modulus for both alloys.

7.8.4 Introduction

Irradiations of ferritic alloys in support of the ADIP program have been carried out in the Experimental Breeder Reactor (EBR) II and the Fast Flux Test Facility (FFTF). During irradiation in FFTF, the specimen were placed in the Materials Open Test Assembly (MOTA] which was capable of monitoring and controlling the temperatures of the canisters containing the specimens. Irradiation effects data on fusion reactor alloys must be obtained from experiments conducted in the existing irradiation facilities Since the fusion reactor environment is still lacking.

Small specimens were used to economize on the available irradiation space. The single specimens electric potential technique was used for the same reason. Specimens were fabricated from HT-9 and 9Cr-1Mo. Previous fracture toughness results from control tests on these alloys have been reported.[1,2] This report compares the baseline data with the postirradiation results to describe the effect of irradiation on the fracture behavior of the materials. In addition, comparisons are made between the fracture responses of HT-9 and 9Cr-1Mo.

7.8.5 Progress and Status

7.8.5.1 Experimental Procedures

Compact tension specimens were fabricated from 3.175 mm thick plate. HT-9 specimens were given a prefabrication heat treatment of 1050°C/0.5hr/AC + 760°C/2.5hr/AC, while 9Cr-1Mo specimens were given a prefabrication heat treatment of 1038°C/0.5hr/AC + 760°C/0.5hr/AC. Reference 2 provides the configuration of the 2.54 mm thick disk-shaped compact tension specimens and the test procedures for fracture toughness tests using the electric potential technique to monitor the precrack length. After each test was completed, the specimen was heat tinted to reveal the crack extension. An empirical calibration curve was established by relating the crack extension and the electric potential output. Continuous crack extensions and J versus a curves were obtained from this calibration curve. Since the specimen was small, the results were analyzed using the J-integral approach. The procedure given in ASTM Standard E813 was followed to measure the fracture toughness of the irradiated material, with some precautions taken with respect to the size of the data exclusion zone.

7.8.5.2 Results and Discussion

Figures 7.8.1 and 7.8.2 show typical load and potential output versus displacement records for HT-9 and 9Cr-1Mo, respectively. These records were used to calculate the J values and continuous crack extensions using the electric potential calibration curve. Figure 7.8.3 shows the continuous J versus Aa curves for both ferritic alloys. The initial portion of J-Δa was fitted to the blunting line to determine the value of J_{1c}. Fracture toughness results are compiled in Table 7.8.1, where the tearing modulus (T), test and irradiation conditions are also listed.

Figures 7.8.4 and 7.8.5 show the range of toughness data available for HT-9 and 9Cr-1Mo. Since there are only two specimens per irradiation condition, the temperature dependence of the fracture properties cannot be established in detail. Figure 7.8.4 shows that increasing test temperature results in a decrease in toughness for both irradiated HT-9 and 9Cr-1Mo. It also shows that the fracture toughness of HT-9 is -30% higher than that of 9Cr-1Mo. The temperature dependence of the tearing modulus is shown in Fig. 7.8.5. In general, the tearing modulus of HT-9 decreases while that of 9Cr-1Mo increases as the test temperature is increased.

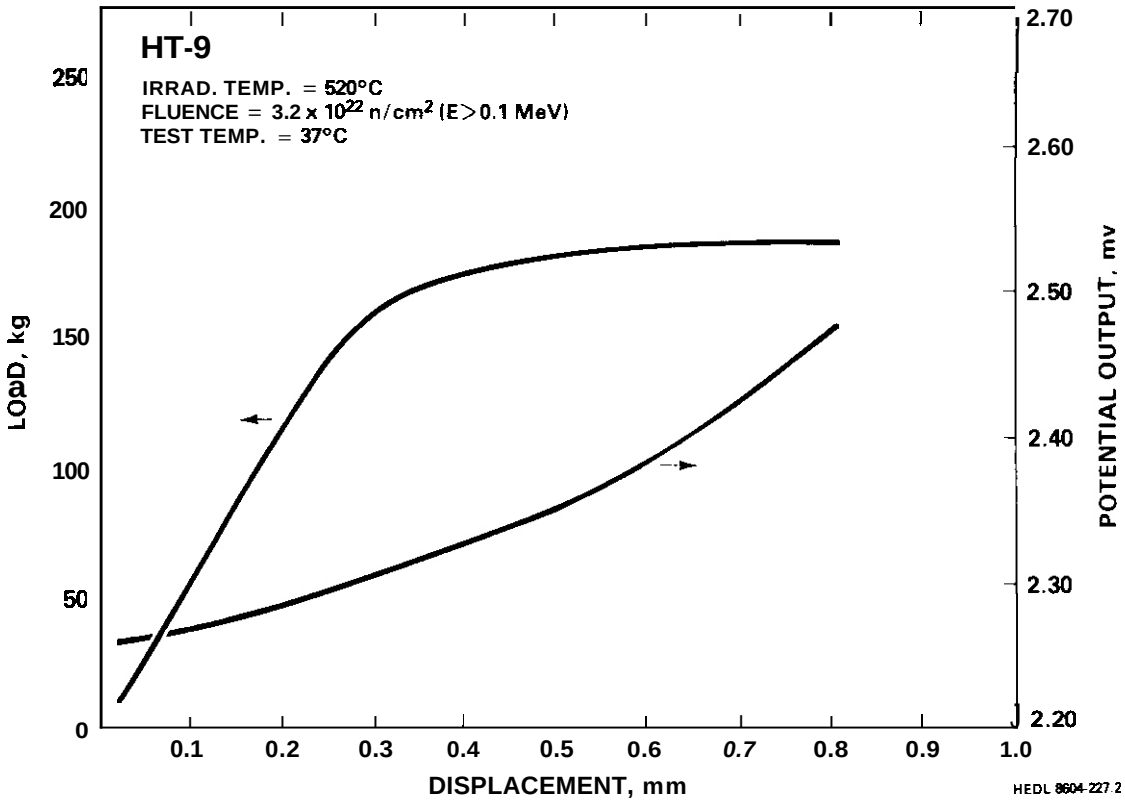

Fig. 7.8.1. Potential output and load vs. load-line displacement for HT-9 irradiated at 520°C.

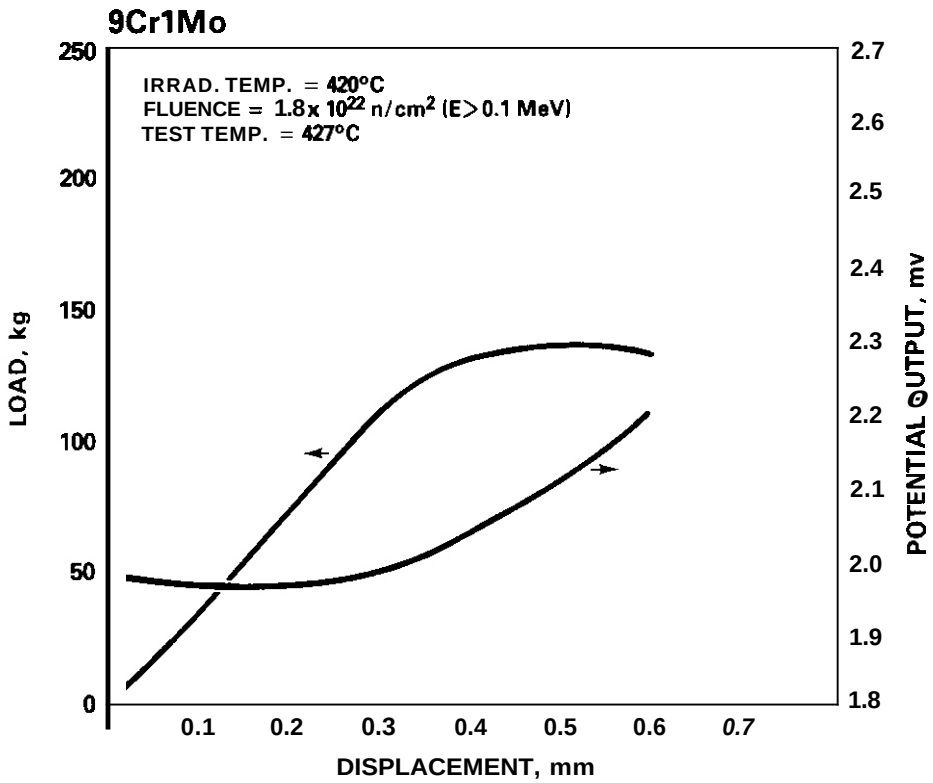

Fig. 7.8.2. Potential output and load vs. load-line displacement for 9Cr-1Mo irradiated at 420°C.

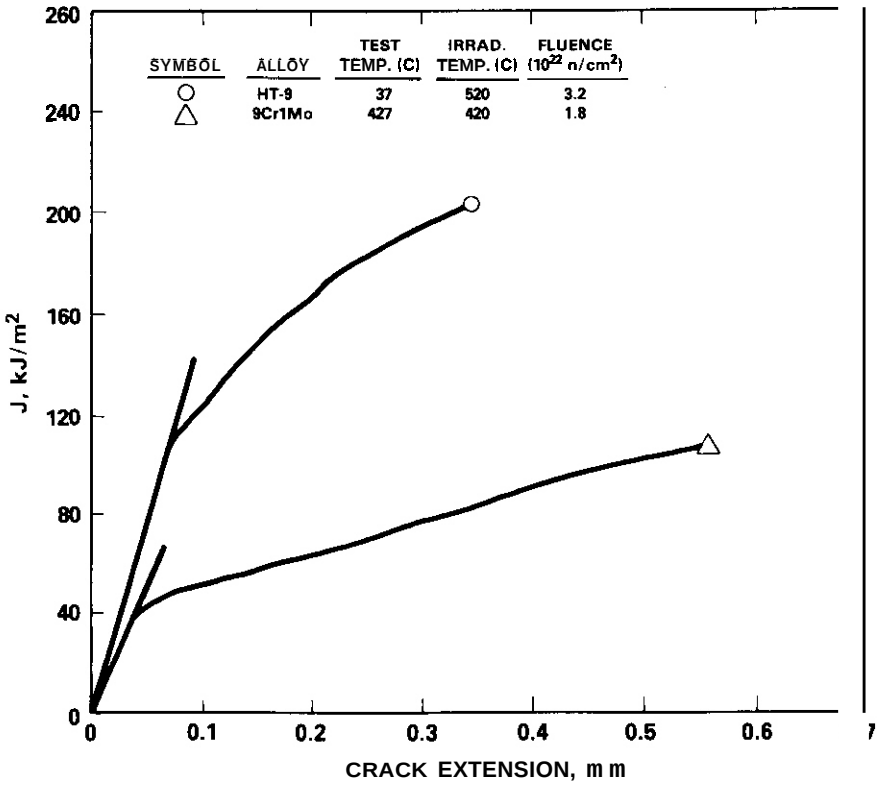

Fig. 7.8.3. J vs. a curves via an electric calibration curve for irradiated HT-9 and 9Cr-1Mo

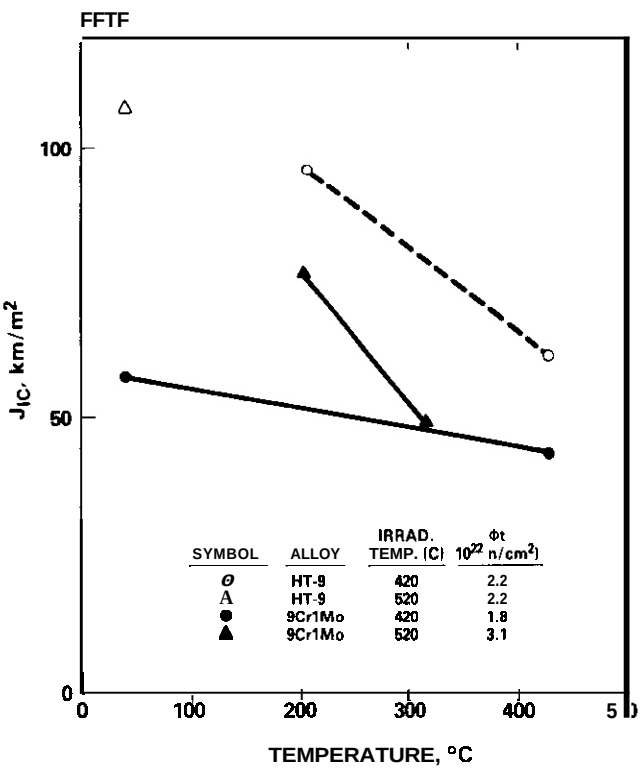

Fig. 7.8.4. Temperature dependence of fracture toughness for irradiated HT-9 and 9Cr-1Mo.

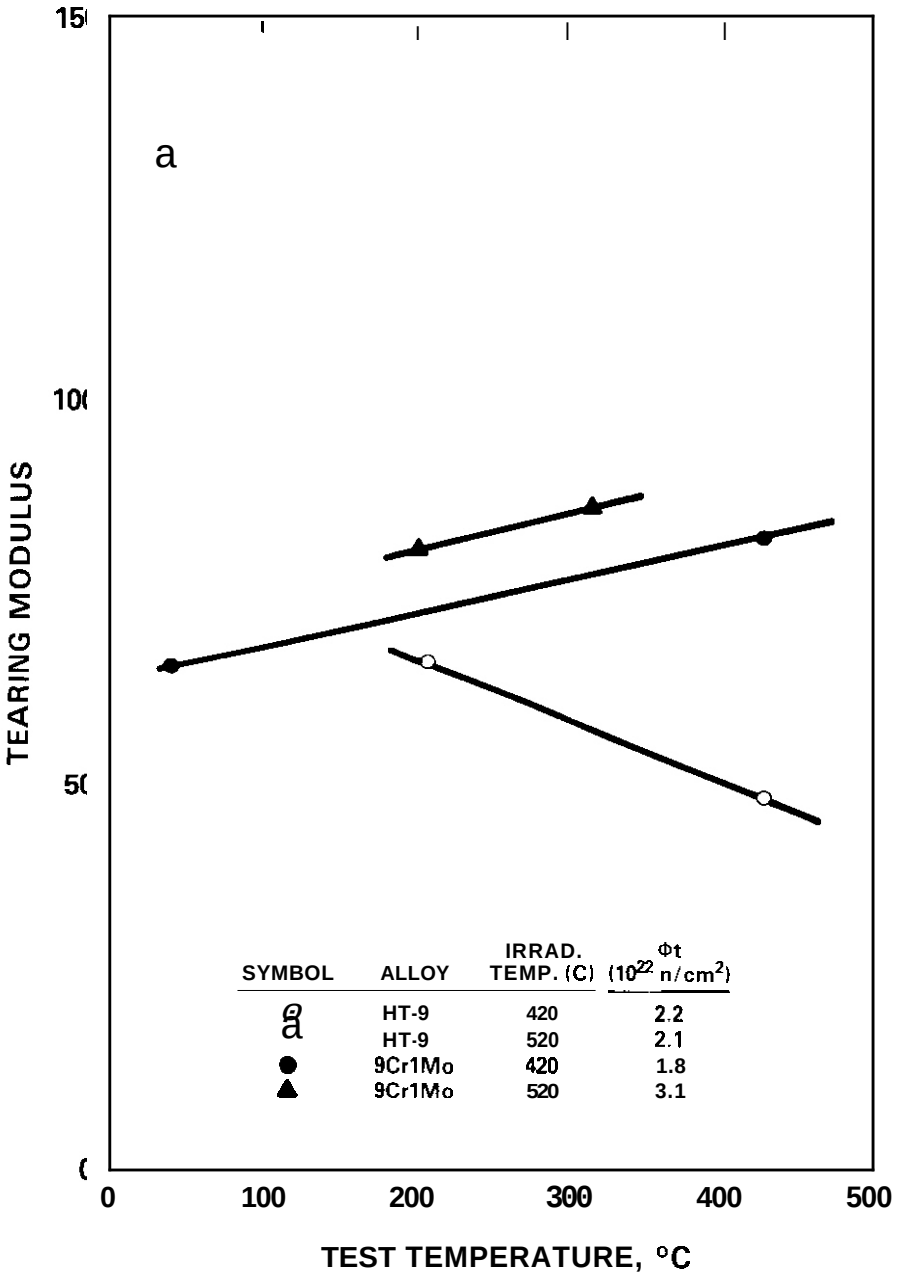

Fig. 7.8.5. Temperature dependence of tearing modulus for irradiated HT-9 and 9Cr-1Mo.

Table 7.8.1. Fracture toughness of ferritic alloys irradiated in FFTF

Alloy	Irradiation Temperature (°C)	Fluence (10^{22} n/cm^2)	Test Temperature (°C)	J_{1c} (kJ/m^2)	Tearing Modulus
HT-9	420	2.2	208	95.4	66.5
	420	2.2	428	61.6	48.9
	520	3.2	37	107.4	131.8
9Cr-1Mo	420	1.8	41	57.2	65.5
	420	1.8	427	43.4	82.7
	520	3.1	202	76.5	81.2
	520	3.1	316	49.2	86.2

As shown in Fig. 7.8.3, the tests were stopped before Aa reached 0.55 mm. Crack growth would be under a mixture of plane stress and plane strain conditions if Aa were too long. The 1.5 mm data exclusion zone size recommended in ASTM E813 is for specimens one inch or larger in thickness, although it is not specified in the standard. For small specimens, the maximum Δa must be smaller than 1.5 mm to ensure that J-controlled conditions are satisfied.3 Both the thickness criterion and J-controlled conditions were satisfied and the J_{1c} values obtained were therefore valid.

In general, the fracture toughness of HT-9 is not significantly degraded after irradiation. Results showed that the value of J_{1c} at 205°C in fact increased as the fluence was increased from zero to 3 x 10^{22} n/cm^2. According to the fracture toughness guideline given in Ref. 4, the fracture toughness of HT-9 irradiated to 3 x 10^{22} n/cm^2 is well above the minimum toughness of about 15 kJ/m^2 required for a structure of thickness 3 mm and a crack depth of 1.5 mm with a sufficient margin of safety.

7.8.6 Conclusions

The major conclusions are:

1. The fracture toughness of both HT-9 and 9Cr-1Mo decreases with increasing test temperature and the toughness of HT-9 was higher than that of 9Cr-1Mo.
2. The tearing modulus of HT-9 decreased but that of 9Cr-1Mo increased as a function of test temperature.
3. Increasing irradiation temperature resulted in an increase in fracture toughness for both alloys.
4. HT-9 showed adequate upper shelf fracture properties after irradiation.

7.8.6 References

1. F. H. Huang and G. L. Wire, "Fracture Toughness Testing on Ferritic Alloys Using Electropotential Techniques," Journal of Nuclear Materials 104, (1982) 1511-1516.
2. F. H. Huang, "J_{1c} Measurements on Single Subsized Specimens of Ferritic Alloys," Journal of Testing and Evaluation 13 No. 4 (1985) 257-264.
3. J. W. Hutchinson and P. C. 'Paris, "Stability Analysis of J-Controlled Crack Growth," ASTM STP 668, American Society for Testing and Materials, (1979) 37-64.
4. F. H. Huang, "Fracture Toughness of Irradiated HT-9 for Structural Application," Nuclear Engineering and Design 90 (1985) 13-23.

7.9. Microstructural Examination of 12%Cr Martensitic Stainless steel After Irradiation at Elevated Temperatures in FFTF - Chen-Yih Hsu and T. A. Lechtenberg (GA Technologies, Inc.) and D. S. Gelles (Westinghouse Hanford Company)

7.9.1. ADIP Task

The Department of Energy (DOE) Office of Fusion Energy (OFE) has cited the need to investigate ferritic alloys under the ADIP program task, Ferritic Steel Development (Path E).

7.9.2. Objective

This is a Part of an experiment in the Alloy Development for Irradiation Performance Path E program to he used as a control and comparison in FFTF irradiations with developmental low activation ferritic steels. These experiments were designed to evaluate the microstructural response and precipitation development of this class of ferritic alloys to FFTF neutron irradiation at elevated temperatures.

7.9.3. *Summary*

A remelted 12%Cr martensitic stainless steel (HT-9) has been examined before and after irradiation in the Materials Open Test Assembly (MOTA) of the Fast Flux Test Facility (FFTF), using a scanning transmission electron microscope. The irradiation temperatures were 365°C, 420°C, 520°C, and 600°C with the fluences as high as 7.3 x 10^{22} n/cm^2 (E>0.1 Mev) or 34 dpa. The extracted precipitates from each specimen were identified using a X-ray microanalysis and selected area diffraction. The precipitates in the unirradiated condition **Were** primarily $M_{23}C_6$ carbides which formed at martensite lath and prior austenite grain boundaries. During irradiation at elevated temperatures small amounts of other phases formed which were tentatively identified as the chromium rich α', the nickel-silicon rich G-phase and the intermetallic Chi phase. Irradiation-induced voids were observed only in specimens irradiated at 420oC to a **dose** of 34 dpa; no voids were found for specimens irradiated at 365°C (~11 dpa), 520°C (~34 dpa), and 600°C (~34dpa). These results are not in agreement with previous experiments in that voids have not been reported in this alloy at relatively high fluence level (~67 dpa) following irradiation in other fast-spectrum reactor (EBR-II) but this is the first observation following FFTF irradiations. The present results indicate that cavities can form in HT-9 at modest fluence levels even without significant generation of helium bubbles. Hence, the cavity formation in this **class** of ferritic alloys is not simply due to helium generation hut rather a more complex mechanism.

7.9.4. Progress and Status

7.9.4.1 Introduction

The ferritic alloys are known to he resistant to cavity swelling. Studies on several different commercial ferritic steels irradiated in a fast reactor (EBR-II) to fluences up to 17.6 x 10^{26} n/m^2 or 84 dpa have shown only minimal swelling values[1]. It was reported that no voids were found in a 12Cr-1MoVW steel (HT-9) irradiated in EBR-II to 67 dpa[2] and irradiated in HFIR to doses up to ~23 dpa at temperatures of 380° to 615°C[3-5]. In the ADIP ferritic steel development program, concerns were raised regarding the effect of helium on their swelling resistance. However, radiation induced void swelling was found in 12Cr-1MoVW steel irradiated in the HFIR to a dose of 36 dpa at 300 and 400°C[6,7]. The swelling **was** ascribed to the presence of helium because an order of magnitude more helium is generated in HFIR than in EBR-II. No work has been reported on these steels irradiated in FFTF to comparable fluence level of 36 dpa.

A remelted 12%Cr martensitic stainless steel (HT-9) was irradiated in the form of 3 mm disks in the MOTA-1C experiments of the FFTF. The irradiation experiments were conducted at temperatures of 365°-600°C to damage levels as high as 34 dpa. These experiments were designed to evaluate the microstructural response and precipitation development of this class of ferritic alloys to FFTF neutron irradiation at elevated temperatures. The comparison of microstructures and phases precipitating before and during irradiation is presented in this paper.

7.9.4.2 Specimen Preparation and Experimental Procedures

The alloy investigated was remelted from a commercial grade HT-9 steel in a vacuum induction furnace at GA Technologies Inc. as a part of another experiment in the Path E of the Alloy Development far Irradiation Performance program to be used as a control in irradiations with other developmental alloys. The commercial grade HT-9 steel **was** purchased from Carpenter Technology Inc. Chemical composition of this remelted alloy is given in Table 7.9.1, falling well within the commercial grade of HT-9 steel except the carbon content which is nominally 0.20%. The remelted heat **was** hot rolled to 0.25 mm thick sheet and air cooled. The rolled sheet was heat treated one hour at 1000°C, water quenched and tempered at 700°C for one hour. Disk specimens 3 mm in diameter were punched from the thin sheet. A fully tempered lath martensite was obtained after this heat treatment.

Table 7.9.1. Chemical composition of Fe-12%Cr steel investigated

Cr	Mo	C	Mn	Si	Ni	W	V	S	P
11.92	0.90	0.15	0.50	0.33	0.47	0.44	0.30	0.033	0.012

3 mm disks were engraved and loaded in the MOTA-1C for Irradiation in FFTF. Irradiations were conducted at temperatures of 365°C - 600°C with fluences up to 7.32 x 10^{22} n/cm (E>0.1 Mev). The irradiation conditions are listed in Table 7.9.2.

Table 7.9.2. The irradiatlon conditions of the steel investigated

Specimen ID #	Irradiation Temperature	Neutron Fluence	Disolacement Damage Level
Kx09	365°C	3.03 x 10^{22} n/cm^2	11.3 dpa
K109	420°C	7.27 x 10^{22} n/cm^2	33.5 dpa
K409	520°C	7.32 x 10^{22} n/cm^2	33.8 dpa
K609	600°C	7.32 x 10^{22} n/cm^2	33.8 dpa

Both TEM foils and carbon extraction replicas were prepared for each specimen. The carbide extraction technique involved electrolytic etching in 10% HCl-90% methanol (for 1 sec at 2V), followed by carbon coating and electrolytic stripping of the carbon film. Thin foils were prepared remotely in a hot cell using a twin-jet electropolisher with a electrolyte of 5% perchloric acid and 95% butylalcohol Operating at 90V, 250-300 mA and moderate pump speed. The specimens were examined using a JEM 1200EX scanning transmission electron microscope equipped with standard and ultrathln-window KEVEX X-ray microanalysis detectors operating at 120Kv. For quantitative energy dispersive X-ray (EDX) microanalysis, the integrated counts in one X-ray peak for each element to be analyzed are multiplied by the experimentally determined correction ratios (K-factors) and were also normalized to weight percent concentration. A digital filter method provided the peak integration above background, and correction was made for overlapping K_α and K_β X-ray peaks for elements having adjacent atomic numbers. In this way the elements Al, Si, Ti, V, Cr, Mn, Fe, Ni, Mo, and W are routinely analyzed.

7.9.4.3 Results

Preirradiation microstructure

Figure 7.9.1 shows TEM micrographs of the Ye-12% Cr martensitic steel prlor to irradiation. The structure was essentially all tempered lath martensite with less than 2% delta ferrite. The tempered martensite network was decorated with plate-like and rod-like carbide precipitates along the prior austenite grain boundaries and martensitic lath boundaries indicating that retained austenite was present following the water quench. The weight percent of precipitates in the tempered condition was not measured, but based on comparisons to previous work by the authors, was estimated to be about 3.2%. The Precipitates were identified in the STEM using selected area diffraction and X-ray microanalysis. The EDX results and the dark field diffraction image of Figure 7.9.1b indicate that the carbide precipitates are in the form of chromium-rich $M_{23}C_6$ carbides. The particle sizes range from 50 nm to 400 nm and the average particle size is about 110 nm. The dislocations are ordered in such a way as to produce irregular subgrains within the martensite laths. The standard heat treatment for HT-9 recommends a higher tempering temperature (760°C) but because this steel was incorporated as a comparison Por other alloys in the MOTA experiment and therefore was given a lower temperature temper, a higher dislocation density resulted. The dislocation density would decrease somewhat at higher tempering temperatures and produce more regular subgrains.

Irradiated Microstructures

TEM micrographs of the structure after irradiation at 365°C to a dose of 11 dpa (Kx09) are shown in Figure 7.9.2. Dislocation loops were observed within the martensite laths and small precipitates were evident. By tilting the foll and imaging with one of the precipitate diffraction spots, the phase could be selectively illuminated as seen in Figure 7.9.2b. This may be the Ni-Si rich G-phase which was reported earlier based on the diffraction characteristics and morphology of G-phase observed in irradiated commercial HT-9[2,5]. No evidence of vold swelling was observed in this specimen.

Following irradiation at 420°C to a dose of 34 dpa (K109), a few small cavities were found as noted in Figure 7.9.3 (see arrows). These small cavities were non-uniformly distributed within tempered martensite laths. The cavities are approximately 5 to 20 nm in diameter and the accumulated swelling was not measured but estimated to be much less than 0.01 %. No preference of cavities for lath boundaries, prior austenite grain boundaries, or precipitate interfaces was apparent. A fine dispersion of tiny precipitates (10-15 nm) were observed and a diffraction analysis Suggests the presence of both chromium-rich α' and G-phase. Irradiation Induced dislocation loops and tangles were also observed In the specimen.

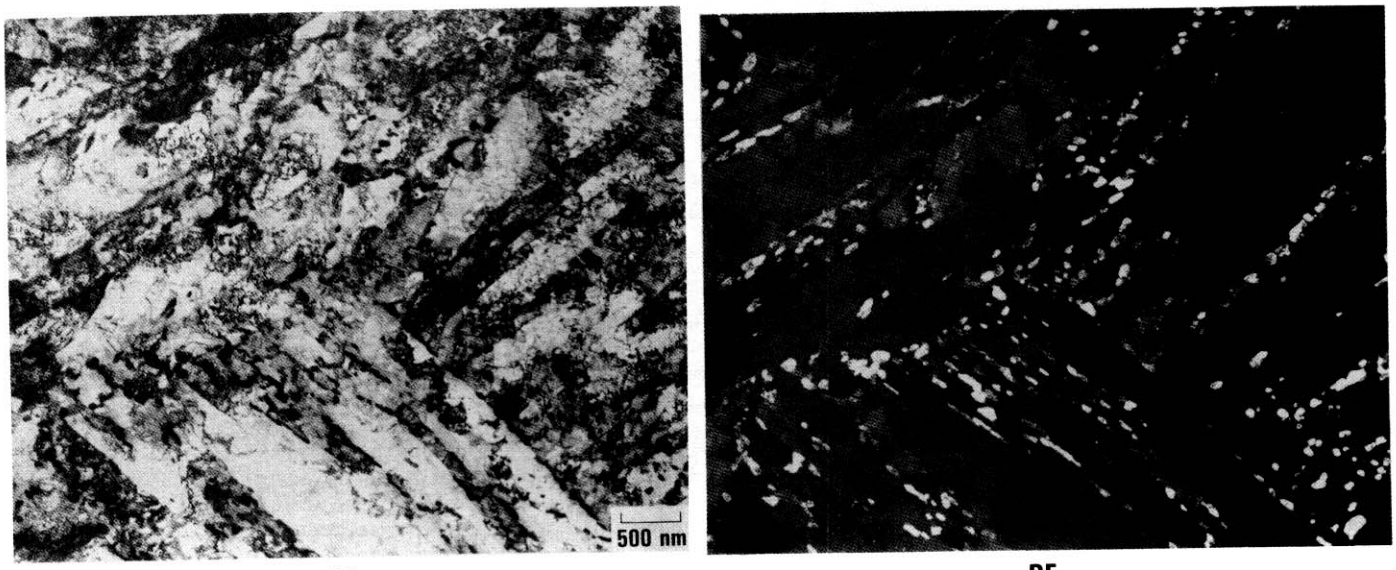

BF
(a)

DF
(b)

Figure 7.9.1. TEM micrographs of quenched and tempered 12% Cr martensitic steel (a) bright field image, and (b) dark field image of $M_{23}C_6$ carbides.

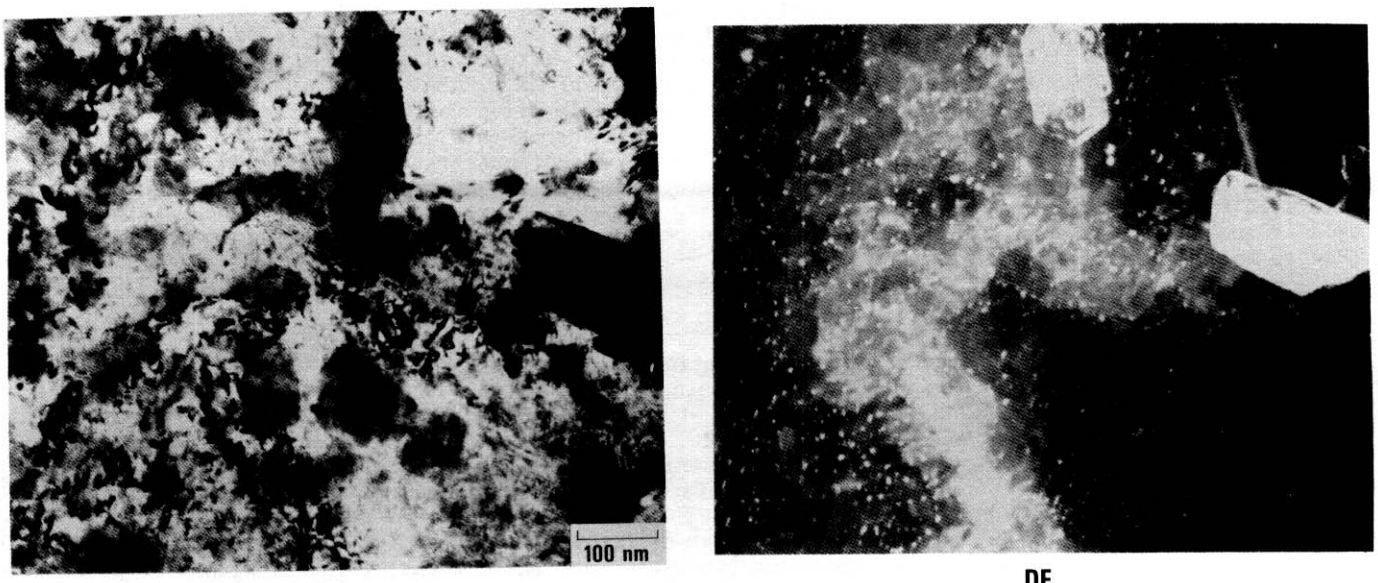

BF
(a)

DF
(b)

Figure 7.9.2. TEM micrographs of 12% Cr martensitic steel irradiated at 365°C to 11 dpa, (a) bright field image, and (b) dark field image.

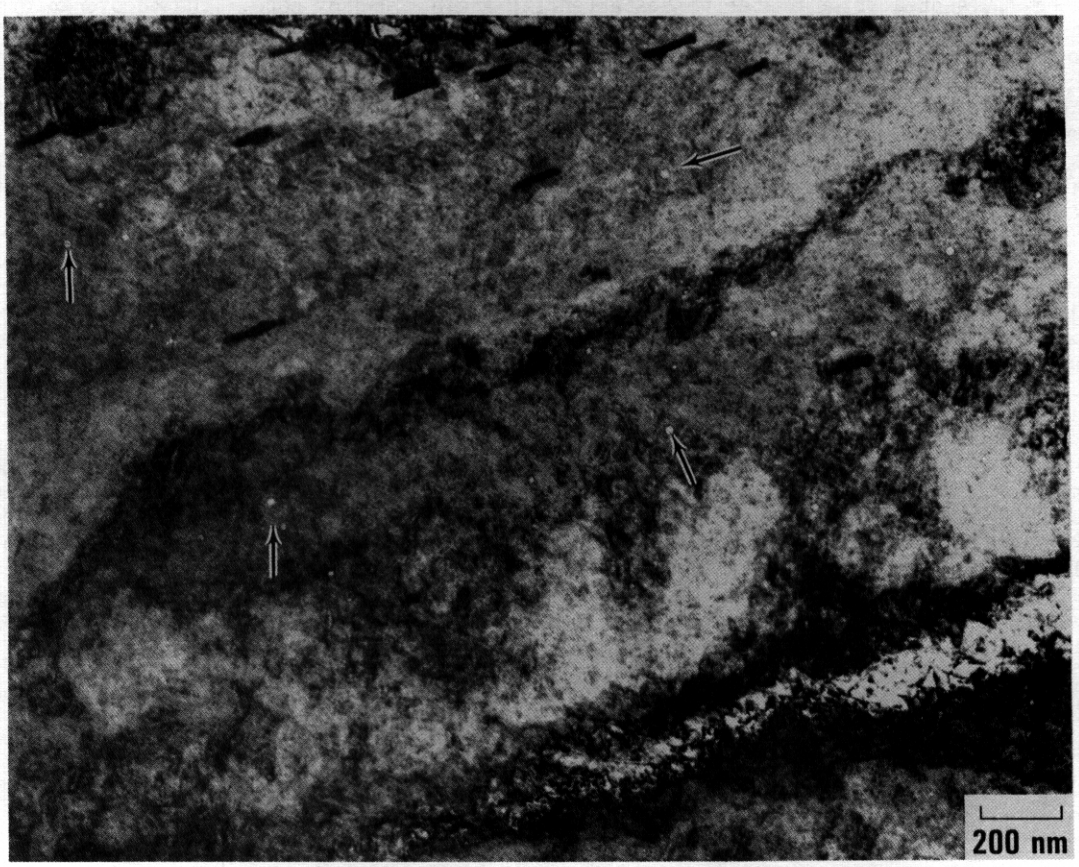

(a)

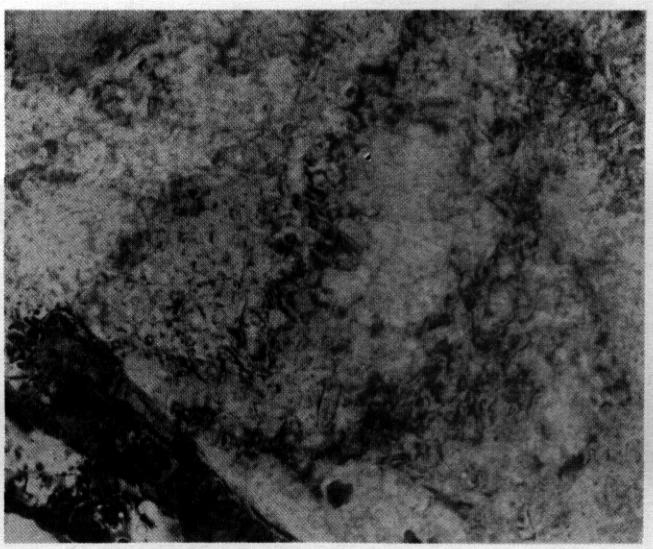

BF

(b)

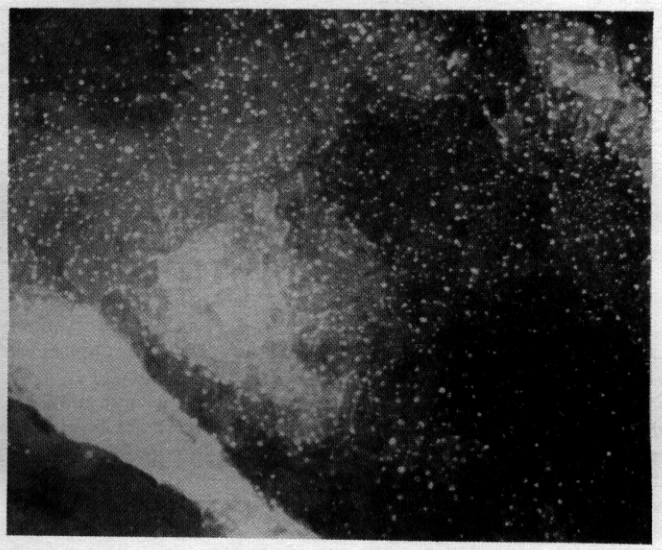

DF

(c)

200 nm

Figure 7.9.3. TEM micrographs of 12% Cr martensitic steel irradiated at 420°C to 34 dpa, showing radiation-induced cavities(arrows) and fine precipitates (a), (b) bright field image, and (c) dark field image at g=3/4(200).

The resulting microstructure of tempered martensite after irradiation at 520°C with 34 dpa (K409) is shown in Figure 7.9.4 at a prior austenite/delta ferrite grain boundary node. The recovered dislocations and subgrain Structure were seen within martensite laths and a noticeable particle coarsening along lath and grain boundaries was observed. No evidence of cavities was found either in martensite or delta ferrite. The ferrite region contained a heavy distribution of blocky precipitate particles and a lower dislocation density than the martensite. The grain boundary separating these region is decorated with precipitation and there is zone denuded of the precipitation adjacent in the ferrite. These blocky precipitates were formed during irradiation at temperature of 520°C. The SAD analysis of these blocky precipitates, based on the previous investigation, is Identified as intermetallic Chi phase and is confirmed by EDX.

Figure 7.9.5 shows the microstructure following irradiation at 600°C to 34 dpa. The microstructure is a fully tempered martensite and no cavities were evident. The dislocation density within the martensite laths was lower and subgrain structures were well formed, and elongate$ rod-like and plate-like precipitates were observed, similar to those found after irradiation at 520 C. The martensite laths have coarsened due to the high irradiation temperature, but pinning by precipitates has slowed the recrystallization process as is seen in Figure 7.9.5(b) (arrow).

Figure 7.9.6 shows TEM micrographs of the extraction replicas for each irradiation condition. Most of these precipitates have rod-like and plate-like shapes, and small precipitates appear equiaxed. The particle densities and particle sizes increase with increasing Irradiation temperature indicating Oswald ripening has occurred and that other phases have precigitated during irradiation. The mean particle sizes for irradiation temperatures of 365°C, 420°C, 520 C. and 600°C are 150 nm, 160 nm. 115 nm, and 190 nm, respectively. The particle size Increases with increasing irradiation temperature. The extracted precipitates were analyzed using energy-dispersive X-ray microanalysis in STEM mode and the results are listed in Table 7.9.3 along with the number of particles selected for analysis in each specimen. The phase identification for these precipitates are only qualitative.

Table 7.9.3. x-ray Microanalysis Results of Precipitates Extracted from the Irradiated Fe-12%Cr Martensitic Stainless Steel

Sample	Weight Percentage (wt%)									Nominal
ID #	Fe	Cr	MO	W	V	Si	Ni	Mn		Composition
Control Specimen	25-29	57-62	6-11	0-4	0-2	0-2	-	-	[20]a	$M_{23}C_6$
K409 (365°C)	28-31	60-72	0-9	0-5	0-1	-	-	-	[10]a	$M_{23}C_6$
K109 (420°C)	25-27	57-68	6-8	0-13	0-1	0-1.5	0-5	-	[10]	$M_{23}C_6$
	20-24	55-56	6-7	-	0-1	3-5	11-12	-	[2]	G+$M_{23}C_6$
	0-1	99-100	-	-	-	-	-	-	[3]	α'
K409 (520°C)	29-32	56-63	0-10	0-6	-	0-1.8	-	0-1	[3]	$M_{23}C_6$
	38-44	44-45	9-12	0-2	0-1	0-1	0-2	-	[2]	Chi+$M_{23}C_6$
	59-65	24-28	6-11	3-8	-	-	0-1	-	[13]	Chi
K609 (600°C)	17-23	64-16	8-11	0-5	0-1	0-2	-	-	[15]	$M_{23}C_6$
	22-34	48-56	12-18	6-8	0-1	-	-	-	[3]	Chi+$M_{23}C_6$
	-	100	-	-	-	-	-	-	[1]	α'
	39-50	16-33	11-23	9-14	0-1	-	0-1	-	[6]	Chi

a Numbers in brackets indicate the number of particles analyzed.

$M_{23}C_6$ carbides were commonly observed for each specimen. The other second-phases formed during irradiation were tentatively identified as chromium-rich α', Fe-Cr-Mo-W intermetallic Chi phase and the nickel-silicon rich G-phase. The intermetallic Chi phase was observed in specimens irradiated at 520°C and then mostly in delta ferrite region. but was also found at 600°C in the martensite. The Chi phase which formed in the martensite contained higher Mo and W concentrations than that formed in the ferrite region. In terms of particle size, Chi phase is larger than α' and G phases. In specimen K109 at 420°C, an uniform distribution of a fine precipitate (~10 nm) was observed in the carbon film. These fine precipitates were too small to be identified using X-ray microanalysis and they are likely to be α' phase.

I.9.4.4 Discussion

The observation of Chi phase in this investigation is in agreement with the observations of Gelles and Thomas who reported Chi phase in HT-9 after irradiation at 455°, 480°, and 540°C[7]. The precipitation of G-phase was found in specimens irradiated at 365°C and 420°C, consistent with previous results on HT-9 following irradiation at 300°C, 400°C, and 425°C[5,7]. No evidence of G-phase was observed after Irradiation at higher temperatures. This indicates that G-phase is likely to form only at lower irradiation temperatures(<450°C). The chromium-rich α' phase precipitated in specimens irradiated

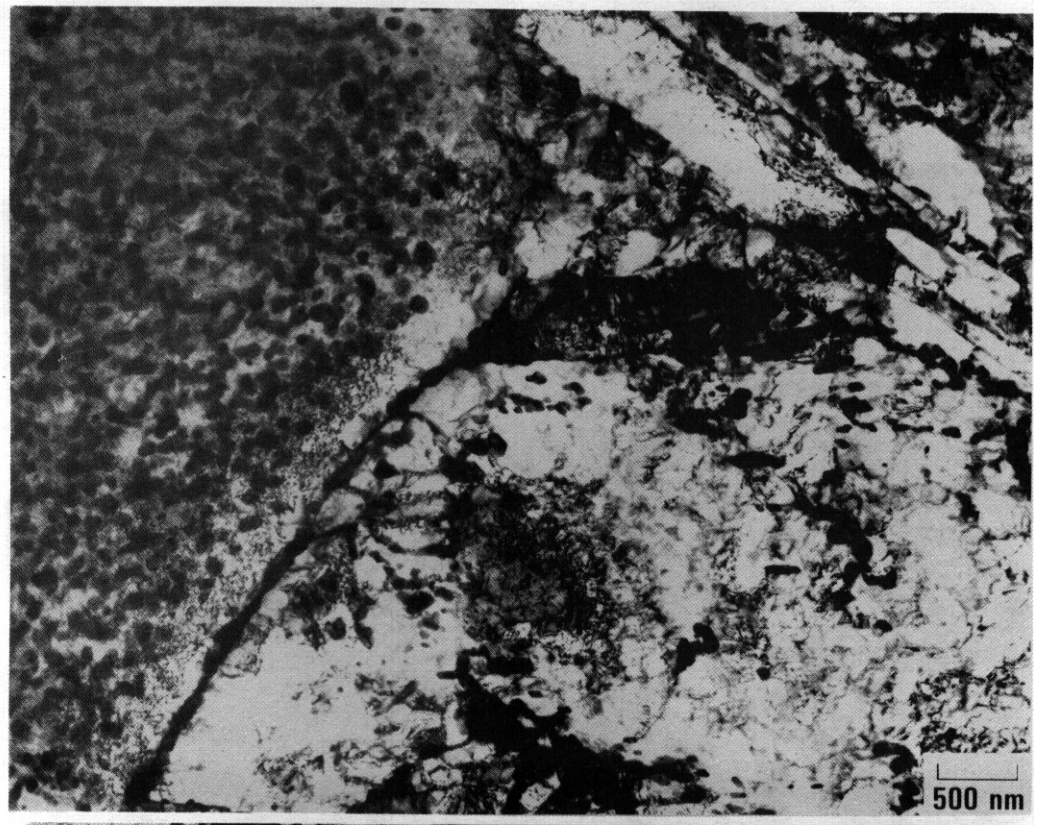

(a)

(b)

g = 110 NEAR 111

Figure 7.9.4. TEM micrographs of 12%Cr martensitic steel irradiated at 520°C to 34 dpa, (a) at node of martensite and delta ferrite, (b) dislocation contrast at g=110 near 111, and (c) g=110 in delta ferrite.

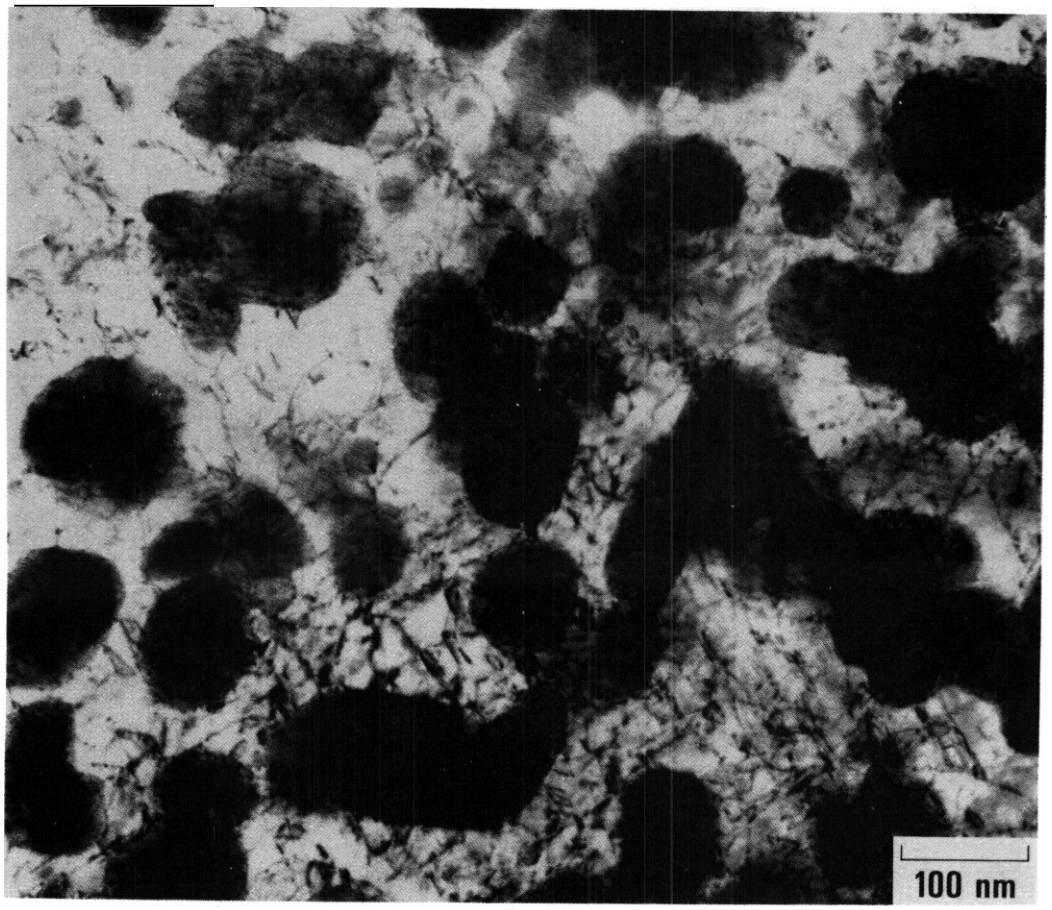

g = 110 IN DELTA FERRITE

(c)

Figure 7.9.4 (Continued) (c) g = 110 in. delta ferrite

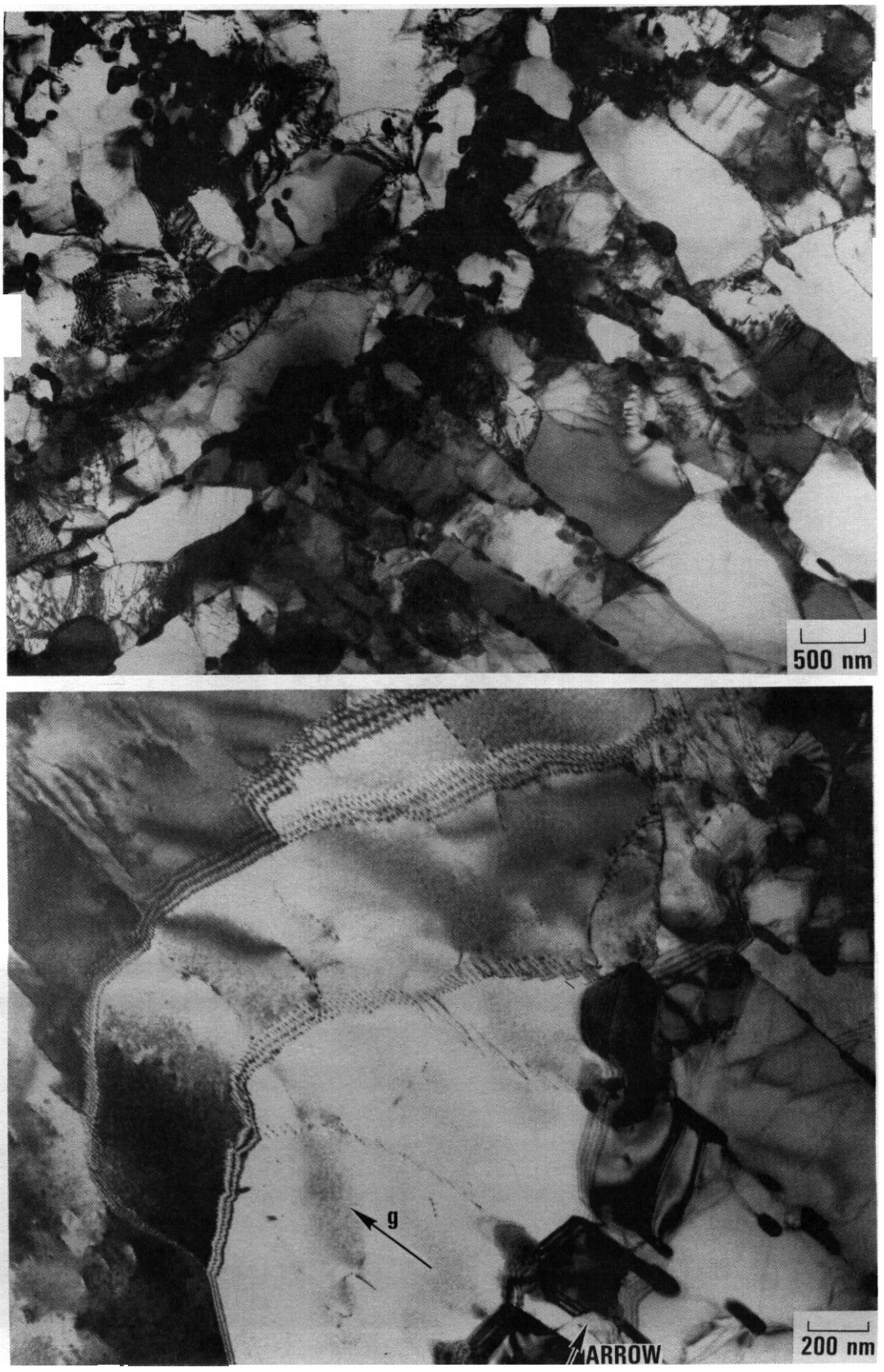

(a)

(b)

DISLOCATION CONTRAST AT g = 110 NEAR 001

Figure 7.9.5. TEM micrographs of 12%Cr martensitic steel irradiated at 600°C to 34 dpa, (a) bright field image, and (b) with dislocation contrast at g-110 near 001 (arrow shows "pinned" subgrain).

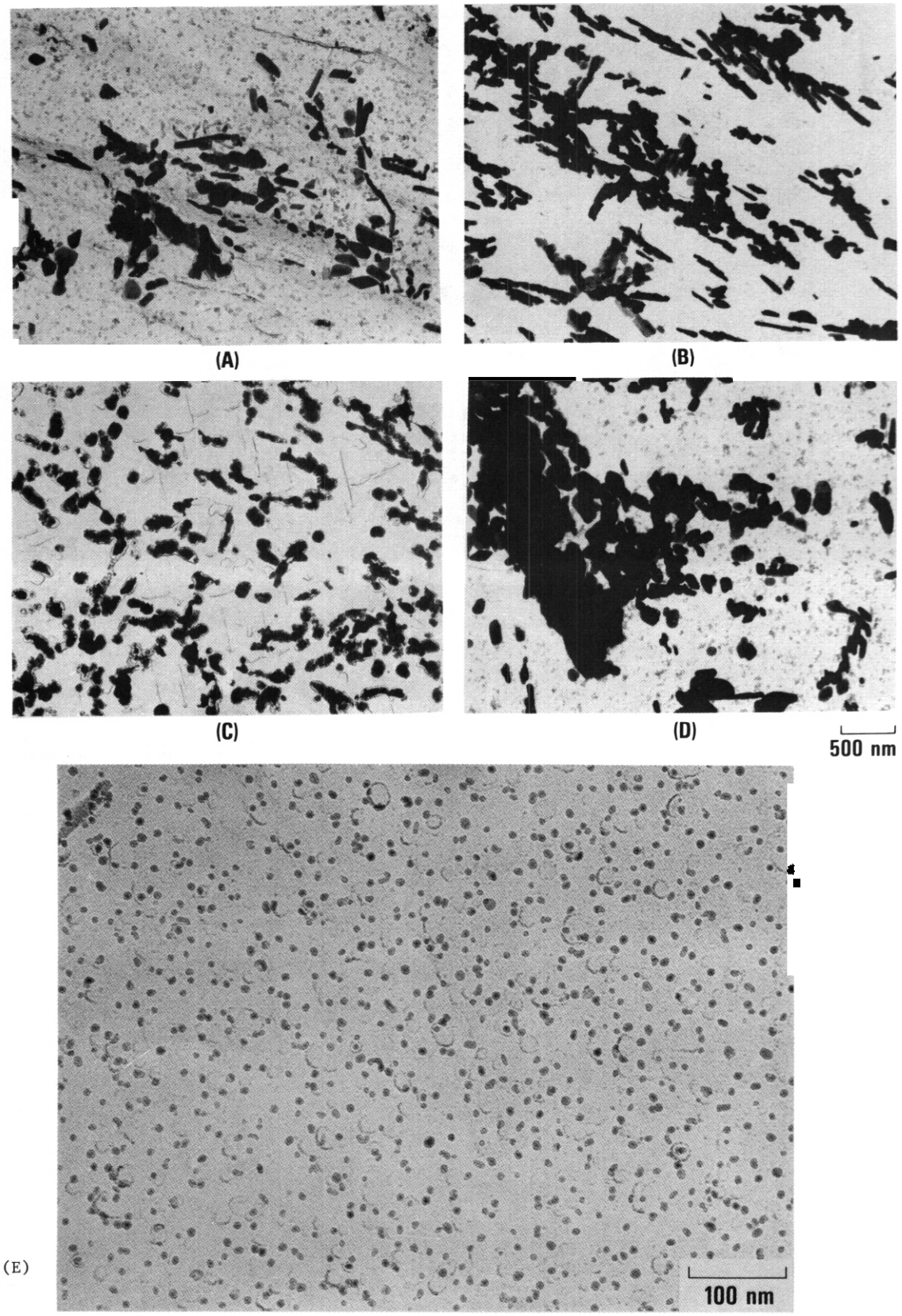

Figure 7.9.6. TEM micrographs of extraction replicas of irradiated 12% Cr martensitic steel, (a) at 365°C to 11 dpa, (b) at 420°C to 34 dpa, (c) at 520°C to 34 dpa, (d) at 600°C to 34 dpa, and (e) high magnification of fine precipitates in the carbon film of (b).

at temperatures of 420°C-600°C, consistent with previous results[7]. The precipitation of G-phase was observed in thin foils but not in the extraction replica of Kx09 specimen irradiated at 365°C and α' phase was seen in the thin foil but not in the extraction replica of K409 specimen irradiated at 520°C. This discrepancy can be attributed to the difficulty of electrolytic extraction of fine precipitates and due to area-to-area variation. Based on the TEM micrographic observations, SAD characteristics and X-ray microanalysis, the phases observed as a function of the irradiation temperature can be plotted on a qualitative basis in Figure 7.9.7. The amount of Chi phase appeared to be higher in this steel than in commercial HT-9 following HFIR irradiation[7]. This is probably because that 0.15% carbon in this steel is not sufficient to bind the Cr and Mo as carbides leaving them free to precipitate as intermetallic Chi phase. The amount of the Chi phase would have been substantially lower if the carbon content of this steel was 0.2% as in commercial HT-9. This is important to note because the irradiation-induced precipitation of α', G, and Chi phases may be the Culprits in increasing strengths and in degrading fracture toughness in HT-9[9].

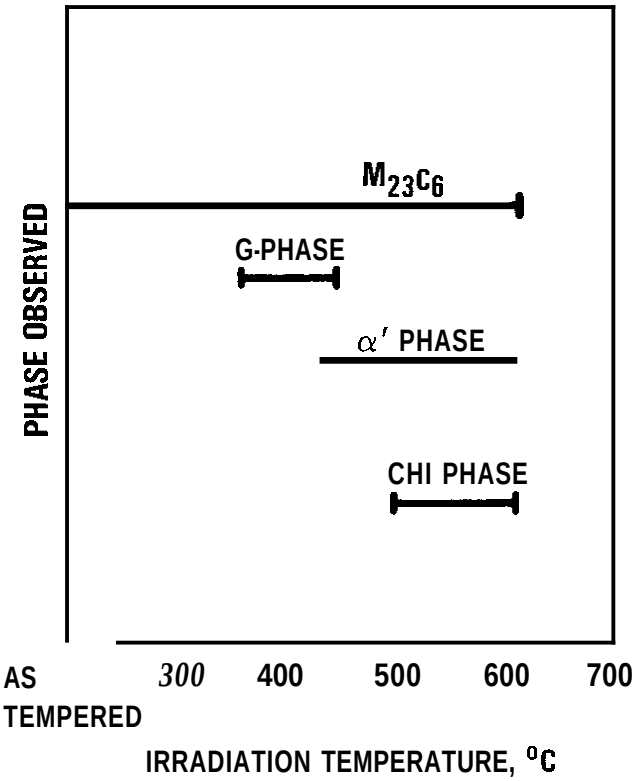

Figure 7.9.7.
Phases observed as a function of irradiation temperature for 12%martensitic steel.

Irradiation induced dislocation loops were seen in specimens irradiated at 365-420°C. At temperatures above 500°C, dislocation and subgrain structures within the martensite laths had recovered into a cell structure characteristic of over tempered martensite. The present results (also see Figure 7.9.7) suggest that lower irradiation temperatures favor the formation of finer precipitates (G-phase) and dislocation loops.

Several studies on 12 Cr-1Mo steels irradiated in fast-spectrum reactors and a mixed-spectrum reactor have been reported previously. Gelles and Thomas[1,2,8] reported that no evidence of irradiation induced cavities was found in irradiated 12Cr-1MoVW steel at 400°-550°C to a fluence of 67 dpa (E> 0.1 MeV). At 84 dpa, cavities Were found only in specimens of 12Cr-1Mo steel irradiated at 425°C and no voids were found at higher temperatures. Little and coworkers[3,4] did not find any cavities in the 12 Cr-1Mo steel following irradiation to ~23 dpa at 380°-615°C. Vitek and Klueh[6] reported that the increased amount of helium produced during HFIR irradiations enhanced the formation of cavities in HT-9 in the temperature range of 300°-600°C and a maximum cavity density was noted at 400°C. Gelles[7] compared microstructures of HT-9 irradiated in HFIR to 39 dpa at 300°-600°C and in ERR-I1 to 29 dpa at 390° and 500°C and reported that irradiation in HFIR promoted helium bubble formation at all temperatures, and some cavity formation at 400°C, whereas no cavities were found in specimens irradiated in ERR-11. The studies used the same heat of HT-9, so the swelling difference was attributed to helium generation and heat-to-heat variations could be ruled out. The conclusions of previous investigations on 12 Cr-1MoVW steels can be summarized as: (1) the onset of cavity formation is promoted by increased helium generation; (2) cavities can be formed in a fast-spectrum reactor at high enough fluence level

(~84 dpa) whereas in HFIR irradiations voids can form at lower damage levels (~35 dpa) in steel Which do not swell; and (3) peak void swelling is in the temperature range of 400°-425°C. In all cases the cavity development was typical of the swelling incubation regime and no significant amount of void swelling has been measured.

In the present investigation, irradiation-induced Cavities were observed only far K109 specimens following FFTF irradiation at 420°C with a dose of 34 dpa. No evidence of cavities was found for specimens irradiated at 365°C (~11dpa), 520°C (34 dpa), and 600°C (34 dpa). The experimental results are generally in agreement with previous data[1-7], and have not been reported For FFTF irradiations. The present results show that Cavities are formed at modest fluence levels (~34 dpa) without the production of significant amounts of helium as compared to HFIR. The possibility of cavity formation in Specimen Kx09 at the lower temperature of 365°C with a fluence much higher than 11 dpa can not be ruled out and deserves further investigation. As previously reported, delta ferrite is more susceptible to the cavity formation, but in thia investigation no Cavities were found at 520°C in the small amount of ferrite in this alloy. At temperatures above 500°C, the onset of cavity formation is likely to be inhibited by thermal mechanisms. although helium generation was found to have promoted bubble formation[7,8]. The absence of voids at temperatures above 500°C may also be due to low helium production.

Ferritic alloys are known to exhibit remarkable resistance to swelling probably due to the inherent resistance lent by the body-centered cubic structure as well as dislocation and precipitation effects. It was proposed that the swelling resistance of HT-9 relative to ferritics arises from G-phase precipitation in-reactor[2]. In the present data, the K109 specimens contain G-phase and cavities; therefore the swelling resistance does not simply arise from the presence of G-phase but may be influenced by Other precipitates, dislocation interaction and dislocation density remnents from the martensite transformation. It has been suggested that the onset of cavity formation is enhanced by helium generation (helium-assisted cavity formation)[6,7]. The present results indicate that cavities can be formed without the production of significant amounts of helium, suggesting that the onset of cavity formation is not simply due to helium generation but rather to a more complex mechanism. In a fusion reactor spectrum the helium content would be on the order of 150 ppm at 11 dpa[10]. Therefore, void swelling in a fusion reactor may be noticeably increased over fission spectrum data.

7.9.5 Conclusions

The microstructure of remelted 12%Cr martensitic steel following FFTF irradiation has been characterized. Several conclusions can be drawn from the present investigation.

(1) Following irradiation in FFTF, irradiation-induced voids were evident only at 420°C at a dose of 34 dpa, consistent with the previous observations. The present results indicate that cavities can form at a modest fluence level even without helium production.

(2) The other phases formed during irradiation experiments were tentatively identified as chromium-rich α', G-phase. and the intermetallic Fe-Cr-Mo Chi phase and their phase stability is mainly a function of temperature.

(3) The present results suggest that lower irradiation temperatures favor the formation of finer precipitates (G-phase) and dislocation loops.

7.9.6 Acknowledgements

The authors wish to express their thanks to Dr. T. Reuther and the DOE Office of Fusion Energy for financial support of this work under Contracts to GA Technologies Ino. and the Westinghause Hanford Company. Furthermore, the assistance of the technical staffs at both laboratories are gratefully acknowledged, especially to Ms. E. M. Dieffenbacher for preparing irradiated specimens.

7.9.7 References

1. D. S. Gelles,"Microstructural Examination of Several Commercial Ferritic Steels Irradiated to High Fluence." J. Nuol. Matls.. Vol. 103&104, pp. 975-980, 1981.

2. D. S. Gelles and L. E. Thomas,"Microstructural Examination of HT-9 and 9Cr-1Mo Contained in the AD-2 Experiment," DOE/ER-0045/8, pp.343-61, March 1982, U.S. DOE.

3. E.A. Little and L. P. Stoter,"Microstructural Stability of Fast Reactor Irradiated 10-12 Cr Ferritic-Martensitic Stainless Steels," pp.207-33, in Effects of Radlation on Materials: 11th Conference, ed. H. R. Brager and J. S. Perrin, ASTM-STP-782, ASTM, Philadelphia, 1982.

4. E. A. Little and D. A. Stow,"Void Swelling in Irons and Ferritic Steels II. An Experimental Survey of Materials Irradiated in a Fast Reactor," J. Nuclear Materials., Vol. 87, pp. 25-39 (1979).

5. D. S. Gelles and L. E. Thomas,"Microstructural Examination of HT-9 Irradiated in the HFIR/CTR-32 Experiment," DOE/ER-0045/9, pp. 162-77, September 1982, U.S. DOE.

6. J. M. Vitek and R. L. Klueh,"Microstructure of HFIR-Irradiated 12 Cr-1 MoVW Ferritic Steel," in the Proc. of Topic Conf. on Ferritic Alloys for use in Nuclear Energy Tech., ed. J. W. Davis and D. J. Michel, pp. 551-8, June 1983, The Metallurgical Society of AIME.

7. D. S. Gelles,"Microstructural Comparison of HT-9 in HFIR and EBR-II," DOE/ER-0045/14, ADIP, March 1985, pp. 129-136. US DOE.

8. D. S. Gelles and L. E. Thomas,"Effects of Neutron Irradiation on Microstructure in Experimental and Commercial Ferritic Alloys." ibid, pp. 559-568.

9. T. A. Lechtenberg,"Irradiation Effects In Ferritic Steels," J. Nuclear Materials,133&134 (1985) 149-155.

10. F. M. Mann,"Transmutation of Alloys in MFE Facilities as Calculated by REAC," HEDL-TME 81-37, August 1982.

8. COPPER **AND** ITS ALLOYS

8.1 HYDROGEN EMBRITTLEMENT IN GLIDCOP Al-20 COPPER ALLOY — S. J. Zinkle (Oak Ridge National Laboratory)

8.1.1 ADIP Task

Not included in current ADIP task structure

8.1.2 Objective

The objective of this study is to determine the cause of surface blistering that has been observed in the Magnetic Fusion Energy (MFE) heat of the A1-20 alloy following high-temperature annealing.

8.1.3 Summary

The MFE heat of the A1-20 dispersion-strengthened copper alloy becomes embrittled when annealed in vacuum at temperatures greater than 400°C. A chemical analysis of this heat has found that the alloy contains a significant amount of hydrogen. The hydrogen was apparently introduced by the manufacturer during an attempt to deoxidize the alloy. The MFE heat of Al-20 is therefore subject to swelling and hydrogen embrittlement effects at elevated temperatures even when tested in a hydrogen-free environment.

8.1.4 Progress and Status

8.1.4.1 Introduction

Recent neutron and ion irradiation studies have shown that a series of dispersion-strengthened copper alloys produced by SCM Metal Products exhibit favorable radiation-resistant properties.[1-3] This family of alloys achieves a good combination of high strength (σ_y > 500 MPa) and high electrical conductivity (σ_e > 80% IACS) by creating a fine dispersion of γ-Al_2O_3 particles in the copper matrix. In order to establish a common alloy lot for fusion materials research, H. R. Brager (HEDL) recently purchased a 50-lb heat of the GLIDCOP Al-20 alloy (0.20 wt % Al in the form of γ-Al_2O_3 particles). This material (SCM Metals, lot No. 04506803, from product No. C3571) was tentatively adopted as the MFE reference heat by the attendees of an ADIP workshop on radiation effects in copper alloys held at ORNL on October 3, 1985. Some specimens from this heat are currently being irradiated in the FFTF reactor, but no results are available at this time.

A small portion of the A1-20 MFE heat was transferred to ORNL in October 1985 for characterization and ion irradiation studies. The material was in sheet form with a thickness of 92 mils (2.3 mm). Surface blisters that were several millimeters long were observed in this material following a stress-relief anneal in vacuum at 850°C for 0.5 h. This effect is commonly observed during annealing of metals which contain water vapor ("hydrogen illness") and is obviously undesirable. A study was initiated to determine if a significant concentration of hydrogen was present in the alloy, and also to determine the effects of the residual hydrogen on the alloy's mechanical properties.

8.1.4.2 Results

Detailed chemical analyses were performed on several of the A1-20 foils (Table 8.1.1). The specimens were first mechanically ground and then polished to a mirror finish with a final foil thickness of 78 mils (~2 mm). The matrix oxygen and hydrogen concentrations were determined using high vacuum fusion (gas chromography). The temperature for the vacuum fusion measurements (1800°C) was well above the melting point for the copper matrix (1083°C) and below the melting temperature of Al_2O_3 (2015°C) so that only the matrix gas concentrations were measured. A second A1-20 specimen was dissolved in a ~6 normal solution of nitric acid and the dissolved copper was removed from the solution and weighed using electrochemical gravimetry. The remaining solution was filtered to remove the insoluble residue and then analyzed using inductively coupled plasma spectroscopy (ICP). The insoluble residue from filtering was weighed and analyzed using energy dispersive x-ray spectroscopy (EDS). It was determined to be Al_2O_3 with trace amounts of copper.

It is likely that partial dissolution of the γ-Al_2O_3 particles occurred in the 6 N nitric acid solution, as evidenced by the high Al concentration in the ICP measurements. If all of the Al detected in the ICP measurements is due to dissolved γ-Al_2O_3, then the total initial Al_2O_3 concentration in the MFE Al-20 heat would be 0.316% (residue) + 0.162% (dissolved) = 0.478% Al_2O_3. This corresponds to an aluminum concentration of 0.253% Al, which is somewhat larger than expected for A1-20.

Table 8.1.1. Measured chemical composition of GLIDCOP A1-20 copper alloy (MFE heat) in weight parts per million except where noted

H (matrix)	6	Cu-grav.	99.44%		
O (matrix)	404	Insoluble residue (0.316% Al_2O_3 + 160 ppm Cu)	0.332%		
Ag	<1.9	Cu	63	P	32
Al	860	Fe	100	Pb	<7.6
As	<3.8	Ga	<11	Sb	(7.6
B	23	Hf	<1.5	Se	<7.6
Ba	9.1	Li	<7.6	Si	61
Be	<0.08	Mg	3.0	Sr	<0.19
Ca	79	Mn	0.83	Ti	1.2
Cd	7.4	Mo	<1.5	V	<0.38
co	<0.38	Na	34	Zn	6.5
Cr	1.9	Ni	<2.3	Zr	9.1
Total (ICP of filtered solution)					<1344

Figure 8.1.1 shows a cross-section view of a small blister that formed in the Al-20 alloy following an 850°C vacuum anneal for 0.5 h. Cavitation was found to predominantly occur near the surface of the alloy (presumably because of the lower stress required to form a cavity compared to the interior). However, smaller cavities were also observed throughout the interior of the specimen. Figure 8.1.2 shows an example of one of the larger interior cavities. All of the observed cavities were elongated in the rolling direction. An attempt was made to examine the annealed specimens in a transmission electron microscope.

Y205103

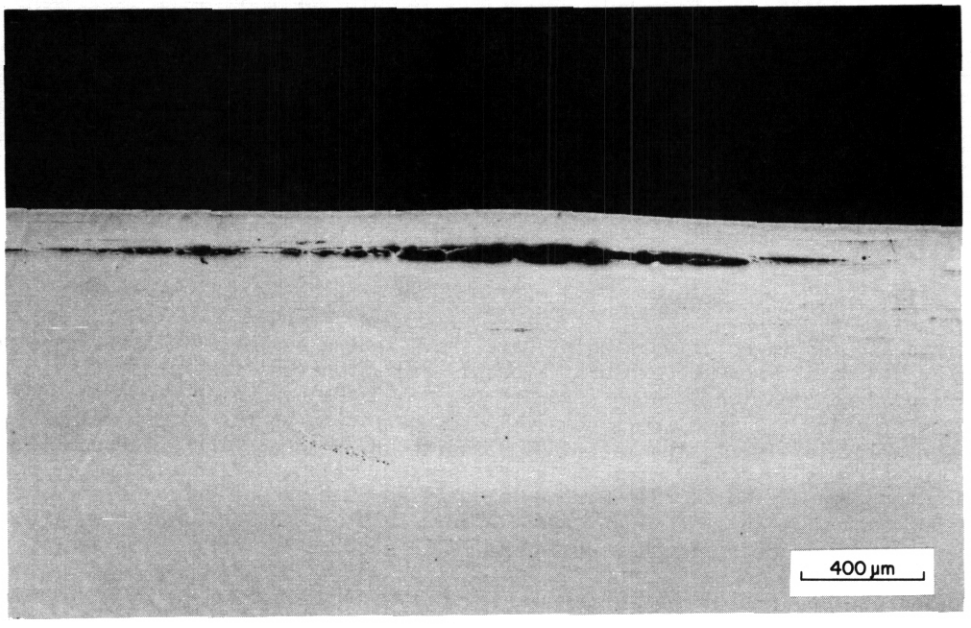

Fig. 8.1.1. Cross-section view of a surface blister that formed in the Al-20 copper alloy following a vacuum anneal at 850°C for 0.5 h.

Y205106

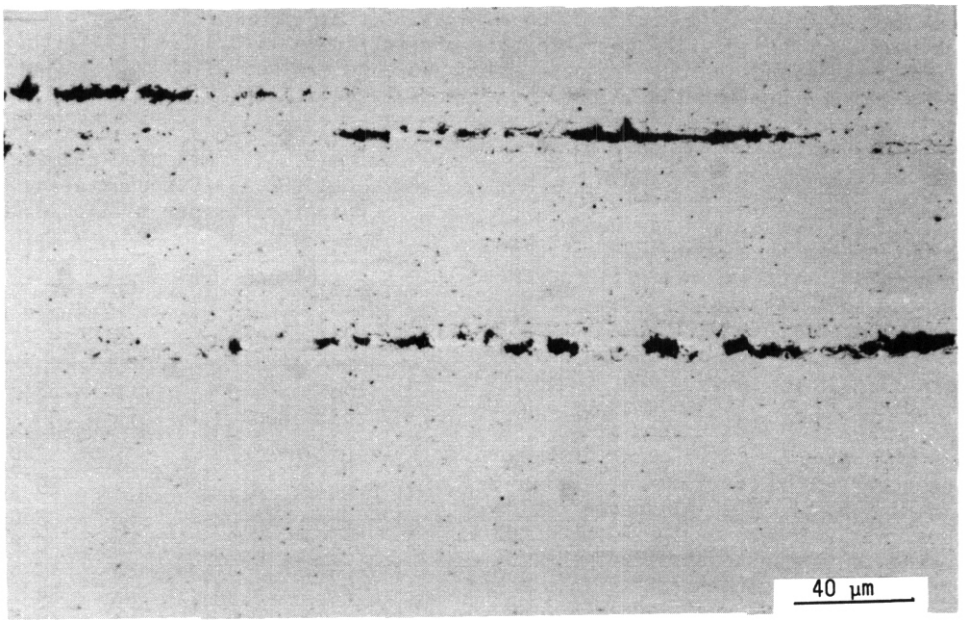

Fig. 8.1.2. Interior cavities observed in the Al-20 copper alloy following a vacuum anneal at 850°C for 0.5 h.

Numerous large holes (≥1 μm) were optically visible in the foil following the electrothinning treatment. It is believed that these holes may have been cavities which were enlarged by electrolytic etching during the final stages of thinning. Only a limited number of small cavities (<100 nm) were observed in the matrix.

Part of the as-received A1-20 stock was cold rolled to a thickness of 21 mils (0.53 mm) and machined to produce sheet tensile specimens with a geometry similar to the SS-1 configuration.' The specimens were then placed in an elevated-temperature tensile machine and annealed in vacuum for 1 h prior to being tested. Figure 8.1.3 shows the yield and ultimate stress and total elongation to failure (2-cm gage length) of the A1-20 alloy as a function of test temperature. As expected, the strength of the alloy decreased monotonically as the test temperature was increased. The elongation to failure increased with increasing temperature up to 400°C, and then decreased rapidly for test temperatures above 400°C. Additional specimens were annealed at 700°C for up to 100 h and then tested at 700°C. The mechanical properties measured after these long-term anneals were slightly improved compared to the 1 h result (Table 8.1.2).

The fracture surfaces of the tensile specimens tested at 400 and 700°C following a 1 h anneal were examined in a scanning electron microscope. The fractographs are shown in Figs. 8.1.4 and 8.1.5, respectively. There is no obvious change in the fracture mode of the alloy between 400 and 700°C despite the rather large change in ductility (9 versus 2%).

Table 8.1.2. Post-anneal tensile properties of GLIDCOP A1-20 (fusion heat) for an anneal and test temperature of 700°C

Ar 1 (	Stress, MPa		Total Elongation in 2 cm (%)
	ield	Ultimate	
1	91	111	1.9
24	128	145	2.5
100	130	147	2.3

8.1.5 Discussion

Hydrogen embrittlement occurs in copper containing >10 ppm O (in the form of Cu_2O) when it is annealed in a reducing atmosphere and then heated at temperatures[s] above 375 to 400°C. The reaction responsible for "hydrogen illness" is $Cu_2O + 2H \rightarrow 2Cu + H_2O$. Embrittlement is due to the expansion of water vapor at elevated temperatures which creates high internal stresses and cracking such as is shown in Figs. 8.1.1 and 8.1.2. The MFE heat of A1-20 has a matrix oxygen level of 400 ppm O (Table 8.1.1) and is therefore susceptible to hydrogen illness. The high-temperature embrittlement behavior shown in Fig. 8.1.3 is typical of that expected for hydrogen illness.

The basic manufacturing process employed by SCM Metal Products to produce their dispersion-strengthened copper alloys consists of blending Cu_2O with a powder mixture of a dilute Cu-Al alloy.[''] The blend is heated for 1 h at 870°C in order to oxidize the aluminum at the expense of Cu_2O. The $Cu\text{-}Al_2O_3$ powder is

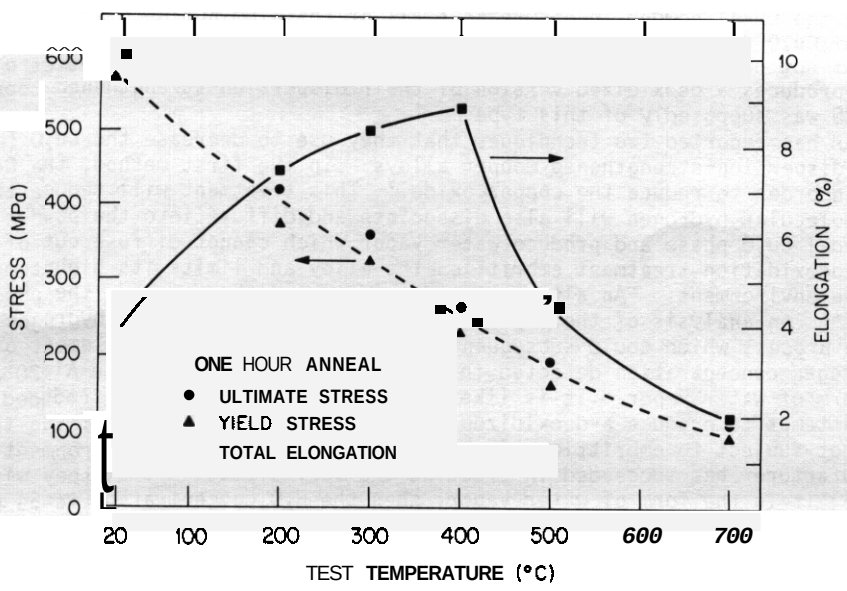

Fig. 8.1.3. Elevated-temperature tensile properties of the A1-20 copper alloy.

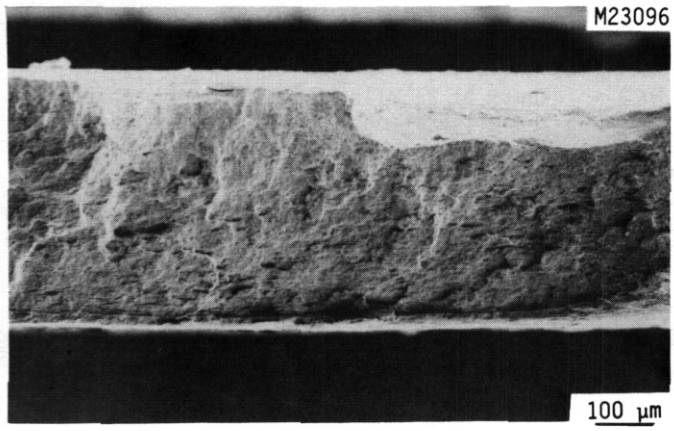

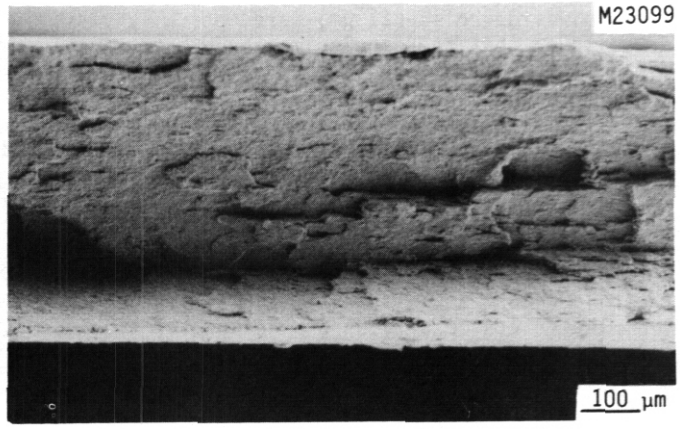

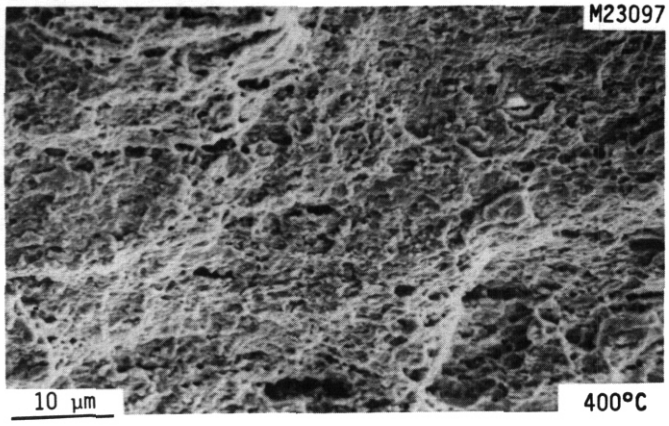

Fig. 8.1.4. Fracture surface of an A1-20 tensile specimen that was annealed for 1 h prior to testing at 400°C.

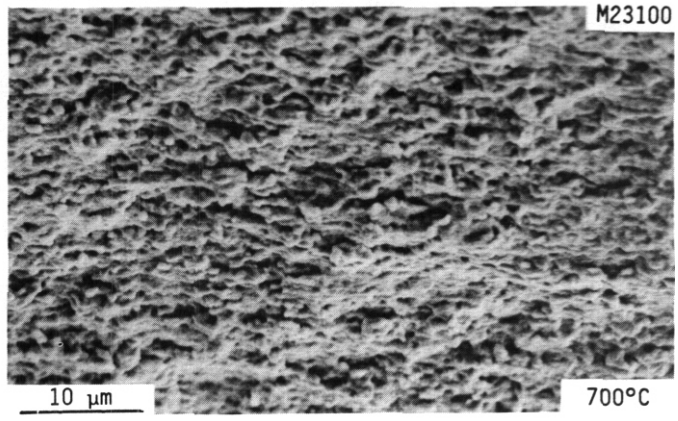

Fig. 8.1.5. Fracture surface of an A1-20 tensile specimen that was annealed for 1 h prior to testing at 700°C.

then fabricated into the shape desired for its particular application. An excess amount of Cu_2O is generally mixed with the Cu-A1 powder to ensure that all of the aluminum becomes oxidized. Therefore, an appreciable amount of Cu_2O exists in the final product. For most applications (hydrogen-free environments), this excess Cu_2O does not have any effect on the electrical or mechanical properties of the alloy. SCM Metal Products also produces a deoxidized version of their dispersion-strengthened copper alloys. The MFE heat of GLIOCOP A1-20 was supposedly of this type.

The manufacturer has reported two techniques that they use to decrease the Cu_2O (matrix oxygen) concentration in their dispersion-strengthened copper alloys. In the first method, the $Cu\text{-}Al_2O_3\text{-}Cu_2O$ powder is heated in hydrogen in order to reduce the copper oxide.' This treatment will reduce the Cu_2O on the surface of the powder, but molecular hydrogen will also dissociate and diffuse into the powder particles where it can reduce the internal Cu_2O phase and produce water vapor which cannot diffuse out of the metal. The net result is that this deoxidation treatment embrittles the alloy and limits its high-temperature usefulness even in hydrogen-free environments. An alternative deoxidation method exposes the powder to a dissociated ammonia atmosphere."' An analysis of the $Cu_2O\text{-}NH_3OH$ reaction indicates that hydrogen is also produced during the reduction process which could subsequently lead to hydrogen embrittlement of the alloy.

The matrix hydrogen concentration detected in the chemical analysis of the A1-20 alloy (Table 8.1.1) is presumably in the form of water vapor. It is likely that this hydrogen was introduced into the alloy during the manufacturer's attempt to produce a deoxidized heat. The purpose of deoxidizing this alloy is to create a material that is not subject to embrittlement when exposed to a hydrogen environment. It would therefore appear that the manufacturer has succeeded in creating the very situation that they wished to avoid. If the 6 ppm H (Table 8.1.1) is in the form of water vapor, then the H_2O concentration is 54 ppm by weight. This corresponds to a H_2O/Cu ratio of 1.9×10^{-4}. For comparison, the He/Cu ratio followina a 10 doa irradiation in FFTF[9] is only 7×10^{-7} (0.7 at. ppm He/Cu).

An annealing study on the MFE heat of the A1-20 alloy at the University of Wisconsin has found even greater blisterina effects than those reoorted here." Large blisters were formed throughout the foil with a total swelling ievel of about 40% following a 1 h anneal at 950°C in either vacuum or a salt bath environment. On the other hand, a 1 h vacuum anneal at 950°C on a heat of the A1-20 alloy used in the Los Alamos copper irradiation program[2] did not produce any surface blisters or swelling.[10]

There are no reported observations of hydrogen embrittlement effects (e.g., surface blisters following annealing) in the three heats of GLIDCOP dispersion-strengthened alloys that have been irradiated to date: A1-20 (refs. 1,2), A1-25 (ref. 3), and A1-60 (ref. 2). It will be interesting to determine if the hydrogenated MFE heat of A1-20 exhibits any different irradiated behavior compared to previous studies on GLIDCOP dispersion-strengthened copper alloys. It is possible that increased swelling levels may occur for high dose irradiations at temperatures above 400°C.

8.1.6 Conclusions

An alloy that is susceptible to hydrogen embrittlement is obviously not desirable for fusion reactor applications due to the high hydrogen concentration that will be generated. Alternative deoxidation or manufacturing techniques should be pursued for the dispersion-strengthened copper alloys.

8.1.7 References

1. J. A. Spitznagel et al., "AIME Symposium on Irradiation Effects Associated with Ion Implantation, Toronto, October 1985; proceedings to be published in ***Nuclear Instruments Meth. Phys. Research B.***

2. R. J. Livak et al., paper presented at the 2nd International Conference on Fusion Reactor Materials, Chicago, April 1986; proceedings to be published in ***Journal of Nuclear Materials.***

3. H. R. Brager, "Effects of Neutron Irradiation to 63 dpa on the Properties of Various Commercial Copper Alloys," paper presented at the 2nd International Conference on Fusion Reactor Materials, Chicago, April 1986; proceedings to be published in ***Journal of Nuclear Materials.***

4. R. L. Klueh, p. 53, ***ADIP Semiennu. Prog. Rept. Sept. 30, 1984***, DOE/ER-0045/13, U.S.DOE, Office of Fusion Energy.

5. E. A. Kolachev, Hydrogen Embrittlement of Nonferrous Metals (Israel Program for Scientific Translations, 1968).

6. ASM Metals Handbook, Vol. 2, "Properties and Selection: Nonferrous Alloys and Pure Metals," 9th ed. (Metals Park, Ohio) 240, 481.

7. A. Nadkarni and J. Synk, p. 151 in ***Copper and Copper Alloys for Fusion Reactor Applications,*** eds. F. W. Wiffen and R. E. Gold, CONF-830466 (1984).

8. A. V. Nadkarni, p. 77 in ***High Conductivity Copper and Aluminum Alloys***, eds. E. Ling and P. W. Taubenblat (TMS-AIME) 1984.

9. R. L. Simons, ***DAFS Quart. Progr. Rep.,*** DOE/ER-0046/19 (November 1984) 12.

10. D. H. Plantz, University of Wisconsin-Madison, Private Communication, May 1986

9. MATERIALS COMPATIBILITY AND HYDROGEN PERMEATION STUDIES

9.1 CORROSION OF Fe-Cr-Mn AND Fe-Cr-Mo ALLOYS IN THERMALLY CONVECTIVE LITHIUM – P. F. Tortorelli and J. H. DeVan (Oak Ridge National Laboratory)

9.1.1 ADIP Task

ADIP Task I.A.3, Perform Chemical and Metallurgical Compatibility Analyses

9.1.2 Objective

The purpose of this task is to determine the corrosion resistance of candidate first-wall materials to slowly flowing lithium in the presence of a temperature gradient. Corrosion and deposition rates are measured as functions of time, temperature, additions to the lithium, and flow conditions. These measurements are combined with chemical and metallographic examinations of specimen surfaces to establish the mechanisms and rate-controlling processes for dissolution and deposition reactions.

9.1.3 Summary

Experiments with Fe-Cr-Ma and austenitic Fe-Cr-Mn alloys exposed to nonisothermal lithium environments revealed the importance of chromium reactions in the corrosion processes. Such reactions were found to significantly affect the temperature dependence of the corrosion of the 12Cr-1MoVW steel by thermally convective lithium. For the Fe-Cr-(12–20 wt %)Mn alloys, preferential depletion and mass transport of manganese were also important corrosion reactions.

9.1.4 Status and Prowess

Austenitic Fe-Cr-Mn alloys are of particular interest to fusion technology because of their substantially lower residual radioactivity compared to that for the standard nickel-containing austenitic stainless steels. As part of the fusion energy materials effort, a qualitative study of the reactions of these Mn-containing steels with molten lithium was conducted usinq a thermal convection loop. The loop circulated lithium between 500 and 350°C and was constructed of type 316 stainless steel which, because of prior operation with lithium and associated preferential leaching of nickel and chromium, was known to have a considerably higher iron concentration at hot leg surfaces than found in the starting material. The Mn-containing alloy specimens were exposed to lithium in a region of the loop near the top of the hot leg. Because of the nonisothermal nature of the loop, the temperatures of these specimens varied from 500 [maximum loop temperature (T_{max})] to 485°C. Coupons of type 316 stainless steel were placed at the other normally-used specimen positions aroung the remainder of the loop. Two such loop experiments were completed. In each, the specimen set was removed from, and replaced into, the molteen lithium thrice during about 3100 to 3300 h of total coupon exposure. The compositions of the alloys exposed in the upper hot zone of the loop during these two experiments are listed in Table 9.1.1.

The weight change data from both loop experiments and some results from surface analyses have been presented and discussed in previous progress reports.[1-3] During the present reporting period, much more extensive surface analyses of the Mn-containing austenitic steels exposed in the second experiment were completed. Results from scanning electron microscopy are shown in Fig. 9.1.1. The corroded surfaces of the 12 to 20 wt % Mn alloys tended to be covered with "nodules" that were principally composed of chromium, as determined by energy dispersive x-ray (EDX) analysis. On a few of these specimens, an underlying, porous surface could be observed in gaps between nodule aggregates, while the nodules completely covered the surfaces of other coupons. As shown in Fig. 9.1.1, examination of polished cross sections showed that porosity developed on every specimen and that the depth of the porous layer varied among the specimens without any direct relationship to the density of the overlying nodules. Figure 9.1.2 shows extremes in the development of these porous layers; it includes microprobe elemental x-ray maps indicating manganese depletion throughout the porous corrosion layers and chromium-rich phases both on the surface and within these altered zones. These observations were confirmed by wavelength dispersive x-ray profiles of the cross sections of selected specimens obtained with the electron microprobe; a typical depth profile is shown in Fig. 9.1.3. Compositional data obtained from EDX analyses of the normal and cross sectional surfaces in the scanning electron microscope were consistent with the electron microprobe results.

The location of type 316 stainless steel specimens in the cold leg during the loop experiments allowed the cold zone deposition reactions to also be characterized by weight changes and microstructural analyses. As described previously,' the coldest loop coupon (350°C) gained considerable weight during the experiment in which the 30 wt % Mn steels were exposed in the hot zone. Numerous large deposits formed at the coldest loop coupon positions. Previous' and present EDX analyses showed that, in both loop experiments, such deposits were principally composed of nickel (dissolved from the loop) and manganese.

The previously reported] observation of mixed weight gains and losses for the steels containing 12 to 20% Mn indicated a competition between dissolution and weight gain reactions. In agreement with results from experiments in static lithium,* the present EDX analyses, microprobe imaging, and depth profile data (Figs. 9.1.2 and 9.1.3) indicate that the reactions include concentration gradient chromium transport among the specimens and loop wall in the hot zone, a small amount of nickel redistribution to the Fe-Cr-Mn specimens, and preferential dissolution of manganese. Such competing reactions can lead to a net weight gain if the addition of reacted material due to dissimilar metal mass transfer is greater than that lost by dissolution of manganese and other elements. In the case of the 30 wt % Mn alloys (X75, R77, and R80),[1] this preferential dissolution obviously dominated the corrosion processes and resulted in large weight

Table 9.1.1. Compositions of alloys exposed to thermally convective lithium between 500 and 480°C[a]

Alloy	Composition (wt %)[b]						
	Mn	Cr	Ni	C	N	Si	Fe
x75	30	2	0.5	0.1	0.15	0.4	bal
R77	30	2	0.5	0.6	0.15	0.4	bal
R80	30	10	0.5	0.50	0.10	0.4	bal
18-18+	18	18	0.5	0.1	0.4	0.6	bal
Age 18-18+	18[c]	18	0.5	0.1	0.4	0.6	bal
AMCR	17	10	0.7	0.2	0.06	0.6	bal
R88	15	15	0.5	0.3	0.30	0.4	bal
R87	15	15	0.5	0.1	0.1	0.4	bal
NIT-32	12	18	1.5	0.1	0.4	0.6	bal
PCMA-2	17	15	0.01	0.06	0.001	0.04	bal
PCMA-4	19	10	0.01	0.09	0.002	0.02	bal
PCMA-6	14	16	0.01	0.18	0.003	0.02	bal
PCMA-7	19	15	0.01	0.38	0.005	0.02	bal
PCMA-9	18	20	0.01	0.26	0.006	0.03	bal
CN13	1.7	17	14.0	0.05		0.6	bal
316 SS	2	17	10	0.05		0.4	bal

[a]PCMA alloys developed at Oak Ridge National Laboratory; other alloys supplied by Hanford Engineering Development Laboratory.

*Analyses provided with alloy material.

[c]Electron beam techniques revealed Mn concentration of 12 wt %. This correction probably applies to the 18-18+ alloy also.

losses of these steels and the presence of Mn deposits in the cold zone. For the 12 to 20 wt % Mn specimens, the porous layer was generally deeper and more uniform for the alloys showing net weight losses. Conversely, the Fe-Cr-Mn steel with the largest weight gain after 3096 h (Age 18-18+) showed a very thin dissolution zone, and the one with the next greatest increase in weight (R87) showed a somewhat thicker, but very irregular corrosion layer. Both the trend of initial weight losses or small weight gains followed by monotonic increases in weight' and the observation of many chromium-rich reaction products on top of the dissolution zones (Figs. 9.1.1-9.1.3) indicate that, in many cases, manganese depletion makes the principal contribution to the weight change of the Fe-Cr-(12-20 wt %) Mn alloys during the early stages of exposure. Subsequently, chromium transport and reaction become dominant and lead to weight gains. The presence of materials of different compositions in the hot zone probably exacerbated the latter reactions.

The exact nature of the reaction(s) involving chromium is not known. The starting concentrations of chromium, nitrogen, and carbon (or the concentration ratios of Cr/N and Cr/C) did not correlate with the weight change data or microstructural results. Nevertheless, the chromium reactions may be driven by the relatively high nitrogen concentrations of some of the Fe-Cr-Mn alloys (Table 9.1.1). Reactions between Cr and N and between Li, Cr, and N are possible[5-7] and could lead to increased dissolution and/or reaction product formation at specimen surfaces. The significant intergranular penetration observed for some of these alloys in static lithium[4,5,8,9] was related to the presence of such reaction products at grain boundaries. In contrast, there was no evidence for intergranular attack of the alloys exposed in the present experiments even though several of the compositions were common to both studies. The reason for such a

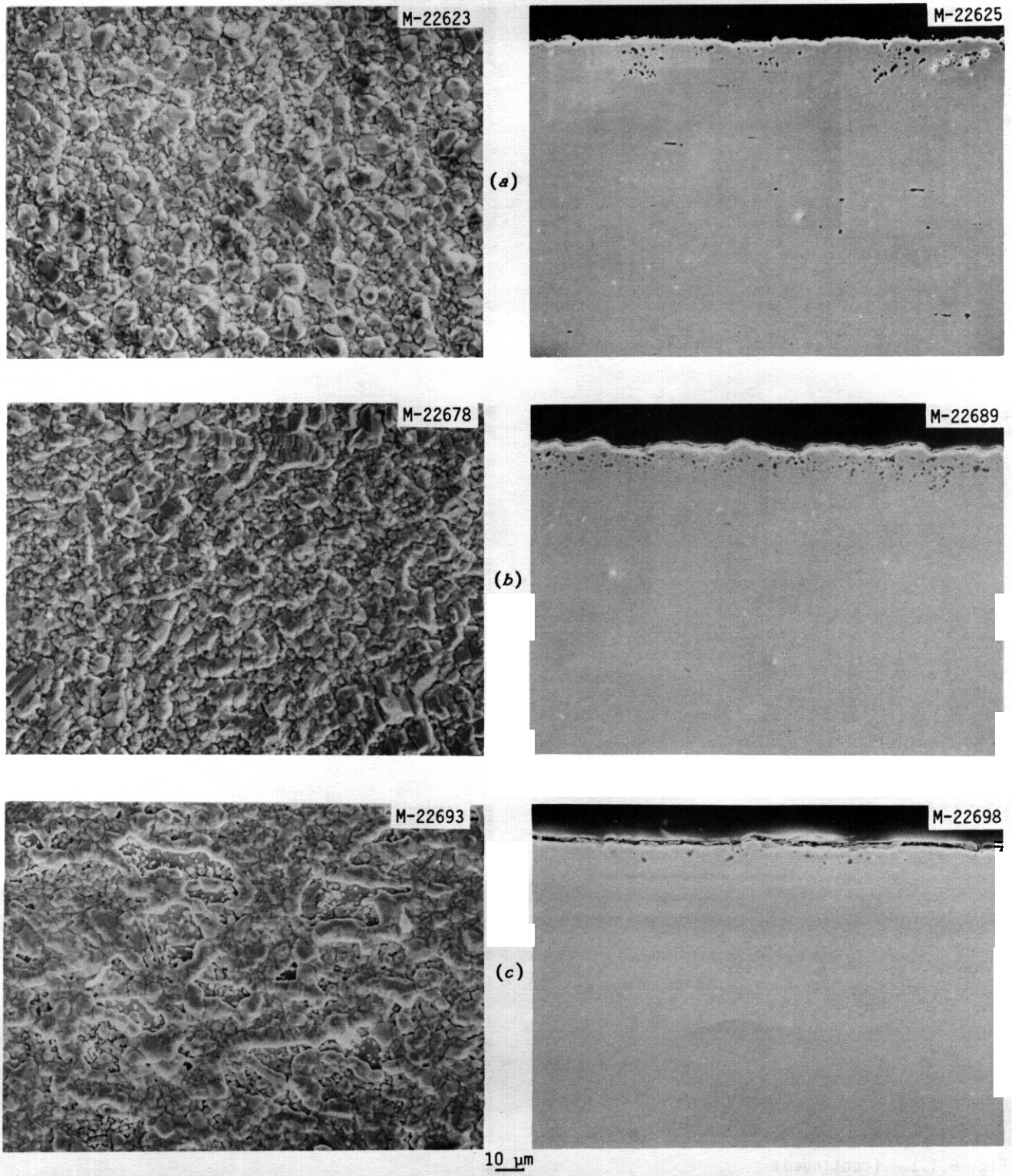

Fig. 9.1.1. Scanning electron micrographs showing representative normal and cross sectional views of Fe-Cr-Mn alloys exposed to thermally convective lithium for 3096 h. (*a*) R87, 500°C. (*b*) PCMA-6, 500°C. (*c*) PCMA-2, 495°C. (*d*) PCMA-9, 495°C. (e) Age 18-18+, 490°C. (*f*) PCMA-7, 490°C. (*g*) NIT-32, 485°C. (*h*) PCMA-4, 485°C. (Figure continued.)

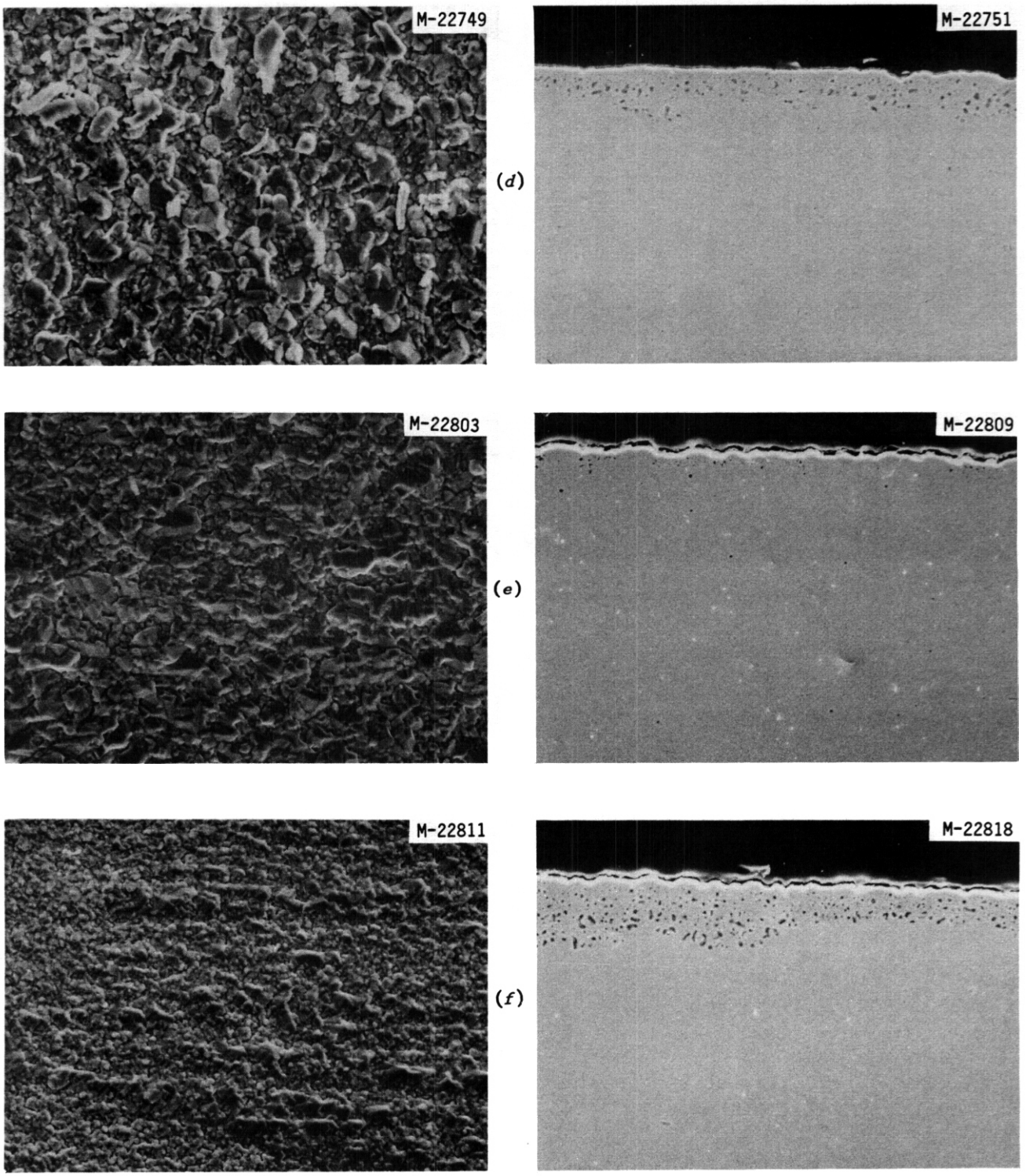

Fig. 9.1.1. (continued)

10 μm

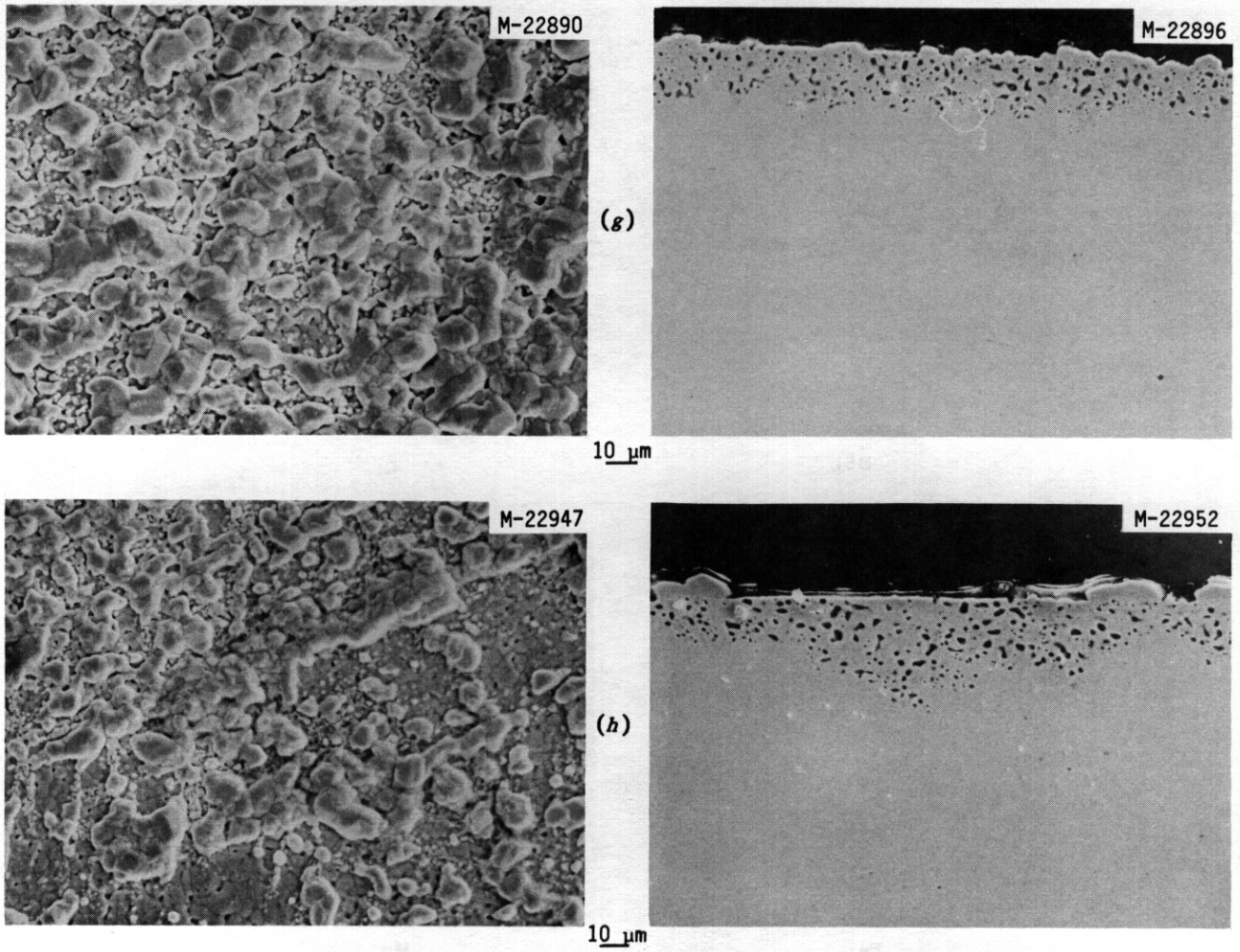

Fig. 9.1.1. (continued)

ORNL-PHOTO 1234-86

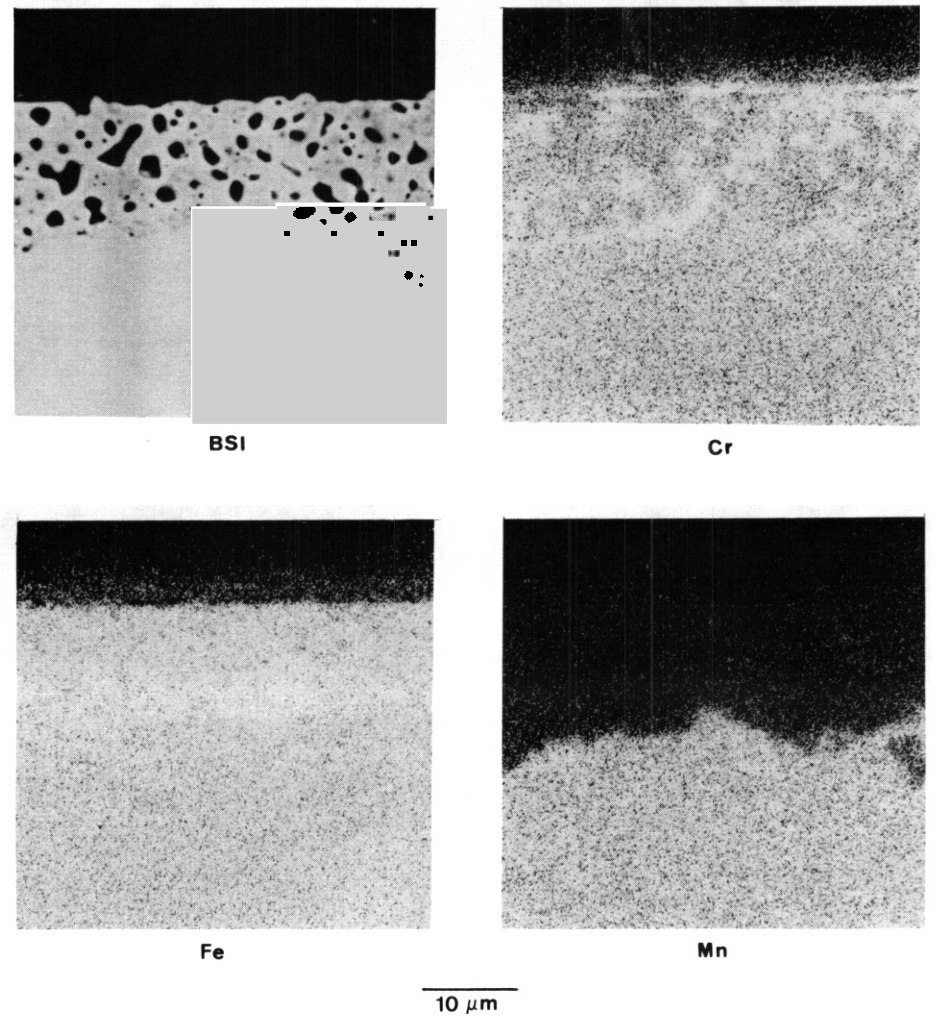

Fig. 9.1.2. Backscattered electron images (BSI) and elemental x-ray maps of Fe-Cr-Mn alloys exposed to thermally convective lithium for 3096 h. (*a*) NIT-32, 485°C. (*b*) Age 18-18+, 490°C. (Figure continued).

ORNL-PHOTO 1235-86

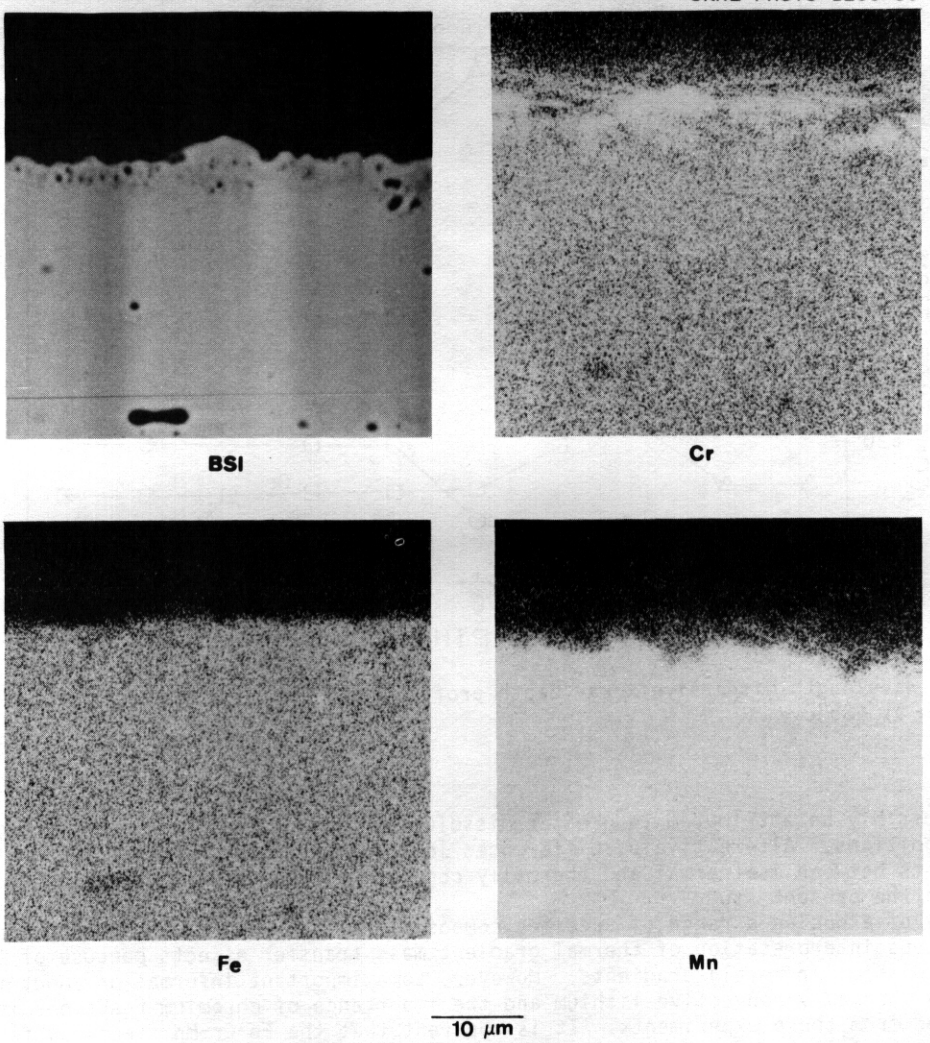

Fig. 9.1.2. (continued)

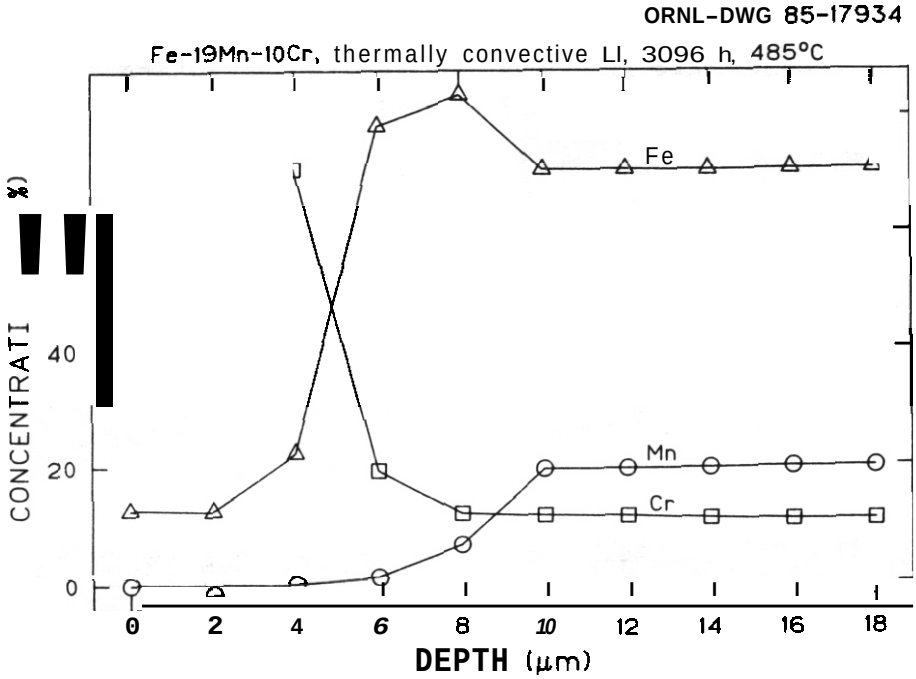

Fig. 9.1.3. Wavelength dispersive x-ray depth profile for PCMA-4 exposed to thermally convective lithium for 3096 h at 485°C.

discrepancy may possibly be attributed to greater dissolution and preferential leaching under the nonisothermal loop conditions. Alternatively, differences in local solution chemistry and/or interstitial concentration gradients between isothermal and thermally convective conditions may explain the absence of grain boundary attack in the present study.

The necessity of exposing a ranqe of specimen compositions in a loop of yet another composition precludes an unambiguous interpretation-of thermal gradient mass transfer effects because of the introduction of concentration (dissimilar metal) gradients. However, some important information about the corrosion of Fe-Cr-Mn alloys by thermally convective lithium and the importance of chromium reactions in this system was nevertheless gained from these experiments. It is apparent that the Fe-Cr-Mn steels suffer from the same effects of nonisothermal lithium exposure as do nickel-containing austenitic alloys (preferential dissolution, porosity formation, and extensive mass transport of soluble species to cold zone). Indeed, the measured weight losses of the steels containing 30 wt % Mn after 3340 h at 490 to 500°C (217-391 g/m^2) were much greater than that measured for a Fe-Cr-30 wt % Ni alloy exposed for 2832 h at 500°C (28 g/m^2),[10] despite the competing weight gain reaction with chromium. Such Fe-Cr-Mn alloys are clearly not suitable for use in lithium systems at elevated temperature, Furthermore, the 12 to 20 wt % Mn alloys experienced significant degradation despite the low net weight changes and are not expected to be particularly corrosion resistant in thermally convective lithium.

In a previous progress report,' weight change data for 12Cr-1MoVW steel exposed to thermally convective lithium circulating between 600 and 450°C in a 12Cr-1MoVW steel loop was presented and compared to earlier data obtained from the same lithium loop operating between 500 and 350°C.[11] While a typical mass transfer weight change profile was not observed in the lower temperature loop experiment, the weight changes from the loop exposure at T_{max} = 600°C seemed to be more consistent with what is expected in the case of thermal gradient mass transport: there were weight losses at the hottest part of the loop and weight gains elsewhere. However, to truly determine the extent of thermal gradient mass transfer in the higher temperature experiment, vis-a-vis other reactions, scanning electron microscopy and associated EDX analysis were recently used to examine surfaces of selected specimens from both the hot and cold legs of the loop. As shown in Fig. 9.1.4, marked differences in surface morphology were observed. The surface of the coupon exposed at T_{max} (600°C, H3) was not severely roughened during its 6962 h of exposure to lithium, but it was depleted in chromium relative to its initial concentration. In contrast, the surface of the H5 (~560°C) specimen was extensively modified by exposure and was covered with "nodules" of different sizes. Relative to the starting composition of 12Cr-1MoVW steel, EOX analysis showed the smaller ones to be slightly rich in iron and the large nodules to be highly enriched in chromium (Fig. 9.1.5). The underlying matrix was found to have a similar composition to that of the starting 12Cr-1MoVW steel. Large and small nodules also covered the entire surface of the C4 specimen (530°C, see Fig. 9.1.4) such that none of the underlying matrix could be observed. As with the H5 coupon, the small nodules were slightly iron-rich (average composition, in wt %, of ~88Fe, 10Cr, 1Ni, and 1Mo) and the large ones were highly enriched in chromium (~12Fe, 84Cr, 2Ni, and 1Mo). Finally, the specimen positioned at the coldest point in the loop (C8, 450°C) was covered nonuniformly with small nodules that were somewhat iron- and nickel-rich.

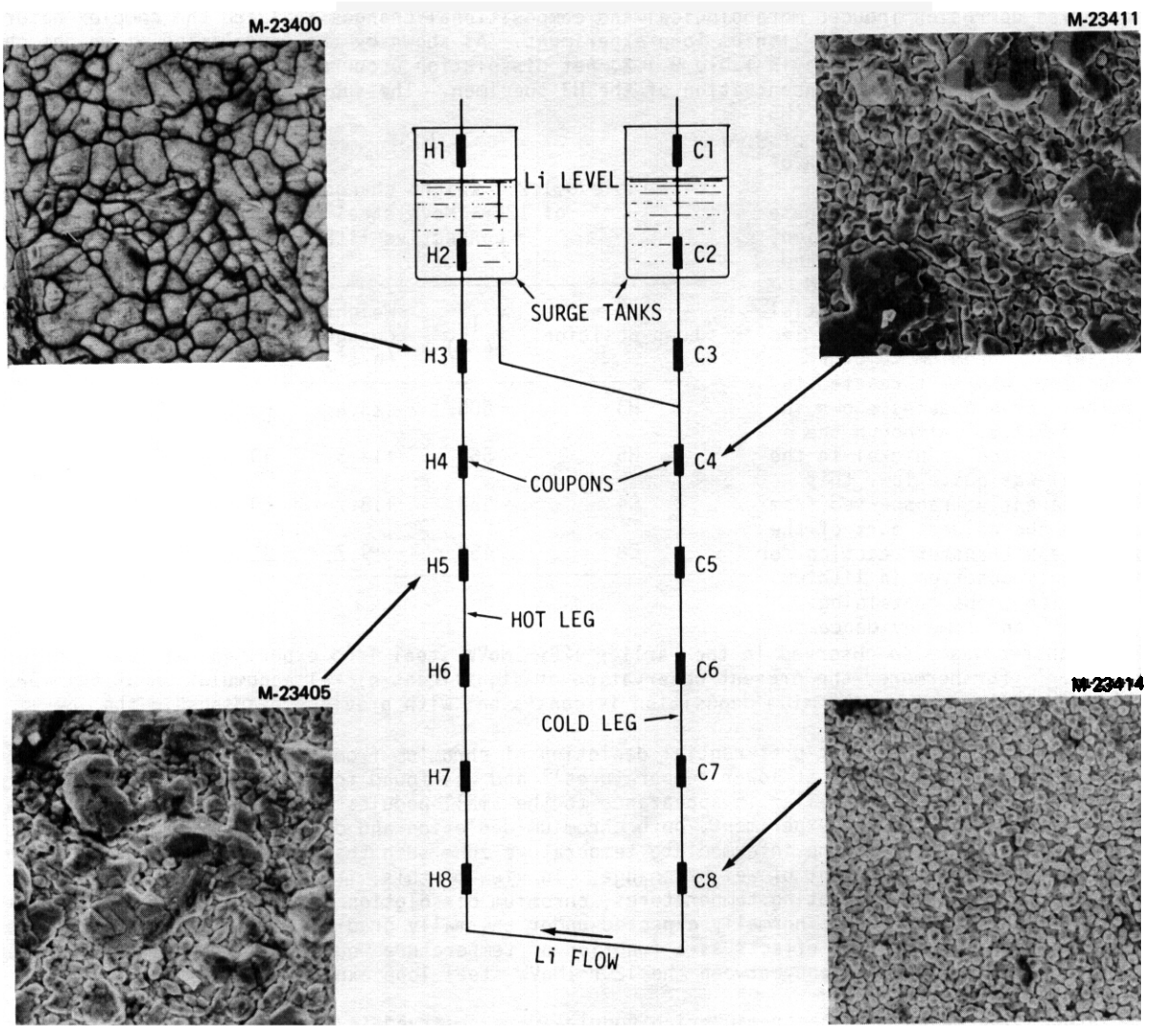

Fig. 9.1.4. Scanning electron micrographs of 12Cr-1MoVW steel specimens exposed for 6962 h to thermally convective lithium circulating between 600 and 450°C.

The observed corrosion-induced morphological and compositional changes indicate the complex nature of the reactions that occurred in this lithium loop experiment. As shown by the correlation of weight change and overall surface composition data in Table 9.1.2, net dissolution occurred at 600°C with a resulting decrease in the chromium surface concentration of the H3 specimen. The substantial chromium enrichment observed at positions both upstream (H5, ~560°C) and downstream (C4, –530°C) of this coupon was due to the formation of the large nodules and led to the significant measured weight gains of these specimens. At the C8 (450°C) position, a smaller weight gain was measured and an enrichment in nickel was detected. It therefore appeared that preferential dissolution of chromium around T_{max} led to the transfer of chromium to other parts of the loop, where it reacted to form the rather large nodules shown in Figs. 9.1.4 and 9.1.5. Although the starting concentration of nickel in the 12Cr-1MoVW steel was quite low, this element was apparently transported from the hot zone to the coldest part of the loop. Such a mass transfer reaction for nickel is commonly observed in lithium thermal convection loops containing Fe-Ni-Cr alloys[12] and some evidence for such nickel transfer was also observed in the earlier 12Cr-1MoVW steel loop experiment at lower temperatures (T_{max} = 500°C).[11] Furthermore, the present observation of significant nickel accumulation at a lower temperature than that for maximum chromium deposition is consistent with previous findings in the lithium-Fe-Ni-Cr system.[12]

Table 9.1.2. Weight changes and surface compositions of 12Cr-1MoVW steel exposed to thermally convective lithium for 6962 h

Loop position	T (°C)	Weight change (g/m²)	Surface composition (wt %)			
			Fe	Cr	Ni	Mo
H3	600	–23.6	90.2	9.1	0.4	0.3
H5	560	+13.3	50.3	45.6	1.9	2.1
c4	530	+18.7	60.7	36.7	1.3	1.2
C8	450	+9.7	92.1	5.6	1.9	0.6

It is interesting to note that preferential depletion of chromium from 12Cr-1MoVW steel has also been observed in lithium loops operated at lower temperatures[13] and was found to be associated with the formation of "dimples" that were somewhat similar in appearance to the small nodules observed on the H5 and C4 specimens. Apparently, in the present experiment, both chromium depletion and deposition/reaction are occurring on the same specimen surfaces in the intermediate temperature zone such that the relative magnitudes of these processes determine the extent of weight change. In view of this, it is quite possible that, for Fe-Cr-Mo steels at lower loop operating temperatures, chromium dissolution at T_{max} will not be sufficient to cause the significant weight losses normally expected under thermally gradient mass transfer conditions. Such a change in overall corrosion effects as a function of temperature would be consistent with the above described differences in observations between the 12Cr-1MoVW steel loop experiments conducted at T_{max} = 600 and 500°C, respectively.

It is interesting to note that chromium-rich nodules were observed in both the lithium loop experiments with Fe-Cr-Mn and with Fe-Cr-Mb alloys. As discussed above for the Fe-Cr-Mn experiments, the chromium reaction(s) may involve nitrogen in the lithium and/or alloy. Such results from these two different alloy systems serve as additional evidence of the importance of chromium reactions in lithium systems and of the interplay between typical mass transfer (dissolution/deposition) processes and chemical reactions in determining the overall corrosion effects and their temperature dependence in nonisothermal lithium environments.

9.1.5 Conclusions

1. Results from lithium thermal convection loop experiments with Fe-Cr-Mn and Fe-Cr-Mo alloys revealed the importance of chromium reactions in influencing overall corrosion behavior.

2. Surface analyses of Fe-Cr-(12–20 wt %)Mn alloys exposed to thermally convective lithium at 485 to 500°C for 3096 h confirmed the existence of competing mechanisms of weight loss resulting from manganese transport and weight gain due to chromium reactions. For these alloys, it appeared that manganese depletion dominated initially, but that it was then offset bv chromiun reactions that were exacerbated bv dissimilar metal gradients in the hot leg. Despite their lower long-term radio-activity, the corrosion of such Fe-Cr-Mn alloys by lithium appears problematic.

3. In a thermal convection loop circulating lithium between 600 and 450°C for 6962 h, chromium depletion from 12Cr-1MoVW steel was significant, particularly at 600°C, but chromium surface products formed at intermediate temperatures. Thermal gradient mass transfer was more important in this experiment than it was in one conducted at lower loop temperatures (500–350°C).

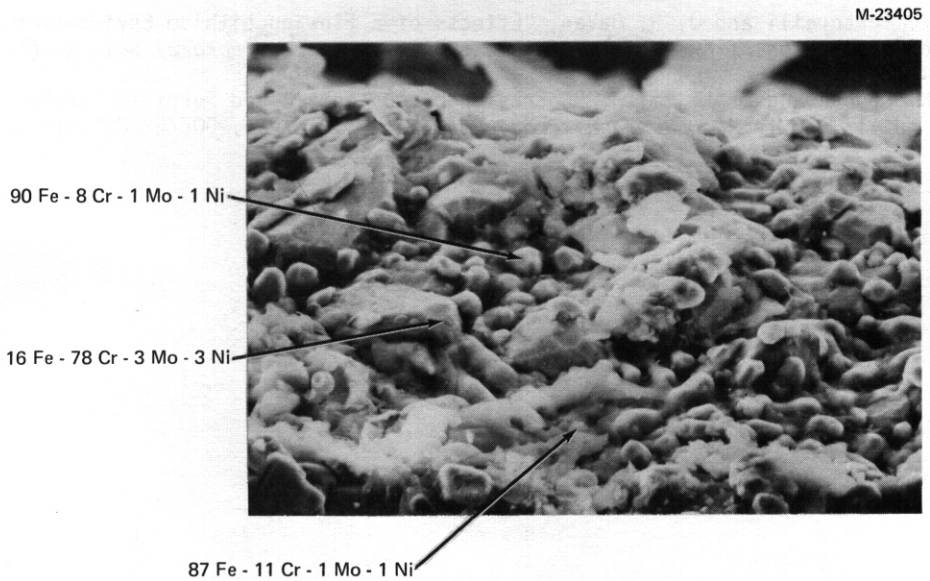

Fig. 9.1.5. Scanning electron micrograph of 12Cr-1MoVW steel exposed for 6962 h to thermally convective lithium at about 560°C; approximate compositions in wt % were obtained by energy dispersive x-ray analysis and represent average of data taken from several surface features of similar type.

9.1.6 References

1. P. F. Tortorelli and J. H. DeVan, "Corrosion of Low Activation Austenitic Alloys and Standard Fe-12Cr-1MoVW Steel in Thermally Convective Lithium," pp. 189–95 in *ADIP Semiann. Prog. Rep. Sept. 30, 1984,* DOE/ER-0045/13, U.S. DOE, Office of Fusion Energy.

2. P. F. Tortorelli and J. H. DeVan, "Thermal Convection Loop Studies of the Lithium Corrosion of Low Activation Austenitic Alloys and Standard Fe-12Cr-1MoVW Steel," pp. 197–204 in *ADIP Semiann. Prog. Rep. March 31, 1985,* DOE/ER-0045/14, U.S. DOE, Office of Fusion Energy.

3. P. F. Tortorelli, J. H. DeVan, and C. T. Liu, "Corrosion of Low Activation Austenitic Steels and Ordered Alloys in Thermally Convective Lithium," pp. 180–87 in *ADIP Semiann. Prog. Rep. Sept. 30, 1985,* DOE/ER-0045/15, U.S. DOE, Office of Fusion Energy.

4. V. Coen et al., "Compatibility in Li and in Li-Containing Traces of LiH of Low Ni, Cr-Mn Austenitic Stainless Steels," *J. Nucl. Mater.*

5. E. Ruedl and T. Sasaki, "E ion in a Cr-Mn Austenitic Steel," *J. Nucl. Mater.* **116** (1983)

6. W. F. Calaway, "The Reaction of Chromium with Lithium Nitride in Liquid Lithium," pp. 181-8-26 in *Proc. Second. Int. Conf. on Liq. Metal Technol. in Energy Production,* U.S. DOE, CONF-800401-P2, 1980.

7. M. G. Barker et al., "The Interaction of Chromium with Nitrogen Dissolved in Liquid Lithium," *J. Nucl. Mater.* **114** (1983) 143–49.

8. E. Ruedl, V. Coen, T. Sasaki, and H. Kolbe, "Intergranular Lithium Penetration of Low-Ni, Cr-Mn Austenitic Stainless Steel," *J. Nucl. Mater.* **110** (1982) 28–36.

9. E. Ruedl, V. Coen, T. Sasaki, and H. Kolbe, "Phase Stability and Corrosion of Cr-Mn Austenitic Steels Exposed to Pure Lithium," *J. Nucl. Mater.* **122** and **123** (1984) 1247–51.

10. P. F. Tortorelli and J. H. DeVan, "Effect of Nickel Concentration on the Mass Transfer of Fe-Ni-Cr Alloys in Lithium," *J. Nucl. Mater.* **103** and **104** (1981) 633–38.

11. P. F. Tortorelli and J. H. DeVan, "Corrosion of an Fe-12Cr-1MoVW Steel in Thermally Convective Lithium," pp. 215–21 in *Proc. Topical Conf. on Ferritic Alloys for Use in Nuclear Energy Technologies,* J. W. Davis and D. J. Michel, eds., AIME, 1984.

12. P. F. Tortorelli and J. H. DeVan, "Effects of a Flowing Lithium Environment on the Surface Morphology and Composition of Austenitic Stainless Steel," *Microstructural Sci.* 12 (1985) 213–26.

13. O. K. Chopra and D. L. Smith, "Corrosion of Austenitic and Ferritic Steels in Flowing Lithium Environment," pp. 171–79 in *ADIP Semiann. Pros. Rep. Sept. 30, 1985,* DOE/ER-0045/15, U.S. DOE, Office of Fusion Energy.

9.2. THERMAL CONVECTION LOOP CORROSION STUDIES OF FERROUS ALLOYS EXPOSED TO MOLTEN Pb-17 at. % Li — P. F. Tortorelli and J. H. DeVan (Oak Ridge National Laboratory)

9.2.1 ADIP Task

ADIP Task I.A.3, Perform Chemical and Metallurgical Compatibility Analyses.

9.2.2 Objective

The purpose of this task is to determine the corrosion resistance of candidate first-wall materials to slowly flowing Pb-17 at. % Li in the presence of a temperature gradient. Dissolution and deposition rates are measured as functions of time, temperature, and additions of minor elements to the lead-lithium. These measurements are combined with chemical and metallographic examinations of specimen surfaces to establish the mechanisms and rate-controlling processes for the dissolution and deposition reactions.

9.2.3 Summary

Longer-term (>6000 h) data for type 316 stainless steel and 12Cr-1MoVW steel exposed to thermally convective Pb-17 at. % Li yielded more extensive information about dissolution rates and environmentally-induced surface modification of these alloys. The austenitic steel suffered greater corrosion and irregular penetration and dissolution by the lead-lithium, whereas the 12Cr-1MoVW steel tended to corrode uniformly at a lower rate. A model for the nonuniform penetration of type 316 stainless steel by Pb-17 at. % Li was suggested.

9.2.4 Progress and Status

Specimens of type 316 stainless steel and 12Cr-1MoVW steel are being exposed to thermally convective Pb-17 at. % Li in two different loop experiments. In one thermal convection loop (TCL), type 316 stainless steel coupons are contained in type 316 stainless steel piping that previously had circulated lithium for over 10,000 h. A second TCL contains 12Cr-1MoVW steel specimens and is made from 9Cr-1Mo steel. It had not seen previous service. Both loops are circulating Pb-17 at. % Li at a maximum temperature of 500°C, but the temperature differential is higher in the case of [illegible] 150°C) than the type 316 stainless steel (100°C). (The details of the procedure for [illegible] lead-lithium used in both loops were described earlier.)[1]

As reported previously,[2] the molten lead-lithium environment was quite aggressive. Substantial weight losses were measured for both type 316 stainless steel and 12Cr-1MoVW steel through about 3000 h of exposure. The former steel was corroded to a much greater extent; its weight losses at 500°C were higher and a relatively deep ferritic surface layer formed upon exposure to the Pb-17 at. % Li. This type of corrosion layer, which was found to be severely infiltrated by lead,[3] was in contrast to the rather uniform corrosion of the 12Cr-1MoVW steel.[2] During the current reporting period, continuation of the two loop experiments yielded additional weight loss and surface analytical data for more than 6000 h of exposure. Examination of a polished cross section of a type 316 stainless steel specimen exposed to the Pb-17 at. % Li for 6384 h at 500°C (Fig. 9.2.1) showed continued growth of the penetrated surface layer previously observed at shorter exposure times.[2,3] Electron microprobe analysis of the cross section shown in Fig. 9.2.1 revealed substantial depletion in nickel and chromium relative to the matrix (or starting) composition (Table 9.2.1). It is interesting to note that, although the compositional data for the specimen exposed for 6384 h (Table 9.2.1) showed rather uniform concentrations of nickel and chromium throughout the corrosion layer, the measured concentrations of these elements in a corrosion layer formed after 2472 h of exposure[2] varied between the values noted in Table 9.2.1 and those levels typically found in the starting material. In direct contrast to the case of type 316 stainless steel, no localized corrosion of the exposed Fe-12Cr-1MOVW steel specimens was observed for exposures as long as 6048 h.

Longer-term weight loss data have now been obtained for both type 316 stainless steel and 12Cr-1MoVW exposed to thermally convective Pb-17 at. % Li and are shown in Fig. 9.2.2. As discussed previously,[2,3] the use of low temperature molten lithium to remove residual lead-lithium from exposed specimens can lead to partial or complete detachment of the penetrated layer on type 316 stainless steel. Therefore, the data of Fig. 9.2.2 represent measurements from individual coupons, which were cleaned in the standard manner after loop exposure and not re-exposed. If the "spongy" layer happened to be removed during the cleaning process, re-exposure of the specimen would result in the growth of a new layer and cause more rapid corrosion than if the layer had remained. This is thus somewhat different from many (but not all) lithium loop experiments with austenitic stainless steel, where the corrosion layer is not lost during the process of lithium removal prior to weighing. In the case of lithium, reinsertion of the specimens does not normally expose a fresh austenitic surface. A striking illustration of this effect in lead-lithium is shown in Fig. 9.2.3, which compares the weight loss measurements from several coupons exposed for different times to weight loss data obtained from a single type 316 stainless steel specimen that was repeatedly exposed to thermally convective Pb-17 at. % Li, cleaned, weighed, and re-exposed. Note the much higher weight losses for the single specimen curve. Furthermore, the weight loss kinetic behavior was quite different; for the multiple specimen curve, weight loss kinetics were described by

$$w = k_e t^{0.7} , \qquad (1)$$

where w is weight loss, k_e is an effective rate constant, and t is exposure time, while, in the case of the single specimen data,

$$w = k_l t \quad , \qquad (2)$$

where k_l is the linear rate constant. Presumably, the cleaning procedure removed the surface layer and exposed some fresh, nickel-containing surface each time the specimen was put in the loop so that the initial high corrosion rate noted in the multiple specimen case (and in other austenitic stainless steel-liquid metal systems)' was maintained. Therefore, in order to avoid any such difficulties, different specimens were used for each data point in order to generate the mass loss versus time results shown in Fig. 9.2.2.

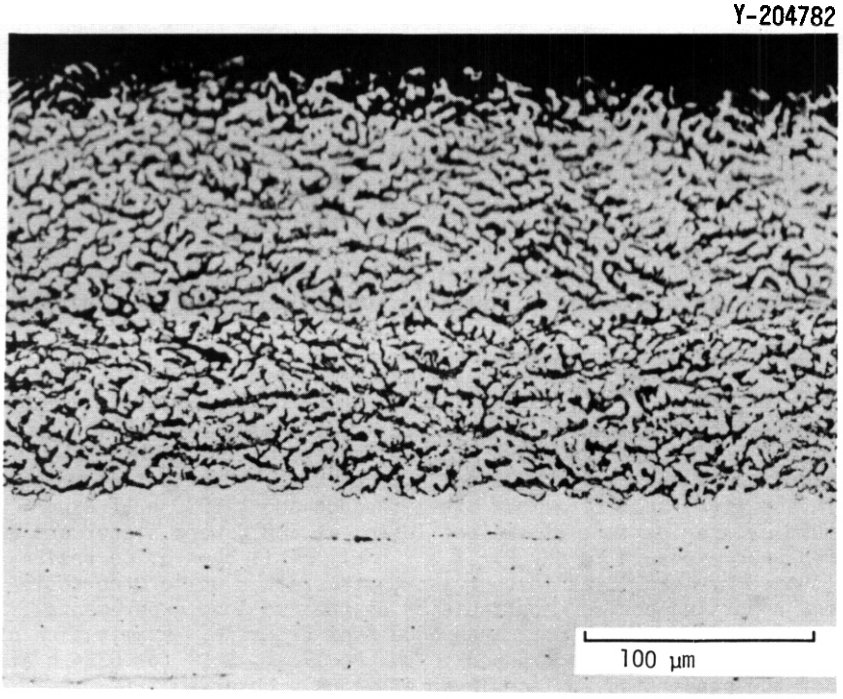

Fig. 9.2.1. Polished cross section of type 316 stainless steel exposed to thermally convective Pb-17 at. % Li at 500°C for 6348 h.

Although the specimen cleaning procedure does not strip any corrosion layer from the 12Cr-1 MoVW steel specimens, the same coupon exposure methodology was used for these specimens to generate the mass loss kinetics data in a consistent manner.

The data presented above clearly indicate that the austenitic stainless steel is much more susceptible to corrosive attack by Pb-17 at. % Li than the 12Cr-1MoVW steel. The poorer corrosion resistance of the austenitic stainless steel vis-a-vis the Fe-Cr-Mo alloy was apparent not only in the much greater mass losses, but also by the appearance of the steel surfaces. The relatively uniform dissolution of the Fe-12Cr-1 MoVW steel was in sharp contrast to the deep, irregular attack of the type 316 stainless steel. The weight loss behavior with time also differs for the two alloys; as shown in Fig. 9.2.2, the weight losses of the type 316 stainless steel follow a power curve relationship with exposure time [Eq. (1)], while those of the 12Cr-1MoVW steel are approximately linearly dependent on time such that

$$w = k_j t \quad , \qquad (3)$$

where w and t are as defined above and k_j is the linear rate constant. The differing corrosion morphologies and weight loss kinetics for the two types of alloys are similar to those noted from other Pb-17 at. % Li studies with these steels' and also reflect what is typically observed in molten lithium environments (see, for example, ref. 6).

As described elsewhere for type 316 stainless steel in lithium,' a relationship of the form of Eq. (1) can be interpreted as being indicative of a mixed control process consisting of parabolic and linear terms:

$$w = k_p t^{1/2} + k_j t \quad , \qquad (4)$$

Table 9.2.1. Wavelength dispersive analysis of the polished cross section of type 316 stainless steel exposed to Pb-17 at. % Li for 6348 h at 500°C

Location	Concentration (wt %)			
	Ni	Fe	Cr	Mo
Outer edge of corrosion zone	3.8	86	7.4	2.5
Middle of corrosion zone	3.7	85	8.3	2.4
Middle of corrosion zone	3.5	83	8.9	2.4
Near edge of internal void	3.3	86	7.5	2.6
Near edge of internal void	3.8	85	7.9	2.2
In corrosion zone next to interface with matrix	3.0	84	7.7	2.5
In matrix next to interface with corrosion zone	13	65	17	2.2
Deeper into uncorroded matrix	13	65	18	2.4

where the first term dominates at early exposures, when nickel is being dissolved at a relatively high rate, and the second term becomes more important at longer times, when the constituents of the steel are released into the liquid metal in proportion to their starting concentration,' A weight loss (or dissolution) rate can then be obtained from long-term data by determination of the slope of the weight loss versus time curve (Kj). Such a procedure is commonly used for liquid metal corrosion when linear kinetics have been established and was used in the present case for $t > 3000$ h to get an approximate rate constant (dissolution rate) of 76 $mg/m^2 \cdot h$ for type 316 stainless steel exposed to thermally convective Pb-17 at. % Li at 500°C. This value can then be compared to that determined from the weight loss data for the 12Cr-1MoVW steel [K1, see Eq. (3)]: 21 $mg/m^2 \cdot h$. However, because of the basic difference in corrosion morphologies, such a comparison between the austenitic stainless steel and the 12Cr-1MoVW alloy is not a definitive one, and a comparison between the decrease in sound metal thickness of each steel is more appropriate. At a given exposure, the difference in surface recession rate of type 316 stainless steel and 12Cr-1MoVW steel is relatively greater than the weight losses because simple mass change does not account for the lack of integrity of the porous layer on the austenitic alloy. Such determinations of corrosion losses by thickness changes therefore increase the difference in susceptibility between type 316 stainless steel and 12Cr-1MoVW steel relative to that obtained from the weiqht loss measurements.

Any mechanistic explanation for the type of corrosion layer that forms on the exposed type 316 stainless steel must also be consistent with the observation that the Fe-12Cr-1MoVW steel corrodes quite differently. This leads to consideration of a model in which the higher solubility and preferential dissolution of nickel account for the nonuniform nature of the corrosion of type 316 stainless steel. Such a model can be based on the work of Harrison and Wagner,[8] who showed that preferential leaching of one component of a solid alloy into a liquid metal can destabilize the solid-liquid interface to produce a highly irregular, porous surface that is very similar to what is observed in the present case for type 316 stainless steel. If one elemental component is dissolving rapidly, a slight physical or chemical perturbation of the interface between the solid and liquid can develop into large scale nonuniformity of this surface. On the other hand, Harrison and Wagner[8] also showed that when the solubilities of alloy components in the liquid metal do not differ greatly from one another (as in the present case of the Fe-Cr steel), the

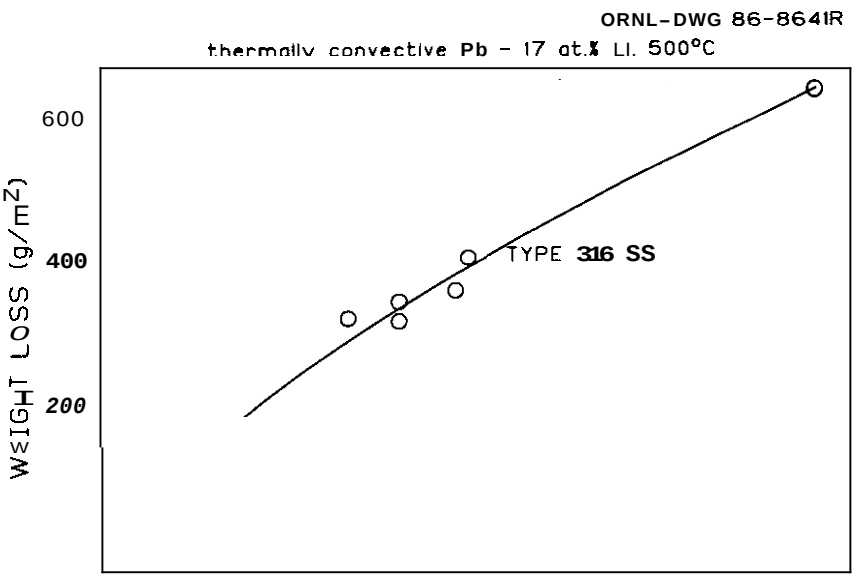

Fig. 9.2.2. Weight loss versus exposure time for type 316 stainless steel and 12Cr-1MoVW steel exposed to thermally convective Pb-17 at. % Li at 500°C.

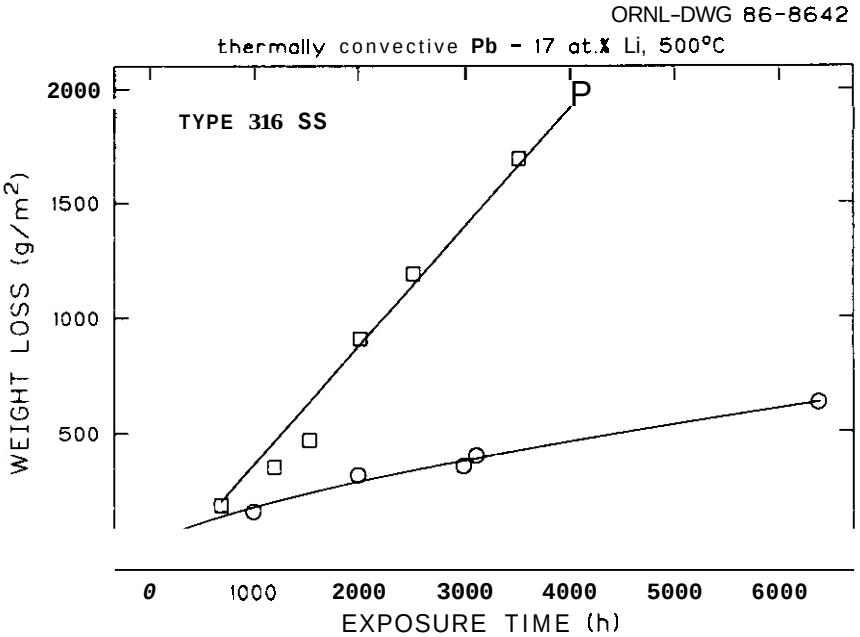

Fig. 9.2.3. Weight loss versus exposure time for type 316 stainless steel exposed to thermally convective Pb-17 at. % Li at 500°C. Circles represent data from individual specimens exposed only once. Squares are data for specimen that was repeatedly cleaned and reexposed.

solid alloy-liquid metal interface should remain macroscopically plane in accordance with our observations for the 12Cr-1MoVW steel exposed to Pb-17 at. % Li.

Much of the experimental work of Harrison and Wagner[1] involved copper-nickel alloys in molten silver at 1000°C, where copper was preferentially depleted. Although solid state diffusion can play an important role under such conditions, calculations show that, in the present case of preferential leaching of nickel at 500°C, the influence of such diffusion is negligible even at the extended exposure times of this study. Nevertheless, for the case where many thin liquid zones infiltrate the solid alloy (in a somewhat similar, though idealized, manner to what is observed in the present experiments), the concentration of nickel in these liquid regions can be considered a function of time and distance from the original surface such that liquid phase diffusion is the important factor in growth of the zones. For this case, where the liquid zones are fairly close together, Harrison and Wagner[1] derived an expression relating the depth of penetration of the liquid metal, x, to exposure time:

$$x \approx 2\,(K N_{Ni}^{(0)} D_{Ni}^{l} t)^{1/2}\ , \qquad (5)$$

where K is the distribution coefficient of Ni between the liquid and solid, $N_{Ni}^{(0)}$ is the initial mole fraction of Ni in the alloy, and D_{Ni}^{l} is the diffusion coefficient of nickel in the liquid phase. While recognizing that measurements of x from present observations are somewhat inaccurate due to possible removal of some of the corrosion layer during specimen cleaning (see above), it is interesting to note that, when x is measured from micrographs of the cross sections of the appropriate stainless steel specimens, such data follow a similar time dependence to that predicted by Eq. (5):

$$x = At^{0.6}\ . \qquad (6)$$

Such relatively good agreement can serve as additional support for the validity of this model in describing the observed corrosion process.

It is informative to compare the corrosiveness of Pb-17 at. % Li to that of another possible tritium breeding fluid — lithium. Under similar conditions, the general characteristics of the corrosion processes are the same for the two liquid metals. In both environments, austenitic stainless steels form a spongy surface layer and exhibit a power curve dependence of weight loss on time,[4,6] while Cr-Mo steels corrode uniformly and show linear weight loss kinetics.[6] However, although overall similar corrosion processes may occur in both systems, Pb-17 at. % Li is much more aggressive than pure lithium. Weight losses, depths of the ferritic layers on type 316 stainless steel, and dissolution rates are all substantially greater in lead-lithium. Furthermore, while porous ferritic layers form on type 316 stainless steel in both Pb-17 at. % Li and lithium, there are differences in their morphologies. Those induced by lead-lithium appeared to have greater and more extended voidage. The greater aggressiveness of lead-lithium toward ferrous alloys is consistent with the generally more rapid corrosion kinetics observed in pure lead environments (see for example, ref. 9).

In both lead-lithium and lithium environments, the greater corrosion susceptibility of the type 316 stainless steel relative to the Fe-12Cr-1MoVW alloy can be attributed to the presence of nickel in the former steel. Other studies with pure lead* and pure lithium** have shown that corrosion of Fe-Cr-Ni alloys increased with increasing concentration of nickel, which has relatively high solubilities in molten lead and lithium relative to chromium and iron. Furthermore, as discussed above, the preferential leaching of nickel can lead to the severe type of corrosive attack observed for type 316 stainless steel.

9.2.5 Conclusions

1. Results from 500°C exposures of type 316 stainless steel and 12Cr-1MoVW steel to thermally convective Pb-17 at. % Li for greater than 6000 h revealed severe, nonuniform attack of the type 316 stainless steel that resulted in the formation of extensive ferritic corrosion layers and uniform corrosion of the 12Cr-1MoVW steel. The presence of the ferritic layer on the type 316 stainless steel and the effects of specimen cleaning on its integrity were shown to be important considerations in evaluating the data for this steel and in comparing corrosion losses for the two types of alloys. The type 316 stainless steel was more susceptible than the Fe-Cr-Mo alloy to corrosion by Pb-17 at. % Li. In addition, both alloys were corroded to a greater extent in Pb-17 at. % Li than in lithium under similar exposure conditions.

2. A model from the literature was suggested as an appropriate explanation for the deeply penetrating, irregular corrosion of the type 316 stainless steel by Pb-17 at. % Li. It was based on the preferential dissolution of nickel and the instability of a slightly irregular surface under such conditions. Such a model explains not only the formation of such a layer and its growth kinetics, but also the contrasting uniform corrosion for 12Cr-1MoVW steel.

9.2.6 References

1. P. F. Tortorelli and J. H. DeVan, "Corrosion of Type 316 Stainless Steel in Flowing Pb-17 at. % Li," pp. 203–05 in *ADIP Semiann. Prog. Rep. Sept. 30, 1983,* DOE/ER-0045/11, U.S. DOE, Office of Fusion Energy.

2. P. F. Tortorelli and J. H. DeVan, "Corrosion of Type 316 Stainless Steel and 12Cr-1MoVW Steel in Thermally Convective Pb-17 at. % Li," pp. 188–94 in *ADIP Seniann. Prog. Rep. Sept. 30, 1985,* DOE/ER-0045/15, U.S. DOE, Office of Fusion Energy.

3. P. F. Tortorelli and J. H. DeVan, "Corrosion of Type 316 Stainless Steel and 12Cr-1MoVW Steel in Flowing Pb-17 at. % Li," pp. 196–99 in *ADIP Semiann. Prog. Rep. Sept. 30, 1984,* DOE/ER-0045/13, U.S. DOE, Office of Fusion Energy.

4. P. F. Tortorelli and J. H. DeVan, "Mass Transfer Kinetics in Lithium-Stainless Steel Systems," pp. 81–88 in *Proc. 3rd Intern. Conf. on Liquid Metal Engineering and Technol.*, vol. 3, The British Nuclear Energy Society, 1985.

5. O. K. Chopra and D. L. Smith, "Corrosion of Ferrous Alloys in Eutectic Lead-Lithium Environment," *J. Nucl. Mater.* 122 and 123 (1984) 1219–24.

6. O. K. Chopra and P. F. Tortorelli, "Compatibility of Materials for Use in Liquid-Metal Blankets of Fusion Reactors," *J. Nucl. Mater.* 122 and 123 (1984) 1201–12.

7. J. R. Weeks and H. S. Isaacs, "Corrosion and Deposition of Steels and Nickel-Base Alloys in Liquid Sodium," *Adv. in Corrosion Sci, 3* (1973) 1–66.

8. J. O. Harrison and C. Wagner, "The Attack of Solid Alloys by Liquid Metals and Salt Melts," *Acta Met.* 7 (1959) 722–35.

9. R. C. Asher, D. Davies. and S. A. Beetham, "Some Observations on the Compatibility of Structural Materials with Molten Lead," *Corrosion Sci.* 17 (1977) 545–57.

10. P. F. Tortorelli and J. H. DeVan, "Effect of Nickel Concentration on the Mass Transfer of Fe-Ni-Cr Alloys in Lithium," *J. Nucl. Mater.* 103 and 104 (1981) 633–38.

9.3 CORROSION OF AUSTENITIC AND FERRITIC STEELS IN FLOWING LITHIUM ENVIRONMENT -- O. K. Chopra and D. L. Smith (Argonne National Laboratory)

9.3.1 ADIP Task

ADIP Task I.A.3, Perform Chemical and Metallurgical Compatibility Analyses.

9.3.2 Objective

The objective of this program is to investigate the influence of a flowing lithium environment on the corrosion behavior and mechanical properties of structural alloys under conditions of interest for fusion reactors. Corrosion rates are determined by measuring the weight change and depth of internal corrosive penetration as a function of time and temperature. These measurements, coupled with metallographic evaluation of the alloy surface, are used to establish the mechanism and rate-controlling process for the corrosion reactions. Initial effort on mechanical properties is focused on fatigue and tensile tests in a flowing lithium environment of controlled purity.

9.3.3 Sumnary

Corrosion data are presented for ferritic HT-9 and Fe-9Cr-1Mo steels and austennitic Type 316 stainless steel in a flowing lithium environment at temperatures between 372 and 538°C. Metallic elements detected on the corrosion specimens indicate the presence of corrosion products on the alloy surfaces. These products are ternary nitrides of lithium and major alloy constituents.

9.3.4 Progress and Status

The corrosion behavior of several ferritic and austenitic steels is being investigated in a flowing lithium environment. The corrosion tests are conducted in a forced-circulation lithium loop consisting of three test vessels and a secondary cold-trap purification loop. A detailed description of the loop and the test procedure have been presented earlier.[1-3] The temperature and time of exposure and the loop operating conditions for the various corrosion tests are given in Table 9.3.1. Lithium was circulated at ~1 L/min in the primary loop, and the concentrations of C and H in lithium were ~10 and 120 wppm, respectively.

The corrosion data and metallographic evaluation of ferritic HT-9 and Fe-9Cr-1Mo steel and austenitic Type 316 stainless steel exposed to flowing lithium at 538, 482, 427, and 372°C have been reported earlier.[4] Corrosion data for ferritic HT-9 and Fe-9Cr-1Mo steel in flowing lithium at temperatures between 372 and 538°C indicate that after an initial transient period of ~500 h, the weight losses for ferritic steels increase linearly with time and yield a constant dissolution rate. The dissolution rates increase with an increase in temperature. An Arrhenius plot of the dissolution rates yields an activation energy of 16.3 kcallmole. The dissolution behavior of the two steels is identical. After exposure to lithium, the alloy surfaces develop a dimpled appearance. A dimpled surface structure is fully developed after ~1000 h of exposure and the size of the dimples does not change with additional exposure. However, the size of dimples decreases with a decrease in temperature. The formation of a dimpled structure is associated with depletion of chromium from the alloy surface and leads to significant weight loss during the initial period of exposure. Limited data (i.e., Run 6) indicate some downstream effects on the dissolution behavior of alloys. Iron-rich deposits were observed on the surfaces of HT-9 and Fe-9Cr-1Mo specimens located downstream (at 482°C) from the maximum loop temperature position (538°C).

The dissolution rates for austenitic Type 316 SS reach a steady state after an initial ~1500-h period characterized by rapid dissolution. The steady-state dissolution rates are relatively insensitive to variations in temperature. The dissolution rates for annealed or 20% CW Type 316 stainless steel exposed to lithium at temperatures between 312 and 538°C range from 1.5 to 2.5 $mg/m^2 \cdot h$. The weight losses after the initial transient stage (i.e., 500- to 1000-h exposure) range between 15 and 30 g/m^2 after exposure at 427 or 482°C and between 3 and 15 g/m^2 after exposure at 372 or 538°C. The initial dissolution stage is associated with the formation of a ferritic surface layer due to depletion of nickel from the steel. This transient stage appears to play an important role in controlling the nature of the surface modifications and, consequently, in the overall dissolution behavior of austenitic steels. Specimens with large weight losses develop a well-defined dimpled structure and deep cavities. The surfaces of these specimens are depleted of nickel, and the chromium content ranges from 8 to 10%. Specimens with small weight losses, i.e., <10 g/m^2, develop a very fine dimpled structure (e.g., at 372°C) or a cellular structure (e.g., at 538°C).

The steady-state dissolution rates of the various sets of ferritic steels and Type 316 SS exposed to flowing lithium are given in Table 9.3.2. The Arrhenius plots of the data are shown in Fig. 9.3.1. The results indicate that the dissolution rates for HT-9 and Fe-9Cr-1Mo steel increase by a factor of ~10 when the temoerature increases from 400 to 550°C. The Arrhenius plot for the dissolution rates yields an

Table 9.3.1. Lithium loop operating conditions for various corrosion tests

Test Run	Loop Temperature (°C) Test Vessel	Spec. Exp. Vessel[a]	Supply Vessel	Cold Trap	N Content in Lithium (wppm)	Exposure Time (h) Test Vessel	Spec. Exp. Vessel
1	482	482	432	212	<50	1295	5000
2	482/427[b]	482	407	230[c]	–250	-	1997
3	427	482	407	230	–100	1100	-
4	482	427	410	212	<100	5521	6501
5	427	372	372	206	–100	5023	4955
6	538	482	410	208	–50	3655	3330

[a]Lithium flow was from test vessel to specimen exposure vessel.
[b]Test vessel temperature changed from 482 to 427°C after 1540 h.
[c]No flow occurred through cold trap after 890 h due to plugging. Plugged sections were replaced and flow started after an additional 480 h.

Table 9.3.2. Dissolution rates of ferritic and austenitic steels exposed to flowing lithium

Test Run	Specimen Location[a]	Temp. (°C)	Maximum Time (h)	Dissolution Rate (mg/m^2 h) HT-9	9Cr-1Mo	316 SS	316 CW
4	Test Vessel	482	5521	0.173	0.144	1.61	1.58
4	Spec. Exp. Vessel	427	5739	0.064	0.066	2.21	2.18
	Spec. Exp. Vessel	427	6501	0.070	0.070	-	-
5	Test Vessel[b]	427	5023	0.077	0.062	9.17	6.34
5	Spec. Exp. Vessel	372	4955	0.029	0.030	2.11	2.48
6	Test Vessel	538	3655	0.401	0.391	2.05	1.41
	Test Vessel	538	2271	-	-	1.75	-
6	Spec. Exp. Vessel'	482	3330	-	-	2.05	1.84

[a]Corrosion soecimens were exposed in the test and specimen exposure vessels. Lithium flow was from test vessel to specimen exposure vessel.
[b]Dissolution rates for HT-9 and 9Cr-1Mo were obtained from combined data of Runs 4 and 5.
[c]Large deposits were observed on specimen surfaces. Ferritic steels showed little or no weight loss.

activation energy of 16.3 kcallmole. However, the dissolution rates for Type 316 SS are insensitive to changes in temperature. The steady-state dissolution rates range betwen 1.5 and 2.5 mg/m^2 h; the values are higher at lower temperatures.

For the ferritic steels, the temperature dependence of dissolution rates in lithium (i.e., activation energy Q = 16.3 kcallmole) is lower than that observed in flowing Pb-17Li (i.e., Q = 22.1 kcale/mole) and comparable to that observed in flowing sodium (i.e., Q = 17.5 kcal/mole).[5] In flowing sodium, the dissolution rates of ferritic steels are very sensitive to the oxygen content in sodium. Limited data in flowing lithium indicate that an increase in nitrogen in lithium increases the dissolution rates.[4] The data in Fig. 9.3.1 were obtained in lithium containing 1 0 0 wppm nitrogen. The influence of nitrogen on the dissolution behavior of ferritic steels needs to be established quantitatively.

The dissolution rates of austenitic Type 316 SS show an anomalous behavior, i.e., the rates are insensitive to a change in temperature in the range of 372 and 538°C. However, the data for total weight loss show significant variation. The large weight losses for austenitic steels arise primarily from the depletion of nickel from the steel and the alloy surfaces develop a porous ferrite scale. For most specimens, the surface nickel content is <1% irrespective of the temperature of exposure or total weight

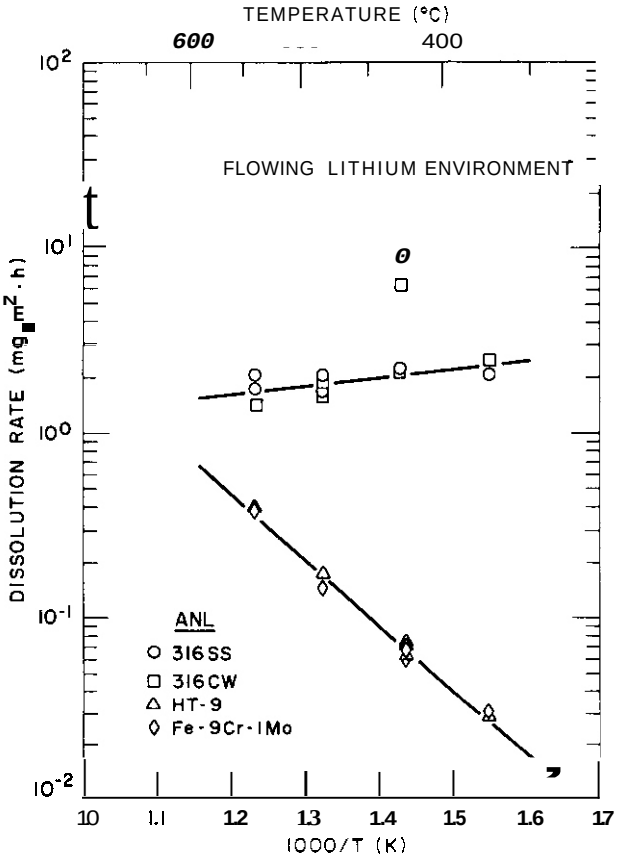

Fig. 9.3.1. Arrhenius plot of dissolution rate data for ferritic and austenitic steels exposed to flowing lithium.

loss of the specimens. However, the depletion of chromium is greater for specimens that show large weight loss and porosity, e.g., specimens exposed in high-nitrogen lithium (run 2). Nitrogen can react with alloy elements and lithium to form stable ternary nitrides, such as Li_9CrN_5 and Li_3FeN_2, and thus accelerate the dissolution process of ferrous alloys.[6,7]

The ternary nitrides are soluble in alcohol or water and, therefore, are not observed on clean corrosion specimens. The presence of the ternary nitrides was investigated by chemical analysis of the alcohol used for cleaning HT-9 or Type 316 SS specimens exposed for ~500 h in lithium at 538°C and 482°C (downstream location). The solutions were filtered before the analysis. The concentrations of major elements expressed as wppm of lithium dissolved in the methanol solutions are given in Table 9.3.3. The solutions used for cleaning the corrosion specimens contain significant amounts of Cr, Fe, and Mo. The Ni content in these solutions is the same as that in lithium solutions. The residues collected from the solutions contained primarily Cr and Fe. Ultraviolet-visible absorption spectroscopy of the solutions show that the chromium is present in the 6^+ oxidation state. These results indicate that corrosion products are present on the alloy surfaces. These products are probably ternary nitrides of Cr and Fe and they dissociate during the cleaning process.

9.3.5 Conclusions

The corrosion data indicate that dissolution of major alloy elements as well as chemical reactions, e.g., between nitrogen and chromium or iron, influence the corrosion behavior of ferrous alloys in flowing lithium. The formation of reaction products on the alloy surfaces may influence the dissolution behavior, particularly the dissolution of nickel from austenitic steels. Additional information on the effects of system parameters, such as lithium purity, system AT, location, etc., on the corrosion processes is needed to quantitatively establish the dissolution rates of ferrous alloys in lithium.

Table 9.3.3. Spectrochemical analysis of methanol used for cleaning corrosion specimens exposed to lithium at 538 and 482°C

	Major Elements (wppm)							
	538°C				482°C			
Alloy	Cr	Fe	Ni	Mo	Cr	Fe	Ni	Mo
HT-9	19	67	<15	10	42	33	<15	12
316 SS	46	68	13	135	207	31	14	60
Lithium	<5	17	13	<10	<5	18	<15	<10

9.3.6 References

1. O. K. Chopra and O. L. Smith. "Environmental Effects on Properties of Structural Alloys in Flowing Lithium." pp. 176-182 in Alloy Development for Irradiation Performance: Semiannual Progress Report for Period Ending March 31, 1984, DOE/ER-0045/12, Oak Ridge National Laboratory, Oak Ridge, TN, July 1984.
2. O. K. Chopra and D. L. Smith, "Environmental Effects on Properties of Structural Alloys in Flowing Lithium," pp. 182-191 in Alloy Development for Irradiation Performance: Semiannual Progress Report for Period Ending March 31, 1985, DOE/ER-0045/14, Oak Ridge National Laboratory, Oak Ridge, TN, July 1985.
3. O. K. Chopra and D. L. Smith, "Corrosion of Ferrous Alloys in a Flowing Lithium Environment," J. Nucl. Mat. 133&134, 861-866 (1985).
4. O. K. Chopra and D. L. Smith, "Corrosion of Austenitic and Ferritic Steels in Flowing Lithium Environment," pp. 171-179 in Alloy Development for Irradiation Performance: Semiannual Progress Report for Period Ending September 30, 1985, DOE/ER-0045/15, Oak Ridge National Laboratory, Oak Ridge, TN, February 1986.
5. M. G. Barker, P. Hubbersteg, A. T. Dadd, and S. A. Frankham, "The Interaction of Chromium with Nitrogen Dissolved in Liquid Lithium," J. Nucl. Mater. 114, 143-149 (1983).
6. E. Ruedl and T. Sasaki, "Effect of Lithium on Grain-Boundary Precipitation in a Cr-Mn Austenitic Steel," J. Nucl. Mater. 116, 112-122 (1983).

9.4 ENVIRONMENTAL EFFECTS ON PROPERTIES OF STRUCTURAL ALLOYS IN FLOWING Pb-17Li -- O. K. Chopra and O. L. Smith (Argonne National Laboratory)

9.4.1 AOIP Task

AOIP Task I.A.3, Perform Chemical and Metallurgical Compatibility Analyses.

9.4.2 Objective

The objective of this program is to investigate the influence of a flowing Pb-17 at. % Li environment on the corrosion behavior and mechanical properties of structural alloys under conditions of interest for fusion reactors. Corrosion behavior is evaluated by measuring the weight change and depth of internal corrosive penetration of alloy specimens exposed to flowing Pb-17Li for various times. The dissolution rates are determined as a function of temperature. Metallographic examination of the alloy surface is used to establish the mechanism and rate-controlling process for the corrosion reactions. Initial effort on mechanical properties is focused on tensile tests in a flowing Pb-17Li environment.

9.4.3 Sumnary

Corrosion data have been obtained on ferritic HT-9 and Fe-9Cr-1Mo steel and austenitic Type 316 stainless steel in a flowing Pb-17 at. % Li environment at temperatures between 371 and 482°C. The corrosion behavior is evaluated by measurements of weight loss and depth of internal corrosion as a function of time and temperature.

9.4.4 Progress and Status

The effects of a flowing Pb-17Li environment on the corrosion behavior and mechanical properties of ferritic and austenitic steels are being investigated.[1-5]

Tests are conducted in a forced-circulation loop consisting of a high-temperature test vessel, a heat exchanger section, and a cold-temperature chamber. The total volume of the loop was ~2 liters. A detailed description of the loop has been presented earlier.[2] Flat corrosion coupons, ~73 x 10 x 0.26 mm in size, of HT-9 alloy, Fe-9Cr-1Mo, and Type 316 stainless steel were exposed to flowing Pb-17Li, and the corrosion behavior was evaluated by measurements of weight loss and the depth of internal corrosive penetration. Four corrosion test runs of 2000 to 4000 h each were conducted at maximum temperatures of 371, 427, 454, and 482°C, respectively. For each test run, specimens were exposed at the maximum temperature position as well as at a downstream location. During runs 1 to 3, the temperature at the downstream position was 15 to 25°C lower than the maximum temperature, whereas the temperature at both locations was 371°C during run 4. The specimens were periodically removed from the loop for weight change measurements. For all corrosion tests, the cold-leg temperature was maintained at 300°C and the Pb-17Li alloy was circulated at a rate of ~350 cm^3/min. Several analyses of the eutectic alloy showed that the concentrations of O, H, and N were 260, 22, and <10 wppm, respectively.

9.4.4.1 Ferritic Steels

The corrosion behavior was evaluated by measuring the change in weight of the specimens exposed to flowing Pb-17Li for different times. The weight losses for HT-9 and Fe-9Cr-1Mo steel exposed at the maximum temperature location at 482, 454, 427, and 371°C are shown in Fig. 9.4.1a. The results indicate that the weight losses for both steels increase linearly with time and yield a constant dissolution rate. Specimens exposed at 482°C show significant weight loss after the initial 500-h exposure to Pb-17Li. The weight losses and dissolution rates for Fe-9Cr-1Mo steel relative to those for HT-9 alloy are comparable at 371°C and slightly lower at the higher temperatures. The dissolution rates for both steels increase with an increase in temperature.

The corrosion behavior of the specimens, which were exposed downstream from the maximum temperature location, is shown in Fig. 9.4.1b. The weight losses for these specimens also increase linearly with time and yield a constant dissolution rate. However, for a given time and temperature of exposure, the total weight loss and dissolution rate are lower than those observed for specimens exposed at the maximum temperature location. Downstream effects were quite obvious during run 4. For example, specimens of HT-9 and Fe-9Cr-1Mo steel exposed at the downstream location showed little or no weight loss.

Metallographic examination of HT-9 and Fe-9Cr-1Mo specimens from the various corrosion tests showed uniform dissolution as well as preferential attack along grain boundaries and martensitic lathe boundaries. Micrographs of the surface of HT-9 specimens exposed to flowing Pb-17Li at 427 and 482°C are shown in Fig. 9.4.2. The preferential attack is quite pronounced at 482°C and the specimen surface developed an etched appearance. The large weight loss after the initial 500-h exposure at 482°C may be attributed to such surface modifications. The specimens exposed at 482°C also show significant internal

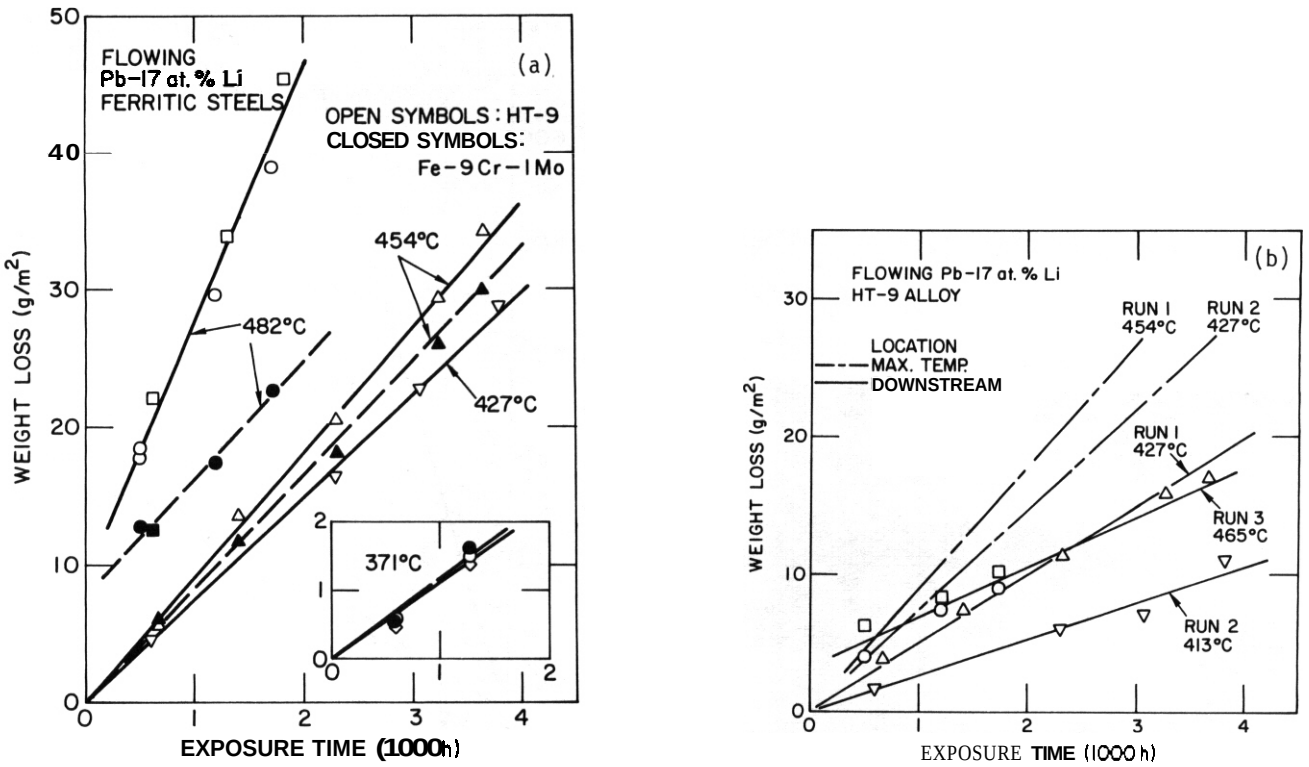

Fig. 9.4.1. Weight loss versus exposure time for ferritic steel specimens exposed to flowing Pb-17Li at (a) the maximum loop temperature and (b) downstream location.

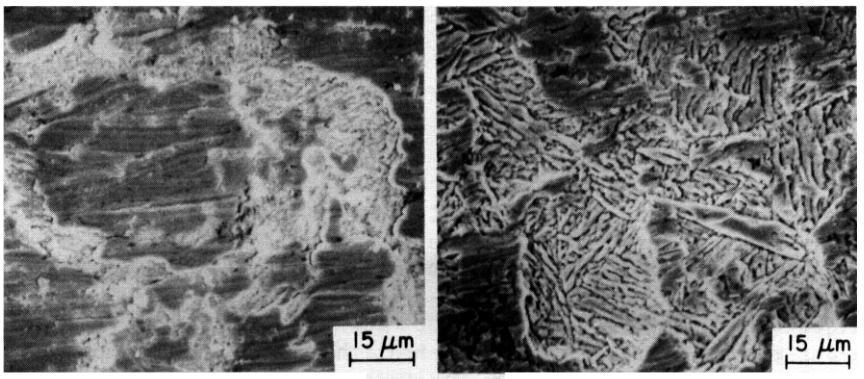

427%. 3808 H 482°C, 1720 H

Fig. 9.4.2. Micrographs of the surface of HT-9 alloy exposed to flowing Pb-17Li at (a) 427°C ana (b) 482°C.

corrosion, Fig. 9.4.3. The gray stringers observed at the surface are rich In chromium and correspond to the preferential attack along martensitic lathe boundaries. The specimens, which were located downstream at 465°C from the specimens exposed at 482°C (run 3), showed little or no internal corrosion. Examination of ferritic steel specimens fran tests at lower temperatures, i.e., runs 1, 2, and 4, revealed little or no internal corrosion.

9.4.4.2 Austenitic Stainless Steels

The corrosion behavior of annealed and 20% cold-worked Type 316 stainless steel exposed to flowing Pb-17Li at maximum loop temperatures of 482, 454, 427. and 371°C Is shown in Fig. 9.4.4. The weight losses for austenitic steels are an order of magnitude greater than those for the ferritic steels. Steady-state dissolution behavior achieved after an initial period of –500 h is characterized by very high dissolution rates. The large weight losses during the initial transient period represent the formation of a ferritic

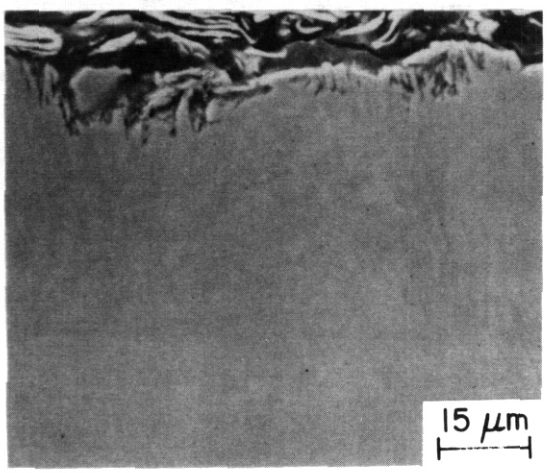

Fig. 9.4.3. Internal corrosion in HT-9 alloy exposed for 1729 h to flowing Pb-17Li at 482°C.

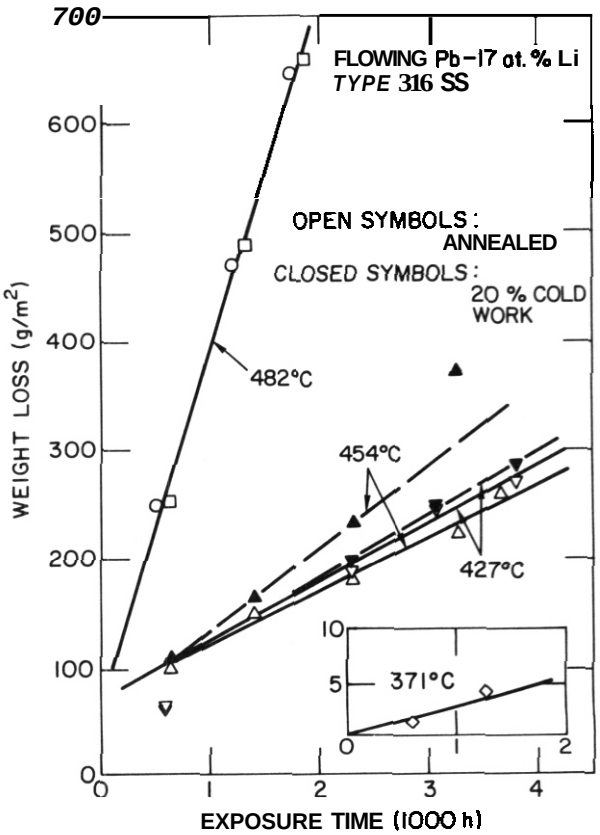

Fig. 9.4.4. Weight loss versus exposure time for Type 316 stainless steel specimens exposed to flowing Pb-17Li at the maximum loop temperature position.

surface layer due to complete depletion of nickel arid, to a lesser extent. chromium from the steel. The ferrite layer is very porous and breaks off easily. The thickness of the ferrite layer increases with time, e.g., at 454°C, the thickness increases from 26 μm at 1400 h to 47 μm after 3700 h.

Downstream effects were also observed for the austenitic stainless steel specimens. For a given time and temperature of exposure, the total weight loss and dissolution rate for the downstream specimens were lower than those for the specimens exposed at the maximum temperature location. The thickness of the ferrite layers was significantly smaller for the downstream specimens. For example, the average values for Type 316 stainless steel specimens exposed for ~1800 h at the maximum loop temperatures of 482. 454. and 427°C were 100, 30, and 17 μm, respectively. The thickness of the ferrite layer for specimens exposed downstream at 465°C for the same time was 23 μm. However, the composition of the ferrite layer was similar for all specimens. The distribution of major elementts, i.e., Ni, Cr, and Fe, across the ferrite layer on annealed Type 316 stainless steel exposed downstream at 465°C is shown in Fig. 9.4.5. The compositional changes in the ferrite layers formed in flowing Pb-17Li are different from those observed in austenitic steels exposed to a flowing lithium environment. Type 316 stainless steel exposed to lithium shows a slight depletion of chromium near the surface region of the ferrite layer, i.e., the distribution of chromium follows a diffusion profile.[6] Specimens exposed to Pb-17Li show a significant loss of chromium over the entire ferrite layer; the concentrations of chromium and nickel decrease rapidly across the scale/metal interface.

9.4.4.3 Dissolution Rates

The steady-state dissolution rates for HT-9, Fe-9Cr-1Mo, and annealed and 20% cold-worked Type 316 stainless steel in flowing Pb-17Li are given in Table 9.4.1. The Arrhenius plots of the results from the present investigation and data from other studies are shown in Fig. 9.4.6. Dissolution rate data obtained from other investigators[7-9] are also plotted in Fig. 9.4.6 and show good agreement with the results fran the

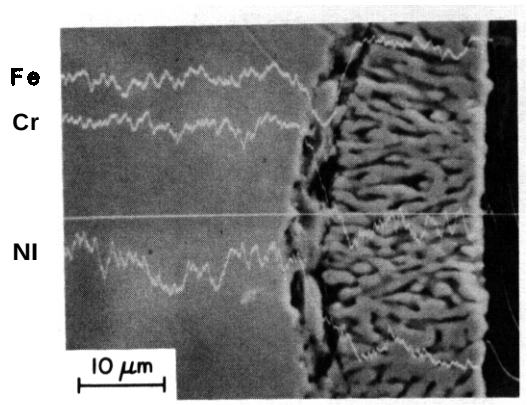

Fig. 9.4.5. Concentration profiles for major elements across the ferritic layer of Type 316 stainless steel exposed to Pb-17Li for 1729 H at 465°C.

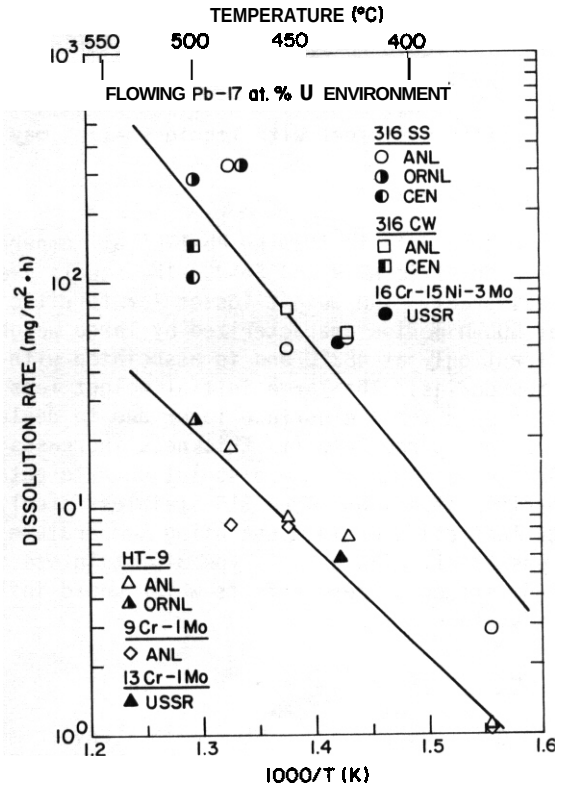

Fig. 9.4.6. Arrhenius plots of dissolution data for ferritic and austenitic steels exposed to flowing Pb-17Li. ANL: Argonne National Laboratory; ORNL: Oak Ridge National Laboratory; CEN: Centre D'Etudes Nucleaires, France; USSR: Soviet Union contribution to INTOR.

Table 9.4.1. Dissolution rates for ferritic and austenitic steels exposed to flowing Pb-17Li

Run Number	Temp. (°C)	Maximum Time (h)	Dissolution Rate ($mg/m^2 \cdot h$) HT-9	9Cr-1Mo	314 SS	316 CW
1	454	3663	9.0	8.2	50.1	75.9
1	427[a]	3663	5.1	4.9	26.1	27.4
2	427	3808	7.4	-	55.1	58.6
2	413[a]	3808	2.6	-	23.9	31.1
3	482	1849	18.3	8.3	325.1	-
3	465[a]	1849	3.8	1.9	45.0	-
4	371	1269	1.1	1.1	2.8	-
4	371[a]	1269	0.4	0.4	1.0	-

[a]Specimens were located downstream fran the maximum loop temperature position.

present study. The lines represent the best fit for the dissolution rates of ferritic HT-9 and Fe-9Cr-1Mo steels and Type 316 stainless steel. The results yield activation energies of 22.1 and 28.6 kcal/mole for ferritic and austenitic steels, respectively.

The dissolution rates for ferritic steels are a factor of 5 to 10 lower than those for the austenitic Type 316 stainless steel. Mass transfer and deposition are likely to be the most restrictive criteria for corrosion in liquid Pb-17Li first wall/blanket systems. Assuming a corrosion limit of 20 μm/yr, i.e., 22 $mg/m^2 \cdot h$ uniform dissolution, would yield a maximum operating temperature of ~500°C for HT-9 alloy and ~410°C for Type 316 stainless steel in circulating Pb-17Li systems. The results indicate that the use of Type 316 stainless steel with liquid Pb-17Li may be impractical.

9.4.5 Conclusions

Corrosion data in flowing Pb-17Li at temperatures between 371 and 482°C indicate that the dissolution rates for ferritic HT-9 and Fe-9Cr-1Mo steels are an order of magnitude lower than those for Type 316 stainless steel. The weight losses for ferritic and austentic steels increase linearly with time after an initial 500-h period characterized by large weight loss. The initial weight loss for ferritic steels is significant only at 482°C and is associated with preferential attack along grain boundaries and martensitic lathe boundaries. The large initial weight loss for Type 316 stainless steel is associated with the formation of a ferrite surface layer due to depletion of nickel and chromium from the steel. The ferrite layer is very porous and its thickness increases with time.

Arrhenius plots of the dissolution rate data yield activation energies of 22.1 and 28.6 kcal/mole for the ferritic steels and Type 316 stainless steel, respectively. For a corrosion limit of 20 μm/yr, the results indicate a maximum operating temperature of ~500°C for ferritic steels and ~410°C for Type 316 stainless steel. The use of Type 316 stainless steel with a Pb-17Li environment may not be practical. Data also indicate downstream effects which would influence the dissolution behavior of alloys in circulating Pb-17Li systems.

9.4.6 References

1. O. K. Chopra and D. L. Smith, "Environmental Effects on Properties of Structural Alloys," pp. 216-200 in Alloy Development for Irradiation Performance: Semiannual Progress Report for Period Ending September 30, 1983, DOE/ER-0045/11, Oak Ridge National Laboratory, Oak Ridge, TN, March 1984.

2. O. K. Chopra and D. L. Smith, "Corrosion of Ferrous Alloys in Eutectic Lead-Lithium Environment," J. Nucl. Mater. 122-123, 1219-1224 (1984).

3. O. K. Chopra and D. L. Smith, "Corrosion of Structural Alloys in Flowing Pb-17Li Environment," pp. 183-189 in Alloy Development for Irradiation Performance: Semiannual Progress Report for Period End March 31, 1984, DOE/ER-0045/12, Oak Ridge National Laboratory, Oak Ridge, TN, July 1984.

4. O. K. Chopra and D. L. Smith, "Environmental Effects on Properties of Structural Alloys in Flowing Lithium," pp. 192-196 in Alloy Development for Irradiation Performance: Semiannual Progress Report for Period Ending March 31, 1985, DOE/ER-0045/14, Oak Ridge National Laboratory, Oak Ridge TN, July 1985.

5. O. K. Chopra and D. L. Smith, "Environmental Effects on Properties of Structural Alloys in Flowing Lithium," pp. 167-170 in Alloy Development for Irradiation Performance: Semiannual Progress Report for Period Ending September 30, 1985, DOE/ER-0045/15, Oak Ridge National Laboratory, Oak Ridge, TN, February 1986.

6. O. K. Chopra and D. L. Smith, "Corrosion of Ferrous Alloys in a Flowing Lithium Environment," J. Nucl. Mater. 133&134, 861-866 (1985).

7. P. F. Tortorelli and J. H. DeVan, "Corrosion of Type 316 Stainless Steel and 12Cr-1MoVW in Thermally Convective 19-17 at. % Li," pp. 205-207 in Alloy Development for Irradiation Performance: Semiannual Progress Report for Period Ending March 31, 1985, DOE/ER-0045/14, Oak Ridge National Laboratory, Oak Ridge, TN, July 1985.

8. P. Fauvet, J. Sannier, and G. Santarini, "Corrosion of 316L Stainless Steel in Flowing 17Li83Pb Alloy," 13th Symposium on Fusion Technology, Varese, Italy, September 1984.

9. V. I. Nikitin et al., "Experimental Study of Selected Structural Materials Corrosion Resistivity in Pb-Li Eutectic," USSR Contribution to Phase IIA of the INTOR Workshop, October 1982.

10. STATUS OF IRRADIATION EXPERIMENTS AND MATERIALS INVENTORY

10.1 FUSION PROGRAM RESEARCH MATERIALS INVENTORY – T. K. Roche (Oak Ridge National Laboratory). J. W. Davis (McOonnell Douglas Astronautics Company – St. Louis Division), and T. A. Lechtenberg (GA Technologies)

10.1.1 ADIP Task

ADIP Task I.D.l, Materials Stockpile for Magnetic Fusion Energy Programs.

10.1.2 Objective

Oak Ridge National Laboratory maintains a central inventory of research materials to provide a common supply of materials for the Fusion Reactor Materials program. This will minimize unintended material variations and provide for economy in procurement and for centralized record-keeping. Initially this inventory is to focus on materials related to first-wall and structural applications and related research, but various special-purpose materials may be added in the future.

The use of materials from this inventory that is coordinated with or otherwise related technically to the Fusion Reactor Materials program of the Department of Energy is encouraged.

10.1.3 Materials Requests and Release

Materials requests shall be directed to the Fusion Program Research Materials Inventory at ORNL (Attention: T. K. Roche). Materials will be released directly if *(a)* the material is to be used for programs funded by the Office of Fusion Energy, with goals consistent with the approved Materials Program Plans of the Materials and Radiation Effects Branch and *(b)* the requested amount of material is available without compromising other intended uses.

Materials requests that do not satisfy both *(a)* and *(b)* will be discussed with the staff of the Reactor Technologies Branch, Office of Fusion Energy, for agreement on action.

10.1.4 Records

Chemistry and materials preparation records are maintained for all inventory materials. All materials supplied to program users will be accompanied by summary characterization information.

10.1.5 Summarv of Current Inventory and Material Movement During Period October 1. 1985 through March 31. 1986

A condensed, qualitative description of the content of materials in the Fusion Program Research Materials Inventory is given in Table 10.1.1. This table indicates the nominal diameter of rod or thickness of sheet for product forms of each alloy and also indicates by weight the amount of each alloy in larger sizes available for fabrication to produce other product forms as needed by the program. No material was added to the inventory during this reporting period. Table 10.1.2 gives the materials distributed from the Inventory.

Alloy compositions and more detail on the alloys and their procurement and/or fabrication are given in this and earlier ADIP progress reports.

Table 10.1.1. Summary status of materials available in the fusion program research materials inventory

Alloy	Product form			
	Ingot or bar[a] weight (kg)	Rod diameter (mm)	Sheet thickness (mm)	Thin-wall tubing wall thickness (mm)
		Path A Alloys		
Type 316 SS	900	16 and 7.2	13 and 7.9	0.25
Path A PCA[b]	490	12	13	0.25
USSR Cr-Mn steel'		10.5	2.6	
NONMAGNE 30[d]		18.5	10	

Table 10.1.1 (continued)

Alloy	Product form			
	Ingot or bar[a] weight (kg)	Rad diameter (mm)	Sheet thickness (mm)	Thin-wall tubing wall thickness (mm)
		Path B Allays		
PE-16	140	16 and 7.1	13 and 1.6	0.25
E-1	180			
B-2	180			
B-3	180			
B-4	180			
B-6	180			
		Path C Allays		
Ti-64			2.5 and 0.76	
Ti-62428		63	6.3., 3.2. 0.76	
Ti-5621s			2.5 and 6.76	
Ti-38644			0.76 and 0.25	
Nb-l%Zr		6.3	2.5, 1.5, 0.76	
Nb-5%Mo-1%Zr		6.3	2.5, 1.5, 0.76	
V-20%Ti		6.3	2.5, 1.5, 0.76	
V-15%Cr-5%Ti		6.3	2.5., 1.5., 0.76	
VANSTAR-7		6.3	2.5, 1.5, 0.76	
		Path D Allay		
LRO-37e			3.3, 1.6, 0.8	
		Path E Allays		
HT9 (AOD fusion heat)[f]	3400		28.5, 15.8, 9.5, 3.1	
HT9 (AOD/ESR fusion heat)	7000	25, 50, 75	28.5, 15.8, 9.5, 3.1	
HT9			4.5 and 18	
HT9 + 1%Ni			4.5 and 18	
HT9 + 2% Ni			4.5 and 18	
HT9 + 2% Ni + Cr adjusted			4.5 and 18	
T-9 modified[g]			4.5 and 18	
T-9 modified + 2% Ni			4.5 and 18	
T-9 modified + 2% Ni + Cr adjusted			4.5 and 18	
2 1/4 Cr-1Mo			h	

[a]Greater than 25 mm, minimum dimension.

[b]Prime candidate alloy.

[c]Rod and sheet of a USSR stainless steel supplied under the U.S./USSR Fusion Reactor Materials Exchange program.

[d]NONMAGNE 30 is an austenitic steel with base composition Fe-14%Mn-2%Ni-2%Cr. It was supplied to the inventory by the Japanese Atomic Energy Research Institute.

[e]LRO-37 is the ordered alloy $(Fe,Ni)_3(V,Ti)$ with composition Fe-39.4%Ni-22.4%V-0.43%Ti.

[f]Alloy 12Cr-1MoVW with composition equivalent to Sandvik alloy HT9.

[g]T-9 modified is the alloy 9Cr-1MoVNb.

[h]Material is thick-wall pipe, rerolled as necessary to produce sheet or rod.

Table 10.1.2. Fusion program research materials inventory disbursements October 1, 1985 through March 31, 1986

Alloy	Heat	Product form	Dimension[a] (mm)	Quantity (m^2)	Sent to
Path A Alloys – Austenitic Stainless Steels					
Type 316SS[b]	X-15893	Sheet	0.76	0.076	Radiation Effects Group, M&C Division, ORNL
Path C Alloys – Reactive and Refractory Alloys					
V-15Cr-5%Ti	CAM 834	Sheet	0.86	0.058	Radiation Effects Group, M&C Division, ORNL
V-20% Ti	CAM 833	Sheet	0.91	0.012	Grumman Aerospace Corp.
Vanstar-7	CAM 836	Sheet	0.76	0.010	Grumman Aerospace Corp.

[a]Characteristic dimensions: thickness for plate and sheet, diameter for rod and tubing.

[b]Program reference material.

10.2 IRRADIATION EXPERIMENT STATUS AND SCHEDULE – M. L. Grossbeck (Oak Ridge National Laboratory)

A large number of planned, in-progress, and completed reactor experiments support the ADIP program. Table 10.2.1 summarizes the parameters that describe completed experiments. Experiments that have been removed from the reactor recently, that are now undergoing irradiation, or that are planned for future irradiation are shown in the schedule bar charts of Table 10.2.2.

Experiments were under way during the reporting period in the Oak Ridge Research Reactor (ORR) and the High Flux Isotope Reactor (HFIR), which are mixed-spectrum reactors, and in the Fast Flux Test Facility (FFTF), which is a fact reactor.

During the reporting period, four irradiation vehicles were removed from the HFIR. All were part of the U.S./Japan cooperative irradiation program. No new capsule irradiations were initiated in HFIR, reflecting the trend to longer irradiation times and fewer capsules as well as the period of planning advanced irradiation techniques such as those using isotopic tailoring.

Spectral tailoring experiments continue irradiation in the ORR also as part of the joint U.S./Japan program. In addition, a large irradiation experiment continues in the FFTF. Specimens are scheduled for discharge in July 1986 with new specimens being added and irradiation continued.

Table 10.2.1. Descriptive parameters for completed AOIP program fission reactor irradiation experiments

Experiment	Major Objective	Alloy	Temperature (°C)	Displacement Damage (dpa)	Helium (at. ppm)	Duration (months)	Date Completed
		Experiments in ORR					
ORR-MFE-1	Scope the effects of composition and microstructure on tehsile, fatigue, and irradiation creep	Paths A, B, C	250–600	2	<10	4	6/78
om-m-2	Scope the effects of composition and microstructure on tensile, fatigue, and irradiation creep	Paths A, B, C	300–600	6	'60	15	4/80
ORR-MFE-5	In-reactor fatigue crack growth	Path A	325–460	1	<10	2	2/81
		Experiments in EBR-II					
Subassembly X-264	Effect of preinjected helium on microstructure, tensile properties and irradiation creep	316, PE-16, V–20%Ti, V–15%Cr–5%Ti, Nb–1%Zr	500–825	8	2–200	4	1/77
AA-X, Subassembly X-287	Effect of preinjected helium on microstructure, tensile properties, and irradiation creep	316, PE-16, V–20%Ti, V–15%Cr–5%Ti, Nb–1%Zr	400–700	20	2–200	23	12/78
AD-1, Subassembly X-217D	Stress relaxation Swelling, fatigue crack growth, and tensile properties	Ti alloys Ti alloys	450 370–550	2 25		1 14	1/78 9/79
AD-2, Subassembly X344B	Tensile, fatigue, fracture toughness, Charpy, microstructure, and crack growth	Path E	390, 450, 500, 550	14,30		10,24	6/81, 4/83
		Experiments in HFIR					
HFIR-CTR-3	Swelling and tensile properties	PE-16, Inconel 600	300–700	4.3–9	350–1800	3	2/75
HFIR-CTR-4	Swelling and tensile properties	PE-16	300–700	2.2–4.5	100–350	2	3/77
HFIR-CTR-5	Swelling and tensile properties	PE-16, Inconel 600	300–700	4.3–9	350–1800	3	6/15
HFIR-CTR-6	Swelling and tensile properties	PE-16, Inconel 600	300–700	4.3–9	350–1800	3	4/75
HFIR-CTR-7	Swelling and tensile properties	PE-16	300–700	9–18	1250–3000	7	8/17
HFIR-CTR-8	Swelling and tensile properties	PE-16	300–700	9–18	1250–3000	7	8/77
HFIR-CTR-9	Swelling and tensile properties	316, 316 + Ti	280–680	10–16	400–1000	6	5/77
HFIR-CTR-10	Swelling and tensile properties	316, 316 + Ti	280–680	10–16	400–1000	6	5/77
HFIR-CTR-11	Swelling and tensile properties	316, 316 + Ti	280–680	10–16	400–1000	6	5/17
HFIR-CTR-12	Swelling and tensile properties	316, 316 + Ti	280–680	7–10	200–500		2/77
HFIR-CTR-13	Swelling and tensile properties	316, 316 + Ti	280–680	7–10	200–500		2/77

Table 10.2.1. (continued)

Experiment	Major Objective	Alloy	Temperature (°C)	Displacement Damage (dpa)	Helium (at. ppm)	Duration (months)	Date Completed
HFIR-CTR-14	Fatigue	316	430	9–15	400–100[illegible]	[illegible]	11/77
HFIR-CTR-15	Fatigue	316	550	6–9	200–400	4	10/78
HFIR-CTR-16	Weld characterization, swelling, and tensile properties	316, PE-16, Inconel 600	55	6–9	150–270	4	8/71
HFIR-CTR-17	Weld characterization	316	280–620	7–13	180–460	5.5	10/77
HFIR-CTR-18	Swelling and tensile properties	316, PE-16	280–700	17–27	1600–560	12	6/78
HFIR-CTR-19	Weld characterization	316	280–620	7–10	200–500	4	12/77
HFIR-CTR-20	Fatigue	316	430	6–9	200–400	4	1/78
HFIR-CTR-21	Fatigue	316	550	9–15	400–100	7	7/78
HFIR-CTR-22	Fatigue	316	430	6–9	200–400	4	3/78
HFIR-CTR-23	Fatigue	PE-16	430	6–9	370–100	3.5	2/79
HFIR-CTR-24	Temperature calibration and tensile properties	316	300–620	2.2	30	1	12/78
HFIR-CTR-26	Swelling and tensile properties	316	284–620	30	1900	10	4/80
HFIR-CTR-27	Swelling and tensile properties	316	284–620	56	3500	18	1/81
HFIR-CTR-28	Swelling and tensile properties	316	370–560	30	1900	10	12/80
HFIR-CTR-29	Swelling and tensile properties	316	370–560	56	3500	18	8/81
		Experiments in HFIR					
HFIR-CTR-30	Swelling, microstructure, and ductility	Paths A, B, C, D, and E	300–600	40	<15,000	14	11/81
HFIR-CTR-31	Swelling, microstructure, and ductility	Paths A, B, C, D, and E	300–600	20	< 7,500	8	5/81
HFIR-CTR-32	Swelling, microstructure, and ductility	Paths A, B, C, D, and E	300–600	10	< 3,000		12/81
HFIR-CTR-33	Swelling, tensile properties, and weld characterization	Paths A and E	55	10	< 510		10/80
HFIR-CTR-34	Charpy	Path E	300, 400	10	0–75		5/82
HFIR-CTR-35	Charpy	Path E	300, 400	10	0–75		5/82
HFIR-CTR-36	Fatigue	316 PCA	430, 550	30	2,000	13	5/83
HFIR-CTR-39	Swelling and tensile properties	Path E	300–500	12	0–90		10/82
HFIR-CTR-40	Swelling and tensile properties	Path E	300–500	12	0–90		12/82
HFIR-CTR-41	Swelling and tensile properties	Path E	300–500	12	0–90		[illegible]
HFIR-CTR-42	Swelling, tensile microstructure	Paths A, D	300–600	20	1100	8	6/83
HFIR-CTR-43		Similar to HFIR-CTR-42					
HFIR-CTR-44[a]	Swelling, tensile	Path A	250–400	10	[illegible]		5/83
HFIR-CTR-45		Similar to HFIR-CTR-44					
HFIR-CTR-46	Charpy	Path E	300–400	10	75	[illegible]	6/83
HFIR-MFE-RB1	Swelling, microstructure, crack growth, fracture toughness, Charpy, tensile, and fatigue	Path E	55	10	90	8	7/82
HFIR-MFE-RB2	Swelling, microstructure, crack growth, fracture toughness, Charpy, tensile, and fatigue	Path E	55	2	200	17	7/83
HFIR-MFE-T1	Swelling, tensile fatigue	Path E	55	30	<300	12	8/82
HFIR-MFE-T2	Swelling and tensile fatigue	Path E	55	9	< 75	3	5/81
HFIR-MFE-T3	Impact properties	Path E	55	10	< 85	4	12/81

[a] Similar U.S. /RC/IN

Table 10.2.2. Objectives and schedule for current and planned ADIP program reactor irradiation experiments

Experiment designation	Major objective
A. Oak Ridge Research Reactor	
ORR-MFE-4	Effect of irradiation on tensile, fatigue, and irradiation creep of path A PCA (Prime Candidate Alloy) and path B base research alloys. Spectral tailoring to maintain correct He/dpa ratio. (1)
ORR-MFE-6J	Swelling, tensile, irradiation creep fatigue, crack growth, and microstructure of path A alloys. 60 and 200°C. Evaluated at 10 to 15 dpa intervals. Employs spectral tailoring to achieve fusion He:dpa value.
ORR-MFE-7J	Similar to ORR-MFE-6J but 300 and 400°C.
B. Fast Flux Test Facility (FFTF)	
FFTF MOTA Fusion Experiment	Microstructural and mechanical properties of Path A, C, and E alloys.

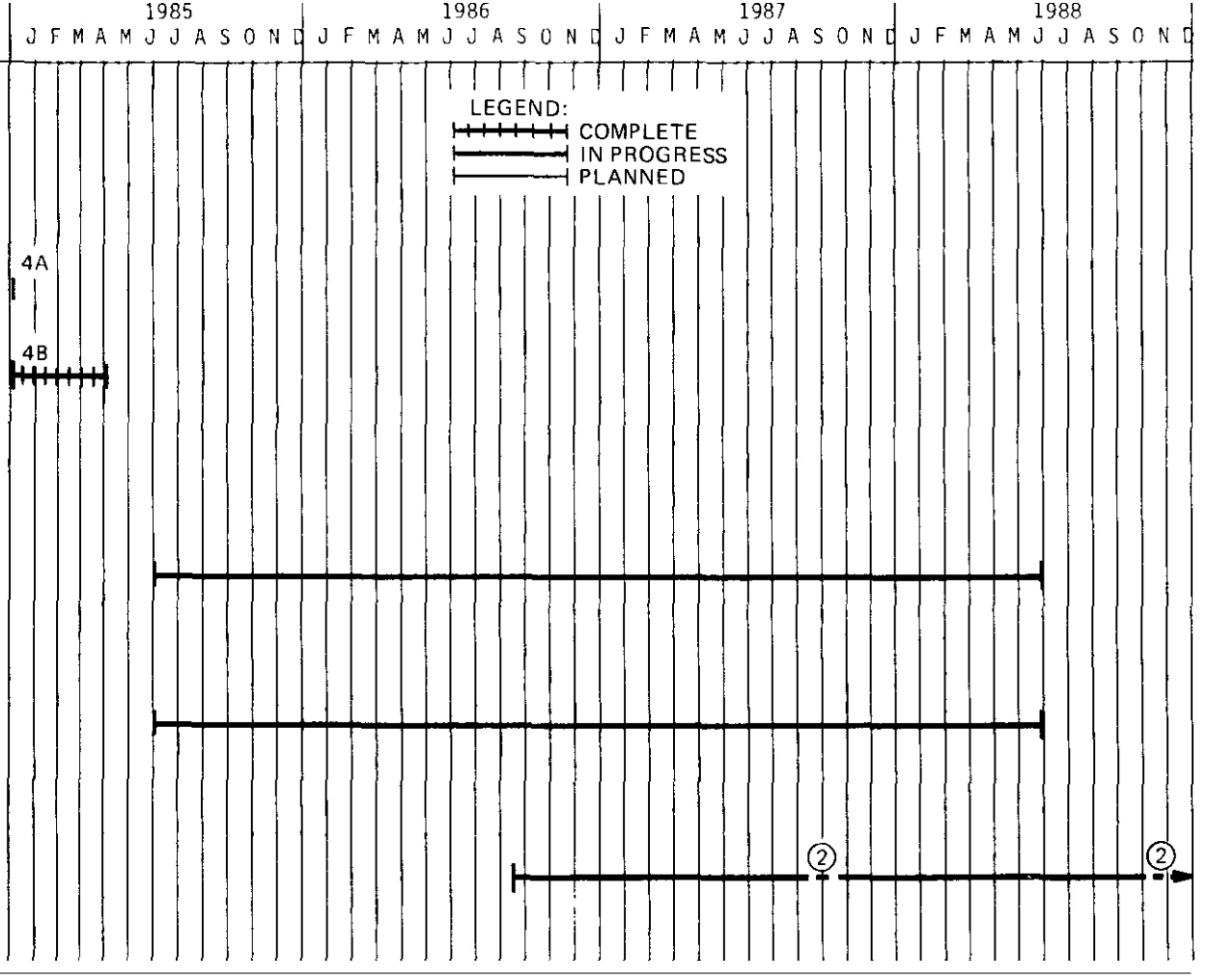

(1) MFE 4A operated at 330 and 400 C MFE 4B operated at 500 and 600 C

(2) Removed for specimen discharge.

(3) Reactor down for refueling.

(4) The HFIR-JP experiment series is a joint program shared by the U.S. and Japan Fusion Reactor Materials activities.

Experiment designation	Major objective
C. High Flux Isotope Reactor (HFIR)	
HFIR-CTR-36	Fatigue properties of path A alloys. 30 dpa, 2000 ppm He.
HFIR-CTR-47	Impact properties of path E alloys. 40 dpa, 400 ppm He, 300 and 400°C.
HFIR-CTR-48	Similar to HFIR-CTR-47.
HFIR-CTR-49	Tensile properties and microstructure of path E alloys. 50 dpa, 70 to 500 ppm He, 300 to 500°C.
HFIR-CTR-50	Tensile, swelling, microstructure of path E alloys, 100 dpa, 150 to 1000 ppm He, 400, 600°C.
HFIR-CTR-51	Swelling, tensile properties of low-activation alloys. 20 dpa, 300–600°C
HFIR-CTR-52	Fatigue properties of 316 SS. 10 dpa, 500 ppm He 430°C. Joint experiment with European community and Japan
HFIR-CTR-53	Impact properties of path E alloys. 10 dpa 0 ppm He, 200, 300°C, one-third size Charpy.
HFIR-CTR-54	Similar to HFIR-CTR-53
HFIR-CTR-55	Tensile swelling, microstructure of path E and low activation alloys. 50 dpa, 400 ppm He, 400, 600°C.
HFIR-CTR-56	Tensile, swelling microstructure of path E and low activation alloys. 100 dpa, 150–1000 ppm He, 400, 600°C.

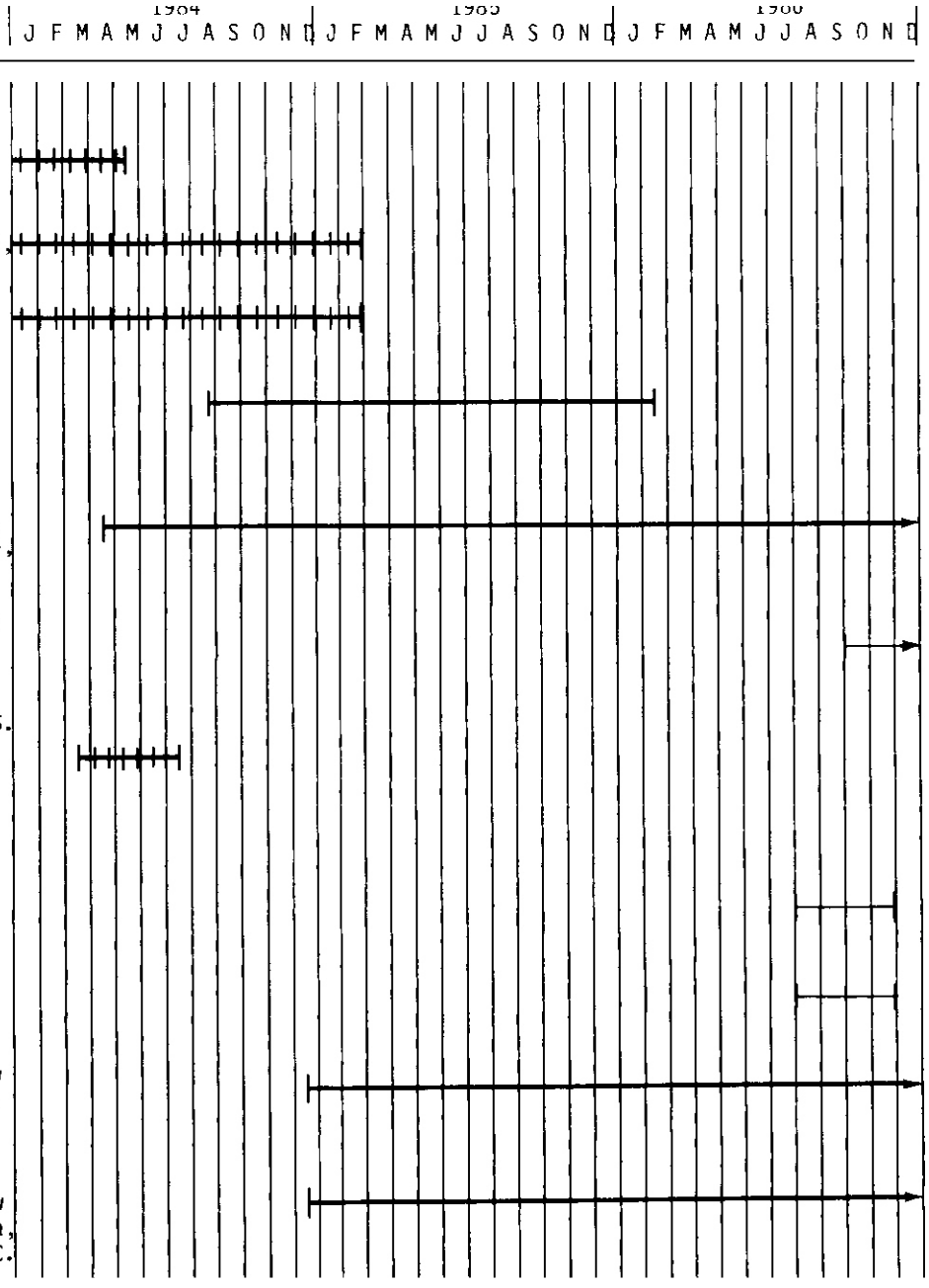

Experiment designation	Major objective
HFIR-JP-1(4)	Swelling, tensile and fatigue properties, and microstructure of path A alloys. 300–600°C, 30 dpa, 2000 ppm He.
HFIR-JP-2	Similar to HFIR-JP-1 but to 50 dpa, 3500 ppm He.
HFIR-JP-3	Similar to HFIR-JP-1.
HFIR-JP-4	Swelling, tensile properties, and microstructure of path A alloys. 55°C, 50 dpa, 2000 ppm He.
HFIR-JP-5	Similar to HFIR-JP-2.
HFIR-JP-6	Similar to HFIR-JP-1.
HFIR-JP-7	Similar to HFIR-JP-1.
HFIR-JP-8	Similar to HFIR-JP-2.

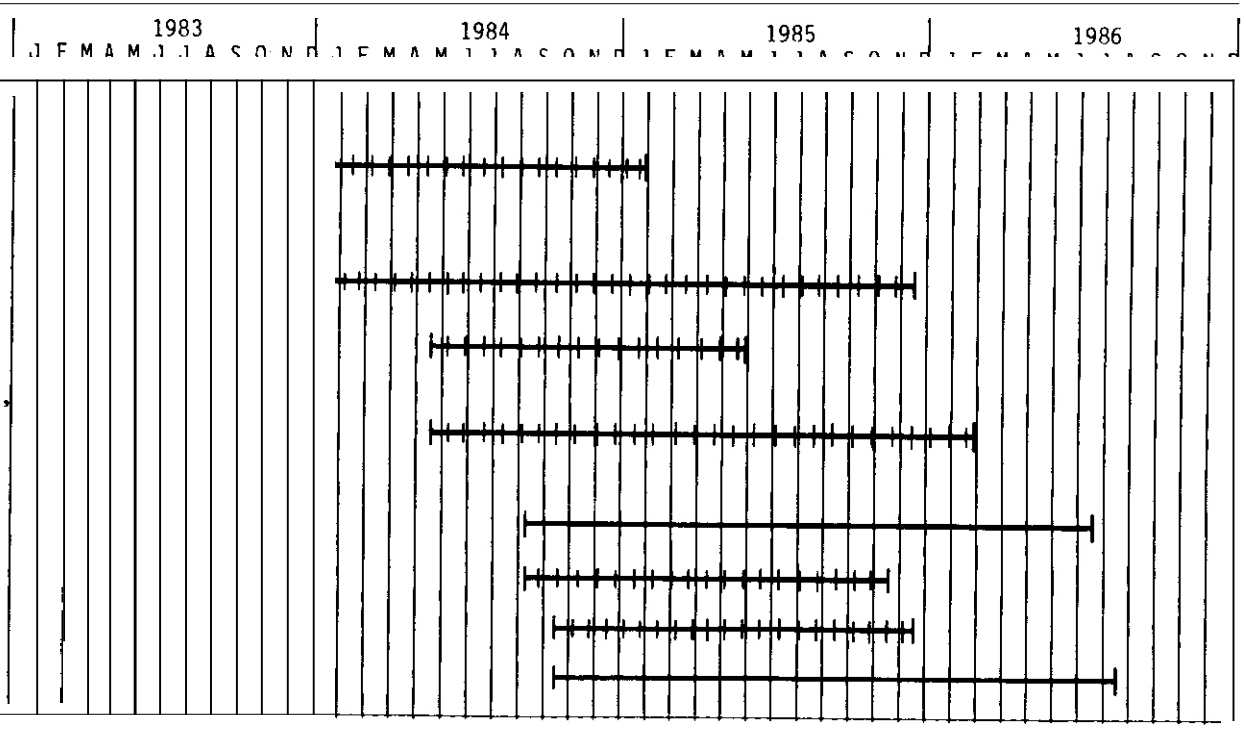

DOE/ER-0045/16
Distribution
Categories
uc-20, 20c

DISTRIBUTION

1–6. Argonne National Laboratory, 9700 South Cass Avenue, Argonne, IL 60439

L. Greenwood
B. A. Loomis
V. Maroni
R. F. Mattas
O. L. Smith
H. Wiedersich

7. Auburn University, Department of Mechanical Engineering, Auburn, AL 36849

B. A. Chin

8–9. Battelle-Pacific Northwest Laboratory, P.O. Box 999, Richland, WA 99352

J. L. Brimhall
J. L. Straalsund

10. Brookhaven National Laboratory, Upton, NY 11973

C. L. Snead, Jr.

11. Carnegie-Mellon University, Pittsburgh, PA 15213

J. C. Williams

12. Colorado School of Mines, Golden, CO 80401

G. R. Edwards

13–196. Department of Energy, Technical Information Center, Office of Information Services, P.O. Box 62, Oak Ridge, TN 37831

For distribution as shown in DOE/TIC-4500 Distribution Categories UC-20 (Magnetic Fusion Energy), and UC-20c (Reactor Materials)

197–203. Department of Energy, Office of Fusion Energy, Washington, DC 20545

M. M. Cohen
G. M. Haas
T. C. Reuther, Jr. (5 copies)

204. Department of Energy, Oak Ridge Operations Office, P.O. Box E, Oak Ridge, TN 37831

Office of Assistant Manager for Energy Research and Development

205. Energy Technology Engineering Center, P.O. Box 1449, Canoga Park, CA 91304

ETEC Library

206–207. GA Technologies, Inc., P.O. Box 81608, San Diego, CA 92138

T. A. Lechtenberg
D. I. Roberts

208–210. Lawrence Livermore National Laboratory, P.O. Box 808, Livermore, CA 94550

E.N.C. Dalder
M. Guinan
C. M. Logan

211. Los Alamos National Laboratory, P.O. Box 1663, Los Alamos, NM 87545

R. J. Livak

212. Massachusetts Institute of Technology, 138 Albany Street, Cambridge, MA 02139

O. K. Harling

213. Massachusetts Institute of Technology, 77 Massachusetts Ave., Cambridge, MA 02139

N. J. Grant

214. McOonnell Douglas Astronautics Company, East, P.O. Box 516, St. Louis, MO 63166

J. W. Davis

215. National Materials Advisory Board, 2101 Constitution Ave., Washington, DC 20418

K. M. Zwilsky

216–217. Naval Research Laboratory, Washington, DC 20375

Superintendent, Materials Science and Technology Division
J. A. Sprague

218. Northwestern University, Department of Materials Science and Engineering, Evanston, IL 60201

J. R. Weertman

219–254. Oak Ridge National Laboratory, P.O. Box X, Oak Ridge, TN 37831

Central Research Library (2 copies)
Document Reference Section
Laboratory Records Department (2 copies)
Laboratory Records Department, RC
ORNL Patent Section
L. A. Berry
E. E. Bloom
O. N. Braski
W. R. Corwin
J. H. DeVan
M. L. Grossbeck
S. Hamada
R. L. Klueh
R. A. Lillie
C. T. Liu
K. C. Liu
L. K. Mansur
P. J. Maziasz
C. J. McHargue
T. K. Roche
A. F. Rowcliffe (2 copies)
M. J. Saltmarsh
J. L. Scott
I. Siman-Tov
M. P. Tanaka
K. R. Thoms
P. T. Thornton (3 copies)
P. F. Tortorelli
J. M. Vitek
C. D. West
S. J. Zinkle

255. Princeton University, Plasma Physics Laboratory, P.O. Box 451, Princeton, NJ 08544

P. Bonanos

256–257. Rensselaer Polytechnic Institute, Troy, NY 12181

D. Steiner
N. Stoloff

258–259. Sandia National Laboratories, Livermore Division 8316, Livermore, CA 94550

W. Bauer
J. C. Lippold

260–261. Sandia National Laboratories, P.O. Box 5800, Albuquerque, NM 87185

M. J. Davis
W. B. Gauster

262. Science Applications, Inc., 1200 Prospect, La Jolla, CA 92037

H. Gurol

263–265. University of California, Department of Chemical, Nuclear, and Thermal Engineering, Los Angeles, CA 90024

M. A. Abdou
R. W. Conn
N. M. Ghoniem

266. University of California, Santa Barbara, CA 93106

G. R. Odette

267. University of Missouri, Department of Mechanical and Aerospace Engineering, Columbia, MO 65211

M. Jolles

268. University of Virginia, Department of Materials Science, Charlottesville, VA 22901

W. A. Jesser

269. University of Wisconsin, 1500 Johnson Drive, Madison, WI 53706

G. L. Kulcinski

270. Westinghouse Electric Company, Advanced Energy Systems Division, P.O. Box 10864, Pittsburgh, PA 15236

W. A. Boltax

271–277. Westinghouse Hanford Company, P.O. Box 1970, Richland, WA 99352

H. R. Brager
D. G. Doran
A. M. Ermi
F. A. Garner
O. S. Gelles
E. C. Opperman
R. W. Powell

278. Westinghouse Research and Development Center, 1310 Beulah Road, Pittsburgh, PA 15235

J. A. Spitznagel

☆ U.S. GOVERNMENT PRINTING OFFICE: 1986-631-056/40072